Density Profiles of Plasmas Confined by the Field of a Levitating, Dipole Magnet

by

Alexander C. Boxer

Submitted to the Department of Physics
in partial fulfillment of the requirements for the degree of

Doctor of Philosophy in Physics

at the

MASSACHUSETTS INSTITUTE OF TECHNOLOGY

September 2008

Author . . . .
Department of Physics
September 5, 2008

Certified by . . . .
Jay Kesner
Senior Research Scientist
Thesis Supervisor

Certified by . . . .
Miklos Porkolab
Professor of Physics
Thesis Supervisor

Accepted by . . . .
Thomas Greytak
Chairman, Department Committee on Graduate Students

Density Profiles of Plasmas Confined by the Field of a Levitating, Dipole Magnet

by

Alexander C. Boxer

Submitted to the Department of Physics
on September 5, 2008, in partial fulfillment of the
requirements for the degree of
Doctor of Philosophy in Physics

Abstract

A 4-channel microwave interferometer (center frequency: 60 GHz) has been constructed to measure the density profiles of plasmas confined within the Levitated Dipole Experiment (LDX). LDX is the first and only experiment built to study plasmas confined by the field of a levitating, dipole magnet in a geometry that exploits plasma compressibility to achieve stability. Theoretical predictions—based partly on observations of planetary magnetospheres—suggest that dipole-confined plasmas will be driven by fluctuations into pressure and density profiles that are "stationary" to MHD interchange modes. The stationary pressure profile is characterized by an equal amount of entropy per flux-tube while the stationary density profile is characterized by an equal number of particles per flux-tube. These predictions are of interest to nuclear fusion research since they imply that the pressure and density profiles of dipole-confined plasmas can be simultaneously peaked and stable. Measurements with the interferometer show that the total density of LDX plasmas is strongly affected by the following parameters: levitated vs. mechanical support of the central dipole coil; input ECRH frequency and power; background pressure of neutral particles; plasma species. The gradients of the density profiles are, however, largely independent of the experimental conditions and approximate the value predicted for the stationary profile. Non-linear analyses suggest that dipole-confined plasmas are maintained in their stationary pressure and density profiles by a process of self-organized convection. We present measurements indicating that this self-organization process is observed in LDX.

Thesis Supervisor: Jay Kesner
Title: Senior Research Scientist

Thesis Supervisor: Miklos Porkolab
Title: Professor of Physics

Acknowledgments

This thesis could not have existed without the hard work and vision of the entire LDX team to whom the first thanks is due. To Jay Kesner, for his reassuring and zen-like guidance; to Darren Garnier, who would accept nothing short of excellence from me; to Mike Mauel, for his unwavering enthusiasm: Thank you for allowing me to be a part of the Levitated Dipole Experiment. I would also like to thank our technicians, Rick Lations and Don Strahan, who have always been as quick with a helping hand as with a kind word. And to those LDX'ers who have already moved away—Eugenio Ortiz, Ishtak Karim and Alex Hansen— the welcome you showed me when I arrived has not been forgotten. I would like to thank, especially, my fellow graduate student Jen Ellsworth whose help in many aspects of my research was of great value, but whose friendship I value even more. I was also lucky these last two summers to have worked with two undergraduates, Doug Halket and Tom Sidoti, whose assistance was a great help to me. And thanks is owed as well to LDX's newest graduate student, Ryan Bergmann, for keeping me entertained while I wrote this thesis.

More personally, I would like to thank my parents whose love was, for me, both an encouragement and a refuge. And to my sister Abby: how lucky we were to live in the same city and to have had the chance to become this close. What MIT has given me I could happily part with were it not for a few special people whom otherwise I would have not met. Guido Festuccia and Antonello Scardicchio: I think of you both like older brothers. Everything I know about physics I learned from the two of you. But most of all, these years are remarkable to me in that I met the lovely Eva Fast. Living together has been such a wonderful time in my life. Each day a new adventure in our own make-believe world. Each day a new and brighter smile. Be strong, Eva; we'll both muddle-through somehow.

Contents

List of Figures

List of Tables

Chapter 1

Introduction

This year, space enthusiasts are celebrating the fiftieth anniversary of the launch of America's first satellite, *Explorer I*, and, from its data, the discovery of the Earth's natural radiation belts by James Van Allen. Within a few Earth-radii, the Earth's magnetic field resembles that of a dipole magnet and so the radiation belts, being made-up of large populations of charged particles, constitute a giant example of a dipole-confined plasma. In 1958 it was known that certain magnetic field configurations could confine charged particles in trapped orbits. The great surprise from the measurements of *Explorer I* and subsequent satellites was the realization that the Earth's radiation belts were not at all transitory, but a persistent and permanent feature of the Earth's environment. Dipole confinement of plasmas was more extraordinary than anyone had previously supposed.

The discovery of the Earth's radiation belts marks the beginning of modern space science and, in specific, a period of intense speculation into the nature of dipole confinement. Quite early on, a theory was put forward [1], [2], asserting that in order to withstand the magnetohydrodynamic interchange instability, a dipole-confined plasma must adopt a profile satisfying

$$\delta(pV^\gamma) \geq 0.$$

Here p is the plasma pressure, γ is the ratio of specific heats (usually equal to 5/3) and

17

V is the volume of a magnetic flux-tube. Flux-tube volume is obtained by integrating along the length of a closed, magnetic field-line and ascribing to it a cross sectional area that is inversely proportional to the strength of the magnetic field B,

$$V \equiv \oint d\ell/B.$$

According to this account, a dipole-confined plasma can have a stable pressure profile that peaks in the core (pressure gradient pointing inwards) provided that the flux-tube volume increases sufficiently rapidly at the edge (volume gradient pointing outwards). For this reason, the plasma is said to be "stabilized by plasma compressibility". Fundamentally, the meaning of this stability criterion is that the entropy-density within a flux-tube near the core of the plasma must be less than or equal to the entropy-density within a flux-tube located at the plasma's edge.

The stability condition for the pressure profile derives from treating the plasma as a collisional fluid subject to the laws of MHD. In the opposite limit, in which the plasma is treated as collisionless, a separate prescription was derived for the density [3], namely, that in a dipole-confined plasma the density, n, is expected to vary inversely with flux-tube volume, V,

$$n \propto 1/V.$$

Intuitively this means that the total number of particles per flux-tube must be the same throughout the plasma.

These conditions—one for the pressure profile and one for the density profile— were derived for plasmas under very different physical assumptions. However, it can be shown that the two conditions are consistent with each other when the plasma has a pressure profile that is *marginally* stable to interchange modes,

$$\delta(pV^{\gamma}) = 0.$$

The connection between the density and pressure profiles is elucidated by non-linear

analyses of the problem [4], [5] which show that if the plasma deviates from the marginally stable pressure profile, it is restored by a process of self-consistent or "self-organized" convection. Physically, the plasma adopts profiles that remain unchanged or "stationary" even in the presence of interchange modes. At marginal stability, large-scale flux-tube mixing homogenizes the plasma such that both the entropy and number of particles are the same in every flux-tube. Because the field of a dipole falls-off with radius as $B \sim 1/r^3$, the flux-tube volume will vary as $V \sim r^4$ and, consequently, the formulas for the stationary pressure and density profiles become

$$p \sim r^{-20/3}$$
$$n \sim r^{-4}.$$

Thus, far from being homogeneous and flat, the pressure and density profiles of dipole-confined plasmas that are predicted to be stable are also predicted to be highly peaked towards the dipole's center, near $r = 0$. This assertion has immediate bearing on the quest to produce nuclear fusion power here on Earth. If the goal is to confine plasmas that have high density and high pressure for sufficiently long confinement times, then dipole fields may be uniquely suited to meet this challenge.

Even so, while the stability criterion for the pressure profile is not in doubt, there has not previously been much evidence of dipole-confined plasmas exhibiting the relatively steep gradients associated with marginal stability. In most dipole configurations, particle losses along field-lines play a decisive role in limiting the equilibrium confinement. In the case of the Earth's radiation belts, particles are lost by striking the Earth itself at the North and South poles resulting, in some instances, in the production of the aurora borealis or aurora australis. But what sort of plasmas could be confined if particle losses along field lines could be eliminated altogether? Answering this question is the goal of the Levitated Dipole Experiment (LDX), a joint MIT-Columbia University facility located at the MIT Plasma Science and Fusion Center.

LDX can largely eliminate parallel losses because its dipole magnetic field is pro-

duced not by a planet-like solid body but instead by its electromagnetic equivalent: a circular loop of electrical current. This means that particles following the magnetic field-lines near the polar regions of the dipole can travel right through the center of the current loop and out the other side. But if optimal confinement requires that the magnetic field-lines not be obstructed by anything then two problems immediately arise. First, there can be no wires connecting the dipole coil to an external power supply to drive the current; thus by necessity the dipole coil must be superconducting.

The second, more tricky problem is to keep the dipole coil positioned in the middle of a vacuum chamber without using any mechanical supports as these would inevitably interrupt the magnetic field-lines. This being the 21st century, the solution is, naturally, to use magnetic levitation. In LDX, the gravity of the dipole-field coil is counterbalanced by the attractive force from a second magnet located on top of the LDX vacuum chamber. To give a sense of the scale of what is achieved in LDX, consider that the dipole coil is over 1 meter in diameter, weighs 565 kg (over 1,200 pounds) and carries over 1 million amperes of current. At a brisk 5° above absolute zero, the dipole coil can be kept levitating for nearly three hours inside of LDX's 5 meter diameter vacuum chamber.

In the past there has been a number of internal-ring plasma experiments and even a few which employed levitation (e.g., the Levitron experiment at Livermore and the FM-1 Spherator at Princeton). However, it must be stressed that the similarities between these experiments (which were mainly stabilized, toroidal pinches) and LDX are mostly superficial; there is essentially no overlap with LDX from a physics perspective and only a limited overlap from an engineering perspective. The one exception is a new experiment at the University of Tokyo called RT-1 which is similar in geometry to LDX, although smaller, and with a fairly different set of physics objectives. The correct assertion about LDX is that it is the first and only experiment in the world built to study plasmas confined by the field of a levitating dipole magnet in a geometry where plasma compressibility is exploited to achieve stability.

Full operation of LDX—meaning that plasmas were produced while the dipole coil was successfully levitating—began only in November, 2007 although earlier, non-

levitated experiments had been conducted as early as 2004. The thesis in your hands contains, therefore, the very first measurements made anywhere in the world of plasmas confined by the field of a levitating, dipole magnet in a high-compressibility device. In order to study such plasmas, we have designed and built a 4-channel microwave interferometer (center frequency: 60 GHz) to measure profiles of the plasma density as functions of both space and time. Because the geometry of LDX is novel, the design of the LDX interferometer must also be novel. The interferometer, in its own right as a scientific instrument, serves therefore as an important contribution to the field of plasma diagnostics. But more than this, to know the plasma density is, in a meaningful way, as close as one can come to "seeing" a plasma. In this regard, the LDX interferometer has served very much as the experiment's first set of "eyes".

What the interferometer has observed, along with a description of the apparatus and interpretations of its measurements, we report in the following chapters of this thesis. We begin, in Chapter 2, with a basic treatment of the theoretical foundations of dipole confinement. Because LDX is so unique, there does not exist any general account of the theories upon which it is based. I decided, therefore, to compile this information myself. I have done this not only to aid my own understanding but also with the hopes that it may be useful to anyone who wants a general and historical overview of the ideas behind LDX. A description LDX itself, which was built to test experimentally the ideas developed in Chapter 2, is provided in Chapter 3.

Chapters 4 and 5 discuss the interferometer and how its measurements are analyzed. Using the interferometer as a diagnostic of the plasma density is, at root, two separate tasks: The first is to build an interferometer which accurately measures the phase shifts produced by changing plasma densities. This challenge is addressed in Chapter 4 where the instrumental aspects of the LDX interferometer are described in detail. Calibration measurements indicate that the interferometer delivers phase shift measurements that are accurate to within $5°$ and that these correspond to phase uncertainties of just a few percent.

The second task in measuring plasma density with an interferometer is to extract density information from the measured phase-shift data. This issue is taken-up in

Chapter 5. We discuss the assumptions and estimate the errors involved in converting phase-shift data into line-integrated density data and then in converting line-integrated density data into radial density profiles. Radial density profiles computed by Abel inversion generally have more uncertainty than the data from which they are computed, especially at locations near the core. Even so, while the estimates of core density may only be accurate to within 15%, Abel-inverted profiles nonetheless provide vital information for establishing basic trends: Is the density increasing or decreasing; is the profile gradient becoming more steep or more broad?

Indeed, one of the main experimental goals of LDX is to acquire enough observational data to begin to characterize the behavior of LDX plasmas. In Chapter 6 we assemble our density profile measurements into an observational compendium, or atlas of sorts, indicating what types of plasmas are produced in LDX for a given set of experimental conditions. The most important experimental parameters are found to be: levitated vs. mechanical support of the dipole coil; input powers and frequencies of the microwave heating; background pressure of neutral particles; species of plasma gas. The measured trends indicate that total density is strongly dependent on all of the above parameters but that the density profile gradients are largely independent and are reasonably close to the predicted, stationary profile. In this respect, LDX plasmas exhibit a "profile consistency" in the density.

The fact that LDX plasmas exhibit fairly consistent density profiles close to the stationary form—characterized by an equal number of particles per flux-tube—is remarkable since it is unlikely that this arrangement would result from a balance of sources (localized at the microwave resonances) and sinks. In Chapter 7 we present further evidence that the stationary density profile is indeed a "natural" or preferred profile for dipole-confined plasmas. Under special circumstances, LDX plasmas can be forced into a relatively unstable profile characterized by the presence of inverse sawteeth fluctuations and enhanced X-rays from energetic particles hitting the dipole coil. After a period of 1-2 seconds the plasma rapidly transitions into a density profile with a more uniform number of particles per flux-tube. These density transitions occur without any impetus from the externally controlled parameters (e.g., fueling

or ECRH). The profiles subsequent to a density transition are more quiescent and marked by the appearance of a strong, quasi-coherent mode at approximately 500 Hz. Although we do not possess all the pieces to this puzzle, we offer some speculation on the role played by the interaction of the density with the microwave heating at various resonance surfaces in triggering this phenomenon. Additionally we examine the evidence that after one of these density transitions, the profile is maintained in its stationary state by a process of self-organized convection (specifically, a large convective-cell drifting azimuthally around the LDX vacuum chamber) as predicted by non-linear theory.

Because this thesis treats some of the first experimental results from LDX, it is not possible to answer definitively all of the issues that are addressed. In Chapter 8, in addition to a summary of the main results, we examine which of these issues might be ripe for further research. We also offer some speculation as to what may be in store for LDX as more powerful and higher-frequency microwave sources are added to the experiment. In the end, we believe that the information contained in this thesis will serve as an important guidepost for LDX as the experiment moves forward and more is understood. Whatever becomes of LDX or, for that matter, the whole idea of dipole confinement, we are happy to have contributed one piece, however small, to the nuclear fusion puzzle. It is also hoped that you, reader, will find something of interest in these pages—a portion, perhaps, of what the author has found in his research. Enjoy.

Chapter 2

The Dipole-Confinement Idea

2.1   Investigations of the Northern Lights

Scientific interest in plasmas confined by the field of a dipole magnet long predates
experiments in controlled nuclear fusion and even precedes the first usage of the word
"plasma" to refer to an ionized gas. In 1896, the Norwegian physicist Kristian Birke-
land (1867-1917) published a series of papers hypothesizing that the polar aurorae
were caused by streams of cathode rays emitted from the sun and guided into the
Earth's atmosphere by the Earth's magnetic fields [6]. In these works, Birkeland antic-
ipated the ideas of the electron, the solar wind and, more directly, the "field-aligned"
or "Birkeland currents" that are now known to play a key role in the production of
auroral lights. Since direct confirmation of his theories was not possible prior to the
launching of scientific satellites, Birkeland devoted much of his energy to establishing
the plausibility of his ideas by means of experimental demonstrations. From 1901 to
1913, Birkeland conducted a series of experiments with *terrellae*, or "little Earths",
which consisted of placing a dipole magnet—meant to simulate the Earth—inside
of a large vacuum chamber and then, from a cathode, introducing electrons meant
to simulate charged particles emitted from the Sun. In addition to demonstrating
auroral-like behavior, Birkeland also used his *terrellae* to suggest causes for other ce-
lestial phenomena including sunspots, comet tails, Saturn's rings, and zodiacal light.

Another Norwegian, the mathematician Carl Størmer (1874-1957), collaborated
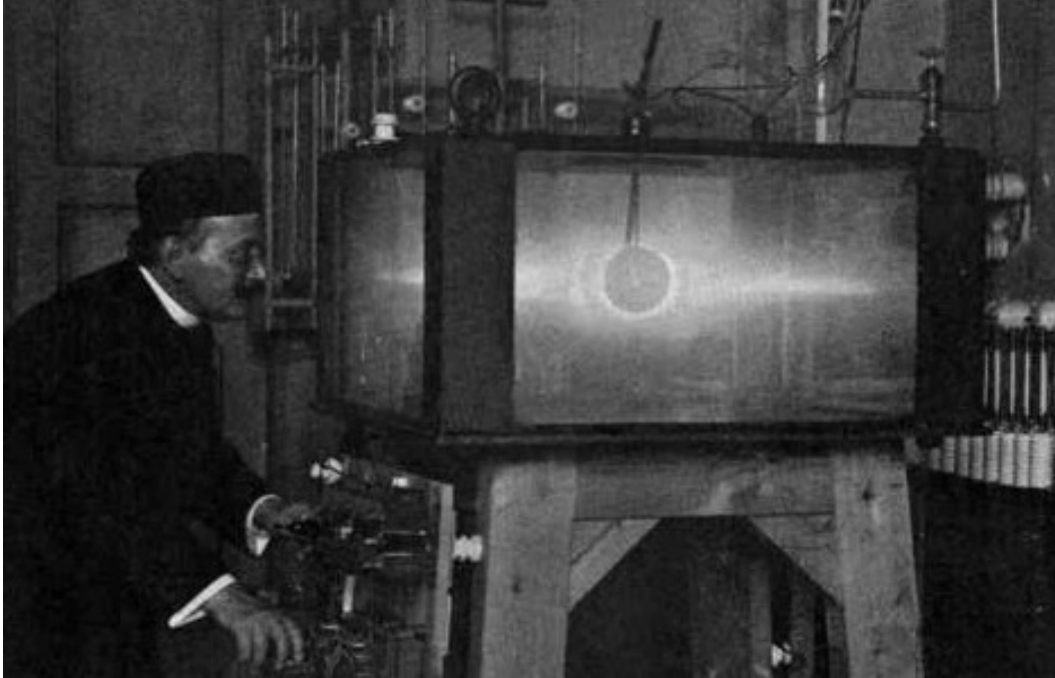
Figure 2-1: Birkeland with his *terrella*, ca. 1910. Note how the plasma is confined mainly in an equatorial disc around the simulated "Earth".

with Birkeland beginning in 1903 and devoted much of his career to caclulating the trajectories of charged particles in the field of a dipole magnet. These lengthy, numerical integrations were performed by hand by Størmer and his students over many years and the results indicated an wide array of possible trajectories. This work, along with analysis from Størmer's many photographs of the northern lights, was later collected in a book entitled *The Polar Aurora* [7]. Importantly, Størmer showed that certain initial conditions lead to orbits that would neither strike the Earth nor escape the planet's magnetic field altogether—that is, some particles could become trapped in the Earth's magnetic field.

Størmer's computations were impressive but of limited utility since in practice only the orbits of particles with very high energies—corresponding to energetic cosmic rays—could be calculated. Particles with lower energies have orbits with greater numbers of turning points, and this makes the integration of their trajectories increasingly complicated if not impossible. A major theoretical advance came from seeing the advantages of orbits in the limit of very large numbers of turning points. In 1940 the Swedish physicist (and later Nobel laureate) Hannes Alfvén (1908-1995)

introduced a perturbation technique for calculating the motion of charged particles in inhomogeneous magnetic fields which he called the *guiding center* method [8]. In this method, each particle is imagined to gyrate with cyclotron motion in a relatively tight radius and only the averaged motions of the centers of these cylcotron orbits are considered.
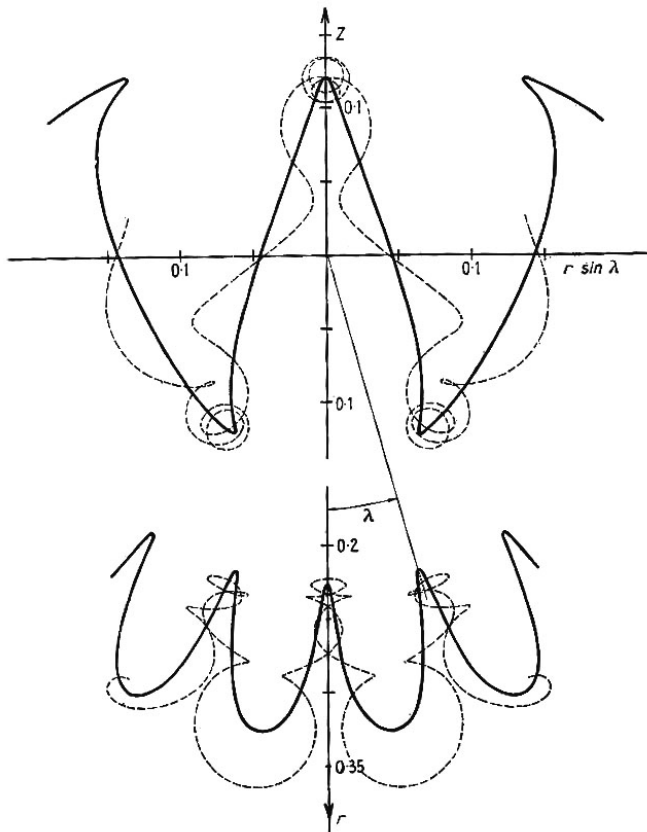
Figure 2-2: Comparison of Størmer and Alfvén orbit calculations for charged particles in a dipole field. The dotted lines are trajectories computed numerically by Størmer; the solid lines are trajectories computed by Alfvén's perturbation method. From ALFVÉN, *Cosmical Electrodynamics* (1950).

One profound insight from Alfvén's perturbation technique is the demonstration that for a charged particle gyrating in a changing magnetic field, the magnetic moment μ, defined as the ratio of perpendicular kinetic energy to magnetic field strength, is conserved to first order:

$$\mu \equiv \frac{W_\perp}{B} = \frac{\frac{1}{2}mv_\perp^2}{B} \tag{2.1}$$

$$\delta(\mu) = 0. \tag{2.2}$$

27

In the case where the magnetic field does not change in time, and if the charged particle has, in addition to its velocity perpendicular to the magnetic field, some velocity parallel to the field (say, in the z-direction) with $\frac{dB_z}{dz} \neq 0$, then Alfvén's guiding center analysis leads to the rather surprising conclusion that the conserved quantities are not the particle's perpendicular energy ($W_\perp$) and parallel energy ($W_\parallel$) independently but rather total energy (W) and magnetic moment (μ). Thus when a charged particle is guided into regions of increasing field strength, $v_\perp$ increases in order to conserve μ with the result that $v_\parallel$ decreases in order to conserve W.

Enrico Fermi, in his famous paper on cosmic rays [9], seems to have been the first to have taken this idea to the next step, namely, that when a point is reached where $v_\parallel$ must vanish entirely, the charged particle actually changes direction and "bounces" back to the region of smaller magnetic field strength. Since $\frac{dB_z}{dz} \neq 0$ along the field lines of a dipole magnet, the phenomenon of "bouncing orbits" is exhibited by charged particles moving in a dipole magnetic field. Making use of this insight, Alfvén was able to render the bulk of Størmer's labors obsolete almost overnight (Fig. 2-2). Along with the invariance of the magnetic moment, a number of Alfvén's other ideas that would become fundamental to the emerging field of plasma physics, remained little known for the better part of a decade until Alfvén published them in his widely influential book, *Cosmical Electrodynamics* in 1950 [10].

2.2   The Discovery of the Magnetosphere

The opening salvo of the space race was the Soviet satellite *Sputnik I*, launched on October 4th, 1957. Both the U.S. and the U.S.S.R. had announced that their scientific efforts for the International Geophysical Year (IGY) would include the launching of artificial satellites; nevertheless, *Sputnik I*—whose preparation and launch day were unannounced—took the world by surprise. The goal of the IGY, which at the time was the largest international scientific collaboration in history, was to further scientific knowledge of all aspects of geophysics, oceanography, and the new field of space science. The period of July, 1957 to December, 1958 had been selected for

the IGY because it was predicted to be at the peak of the sunspot cycle. Needless to say, however, the main impetus for both the Soviet Union and the United States for investing in rocket programs was military: The Soviet Union needed to develop ICBM capability in order to achieve deterrence with the U.S. and the U.S. was keen to develop spy satellites in order to observe Soviet military activity.

The first successful U.S. satellite, and the first satellite that carried a suite of scientific measuring devices, was *Explorer I*, launched on January 31, 1958. This followed the Soviet Union's launch of *Sputnik II* (carrying a dog, Laika) and the embarrassing launch failure of the U.S. *Vanguard* rocket TV-3. From January to September 1958, three *Explorer* satellites were successfully launched (*Explorers I, III, and IV*) which together made the most significant discovery of the whole IGY effort: the presence of large poplulations of charged particles trapped in the Earth's magnetic field. The leader of the scientific team of the *Explorer* satellites was James Van Allen, the foremost expert in the design of radiation detectors (Geiger-Müller tubes and CsI scintillators) for high-altitude cosmic ray detection. Initially the detector data was difficult to interpret since it showed extended regions of zero counts surrounded by regions with very high count rates. Van Allen recounts the moment of discovery as follows:

> "At 3:00 A.M. I packed my work sheets and graph and turned in for the night with the conviction that our instruments on both *Explorers I* and *III* were working properly, but that we were encountering a mysterious physical effect of a real nature. Early the following day [March 29, 1958], I flew back to Iowa City and proudly displayed my graph to Ernest Ray, Carl McIlwain and Joseph E. Kasper. During the previous day McIlwain had made tests with our prototype Geiger tube and circuit using a small x-ray machine and demonstrated that a true rate exceeding about 25,000 counts per second would indeed result in an apparent rate of zero. The conclusion was then immediate—at higher altitudes the intensity was actually at least a thousand times as great as the intensity due to cosmic radiation. Ray's famous (though consciously inaccurate) remark summarized the situation,

Figure 2-3: From left to right: William Pickering, James Van Allen, and Wernher von Braun holding a model of *Explorer I* at a press conference, February 1, 1958.

'My God, space is radioactive!' Our realization that there was actually a very high intensity of radiation at high altitudes rationalized our entire body of data." [11]

The trapped populations of charged particles discovered by Van Allen and the *Explorer* team were soon named the Van Allen radiation belts. Over the next few years, it was realized that the radiation belts make up only part of a larger region in space called the "magnetosphere". This latter term was introduced by Thomas Gold in 1959 who defined it as, "...the region above the ionosphere in which the magnetic field of the earth has a dominant control over the motions of gas and fast charged particles. This region is known to extend out to a distance of the order 10 earth radii; it may appropriately be called the magnetosphere." [2]

2.3 Artificial Radiation Belts: High Altitude Nuclear Detonations

It is darkly amusing to consider that even before the successful launch of *Explorer I* and the discovery of the the radiation belts, scientists at U.S. weapons labs had already proposed experiments to measure the confinement of charged particles trapped in the Earth's magnetic field by exploding nuclear bombs in space. The man most closely associated with this idea is Nicholas Christofilos, who worked at the Livermore Radiation Laboratory and later headed the Astron nuclear fusion experiment. In fact, Van Allen's discovery of Earth's radiation belts was taken by some as indication that the Russians must have beaten the U.S. to become the first to detonate a nuclear weapon in space [12].

The suite of high altitude nuclear tests conceived by Christofilos and implemented by U.S. military in late August and early September of 1958, was codenamed *Operation Argus*. The launch of *Explorer IV*, directed by Van Allen, was planned expressly to measure effects of the Argus blasts and to compare them with the previously detected radiation belts. There were three Argus detonations; each had a small yield (1-2 kilotons) and their altitudes ranged from about 200 to 540 kilometers above sea-level. Christofilos' predictions were confirmed in that the Argus tests did indeed produce populations of particles trapped for extended periods of time. Van Allen later summarized the results:

> "The three higher-altitude Argus bursts produced clear and well-observed effects and gave a great impetus to understanding geomagnetic trapping. About 3% of the available electrons were injected into durably trapped orbits. The apparent mean lifetime of the first two of these artificial radiation belts was about three weeks and of the third, about a month. In each of the three cases a well-defined Störmerian shell of artificially injected electrons was produced. Worldwide study of these shells provided a result of basic importance—a full geometrical description of the locus of trapping of 'labeled' particles. Also, we found that the physical nature of

the Argus radiation, as characterized by our four *Explorer IV* detectors, was quite different than that of the pre-Argus radiation, thus dispelling the suspicion that the radiation observed by *Explorers I* and *III* had originated from Soviet nuclear bomb bursts." [13]

Table 2.1: Artificial Radiation Belts Produced by Nuclear Explosions

Nation	*Test Name*	*Date*	*Altitude* (km)	*Yield* (kilotons)	*Decay Time*
U.S.A.	Argus I	Aug. 27, 1958	200	1.5	0-20 days
U.S.A.	Argus II	Aug. 30, 1958	240	1.5	10-20 days
U.S.A.	Argus III	Sept. 6, 1958	540	1.5	10-20 days
U.S.A.	Starfish	July 9, 1962	400	1,400	1-2 years
U.S.S.R..	K-3	Oct. 22, 1962	290	300	30 days
U.S.S.R..	K-4	Oct. 28, 1962	150	300	30 days
U.S.S.R..	K-5	Nov. 1, 1962	60	300	30 days

Before ratifying the Partial Test Ban Treaty in 1963, the U.S. and the U.S.S.R. conducted hundreds of atmospheric nuclear tests. Seven of these tests resulted in the production of artificial radiation belts [14], [15], details of which are listed in Table 2.1. The largest high-altitude nuclear test was a U.S. blast named *Starfish* in which a massive, 1.4 megaton hydrogen bomb was detonated 400 kilometers above sea-level . In addition to producing an artificial aurora that could be seen all across the Pacific, *Starfish* disabled electrical networks in Hawaii and caused the death of seven satellites, including *Telstar 1*, the world's first communication satellite [16]. On the other hand, the *Starfish* blast provided a thoroughly impressive demonstration of dipole confinement since the mean lifetime for some of the injected electrons was nearly two years!

2.4 Insights from Nuclear Fusion Research

A concerted effort to produce energy by controlled thermonuclear fusion was initiated in the U.K. as early as 1946; in the United States and the Soviet Union, desultory talk of fusion reactors was not turned into an experimental research program until 1951 [17], [18], [19], [20]. In all three countries, nuclear fusion research was connected in some capacity with efforts to manufacture thermonuclear (hydrogen) warheads. This is especially evident in the U.S. where the three principal fusion research sites coincided with the three principal sites in the hydrogen bomb program: Los Alamos, Livermore, and Princeton University (whose participation was called *Project Matter-horn*). Likewise most of the original researchers were involved in some way or other with work on the hydrogen bomb. One ramification of this connection was that in all three countries, fusion research was initially kept classified. The several months leading up to the Second International Conference on the Peaceful Uses of Atomic Energy, held in Geneva in 1958, were taken by all the powers as an opportune time to make public their efforts towards controlled nuclear fusion. Many of the fundamental theoretical ideas of plasma physics, which previously had been kept secret, were now published in scientific journals. Two of these ideas in particular are essential for the theory of plasma confinement in a dipole field and we will discuss them here: (1) A characterization of the motion of charged particles trapped in a magnetic field according to their adiabatic invariants, and (2) an exposition of the theory of the interchange instability. The first idea treats the plasma as a collection of largely collisionless, individual particles; the second idea treats the plasma as a collisional fluid subject to the laws of magnetohydrodynamics.

2.4.1 The Adiabatic Invariants of Trapped Particles

As mentioned perviously, it had been known from Alfvén's work [10] that the magnetic moment, μ, of a charged particle in a changing magnetic field remains constant to first order when the particle's equations of motion are expanded using a guiding-center perturbation. This rather surprising result became the focus of much inquiry in the

early years of fusion research. As Kruskal noted,

> "...the theory of virtually every prospective device for the production of useful energy from controlled thermonuclear fusion has leaned very heavily on the constancy of this magnetic moment, and in those cases for which more or less steady operation was envisioned (stellarator, mirror machine, etc.) it was seen that the requirement that particles remain confined for periods of time encompassing many millions of gyrations could generally be met only if the magnetic moment were in fact constant to a much higher approximation." [21]

A similar problem arose once the Van Allen radiation belts were discovered: Since satellite observations were making it clear that the Earth's magnetic field was highly asymmetric (due to the pressure from the solar wind), how could charged particles nonetheless remain trapped in stable orbits?

The solution to these questions came from considering the concept of *adiabatic invariance* from classical mechanics. Ehrenfest first developed the idea of adiabatic invariance as an attempt to explain the "stationary states" around which the early theories of quantum mechanics were based before the whole of it was reformulated by Schrödinger and Heisenberg. The original question, supposedly asked at the first Solvay conference of 1911 was: What happens to the frequency of a pendulum whose length (and therefore energy) is slowly changed in time? In this scenario, it turns out that the frequency also changes in time, but in such a way that the ratio of energy to frequency, E/ω, remains constant [22]. This phenomenon, called *adiabatic invariance*, is found to obtain whenever the Hamiltonian of a periodic or nearly periodic system is transformed to action-angle coordinates. For a conservative system (constant Hamiltonian), the action, defined as $I \equiv \frac{1}{2\pi} \oint p\,dq$, is a true invariant of the motion. If, however, the Hamiltonian changes slowly in time then the action becomes an *adiabatic invariant*, meaning that the change in I averaged over many periods is zero: $\frac{d}{dt}\bar{I} = 0$ [23].

An analysis in terms of adiabatic invariants has two advantages when compared to standard perturbation techniques. First, it can be shown that an adiabatic invariant is invariant *to all orders.* Indeed it was in the context of fusion research that this general result was first proven [21], [24]. This means that if the particle exhibits a rapid gyration with mean period T in the presence of a slowly changing magnetic field characterized by time-scale τ, with $\tau \gg T$, then $\Delta I \sim e^{-\tau/T}$ [23]. The second advantage of adiabatic invariants is that since they have a geometrical interpretation—they represent the area enclosed by a periodic motion in phase-space—the task of finding nearly conserved quantities in complicated trajectories is made more intuitive.

The motion of a charged particle trapped in a dipole magnetic field has three adiabatic invariants corresponding to three periodic motions. The first is the magnetic moment, μ, as intuited by Alfvén [10]. The second adiabatic invariant is called the *longitudinal invariant*, J, and is made from considering the "bounce" motion— first explored by Fermi [9]—of particles along field lines. The proof of the adiabatic invariance of J is the key to understanding the persistence of the radiation belts; it implies that (provided any changes of the magnetic field occur sufficient slowly) the azimuthal drift of particles around the Earth will always lead the particles back to their original starting points despite the gross azimuthal asymmetries of the Earth's magnetic field. These closed azimuthal drift orbits enclose a fixed amount of magnetic flux, ψ, which is taken to be the third adiabatic invariant.

The First Adiabatic Invariant: μ

For the 2-dimensional problem of a charged particle gyrating in a plane perpendicular to a constant magnetic field, it is straightforward to show that the action of the system, I, is proportional to the magnetic moment, μ. Since the energy of a particle has no dependence on static magnetic fields, the Hamiltonian can be expressed simply as

$$H = \frac{P_\perp^2}{2m} = \frac{P_\theta^2}{2mR^2}.$$ (2.3)

The action, I, is then found to be

$$I = \frac{1}{2\pi} \oint P_\theta d\theta = P_\theta = mv_\perp R. \tag{2.4}$$

For a charged particle gyrating in a magnetic field, $R = \frac{mv_\perp}{qB}$ and so

$$I = \frac{m^2 v_\perp^2}{qB} \propto \frac{\frac{1}{2}mv_\perp^2}{B} \equiv \mu. \tag{2.5}$$

Since the particle's gyration frequency is given by $\omega = \frac{qB}{m}$ we see that the action, I, is proportional to E/ω just as in the case of the pendulum whose length is slowly varied. And just as with the pendulum, if the the Hamiltonian of the charged particle is slowly changed in time (by altering the strength of the B slowly compared to the gyration frequency) the action variable μ, while no longer a true invariant of the motion, remains nonetheless invariant in the adiabatic sense.

Additional insight comes from realizing that the magnetic moment, μ, is also proportional to the magnetic flux, Φ, enclosed by the particle's gyration

$$\Phi = \pi R^2 B = \pi \frac{m^2 v_\perp^2}{q^2 B} \propto \mu. \tag{2.6}$$

Thus the invariance of μ can be understood as arising from the perfect diamagnetism of a charged particle gyrating in a magnetic field—the particle will alter its motion as necessary in order to preserve the enclosed flux, Φ.

The Second Adiabatic Invariant: J

After the magnetic moment, μ, the second adiabatic invariant is called the *longitudinal invariant* and is denoted by J. J is the action variable that comes from considering the "bounce" motion of a charged particle whose motion guides it into regions of differing magnetic field strengths. If the particle is guided into a region of higher magnetic field, $v_\perp$ will increase in order to conserve μ and $v_\parallel$ will decrease in order to conserve W. If a point is reached where $v_\parallel$ must vanish, the charged particle will actually stop and "bounce" back to the region of lower magnetic field. Accordingly

an action variable for this motion will be given by:

$$J = \oint m v_\parallel(s) ds = 2 \int_{a'}^{a} m v_\parallel(s) ds. \tag{2.7}$$

Here a and a' are the conjugate mirror points that represent the maximum excursions of the particle in direction parallel to the magnetic field.

J is often expressed in an alternate form as follows: Define the *pitch-angle*, α, to be the angle between the magnetic field vector, $\mathbf{B}$, and the velocity vector, $\mathbf{v}$, so that

$$v_\parallel = v \cos \alpha$$
$$v_\perp = v \sin \alpha. \tag{2.8}$$

Along a particle's trajectory the ratio of $v_\perp$ to $v_\parallel$ will change, but conservation of μ at all locations, s, along the trajectory implies that

$$\frac{\sin^2 \alpha(s_1)}{B(s_1)} = \frac{\sin^2 \alpha(s_2)}{B(s_2)}. \tag{2.9}$$

Let the weakest field seen by the particle be B_0 and let the pitch angle at this location be α_0. Evidently, the condition for the particle to bounce is that the particle sees a magnetic field B_M of sufficient strength such that,

$$\sin^2 \alpha_0 = \frac{B_0}{B_M}. \tag{2.10}$$

With these definitions we can rewrite J as

$$J = 2mv \int_{a'}^{a} ds \sqrt{1 - B(s)/B_M}. \tag{2.11}$$

The demonstration that the action, J, is in fact an adiabatic invariant is rather subtle and was a matter of controversy for a number of years. The reason is that, unlike μ, the motions that give rise to J are not confined to one plane in phase-space and so the proofs of invariance that were valid for μ are not technically valid for J. Another way to say the same thing is that the magnetic fields necessary for bounce-

motion cannot be linear but must be curved, and curved fields give rise to drifts across field lines (∇B and curvature drifts) [25].This is clear in the standard mirror geometry which consists of a bundle of generally parallel field lines which bulge outwards at the middle and are contracted inwards at either end. Particle confinement in such a geometry requires curved field in order to satisfy simultaneously $\frac{\partial B_z}{\partial z} \neq 0$ [Eq.(2.10)] and $\nabla \cdot \mathbf{B} = 0$.

In a linear magnetic mirror device, the ∇B and curvature drifts cause the trapped particles to precess around the magnetic axis. The same is true for dipole fields since, near the equator, they closely resemble linear magnetic mirrors; in the case of the Earth, the particles drift azimuthally around the planet. Because the Earth's magnetic field is azimuthally asymmetric, a trapped particle will see different magnetic fields during the course of its azimuthal drift and thus will execute different bounce motions. If J is not conserved during its orbit, the particle will not execute the same bounce motion when it returns to its original longitude and so a particle trapped at one longitude might be set free at another. The adiabatic invariance of J was finally settled in 1960 by Northrop and Teller who showed this fact in an elaborate and clever proof [26].

Table 2.2: Adiabatic Invariants for Motion in a Dipole Field

Symbol	Name	Functional Form
μ	magnetic moment	$\frac{1}{2}mv_\perp^2/B$
J	longitudinal invariant	$2mv \int_{a'}^{a} ds \sqrt{1 - B(s)/B_M}$
ψ	flux invariant	$\int_S B dS$

The Third Adiabatic Invariant: ψ

Northrop and Teller's proof of the adiabatic invariance of J was motivated by the *Argus* high-altitude nuclear tests. The outstanding question was to explain the persistence of the radiation belts in spite of the large azimuthal asymmetry of the Earth's magnetic field. But with the adiabatic invariance of J proved, it followed that the

azimuthal orbits of the trapped particles must be closed provided that the fields did not change too rapidly in time; this in turn showed that charged particles trapped in a dipole field would, in the absence of collisions, remain trapped indefinitely.

From this result it is straightforward to see that the magnetic flux, ψ, enclosed by these orbits must be invariant as well. This is because the average drift motion is just that of a charged particle gyrating in a plane perpendicular to the magnetic field— exactly the same one dimensional problem that led to the invariance of the magnetic moment, μ (or, equivalently, its enclosed magnetic flux, Φ). In the same paper where they prove the adiabatic invariance of J, Northrop and Teller also provide a proof of the invariance of ψ [26].

2.4.2   The Interchange Instability

Considerations of adiabatic invariance are, in general, only relevant for plasmas that are largely collisionless. In the opposite limit—that of high collisionality—a plasma can be treated as an electrically conducting fluid (similar to liquid mercury or liquid sodium) using the approximations of magnetohydrodynamics (MHD). Appropriately enough, for many hydrodynamical instabilities that affect fluids there are analogous MHD instabilities that affect plasmas. The most consequential of these—given its potential to violently disrupt most plasma confinement schemes—is the Rayleigh-Taylor instability (*alias* flute, Teller, or interchange instability).

In hydrodynamics, the Rayleigh-Taylor instability details what occurs when two immiscible fluid layers of different densities are accelerated in a direction perpendicular to their planar interface. For instance if a layer of water (more dense) is placed above a layer of oil (less dense), then the action of gravity makes such an arrangement unstable and soon fingers of water will grow downwards—and fingers of oil upwards—as the fluids attempt to change positions. These fingers, in addition to their characteristic shape, have a characteristic growth rate, w, given by [27], [28]:

$$w = \left(g\kappa \, \frac{\rho_2 - \rho_1}{\rho_2 + \rho_1} \right)^{1/2} \tag{2.12}$$
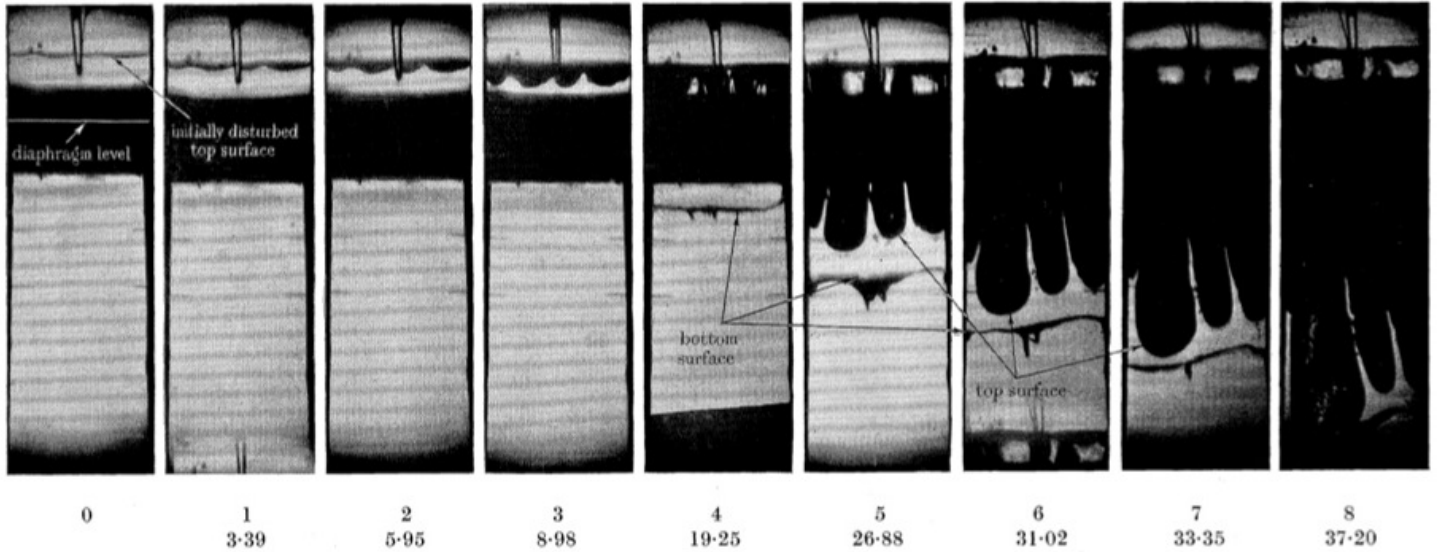
Figure 2-4: Photo Sequence of a Rayleigh-Taylor Instability. Beneath each photograph is written the photograph number and the photograph time in msec. From LEWIS, "Instability of Liquid Surfaces" (1950).

Here ρ_1 and ρ_2 are the densities of the two fluids, g is the acceleration at the interface and κ is the wave-number of a sinusoidal perturbation of the interface. Clearly, the stability or instability of the perturbation depends on the sign of $\rho_2 - \rho_1$; that is, whether the denser fluid is resting on top of the lighter fluid or vice-versa.

This result was first obtained by Lord Rayleigh and published in 1883 [27]. Geoffrey Taylor, unaware of Rayleigh's paper, derived the same equation as part of his investigations into the nature of underwater explosions, taken up at the behest of the British government during the second world war [29]. Somewhat later during that war, Taylor became a consultant to the Manhattan Project and, amongst other contributions, pointed out that the early designs for an implosion-type bomb were susceptible to this instability. Thus, to the Manhattan Project scientists, the problem became known as the "Taylor Instability" and after the war these scientists' influence was such that the term became generally adopted [30]. In 1950 Taylor published a treatment of the instability [28] that was very similar to Rayleigh's but which had the advantage of being accompanied by a paper, written by D.J. Lewis [31], providing experimental confirmation of the result (Fig. 2-4).

The Rayleigh-Taylor instability also afflicts plasmas confined by magnetic fields.

40

In this case, the acceleration g arises from the centrifugal motion of the plasma if the plasma streams along magnetic field lines which are curved. Thus a relatively more dense plasma may expand into the surrounding region of less dense vacuum depending on whether the plasma is on the convex or concave side of the field lines. Edward Teller was the first to intuit that a plasma confined within curved field lines was inherently unstable (Fig. 2-5) and he announced this at a Sherwood conference in 1954 [32], [33]. At the time, it does not appear that any connection was made between the "Teller instability" and the Rayleigh-Taylor instability. As the linear pinch scheme for nuclear fusion was already known to be unstable, the discovery that Teller instabilities afflicted curved field-line configurations led to the realization that all three avenues being pursued by the U.S. nuclear fusion program—the pinch, the stellarator, and the mirror—suffered from fundamental instabilities.
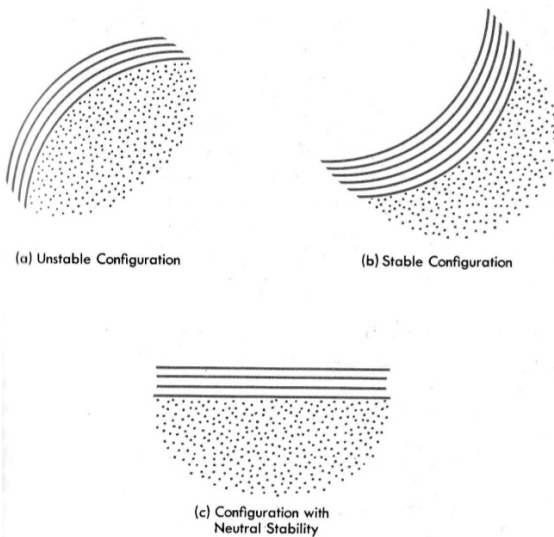
Figure 2-5: Sketches of "bad curvature" (a), "good curvature" (b), and a neutral configuration (c). From BISHOP, *Project Sherwood* (1957).

During the period in which the U.S. nuclear fusion program was gradually declassified (1957-8), an important, early review article summarizing Project Sherwood's theoretical results on plasma stability was published by Marshall Rosenbluth's and Conrad Longmire entitled "Stability of Plasmas Confined by Magnetic Fields" [1]. Rosenbluth and Longmire provide two demonstrations for how a plasma can be susceptible to a Rayleigh-Taylor instability, the first based on single-particle orbits (appropriate for a collisionless plasma) and the second based on MHD (appropriate for a collisional, fluid plasma). In the first case, Rosenbluth and Longmire show that

orbits along curved field lines lead to ∇B and curvature drifts which, if perturbed, give rise to electric fields that compound the perturbation. The growth rate of the instability, w, is given as

$$w = \sqrt{g\kappa} \tag{2.13}$$

where κ is the wave-number of the perturbation and g is the centrifugal acceleration from the ∇B and curvature drifts. Expressed in terms of the radius of curvature, $\mathbf{R}$, this becomes

$$g = \frac{\mathbf{R}}{R^2}\left(v_{\parallel}^2 + \frac{1}{2}v_{\perp}^2\right). \tag{2.14}$$

In their subsequent analysis, Rosenbluth and Longmire approach the stability problem from the perspective of magnetohydrodynamics (MHD). In MHD, flux tubes can be identified with the particles which they contain and, in this way, be given a concrete physical interpretation. A flux tube will, for a given flux Φ, have a volume, V, defined as

$$V \equiv \oint A \, d\ell = \Phi \oint \frac{d\ell}{B}. \tag{2.15}$$

Here A is the cross-sectional area of the flux-tube (taken as the reciprocal of the magnitude of the magnetic field B) and the integral is taken along the length of the closed field line which demarcates the flux-tube. For a plasma which satisfies the equation of state of an ideal gas, the internal energy, E_p, will be

$$E_p = \frac{pV}{\gamma - 1}. \tag{2.16}$$

Here p is the pressure, V is the volume as defined in Eq.(2.15), and γ is the ratio of specific heats which will be the familiar 5/3 for a plasma with a scalar (i.e. non-tensor) pressure.

In addition to thermodynamical energy of the plasma, E_p, a flux tube also has energy stored in the magnetic field, $\mathbf{B}$. For a given flux tube of volume V, the magnetic energy, E_M is written as

$$E_M = \int \frac{B^2}{8\pi} dV. \tag{2.17}$$

Stability analysis in MHD then comes down to this: A plasma will rearrange itself so as to minimize its free energy $E = E_p + E_M$. Given an initial configuration with energy E_I and any accessible configuration with energy E_{II}, the plasma will be stable if $\Delta E = E_{II} - E_I > 0$ and unstable if $\Delta E < 0$.

The simplest stability analyses are those for which the magnetic energy E_M remains the same during any rearrangement of the plasma. In this case, one need only consider the change in the plasma's internal energy E_p. The plasma is stable or unstable to this motion depending on the sign of ΔE_p. The image is then of two flux tubes, each containing the same flux but possibly different amounts of plasma, interchanging positions. Consequently, in the case where instability obtains it is called an
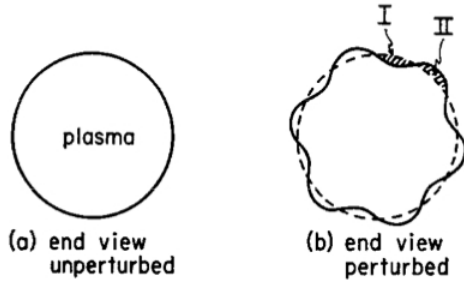
Figure 2-6: Cross section of a plasma cylinder exhibiting the "flutes" characteristic of an interchange instability. From ROSENBLUTH and LONGMIRE, "Stability of Plasmas Confined by Magnetic Fields" (1957).

"interchange instability". Looking along field lines at a cylindrical cross-section of plasma, the characteristic Rayleigh-Taylor fingers (Fig. 2-4) will distort the initial, circular boundary between plasma and vacuum into something shaped more like a fluted column; hence the final name of the instability: the "flute mode" (Fig. 2-6).

The working assumption of MHD is that the plasma is adiabatic, that is, no heat is exchanged between flux tubes and each flux tube satisfies $pV^\gamma = constant$. As they are compressed, flux tubes gain energy and heat-up; as they expand, flux tubes lose energy and cool-down. Given this assumption, ΔE_p can be computed for a pair of flux tubes which initially differ infinitesimally in pressure and volume ($p_{II} = p_I + \delta p, V_{II} = V_I + \delta V$) and which subsequently interchange volumes. Using Eq.(2.16) for E_p and expanding to second order gives [34],

$$\Delta E_p = V^{-\gamma}\delta(pV^\gamma)\delta V. \tag{2.18}$$

Approaching the boundary of the plasma ($p \to 0$), Rosenbluth and Longmire argue that the term $\delta(pV^\gamma)$ is negative since $|\delta p/p| > |\gamma(\delta V/V)|$. Because stability requires $\Delta E_p > 0$, the stability condition thus becomes $\delta V < 0$ in the direction away from the plasma. By further constructions, Rosenbluth and Longmire equate this condition to one involving the radius of curvature, R

$$\int \frac{d\ell}{RrB^2} > 0 \tag{2.19}$$

where r is the radius to the field line in cylindrical coordinates [35]. According to Eq.(2.19), wherever the field lines curve inwards towards the center of the plasma ($R > 0 \Rightarrow \delta V < 0$) the plasma is stable; conversely, wherever the field lines bow outwards from the center of the plasma ($R < 0 \Rightarrow \delta V > 0$) the plasma is unstable. Moreover, by showing how any such instability of this sort leads to Rayleigh-Taylor growth rates, Rosenbluth and Longmire established analytically what Teller had originally surmised: Plasmas confined on the convex side of curved field lines are stable but plasmas confined on the concave side of curved field lines are unstable.

This issue of "good" and "bad curvature" must be addressed in any plasma confinement scheme in order that the plasma not be subject to rapid and virulent interchange modes. In open field line devices, such as the magnetic mirror, this entails the application of additional, asymmetrical or cusped magnetic fields (such as from Ioffe bars) to ensure that in the direction of decreasing plasma pressure, the flux-tube volume also decreases ($\delta V < 0$) in accordance with Eq.(2.18). The objective is to confine the plasma in such a way that the magnetic field increases in every direction outwards from the plasma and hence these configurations are called "magnetic well" or "minimum B" configurations. Intuitively, these configurations share some similarities with the notion that a plasma, being diamagnetic, is expelled from regions of high magnetic field and pushed into regions of low magnetic field.

For toroidal confinement schemes such as the stellarator (and, later, the tokamak), avoiding the interchange instability is achieved by the addition shear in the poloidal component of the magnetic field. In the stellarator, shear was achieved by adding

external, helical current windings around the chamber; in tokamaks, shear is provided by the field produced by the current of the plasma itself. Dipole fields, however, suffer from "bad curvature" everywhere. How such a field can, nevertheless, be used to confine a plasma is discussed in the next section.

2.5   The Nature of Dipole Confinement

At the conclusion of the International Geophysical Year in December, 1958, the world could marvel at the discovery of Earth's natural radiation belts (§2.2), the use of nuclear bombs to produce the first artificial radiation belts (§2.3), and the first glimpses at the newly declassified, international nuclear fusion programs (§2.4).

Over the next few years, basic plasma physics concepts which had been developed for nuclear fusion research were used by space scientists to theorize about the nature of the radiation belts and about plasmas confined by a dipole magnetic field in general. But plasma physics has, since its inception, been philosophically of two minds, regarding plasmas sometimes as a collection of interacting, charged particles and sometimes as an electrically conducting fluid governed by the equations of magnetohydrodynamics (MHD). At issue is the importance of collisions for a particular plasma; even so, it would be misleading to assert that a straightforward limit can be drawn between the single-particle perspective and the fluid perspective based solely on collisionality. Indeed MHD, which is a fluid theory, is famously successful in describing plasmas that are not collisional at all [36].

Competing fluid and particle formalisms also characterize the problem of plasma confinement in a dipole magnetic field. Nevertheless, the hope is that by proceeding correctly, a correct conclusion can be reached in spite of any differences in mental imagery and that the results derived in one collisionality limit are the limiting cases of results derived in the opposite limit. And indeed, for a dipole-confined plasma both the collisionless, single-particle approach and the collisional, fluid approach point to a consistent result: Dipole-confined plasmas will be driven by fluctuations to a stationary profile that is not flat but peaked and characterized by the presence of an

equal number of particles in volumes containing equal magnetic flux.

2.5.1 Collisionless, Single-Particle Approach

McIlwain B, L coordinates

Efforts to understand the trapping of individual, charged particles in a dipole field resulted in an account in terms of the adiabatic invariants μ, J, and ψ as discussed in §2.4.1. The mystery of how particles could remain trapped even in fields with some quadrupole or higher moments was resolved once the invariance of J and ψ was established by Northrop and Teller [26]. This result also led to a new set of coordinates for describing magnetospheric phenomena, developed by Carl McIlwain in 1961, which exploits the fact that particles will remain on orbits with constant J and ψ [37].

McIlwain's system labels each point in space by two coordinates: B, the magnetic field strength and L, a new parameter that stays constant on contours which approximate magnetic field lines. The space around an approximately dipolar magnet is labeled with B, L coordinates by first introducing the coordinates B and I, where I defines a set of surfaces according to

$$I(a) = I(a') = \int_{a'}^{a} ds \ \sqrt{1 - B(s)/B(a)}. \tag{2.20}$$

For a given point a, the integral is to be taken along a field line starting at a and terminating at the conjugate point on the same field line, a'. Clearly I is similar to J as expressed in (2.11), the main difference being that J is a value assigned to moving particles whereas I is a value assigned to fixed locations in space.

If a trapped particle mirrors at a point on a given surface of constant I, it will continue to to mirror at points on the same I surface as it drifts azimuthally around the source of the field. Likewise a particle which mirrors at point where the magnetic field strength is B will continue to mirror at points on the same B surface. The intersections of the B and I surfaces will form a ring which fixes the locus of bounce-points for a given particle throughout its orbit. This is illustrated in Fig. 2-7: A
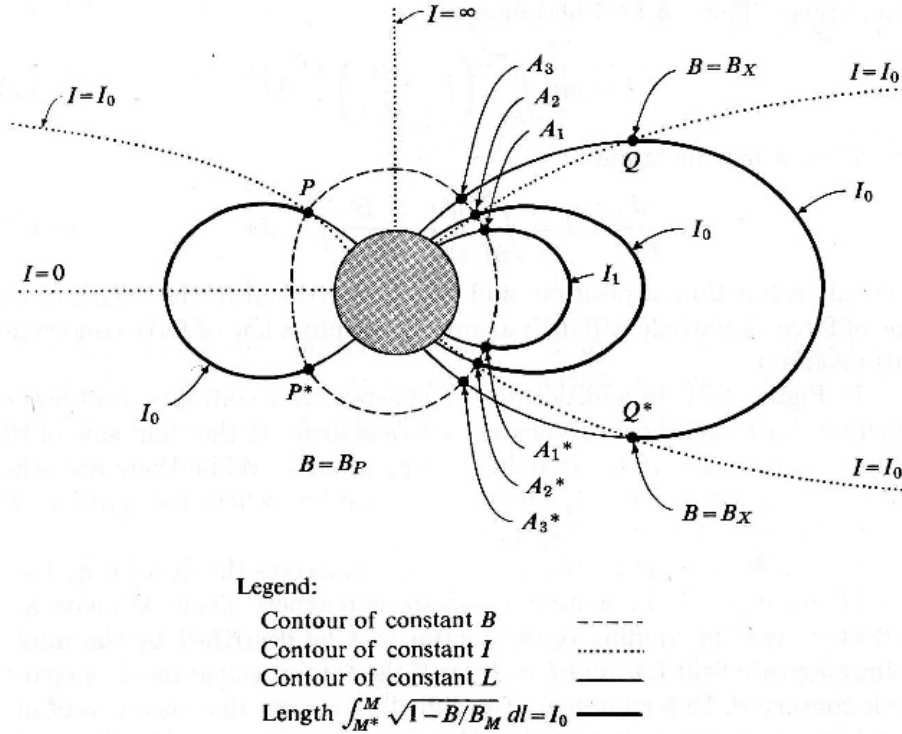
Figure 2-7: Sketch of an inhomogeneous dipole field showing contours of constant B, I, and L used in the McIlwain B, L coordinate system. From O'BRIEN, "Interrelations of Energetic Charged Particles in the Magnetosphere" (1967).

particle originally mirrors at point P lying on surface $B = B_p$ and $I = I_0$; A_1, A_2 and A_3 all lie on the same surface $B = B_p$, but only A_2 lies on the surface $I = I_0$ with the result that the particle, having drifted in longitude, will mirror at point A_2.

A coordinate system of B and I surfaces can thus provide a simple representation of particle drift orbits in the space around a dipole magnet. The downside is that surfaces of constant I were not considered sufficiently intuitive. This prompted McIlwain to introduce a magnetic shell parameter L where, at any given point a, L is defined as the equatorial crossing-point of a particle whose mirror-point is at a. L is usually given in terms of Earth-radii (or other planetary radius, as the case may be) such that a trapped particle that crosses the magnetic equator at a distance of, say, two Earth-radii from the center of the field is considered to lie on the $L = 2$ shell. In this way, surfaces of constant L—upon which particle drift orbits have a simple (constant) representation—will more or less resemble magnetic field lines. B, L coordinates are generally computed numerically from observational data, but for a pure dipole B and

47

L can be defined implicitly in terms of radius, r, and latitude, λ, by [38]

$$r = L\cos^2\lambda \tag{2.21}$$

$$B = \frac{B_0}{r^3}\left(4 - \frac{3r}{L}\right)^{1/2} \tag{2.22}$$

Because particles remain on the same L-shell throughout their azimuthal drift, it follows that surfaces of constant L are also surfaces of constant flux, ψ. Since the former are labeled by their radius in the equatorial plane, the two coordinates (L and ψ) will be related by

$$\psi \sim L^{-1} \tag{2.23}$$

where we have made use of the fact that the magnetic field (being, by assumption, mainly dipolar) scales with radius as $B \sim 1/r^3$.

Particle Diffusion

A population of charged particles trapped in a dipole field can be described in terms of a distribution function, f, expressed in some suitably tractable coordinate system. Starting with a purely collisionless and non-interacting plasma, any distribution function f will remain unchanged ($\partial f/\partial t = 0$) irrespective of which coordinates have been chosen. We can add some additional physics to this account by allowing for the particles to undergo small scattering events resulting in diffusion. Once this is permitted, a representation of the distribution function in terms of the particles' adiabatic invariants, $f = f(\mu, J, \psi)$, becomes far and away the most convenient form. The reason for this is that the adiabatic invariants are time-averages of the particles' motions made over very different time scales; consequently, an analysis of diffusion processes naturally separates the variables according to the time scale of the disturbance.

Some examples can help to clarify this concept: First, we already know that $\partial f(\mu, J, \psi)/\partial t = 0$ for any disturbances which occur at rate that is slow compared to the azimuthal drift period τ_d; by similar reasoning, a disturbance that is rapid compared to the drift period but slow compared to the bounce period, $(\tau_b \ll \tau \ll \tau_d)$

will lead to a diffusion process wherein ψ for a given particle is altered, but J and μ remain unchanged. No equivalent analysis could arise from a representation of the distribution function in terms of coordinates that encoded spatial information only (for example, spherical coordinates, $f = f(r, \theta, \phi)$) because in general even a simple disturbance will mix-up the distribution function in all three variables.

Two diffusion processes are considered to be important in the dynamics of dipole-confined plasmas in space. These are:

- pitch-angle scattering

- radial, or L-shell, diffusion

Pitch-angle scattering is any event that alters a particle's pitch-angle, α, as defined in Eq.(2.8). Pitch-angle scattering breaks the invariance of a particle's magnetic moment, μ, which consequently breaks J as well; ψ, however, remains unchanged because the particle remains on the same field line and so will trace out the same circuit as it drifts azimuthally. Nevertheless, with μ broken, the basic conditions for mirror-trapping given in Eq.(2.10) may no longer apply in which case the particle will travel along the magnetic field line until—in the magnetospheric case—it is neutralized somewhere in the planet's atmosphere. For this reason, pitch-angle scattering is the principal loss-mechanisms for magnetospheric plasmas. Because it breaks the invariance of μ, pitch-angle scattering must be caused by a disturbance that occurs faster than the cyclotron period τ_d. The main culprit is collisions with neutral particles, but various EM waves that are comparable to a particle's cyclotron frequency (e.g. whistler waves) can also play a role [39].

Radial, or L-shell, diffusion arises from low-frequency disturbances that break the flux-invariant, ψ, but which leave μ and J unchanged. By permitting only those collisions that result in small jumps in phase space, the problem can be treated analytically as an exercise in Fokker-Planck diffusion. Within this framework, the distribution function expressed in terms of the coordinates, q_i, will change in time as

$$\frac{\partial f}{\partial t} = \frac{\partial}{\partial q_i} \left(D_{ij} \frac{\partial}{\partial q_j} f \right) \qquad (2.24)$$

and the diffusion coefficients, D_{ij}, are prescribed in terms the secondary moments of the scattering steps, $\langle \Delta q_i \rangle$:

$$D_{ij} = \frac{1}{2} \langle \Delta q_i \Delta q_j \rangle. \tag{2.25}$$

At this point the advantage of using a distribution function expressed in terms of the adiabatic invariants becomes clear since, by our original assumption that the fluctuations of interest do on affect μ or J, the problem reduces to just one dimension:

$$\frac{\partial f(\mu, J, \psi)}{\partial t} = \frac{\partial}{\partial \psi} \left(D_{\psi\psi} \frac{\partial}{\partial \psi} f(\mu, J, \psi) \right). \tag{2.26}$$

This diffusion equation is more commonly expressed in terms of the shell parameter L. By its construction, L is a function of ψ but not of μ or J which means that an equivalent diffusion equation in L will likewise be one-dimensional. Using the relation $\psi \sim L^{-1}$ (2.23), and keeping track of the various Jacobian determinants, Eq.(2.26) transforms to [40]

$$\frac{\partial f(\mu, J, L)}{\partial t} = \frac{\partial}{\partial L} \left(D_{LL} \frac{1}{L^2} \frac{\partial}{\partial L} (L^2 f(\mu, J, L)) \right). \tag{2.27}$$

There is no equivalent one-dimensional equation in terms of the radius, r, because there is no class of fluctuations that leads to diffusion in r without also causing diffusion in the other two coordinates. As it stands, then, Eq.(2.26) and Eq.(2.27) are remarkable even without knowing anything about the functional form the diffusion coefficients. Their significance is that *the direction of particle diffusion is NOT determined by the sign of $\partial f / \partial r$ but rather by the sign of $\partial f / \partial \psi$ or, equivalently, $\partial / \partial L (L^2 f)$. In other words, diffusion will work to equalize the number of particles NOT per unit volume but rather in volumes containing the same amount of magnetic flux,*

$$nV = constant, \tag{2.28}$$

where V is the flux-tube volume defined in Eq.(2.15) and n is the particle number density.

In a dipole magnetic field, the flux-tube volume has a cross sectional area that

varies with radius as $1/B(r) \sim r^3$ and a length (integrated along the closed field-line) proportional to r so that $V(r) \sim r^4$. Equivalently, the volume of an L-shell scales with radius like a spherical shell, namely $V_L(r) \sim r^2$. The consequence of Eq.(2.27) is thus the same: The equilibrium density profile will vary as

$$n(r) \sim 1/r^4. \tag{2.29}$$

The conclusion, then, of a single-particle analysis of dipole confinement is this: Radial diffusion in a dipole-confined plasma works not to flatten the density but to steepen it towards an equilibrium profile characterized by the presence of an equal number of particles per flux-tube. This profile will be driven by fluctuations on the order of the azimuthal drift frequency, τ_d, and will scale with radius as $n(r) \sim 1/r^4$. However, such a profile will not obtain if the dynamics are dominated by higher-frequency events such as collisions that lead to pitch-angle scattering.

In planetary magnetospheres, inward L-shell diffusion is believed to be an important source of particles for the radiation belts. Diffusion induced by ψ-breaking variations of the solar wind pressure against the magnetopause was first hypothesized by Parker in 1960 [41].

2.5.2 Fluid Approach

The single particle approach takes as its assumption that particles can execute their orbits essentially unimpeded and that any interactions can be modeled by a Fokker-Planck diffusion of the distribution function. At the other limit of collisionality, the fluid approach takes as its assumption that collisions are so frequent that the energy has been apportioned amongst the particle according to a thermal (i.e. Maxwellian) distribution. When the latter assumption is valid, the plasma should be well described by the equations of magnetohydrodynamics (MHD). As the early fusion program learned to its chagrin (§2.4.2), no fluid plasma can be confined unless it is stable to the MHD interchange instability. However, a dipole configuration suffers from "bad curvature" (Fig. 2-5) everywhere and therefore should be always vulnerable to

interchange modes.

Once again, Rosenbluth and Longmire's stability condition for interchange modes is [Eq.(2.18)],

$$\Delta E = V^{-\gamma} \delta(pV^{\gamma}) \delta V > 0$$

where p is the pressure, V is the volume, and γ is the ratio of specific heats, taken to be 5/3. The volume, V, is the volume of a flux-tube as defined in Eq.(2.15). In their analysis, Rosenbluth and Longmire assumed that $\delta(pV^{\gamma}) < 0$ as one moves from the plasma core to its vacuum boundary. This is certainly the case in most confinement devices which have an inwardly peaked pressure profile (i.e. pressure gradient is negative) but allow only modest flux expansion. From this came the requirement of having magnetic geometries with "good" curvature ($\delta V < 0$) [Eq.(2.19)].

Nonetheless, it is also possible to conceive of plasmas which satisfy

$$\delta(pV^{\gamma}) \geq 0. \tag{2.30}$$

Such a plasma would have to balance any inward-pointing (i.e., negative) pressure gradient with a sufficiently large, outward-pointing (i.e., positive) gradient of flux-tube volume. If Eq.(2.30) obtains, then whenever two flux-tubes interchange positions, the outer flux-tube will move inwards, compress and rise in temperature (and energy) and the inner flux-tube will move outwards, expand and decrease in temperature (and energy) in such a way that the energy increase of the former flux-tube outweighs the energy decrease of the latter flux-tube. Consequently, interchanges will be energetically unfavorable and the plasma is said to be stabilized by *compressibility*. In this way, compressibility [Eq.(2.30)] allows a plasma to be confined even in "bad" curvature ($\delta V > 0$).

2.5.3 Consistency at Marginal Stability

At a basic level, the condition for the density profile of a dipole plasma ($nV = constant$) and the condition for the pressure profile ($\delta(pV^{\gamma}) \geq 0$) have nothing to

do with each other since they are derived for plasmas under very different physical assumptions. However there is an important, if somewhat subtle argument connecting the density and the pressure when the pressure profile is *marginally* stable to interchange modes

$$\delta(pV^\gamma) = 0. \tag{2.31}$$

In most plasmas, a violation of any MHD stability limit usually leads to a rapid loss of plasma confinement. In a dipole, however, there is a notion that the condition for stability against MHD interchange modes [Eq.(2.30)] is only a "soft" limit, one that does not threaten a loss of confinement. This idea was first explored in 1959 by Thomas Gold in the very same paper in which he coined the word "magnetosphere" [2]. Gold intuited that—just as with a heated, compressible fluid in a gravitational field—a dipole-confined plasma would be subject to a convection which acts to equalize the entropy in every fluid element.[1] In an adiabatic fluid, the entropy-density (which is the entropy per unit mass) is indexed by the quantity pV^γ. Therefore, in the assumption (which is not always met) that the flux-tubes contain an equal number of particles, MHD interchange modes can be identified as the driver of the convective process which works to enforce the condition $pV^\gamma = constant$. What results is a pressure profile that is not just marginally stable to interchange modes, but also "stationary" to interchange modes, meaning that the profile remains unchanged *even while allowing for interchange modes to occur.*

Near marginal stability, therefore, dipole-confined plasmas are expected to be characterized by large-scale, internal convection. Flux-tubes are rapidly interchanged in position but in such a way that the pressure profile remains unchanged. This idea is supported by more recent non-linear MHD analyses performed by Pastukhov and Chudin [4] and Kouznetsov *et al.* [5] which show that a dipole-confined plasma that is displaced from the marginally stable pressure profile is restored to that profile by a process of self-consistent or "self-organized" convection.

With large-scale flux-tube mixing, there is only one possible density profile which—

---

[1]This result is demonstrated in Ref. [42].

like the marginally stable pressure profile—will remain unchanged or "stationary": the profile that is characterized by an equal number of particles per flux-tube. Thus in the presence of flux-tube mixing, the collisionless prescription for the density profile and the collisional prescription for the marginally stable pressure profile become consistent: they are the profiles which are stationary to interchange modes. The physical significance of these stationary profiles is that they describe a plasma with an equal amount of entropy per flux-tube and an equal number of particles per flux-tube.

$$pV^\gamma = constant$$
$$nV = constant.$$
(2.32)

In a dipole field, where flux-tube volume scales with radius as $V \sim r^4$, the stationary pressure and density profiles will scale with radius as

$$p(r) \sim r^{-20/3}$$
$$n(r) \sim r^{-4}.$$
(2.33)

2.6 Experimental Investigations

In the 50 years since the discovery of the Van Allen radiation belts, there has been continuous research into magnetospheric plamsas. Beyond Earth, strong magnetospheres have been found around Mercury, Jupiter, Saturn, Uranus, Neptune, and the Jovian moon Ganymede [43]. Both L-shell diffusion and interchange modes continue to inform the theoretical discussions of planetary magnetospheres, but their importance and scope remains unsettled [44]. An honest assessment must conclude that no simple model can account for the extremely complex dynamics that characterize the space-plasma environment where numerous physical processes are in competition with each other at any one time [45]. Ultimately, the size of even Earth's magnetosphere is so vast that the handful of purpose-built scientific satellites can provide only glimpses of the larger physics.

On the terrestrial front, the *terrella* tradition begun by Birkeland (§2.1) has been

carried forward in numerous laboratory dipole experiments designed to simulate magnetospheric processes [46]. As for nuclear fusion, the first dipole fusion concept was proposed in 1958 by Bo Lehnert from the Royal Institute in Stockholm, Sweden [47], [48]. Lehnert succeeded in building a number of small devices in which the central dipole coil was supported and fed by shielded current leads [49], but the project was scuttled by EURATOM in the 1980's as the international fusion community consolidated its resources increasingly into the Tokamak program.

There have also been a number of non-dipole fusion experiments which are affected by issues related to dipole confinement. In particular, magnetic mirrors share many similarities with dipoles insofar as the fields are purely poloidal, the particles are mirror-trapped, and pitch-angle scattering is an important loss mechanism. The mirror program—especially devices of the "short, fat" variety—were the first to realize that compressibility [Eq.(2.30)] could play a role in plasma stabilization [50].

More superficially, many fusion devices have experimented with internal current-rings, a few of which were even levitated (notably, the Levitron and the FM-1 Spherator), but all of these devices were intended either as cusped, minimum-B configurations or stabilized toroidal pinches. Indeed, Sakharov and Tamm's original idea for adding a poloidal field in the Tokamak was to suspend a current-ring inside the chamber [19]. An interesting table compiled by Braams and Stott [51] lists, quite probably, all of the internal-ring plasma experiments throughout the history of the international fusion program.

Despite the great variety of fusion experiments over the decades, it was not until 1987 that anyone considered a laboratory experiment based upon the dipole-confinement ideas developed in §2.5. In that year, Akira Hasegawa proposed a dipole fusion reactor with a levitating internal coil wherein the plasma, driven by inward radial diffusion, attains peaked pressure and density profiles that are stationary to interchange modes [3]. Hasegawa's initial proposal was rejected by the Department of Energy, due mainly to the then extremely unfavorable climate for non-tokamak fusion experiments. Nevertheless, working in collaboration with Michael Mauel at Columbia University, a smaller, space-science oriented experiment was proposed and

funded by NASA to study the nature of radial diffusion and interchange modes in a dipole-confined plasma. This experiment, called CTX (Collisionless Terrella Experiment), was constructed at Columbia University in 1992 [52] and is still in operation with Mauel as the principal investigator.

At the time that CTX was proposed, Mauel was involved in a collaboration at TFTR (Tokamak Fusion Test Reactor) at Princeton University where, during extended down-times due to plasma disruptions, he would meet with Jay Kesner to discuss Hasegawa's levitated dipole fusion concept—a concept which had the promise of being disruption-free. Mauel had previously worked with Kesner at MIT's tandem-mirror experiment called TARA where Kesner was one of the principal investigators. Numerous publications and presentations later, DOE accepted a 1997 proposal whereupon Kesner and Mauel became the principal investigators of LDX (the Levitated Dipole Experiment), a joint MIT-Columbia University nuclear fusion experiment located at MIT's Plasma Science and Fusion Center. LDX is the only experiment in the world—dipole or otherwise—built to exploit the stabilizing effects of plasma compressibility [Eq.(2.30)] in its goal of confining very high-pressure plasmas. A fuller description of LDX is given in the subsequent chapter of this thesis.

Quite independent of Hasegawa's ideas, a series of levitated dipole devices were built at the University of Tokyo [53], of which the largest is named RT-1 (Ring Trap 1). Based on an entirely different premise than LDX, RT-1 seeks to induce plasma rotation in order to obtain a steep pressure profile that satisfies condition they call the Bernoulli-Beltrami equation [54]. LDX, CTX and RT-1 (along with its smaller prototypes) constitute, at this writing, the sum total of the world's dipole-confined plasma experiments.

Table 2.3: Today's Dipole-Confined Plasma Experiments

	LDX	**RT-1**	**CTX**
Location	MIT	University of Tokyo	Columbia University
Physics	Profiles Shaped by Compressibilty	Bernoulli-Beltrami Profiles	Interchange Mixing and Diffusion
Chamber Radius	500 cm	100 cm	67 cm
Coil Radius	34 cm	25 cm	15 cm
Coil Current	1200 kA-turns	250 kA-turns	150 kA-turns
Levitated	yes	yes	no
Coil Weight	565 kg	110 kg	—
Superconductor	Nb_3Sn	Bi-223	—
Plasma Heating (ECRH)	2.45 GHz (2.5 kW) 6.4 GHz (2.5 kW) 10.5 GHz (10 kW)	2.45 GHz (20 kW) 8.2 GHz (100 kW)	2.45 GHz (1 kW)

Chapter 3

LDX: The Levitated Dipole Experiment

3.1 Overview

The Levitated Dipole Experiment (LDX) is a new and innovative nuclear fusion experiment which has set out to test the idea that a dipole magnetic field can confine stable, high-pressure plasmas of the sort that may one day provide the world with clean, plentiful, nuclear fusion power. LDX plasmas resemble, in many ways, the radiation belts confined by the dipole magnetic fields of the Earth and other planets. In LDX, however, plasma losses along field-lines are minimized by levitating the central, dipole coil. Construction on LDX began in 1998 at MIT's Plasma Science and Fusion Center, first plasma was achieved in August of 2004 and the first successful levitation of the dipole coil was achieved in November, 2007. LDX is the only experiment in the world built to exploit the stabilizing effects of plasma compressibility which, perhaps, may open a path towards the confinement of increasingly high-temperature and high-pressure plasmas. Insofar as it is exploring an entirely new plasma regime, LDX can illuminate much in the way of fundamental plasma physics; insofar as it is a proof-of-concept test for much grander ambitions, LDX could be an image of what nuclear fusion power may look like in the future.
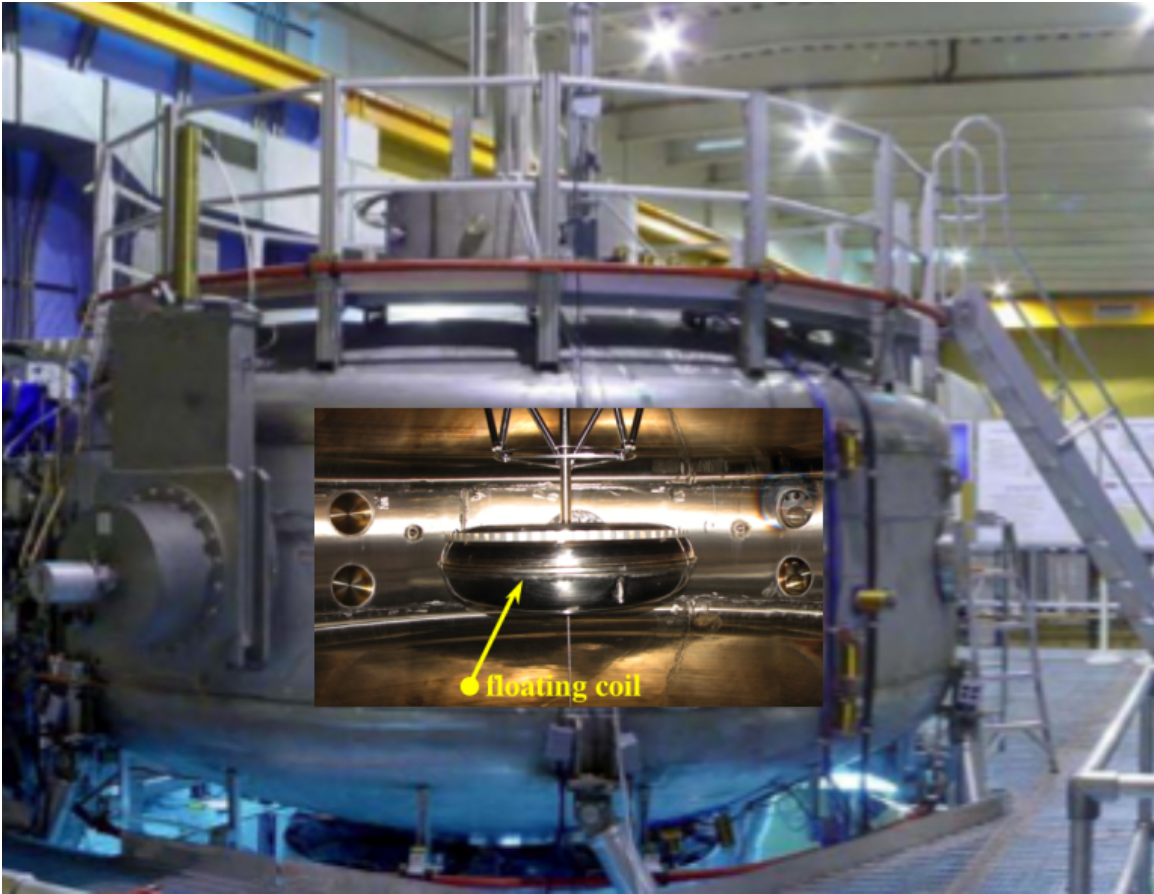
Figure 3-1: The Levitated Dipole Experiment (LDX). The main photograph shows the exterior of the LDX vacuum chamber as seen from the mezzanine level of the laboratory. Superimposed is a photograph of the interior of the LDX vacuum chamber showing the floating, dipole coil.

3.2 Theoretical Motivation

All of the basic theory upon which LDX is based was provided in Chapter 2 of this thesis and especially in §2.5. LDX as built is remarkably close to Akira Hasegawa's original concept [3], which he first proposed 1987. Hasegawa emphasized an effect that was first recognized in the study of (mainly collisionless) space plasmas, namely, that fluctuations can cause the plasma to diffuse into a state characterized by peaked density and pressure profiles which scale with radius, r, according to Eq.(2.33):

$$p(r) \sim r^{-20/3}$$

$$n(r) \sim r^{-4}.$$

In order to achieve such profiles, Hasegawa stressed the necessity of *levitating* the central, dipole coil in order to minimize the loss of particles along field-lines.

Even so, before anyone was willing to build a levitated dipole facility, it was necessary to show that Hasegawa's ideas—which were appropriate for a collisionless plasma—could be applied to highly collisional, fusion-grade plasmas. To this end, the non-linear analyses of Pastukhov [4] and Kouznetsov [5] were crucial in establishing the importance of profiles that are *stationary* to MHD interchange modes [Eq.(2.32)],

$$pV^\gamma = constant$$

$$nV = constant.$$

If a plasma is displaced from a profile that is marginally stable to MHD interchange modes [Eq.(2.31)], a process self-consistent or "self-organized" convection will work to restore the plasma back to its marginally stable state (cf., §2.5.3). Intuitively, MHD interchanges produce a large-scale convection of flux-tubes; the pressure and density profiles which emerge are those profiles that remain unchanged by this process. Flux-tube mixing homogenizes the plasma such that the stationary profiles are characterized by an equal amount of entropy per flux-tube and an equal number of particles per flux-tube.

Two additional, theoretical papers were also of particular importance in extending Hasegawa's basic notions into the collisional plasma regime. The first paper, by Kesner, examined the problem of dipole-confinement using a drift-kinetic analysis [55]. Kesner began by re-deriving the MHD plasma compressibility condition for stability against interchange modes [Eq.(2.30)]

$$\delta(pV^\gamma) \geq 0.$$

It was then shown that plasmas can be stable to interchange modes as well as various electrostatic drift modes in any configuration where the curvature drift frequency, $\widetilde{\omega_d}$, exceeds the diamagnetic drift frequency, ω_*,

$$\widetilde{\omega_d} > \omega_*. \tag{3.1}$$

A second important theory paper, writen by Garnier, Kesner and Mauel [56], provides a full MHD analysis of a plasma in an LDX-like device. Employing the full theoretical machinery of the Grad-Shafranov equation and the MHD energy principle [57], Garnier *et al.* showed that in addition to being stable to interchange modes, LDX plasmas should also be stable to balooning modes and that this stability should hold even at arbitrarily high plasma pressures. Thus, far from being undermined, Hasegawa's ideas of plasma confinement in a levitated-dipole device have been corroborated upon closer examination of the underlying theory.

3.3 A Path to Fusion Power

The fact that plasmas confined in a levitated-dipole device are predicted to be stable even with pressure profiles that vary with radius as $p(r) \sim r^{-20/3}$ [Eq.(2.33)] immediately suggests that such a device might be suitable for a future nuclear fusion reactor. Since dipole theory places no stability limits on the pressure, but only on the pressure gradient, the maximum pressure attainable in a dipole device is set by the edge-pressure and the size of the device. More formally, the condition $\delta(pV^\gamma) = 0$

[Eq.(2.31)] implies that the peak plasma pressure is given by

$$p_{peak} = p_{edge} \left(V_{edge}/V_{peak}\right)^{\gamma}. \qquad (3.2)$$

Consequently, an optimum dipole-confiment device is one which maximizes the magnetic flux expansion, that is, the ratio of V_{edge} to V_{peak}. In other words, an optimum dipole-confinement device consists of a strong, compact dipole coil located inside of a large vacuum chamber. Built along these lines, a dipole fusion reactor may have the following desirable properties [58]:

- $\beta \sim 1$, where β is defined as the ratio of plasma pressure to magnetic pressure: $\beta \equiv 2\mu_0 p/B^2$. In contrast, tokamak-like devices have β-limits of $\beta \sim 0.1$. β is generally taken as a quantity of merit for any plasma confinement scheme.

- Steady state operation. A dipole fusion reaction can be maintained as long as the dipole coil remains levitated whereas tokamaks are pulsed devices.

- Disruption-free operation. The toroidal currents of tokamaks contain a great amount of energy which, on occasion, is violently directed into the walls of the device in potentially hazardous events called disruptions. There is no analogous free-energy source in a dipole device.

- An absence of wall-loading problems. The fact that a dipole fusion device is characterized by large flux expansion [Eq.(3.2)] means that no part of the vessel (e.g. the divertor) is at risk of being destroyed.

- Favorable transport. In the absence of destabilizing drift-frequency modes, a dipole-confined plasma could exhibit "classical transport", where the particle diffusion coefficients scale as $1/B^2$. However, classical transport has, historically, been predicted for almost every fusion device and has generally never been achieved due to the presence of plasma turbulence.

Of course, in addition to the fact that there is no experimental confirmation for any of the above claims (that is why LDX has been built!), a dipole fusion reactor

can be expected to have the following drawbacks:

- Reliance upon a levitating coil. The construction of a superconducting magnet that can be succesfully thermally insulated from the surrounding hot plasma is a major technological challenge. On the other hand, the multi-hour operations of the coils in both LDX and RT-1 [59], [53] are promising and suggest that this challenge can be overcome.

- No D-T fusion. The D-T (deuterium-tritium) fusion reaction has the highest fusion cross-section but also produces an energetic, 14.1 MeV neutron which cannot be trapped magnetically and which therefore can penetrate and heat the levitating coil.

- Large chamber size. In order to maximize the magnetic flux expansion [Eq.(3.2)], it is desirable to have a very large vacuum chamber. This poses a technological challenge in its own right in addition to diminishing the flux through the wall of fusion power necessary to generate heat and ultimately electricity.

Despite these drawbacks, the Department of Energy has chosen to fund LDX in order to get a better sense of the possibilities of dipole cofinement. Moreover, there are replies to the negative points listed above. The first challenge—building a reliable and thermally insulated dipole coil—has already resulted in some early successes, as we have mentioned, and there is no reason to discount further technological advances in high-temperature superconducting materials.

Regarding the second item, the fact that a hypothetical dipole fusion reactor cannot use the D-T reaction is not altogether bad since tritium is highly radioactive, needs to be bred at great expense, and the fast neutron product of the D-T reaction tends to activate and embrittle the materials used to build the reactor facility. A dipole fusion reactor would have to utilize alternate reactions which, unfortunately, have much lower fusion cross-sections. After D-T, the most favorable fusion reaction is D-^{3}He:

$$D +^3 He \longrightarrow {}^4He \ (3.6 \ MeV) + p \ (14.7 \ MeV). \tag{3.3}$$
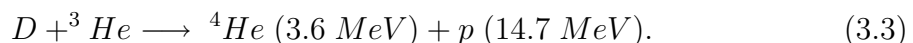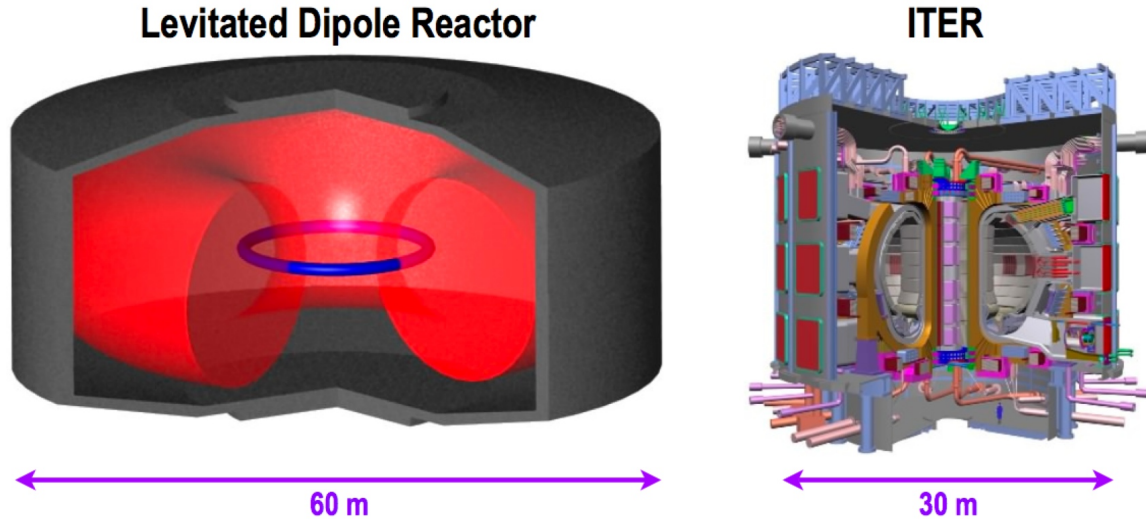
Figure 3-2: A sketch showing the scale of a hypothetical levitated dipole fusion device. At right, a drawing of ITER (a planned, large Tokamak device) is shown for comparison.

A dipole reactor based on the D-^{3}He reaction was considered by Hasegawa *et al.* [60]. A similar device was also considered by Teller *et al.* [61] as a power source for long-distance space travel. However, the success of any such D-^{3}He fusion scheme presupposes the existence of a flourishing lunar mining industry since the moon is, in fact, the nearest source of abundant ^{3}He.

Nevertheless, it is entirely possible that the confinement in a dipole fusion device might be so good that D-D fusion reactions can be utilized:

$$(50\%) \ D + D \longrightarrow \ ^3He \ (0.8 \ MeV) + n \ (2.5 \ MeV)$$
$$(50\%) \ D + D \longrightarrow \ \ T \ (1.0 \ MeV) + p \ (3.0 \ MeV)$$

$$(3.4)$$
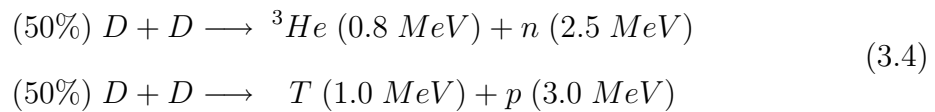
Although the cross-section for this D-D fusion is about 100 times lower than for D-T, D-D fusion is a long-term goal of the fusion community since deuterium can be easily harvested from sea-water and the radioactivity of the waste products is minimal. Kesner *et al.* [62] examined the reactions of Eq.(3.4) and concluded that they would be both feasible and advantageous in a dipole fusion reactor.

3.4 LDX: Major Components

3.4.1 Vacuum Chamber

The LDX vacuum chamber is a large, welded, stainless-steel vessel shaped somewhat like an oblate spheroid (Fig. 3-1) or, possibly, like a "steel pumpkin"[1]. It has the dimensions of height = 3.0 m, diameter = 5.0 m, and it encloses a volume of about 65 m^3. The chamber is evacuated by one turbo-pump and two cryo-pumps which can establish baseline pressures of around 5×10^{-8} Torr.

A central, vertical column connects two large pneumatic hoists (the "upper" and "lower launchers") located above and below the vacuum chamber (Fig. 3-3). The launchers are used to mechanically raise the floating, dipole coil into the mid-plane of the vacuum chamber in preparation for levitation and also to lower the coil back down when experiments have finished. Attached to the launcher system and located below the floating coil is a spring-loaded "lower-catcher" which protects the coil in the event that it falls. An immobile "upper catcher" prevents excessive damage should the floating coil become vertically unstable and "fall-up".

3.4.2 Floating Coil

The "Floating Coil" or "F-Coil" produces the main dipole magnetic field and, as such, is the most important piece of hardware of the experiment. In order to minimize particle losses along the field lines, it is necessary that the field lines not be obstructed by any material impediments. The current in the F-Coil, therefore, cannot be driven by leads extending to an external power supply. Consequently, in order to sustain a current without any external power source, the F-Coil must be superconducting. For the same reason—minimizing losses parallel to the field—the F-Coil cannot be supported in its position at the center of the vacuum chamber with mechanical supports—the F-Coil must be supported in its position by magnetic levitation.

The LDX F-Coil is wound from Nb$_3$Sn superconducting strands and is designed

---

[1] *zucca d'acciaio* [63]
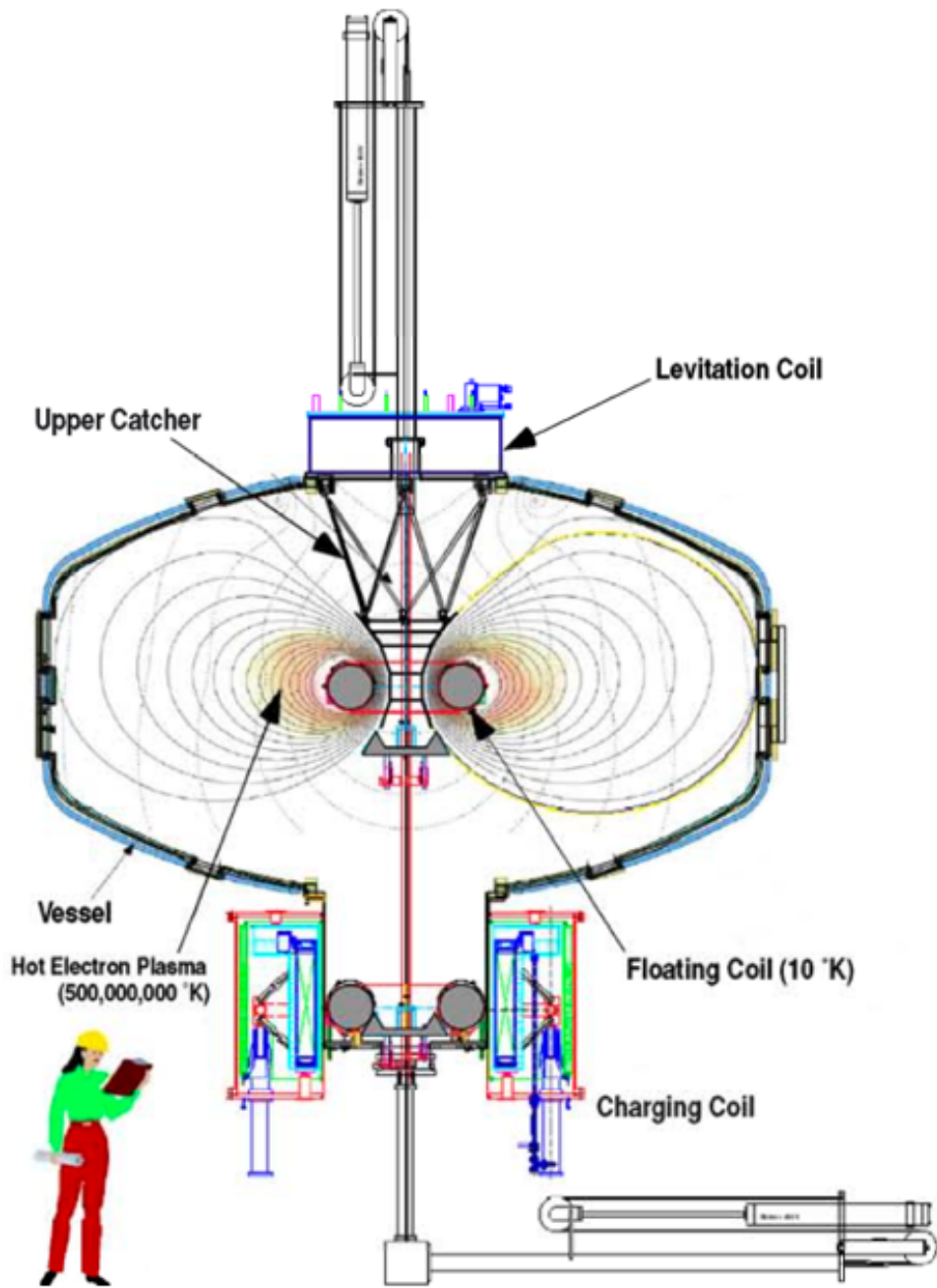
Figure 3-3: Schematic of LDX showing a vertical cross-section of the experiment.

to operate between temperatures of 4.3K and 10 K and carry a current of up to 1.5 MA-turns. The cross-section of the F-Coil is a low-eccentricty ellipse whose center is located at 39.3 cm from the center of the LDX vacuum chamber. The vertical (major) radius of the F-Coil cross-section is 17.4 cm and the horizontal (minor) radius is 17.0 cm. The outermost surface of the outer ring of the F-Coil vacuum shell is located at 57.9 cm from the center of the LDX vacuum vessel[2].
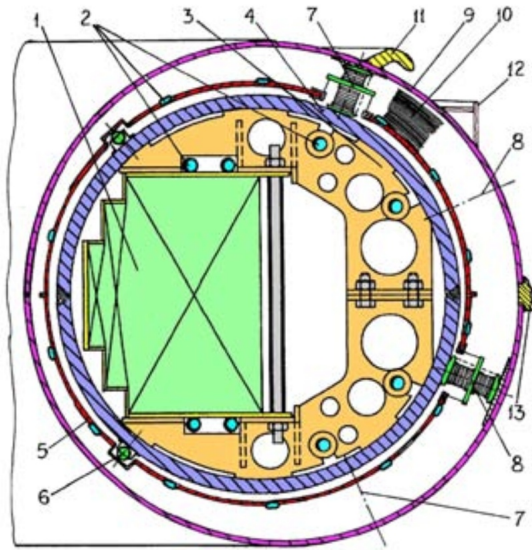
Figure 3-4: F-Coil cross-section. 1—magnet; 2—heat exchanger; 3—gusset; 4—helium vessel; 5—radiation shield; 6—glass ball shield support; 7—vacuum shell and shield support; 8—side bumper; 9—vacuum shell; 10—MLI thermal insulation; 11—lifting disk; 12—laser beam control structure; 13—vacuum shell ring. From Zhukovsky *et al.* "Design and Fabrication of the Cryostat for the Floating Coil of the Levitated Dipole Experiment" (2000).

The great challenge in the design of the F-Coil is to produce a strong magnetic field while minimizing the coil weight and maximizing its thermal insulation. A schematic of the F-Coil cryostat is shown in Fig. 3-4. In addition, the F-Coil was engineered to withstand accelerations of up to 10 times the acceleration of gravity. As built, the F-Coil weighs 565 kg and remains superconducting for approximately 2.5 hours. The manufacture of the coil was completed in two stages: The coil itself was wound by Everson Electric in Bethlehem, PA; after successful tests at MIT, the magnet was then joined to its cryostat, built by Ability Engineering Technology in South Holland, IL. Details of the design and operation of the F-Coil and its crystotat, which together constitute a major technological achievement, can be found in [59], [64] and [65].

---

[2]These measurements, which are not readily found in the literature, were provided by M. Mauel.
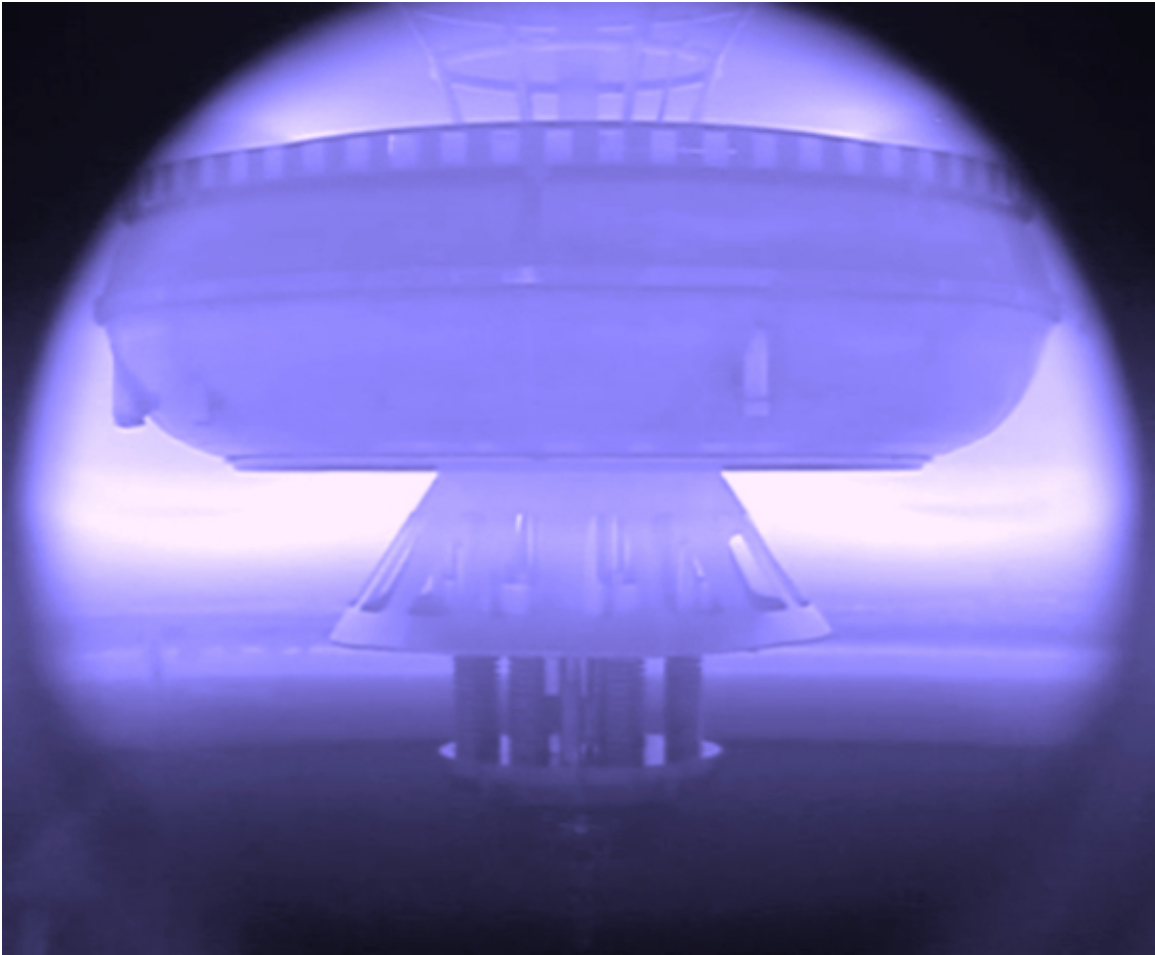
Figure 3-5: A photograph of the F-Coil levitating in the middle of the LDX vacuum chamber and surrounded by plasma. The skirt-like object beneath the F-Coil is the spring-loaded lower launcher. The lower launcher both lifts the F-Coil into position prior to levitation and can catch the F-Coil should it become unstable and fall. The cage-like structure above the F-Coil is the upper catcher which stops the F-Coil if it happens to "fall-up".

3.4.3 Charging Coil

A current is produced in the F-Coil by induction from a second magnet—the "Charging" or "C-Coil". The C-Coil is a very large (92 henries), NbTi superconducting magnet located at the bottom of the LDX vacuum chamber (Fig. 3-3). The C-Coil produces a maximum magnetic field of 3.9 T in the bore, corresponding to 425 amps of current (3.6 MA-turns) and 8.3 MJ of stored energy. The C-Coil was jointly designed by MIT and the Efremov Institute in St. Petersburg, Russia and manufactured by the Efremov Institute. Further details of its design and operation can be found in references [65] and [66].

3.4.4 Levitation Coil and Laser Positioning System

The "Levitation-Coil" or "L-Coil" is the magnet which produces an attractive force on the F-Coil in order to counteract the F-Coil's gravity and allow the F-Coil to levitate. The name "Levitation-Coil" is somewhat confusing since the Levitation-Coil does not itself levitate, but rather is responsible for the levitation of the F-Coil. The L-Coil is a conventional (non-superconducting), water-cooled, copper coil consisting of 80 turns and manufactured by Advanced Engineering Systems in Mertztown, PA. The L-Coil is located on top of the LDX vacuum chamber (Fig. 3-3) and requires about 3,550 amps of current to levitate the F-Coil.

Outside of its sources of current, a magnetic field, **B**, has no curl and can therefore be written as the gradient of a scalar potential which satisfies the Laplace equation. As is well known, such potentials have no local extrema but only saddle points. The energy stored in the field, which varies as B^2, will likewise have no minima and, consequently, no collection of magnets can be held in static equilibrium by the action of their own magnetic fields (Earnshaw's theorem).

On account of this, stable levitation of the F-Coil must employ a system of dynamical feedback between the F-Coil and the L-Coil. Placing the L-Coil above the F-Coil instead of below affords the considerable advantage that the only instability is vertical—the F-Coil can both fall up and fall down. Had the L-Coil been placed be-

low the F-Coil (and generated a magnetic repulsion instead of attraction), the F-Coil would, in addition, be tilt-unstable.

Designed and implemented by Darren Garnier, the levitation control algorithm employs a PID-loop to stabilize the vertical position of the F-Coil. The control algorithm is so well-tuned that vertical excursions of the F-Coil are limited to just a few millimeters . The position of the F-Coil is monitored by 8 lasers and 8 receivers which look inward from the equatorial circumference of the LDX vacuum chamber. The extent to which these lasers are occluded by the F-Coil provides information about the position of the F-Coil and these values, along with the L-Coil current, constitute the main inputs to the levitation control algorithm [65].

3.4.5 The Magnetic Field

Three magnets are required in the Levitated Dipole Experiment: the F-Coil, C-Coil and L-Coil. However, only the F-Coil and the L-Coil are charged during the course of plasma experiments. In our subsequent analysis, it will be necessary to have an accurate model of the magnetic fields and we develop this model here. We represent the F-Coil and L-Coil fields as a collection of coaxial, circular filaments each with current I, radius a and vertical height h. In cylindrical coordinates, the field produced by each filament is [67]

$$
\begin{aligned}
B_\rho &= \frac{-2I(z-h)}{c\rho\sqrt{(a+\rho)^2+(z-h)^2}}\left[K(k)-\frac{a^2+\rho^2+(z-h)^2}{(a-\rho)^2+(z-h)^2}E(k)\right]\\
B_z &= \frac{2I}{c\sqrt{(a+\rho)^2+(z-h)^2}}\left[K(k)+\frac{a^2-\rho^2-(z-h)^2}{(a-\rho)^2+(z-h)^2}E(k)\right].
\end{aligned}
\tag{3.5}
$$

Here c is the speed of light and K and E are the complete elliptic integrals which take the argument k,

$$
k^2 = \frac{4a\rho}{(a+\rho)^2+(z+h)^2}.
\tag{3.6}
$$

71

Because it will be useful in later chapters, we also write-down the corresponding expression for the azimuthal component of the vector potential, A_ϕ [68],

$$A_\phi(\rho, z) = \frac{4Ia}{c\sqrt{(a+\rho)^2 + (z-h)^2}} \left[\frac{(2-k^2)K(k) - 2E(k)}{k^2} \right].$$ (3.7)

The filament parameters are provided from a code written by Darren Garnier which breaks-up the solid shapes of the F-Coil and L-Coil into an arbitrary number of filaments. For our purposes, a modest number of filaments is sufficient. The F-Coil is broken-up into 8 filaments which carry a total current of 1,100,452 A. The L-Coil is broken-up into 5 filaments which carry a total current of 28,200 A. The parameters of these filaments are listed in Table 3.1.

Table 3.1: F-Coil and L-Coil Filament Parameters

Filament	Current (A)	Radius (cm)	Height (cm)
F-Coil			
1	20,442.10	27.17	-1.735
2	20,442.10	27.17	1.735
3	62,786.45	28.50	-3.125
4	62,786.45	28.50	3.125
5	233,508.73	31.50	-4.038
6	233,508.73	31.50	4.038
7	233,508.73	35.97	-4.038
8	233,508.73	35.97	4.038
L-Coil			
1	56,400.00	29.14	157.5
2	56,400.00	38.22	157.5
3	56,400.00	47.30	157.5
4	56,400.00	56.38	157.5
5	56,400.00	65.46	157.5

The magnetic field produced by these filaments is depicted in Fig. 3-6. If we represent the magnetic field using field lines, then there will be some field lines that enclose only the F-Coil and some field lines that enclose both the F-Coil and the
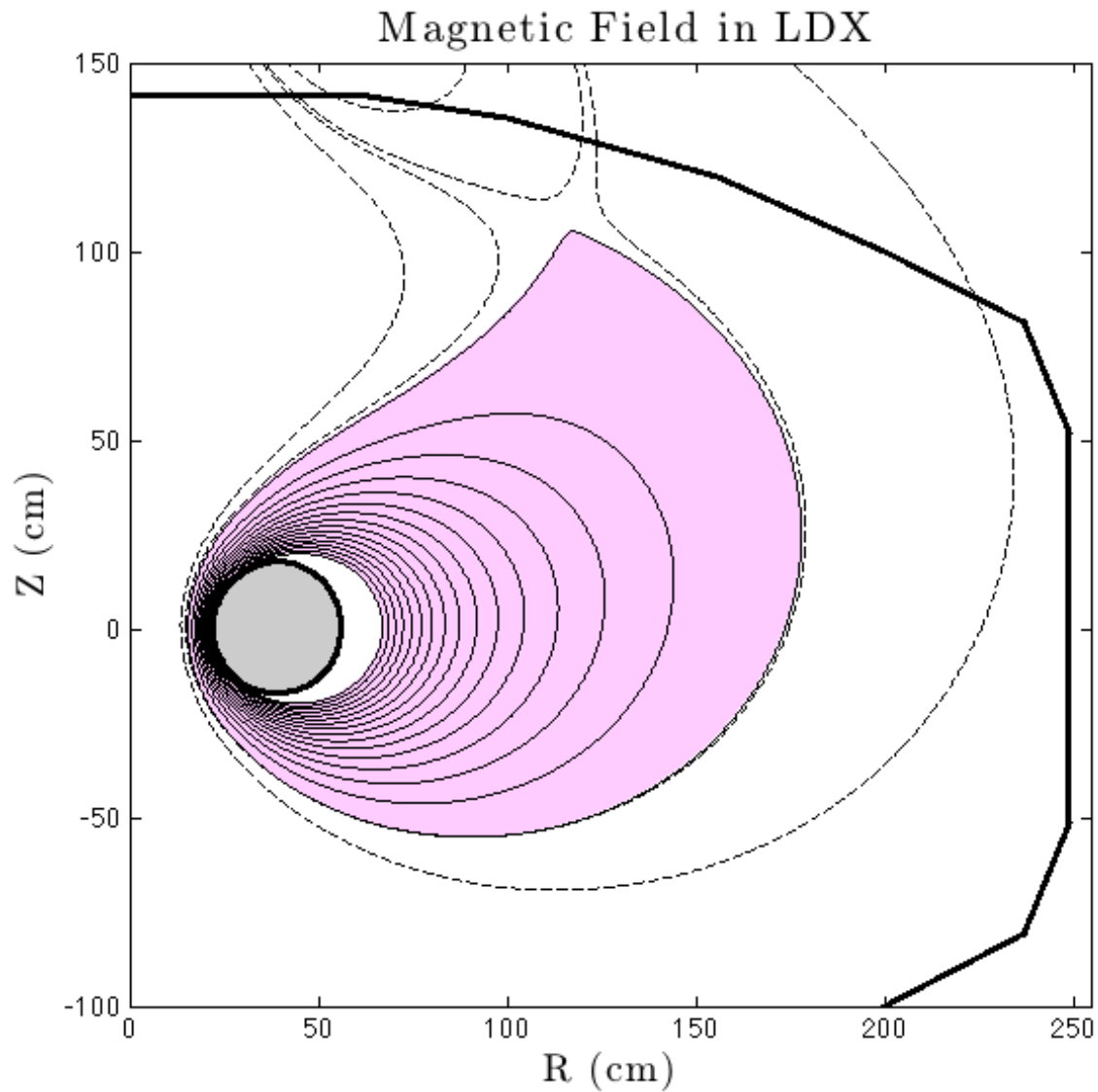
Figure 3-6: Diagram of the magnetic field in LDX. The vacuum chamber is viewed in cross-section from the front and its outline is delineated with thick, black lines. The F-Coil is also shown in cross-section and shaded in gray. The combined fields of the F-Coil and L-Coil produce some field lines which form closed curves entirely within the vacuum chamber (solid lines) and some field lines which do not (dashed lines). The plasma volume (pink shading) falls within the first and last closed field lines. The first closed field line crosses the mid-plane at approximately $R = 66.8$ cm and the last closed field line crosses the mid-plane at approximately $R = 173.5$ cm.

L-Coil. For convenience, we refer to the first class of field lines as "closed" and the second class as "open".

We can label the field lines using the McIlwain L-shell parameter (§2.5.1) which is simply the radial location that the field lines crosses the equatorial mid-plane. Normally, the L-shell parameter is dimensionless; for instance in magnetospheric research, the L-parameter is given as a multiple of planetary radius. In LDX, it is more convenient simply to keep the dimension of length from the center of the vacuum chamber when labeling the field lines. With this convention, the innermost closed field line in LDX is located at L = 66.8 cm and the outermost closed field line is located at L = 173.5 cm. Insofar as a plasma will follow the magnetic field lines, the plasma volume in LDX is bounded by these two field lines.

3.4.6 Microwave Heating

Plasmas in LDX are produced by puffing-in controlled amounts of gas (usually deuterium, but occasionally helium) which is then ionized and heated by high-power microwaves of various frequencies. A "cavity heating" scheme is employed whereby the microwaves are launched into the LDX vacuum chamber in such a way that multiple reflections off the chamber walls make the heating more or less isotropic [69]. Assuming that any first-pass absorption is small and, therefore, that the microwaves can access the plasma from the high-field side, a majority of the power should be absorbed by electrons whose cyclotron frequencies, ω_c, are resonant with the microwaves in a process called ECRH (Electron Cyclotron Resonance Heating). The microwave heating sources on LDX are:

- 2.45 GHz magnetron sourcing up to 2.5 kW of continuous-wave power.

- 6.4 GHz klystron sourcing up to 2.5 kW of continuous-wave power.

- 10.5 GHz klystron sourcing up to 10 kW of continuous-wave power.

ECRH can be expected to deliver most of its power where the microwaves are resonant with either ω_c (fundamental resonance) or $2\omega_c$ (first harmonic resonance).

These locations correspond to shells of constant magnetic field strength. For the 2.45 GHz microwaves, the fundamental resonance surface crosses the equatorial plane at a radial distance of around 81 cm from the center of the LDX vacuum chamber; the first harmonic surface crosses the equatorial plane at a radial distance of about 99 cm. A plot of the 2.45 GHz resonance surfaces is provided in Chapter 7, Fig. 7-8.

For the 6.4 GHz microwaves, the radial distances of the resonant surfaces are 62 cm (fundamental) and 75 cm (first harmonic). However, the shell of the fundamental resonance of is not closed since the inner half of the shell strikes the F-Coil.

The 10.5 GHz klystron—which triples the total heating power—only became operational in May of 2008. As with the 6.4 GHz microwaves, the presence of the F-Coil prevents the 10.5 GHz microwaves from having any equatorial resonances. Instead, the 10.5 GHz microwaves heat the plasma mainly in the "polar regions" above and below the F-Coil. This polar heating is expected to heat a broader swath of magnetic surfaces than the two lower frequency sources which deposit most of their power closer to the equator and therefore over a narrow bundle of field-lines.

3.5   Diagnostics

An inheritance from fusion's early connection with the atomic bomb program is the use of the word "diagnostics" to describe the various measuring devices used to obtain information about plasmas. For with plasmas—just as with nuclear explosions or, more appropriately, in the practice of medicine—interior conditions must be deduced from exterior measurements. Being a new experiment, LDX has a fairly basic diagnostics set which we outline here below.

3.5.1   Probes

A set of three moveable probes are located on the top of the LDX vacuum chamber. An additional moveable probe is located at the northeast port of the chamber midplane. These probes have the option of being used as either swept-voltage probes, floating-voltage probes, or ion-saturation probes Although the probes can extend

over one meter into the chamber, their furthest reach is only about 20 cm inside the last closed magnetic field line (which marks the outermost boundary of the confined plasma). Moreover, because the probes disturb the plasma profiles and are themselves subject to great abuse when extended too far inward, the probes are mainly kept at the plasma boundary. A more thorough description of the LDX probes can be found in reference [70]. Edge temperature and density measurements used in this thesis are obtained from a swept probe that enters the plasma vertically from the southwest-top of the vacuum chamber. A description of these measurements is provided in §5.2.2.

3.5.2 Magnetic Diagnostics

A large number of magnetic pickup coils are placed on the outside of the LDX vacuum chamber. Because plasmas are diamagnetic, any currents induced in the plasma will act to decrease the local strength of the magnetic fields emanating from the F-Coil and L-Coil. The voltages subsequently induced in the pickup coils will be proportional to the local $\partial B/\partial t$ and this signal can either be read directly to giving an indication of the magnetic fluctuations or the signal can be integrated to give a record of $B(t)$.
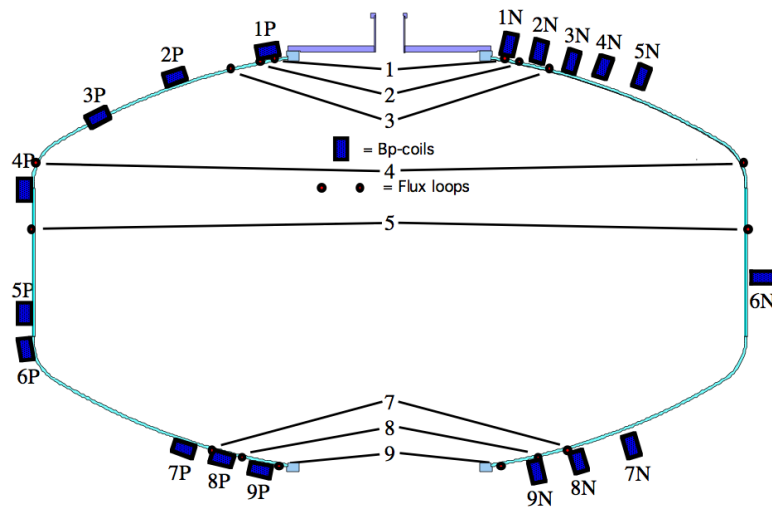
Figure 3-7: Location of magnetic diagnostics. In addition to large flux-loops that encircle the LDX vacuum chamber, there are also pickup coils (B_p coils) positioned on the outside of the chamber. These coils are oriented either parallel to the field (labeled by 'P') or normal to the field (labeled by 'N'). From KARIM, *Equilibrium and Stability Studies of Plasmas Confined in a Dipole Magnetic Field Using Magnetic Measurements* (2007).

There are numerous magnetic diagnostics at various locations around the LDX

vacuum chamber (Fig. 3-7). In addition, a few smaller pickup coils (called Mirnov coils) are located inside the chamber. Of particular interest is Flux-Loop 5 which encircles the entire vessel at a latitude close to the chamber's equator. This loop gives the most straightforward measure of the total plasma diamagnetism which can serve as a rough proxy for the plasma β. A more thorough description of the LDX magnetic diagnostics and their relation to the plasma pressure profile is provided in reference [71]. In this thesis, measurements from Flux-Loop 5 are utilized and discussed in §6.3

3.5.3 Light Detectors

Plasmas, which consist of rapidly moving charged particles, emit electromagnetic radiation over an enormous band of frequencies. The radiation power spectrum provides some indirect information about the temperature of the electrons, the density of neutral particles and general plasma fluctuations. At this writing, the light-detecting diagnostics on LDX are

- NaI hard x-ray detector. The x-rays measured by this device originate primarily from particles striking the F-Coil.

- Photodiodes with a set of atomic line emission filters.

- Visible light spectrometer.

- Visible light video cameras.

- Visible light fast video camera sampling 2,000 frames per second for one second.

- V-band radiometer which measures the power radiated by the plasma at frequencies between 50 GHz and 75 GHz.

3.5.4 Vessel Ion Gauge

The vacuum level inside the LDX vacuum chamber is measured with an off-the-shelf ion gauge. The pressure due to neutral particles changes during the course

of an experimental campaign due to gas-fueling, which is controlled, and also the uncontrollable emission of particles from the both the vacuum chamber walls and the F-Coil. The neutral pressure inside the vacuum chamber has a huge effect on a plasma even when other parameters (such as the ECRH) are kept constant. The vessel ion gauge, consequently, provides one of the most crucial pieces of information about the plasma; without note of this measurement, no reproducibility of the results would be possible.

3.5.5 Microwave Interferometer

Because plasmas have an index of refraction that is a function of their density, interferometers can be used to measure the plasma density. The optimal frequencies in plasma experiments are generally in the microwave bands and in LDX the interferometer operates with a center frequency of 60 GHz. Though difficult to build, the payoff from a successful interferometer can be huge since an interferometer provides a non-perturbative measurement of a fundamental plasma parameter—the plasma density—even in the central core of the plasma. Moreover, unlike for most diagnostics, interferometer data is not dependent on other (possibly unknown) plasma parameters.

Because interferometers take chordal measurements, the data they produce are line-integrals of the plasma density. The LDX interferometer takes data along four chords and these can be inverted to give a rough estimate of the radial density profile. The LDX interferometer has been operating with considerable success and is currently providing the experiment with some of its most important data. A detailed description of the interferometer is given in Chapter 4 and an analysis of the data from the interferometer makes up the remainder of this thesis.

3.6 Results from "Supported-Mode" Experiments

LDX has been conducting plasma experiments since August, 2004. For most of this time the F-Coil was not levitating but held in place by three, small (1.5 cm diameter)

support-rods which fastened the F-Coil to the launcher system. LDX, operated in this way, is said to be in the "supported-mode". In supported-mode, LDX plasmas are susceptible to losses along the field-lines and so the confinement should resemble the confinement in magnetic mirrors.

Initial LDX results [65], [72] showed that while the F-Coil was supported, most of the plasma energy was stored in a small population of hot electrons ($E \sim 50\,\mathrm{keV}$) while the background plasma remained cold. As observed in CTX at Columbia University (§2.6), the hot-electron population of LDX was susceptible to interchange instabilities (§2.4.2). These HEI's (Hot Electron Interchanges) were found to be stabilized once a sufficient rate of gas fueling was established. The threshold fueling rate was necessary to maintain a stable ratio of background plasma to hot-electrons and to compensate for particle losses along the field lines.

Once stable to HEI's, LDX plasmas were observed to enter a higher-density phase of with densities of the order 10^{10} particles per cm^3 and characterized by peak β's of around 20%. The hot-electron population still accounted for most of the energy and accounted for the observation of highly anisotropic pressure profiles characterized by $P_\perp/P_\parallel \approx 5$ [72]. These higher-density plasmas were steady-state and endured for as long as the microwave heating power remained on—typically 5 to 10 seconds. Quite often, a robust plasma "afterglow" would endure for many seconds after the termination of the ECRH indicating the persistence of the trapped, hot-electron population.

Fluctuation studies revealed the occasional presence of a quasi-coherent mode at around 2-4 kHz [73]. This mode was observed on the Mirnov coils, interferometer and photodiodes. The frequency of this mode could be altered or washed-out entirely in response to changes in the gas fueling and corresponding changes in the density profile. The spacing of the Mirnov coils indicated that the fluctuation was dominated by an azimuthal, $m = 1$ component.

Chapter 4

The LDX Microwave Interferometer

4.1 General Remarks

A four-channel microwave interferometer (center frequency: 60 GHz) provides LDX with the capability of measuring the plasma density as a function of both space and time. The interferometer is presently the most sophisticated diagnostic on the experiment and provides LDX with some of its most important data. Interferometers, when operating successfully, have three advantages that are rare amongst plasma diagnostics:

- Interferometer measurements depend upon just one plasma parameter.

- The measurements do not perturb the plasma in any way.

- Measurements can be made even in the plasma's central core.

An interferometer, therefore, can serve very much like an experiment's eyes, especially insofar as knowing the plasma density is, quite probably, as close as one can get to visualizing the plasma itself.

Fundamentally, interferometers work as plasma density diagnostics because a plasma has an index of refraction that is a function of its density. In the equato-

rial plane of LDX the magnetic field, **B**, is mostly vertical. This geometry provides an opportunity to make an interferometer using O-mode ("ordinary"-mode) waves which are electromagnetic plane-waves that have an electric field vector, **E**, parallel to an external, ambient magnetic field, **B**, and a propagation vector, **k**, perpendicular to the external magnetic field:

$$\mathbf{k}_{wave} \perp \mathbf{B}_{external}$$
$$\mathbf{E}_{wave} \parallel \mathbf{B}_{external}.$$

(4.1)

The considerable advantage of using O-mode waves is that, of all the waves which can propagate through a magnetized plasma, O-mode waves have one of the simplest dispersion relations [74]:

$$N(\omega) = (1 - n/n_c(\omega))^{1/2}.$$

(4.2)

Here N is the index of refraction, n is the plasma density and $n_c(\omega)$ is the cutoff density for a wave of frequency ω. For a 60 GHz wave, $n_c = 4.46 \times 10^{13}$ cm^{-3}.

Thus, provided that the plasma density is less than the cutoff density of the interferometer's probing beam ($n < n_c(\omega)$), the interferometer will record a phase shift containing information about the plasma density along the beam's trajectory. Measuring the plasma density, then, is properly two separate tasks: First, the building of an instrument that faithfully records the phase shifts of the wave through the plasma and second, the conversion of those phase shifts into a plasma density. This chapter deals with the first of these tasks, that is, the design, construction and calibration of a microwave interferometer. The interpretation of the interferometer data is addressed in chapter 5.

4.2 Design

4.2.1 Overview

The LDX interferometer—like most interferometers found on plasma experiments—is of the Mach-Zehnder type. In Mach-Zehnder interferometers, a beam is split into
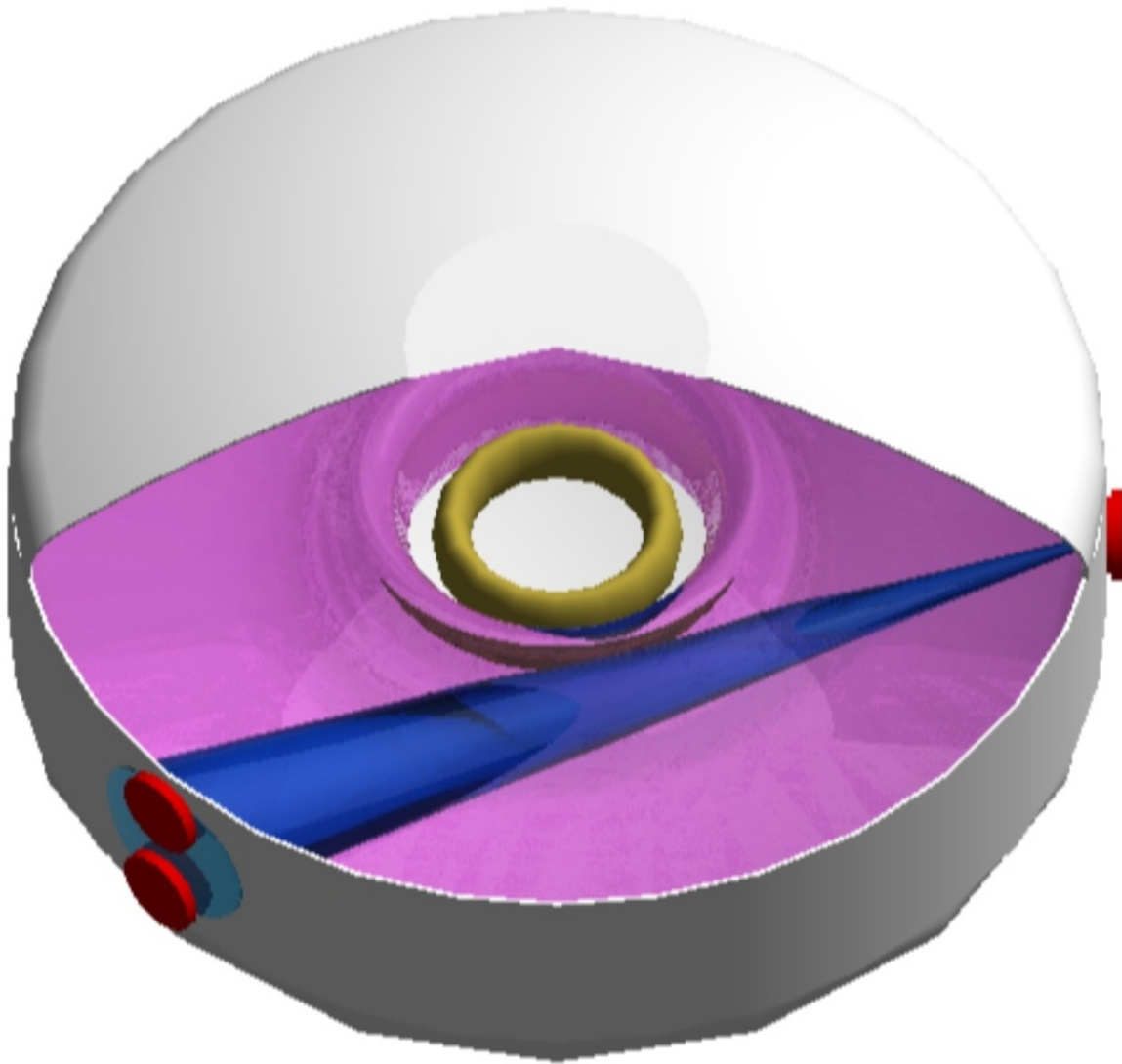
Figure 4-1: Illustration of the LDX microwave interferometer. The image is a cutaway of the LDX vacuum chamber as seen from the north of the laboratory, looking from above. The Floating-Coil, drawn in gold, is surrounded by a pink plasma. A 60 GHz probing beam (blue) is launched from one side of the vessel to the other. The beam spreads out as it propagates, but most of the power is contained within a cone of about $10°$. Four receivers (not shown) are placed around the mid-plane of the vessel within the area illuminated by the beam. Also not shown is an additional beam which travels through wave-guides around the outside of the vessel. This second beam, which has no contact with the plasma, serves as a reference. Mixing the probing beam, which traverses the plasma, with the reference beam, which does not traverse the plasma, yields the phase-shift due to the plasma's changing density.

two halves which are sent down different paths ("legs") of equal length. On one leg, the *optical* path length is allowed to change, meaning that some optical material along this leg has an index of refraction which may change in time. Along the other leg, the optical path length remains fixed. At the end of their separate travels, the two beams (called the "probing" and "reference" beams) are rejoined and the phase of the combined beam is measured at a fixed location. Changes in the measured phase indicate changes in the refractive index along the path of the probing beam. In the LDX interferometer, the probing beam traverses a path through the plasma, the reference beam traverses a path around the outside of the vessel and phase shifts indicate changes in the plasma density.

Building upon this basic premise, the LDX interferometer is distinguished by the following design elements:

- The LDX interferometer is a heterodyne system that uses two, free-running, 60 GHz oscillators offset by an intermediate frequency of 70 MHz.

- Four channels of data are obtained from just one transmitted beam by placing four receivers at different locations within the transmitted beam's 3 dB beamwidth.

- Phase shifts are detected in quadrature at 70 MHz.

Although interferometry has been used to measure plasma densities since nearly the beginning of the fusion program, the novel geometry of LDX necessitates a novel interferometer design. Two recent review articles [75], [76] underscore that none of the interferometers found on other experiments—taken individually—can serve as a model for the LDX interferometer. In particular, most microwave interferometers tend to be used over short distances and usually along just one line of sight. Interferometers on larger experiments with higher densities need higher frequency sources, such as CO_2 lasers, which means there is a diminishing technological overlap with microwave devices.

LDX, in contrast to other fusion facilities, is physically a very large experiment that operates at relatively low densities. Our goal was to build an interferometer that

could measure the density over a wide swath of the vacuum chamber and also over a reasonably wide range of densities. In addition, we wanted to design an interferometer that was elegant, robust, reasonably inexpensive, and readily upgraded from one to multiple channels. We are confident that interferometers in any future dipole experiment can be built successfully using the LDX interferometer as a template (though at a higher frequency to measure higher densities) . The LDX interferometer's most salient design features, along with their rationales, are described below.

4.2.2 Choosing the Frequency

The most important feature of any interferometer is its operating frequency since this dictates which components and technology are used to build the device. In general, all optically refractive materials exhibit some dispersion—that is, they possess an index of refraction which is a function of wave frequency. The optimum frequency of an interferometer is constrained by the dispersion relation from both above and below:

- The interferometer frequency must be low enough that phase shifts are large enough to be distinguished from the background noise.

- The interferometer frequency must be high enough that the beam trajectory closely approximates a straight line. At low frequencies, refraction can cause the arc length of the beam's trajectory to curve by an amount comparable to a wavelength. When this happens, phase shifts due to the refractive medium and phase shifts due to the new, longer trajectory cannot be decoupled and the phase information becomes much harder to interpret. In extreme cases, a highly refracted beam may miss its receiver altogether or even be reflected backwards.

For an O-mode wave through a plasma, the dispersion relation is given by Eq.(4.2) which, as previously noted, is a function of the plasma density. At the optimum frequency—corresponding to expected phase shifts of at most a few wavelengths— the index of refraction of the plasma should deviate only slightly from unity. Applied

to Eq.(4.2), this constraint means that the cutoff density for the wave, n_c, should always be around 10 to 100 times greater than the plasma density, n. However, because the design of the LDX interferometer commenced before LDX had produced its first plasma, the expected plasma densities in LDX had to be estimated in order to choose a suitable frequency for the interferometer.

Plasmas created by ECRH (as in LDX) are generally limited by the cutoff density of their ECRH sources since no heating can occur in regions which cannot be accessed by the heating microwaves. In LDX, the highest frequency source of the initial ECRH sources was 6.4 GHz (§3.4.6). The cutoff density for a given wave, $n_c(\omega)$, is simply the density at which the plasma frequency, ω_p, equals the wave frequency, ω. In Gaussian units, this relationship is

$$n_c(\omega) = \left(\frac{m_e}{4\pi e^2}\right)\omega_p^2 = \left(\frac{m_e}{4\pi e^2}\right)\omega^2$$
$$n_c \approx 1.24 \times 10^{-8} \cdot f^2$$

(4.3)

Here m_e is the mass of the electron, e the charge of the electron, and $f \equiv \omega/2\pi$ is the frequency in Hz. The cutoff density for 6.4 GHz microwaves is 5.1×10^{11} particles per cm^3.

Taking the 6.4 GHz cutoff density as an estimate for the maximum plasma density, the interferometer beam frequency was chosen to be 60 GHz since a wave at this frequency has a much higher cutoff density of 4.5×10^{13} cm^{-3}. By this reckoning, the index of refraction [Eq.(4.2)] for a 60 GHz beam will always be within 1% of unity, even at the location of the peak density. Subsequent measurements with the interferometer have confirmed the estimate of $\sim 10^{11}$ particles per cm^3 in LDX to be correct. The reason that 60 GHz was chosen and not, say, 70 GHz is that 60 GHz falls right in the middle of the V-band (50-75 GHz) specification of standardized microwave components.

4.2.3 Heterodyning

Because the operating frequency is 60 GHz, the design of the LDX interferometer is compelled to take into consideration the basic limitations of V-band microwave technology. Chief among these are the phase stability and power output of standard 60 GHz frequency sources. The issue of phase stability is addressed by a technique called heterodyning which is discussed in this subsection. Power considerations are taken up in §4.2.4.

Heterodyning is the use of two or more different frequency sources to detect a signal encoded in a wave. Heterodyne receiving is the basis of radio and television communication and affords a number of advantages over simpler, single-frequency detection schemes. Without the advantages of heterodyning, the LDX interferometer would not function.

The LDX interferometer is, fundamentally, an FM radio transmitter and receiver. Like radio, the interferometer employs a high-frequency carrier wave—in this case 60 GHz—to transmit information wirelessly across a distance. The actual information or "signal" is encoded in time-varying phase shifts (frequency modulations) of the carrier wave. In the FM radio analogy, the changing plasma density is analogous to the changing tones of a human voice. In principle, the signal can be obtained by mixing the modulated carrier wave with a reference wave at the unmodulated carrier frequency—the frequencies subtract and what remains is the desired signal. In practice, however, it is usually preferable to mix the carrier wave with a slightly different frequency resulting in a wave at the beat frequency. In this scenario, the signal is then demodulated from the beat frequency wave.

In the terminology of radio, the high-frequency carrier wave, transmitted from a distant source, is called the RF (for "radio frequency"); the second frequency source, which is present in the receiver, is called the LO ("local oscillator"); the beat frequency which results from mixing the RF and LO is called the IF ("intermediate frequency"). Described in these terms, the frequencies used in the LDX interferometer are:

- RF = 60.00 GHz

- LO = 60.07 GHz

- IF = 70 MHz

Advantages of Heterodyning

Heterodyning was originally implemented in the early days of radio because components were better, cheaper, and easier to work with at the lower frequency of the IF than at the higher frequency of the RF. This same reason also contributed to the decision to use heterodyning in the LDX interferometer—components in the MHz range are significantly cheaper and easier to work with than components in the GHz range. Nevertheless, *the most crucial benefit of heterodyning is that it greatly improves the phase stability of the interferometer.* Without this added stability, the LDX interferometer would not work.

In a simple Mach-Zehnder setup, two beams from the same frequency source traverse different optical paths and, at a set location, the phase of the recombined beam is measured. If the frequency source is not perfectly constant over time, non-uniformities in the sequence of phase fringes propagate down both legs of the interferometer. If, in addition, the lengths of the two legs are not exactly equal, these non-uniformities will reach the observation location at different times for each leg causing spurious phase shifts to be measured.

Since every frequency source exhibits some spread of output frequencies, it is an iron rule that the two legs of an interferometer must be of equal length to within a few wavelengths, otherwise signal measurements will be dominated completely by phase noise. However, in the LDX interferometer, where the wavelength of the 60 GHz probing beam is only 5 mm, this condition is impossible to satisfy. On the other hand, *if the probing beam is compared with a reference offset by some intermediate frequency, it is only necessary to ensure that the two legs of an interferometer be equal to within a few wavelengths of the IF in order to achieve phase stability.*

This notion is based on the recognition that most of the phase noise of a high-frequency source is random and found within a narrow band centered around the

source's nominal output. That is, most of the noise is also high-frequency and, as such, can be averaged to zero. The problem with using a reference at the same frequency as the carrier wave is that all of the noise gets downshifted to frequencies centered around zero; this in turn washes-out entirely any low-frequency signal of interest. Heterodyning exploits the fact that in most radio transmission setups, an intermediate frequency, f_{IF}, can be found that is much lower than the carrier frequency, f_{RF}, but simultaneously much higher than the signal of interest, f_{signal}:

$$f_{RF} \gg f_{IF} \gg f_{signal}. \tag{4.4}$$

Consider, as in the LDX interferometer, the comparison of a 60.00 GHz RF with a 60.07 GHz LO. Over 850 fringes will pass by a detector during one period of the 70 MHz intermediate frequency. We imagine that the phase of a realistic, non-ideal 60 GHz frequency source sometimes leads and sometimes lags an ideal 60 GHz wave but over periods of a few fringes, not hundreds of fringes. Consequently, even 70 MHz is slow enough to average out most of the noise from a non-ideal, 60 GHz frequency source.

A smaller amount of phase noise still remains at 70 MHz, but much of this is eliminated (for the same reason as before) by making the probing and reference legs of the interferometer roughly the same number of wavelengths. But now the critical wavelength, λ_{IF}, is that of the 70 MHz intermediate frequency

$$\lambda_{IF} = 429 \text{ cm} = 14.1 \text{ ft.} \tag{4.5}$$

Needless to say, this tolerance is significantly more feasible than 5 mm, which is the wavelength of the 60 GHz RF.

In fact, there is an inherent asymmetry in the design of the LDX interferometer which can be seen in Fig. 4-2. The path lengths from the LO to each of the mixers are of equal length to well within one wavelength of the IF. However, because most of the power from the RF oscillator is needed for transmission across the vacuum chamber (§4.2.4), the path lengths from this oscillator to the mixers are not at all
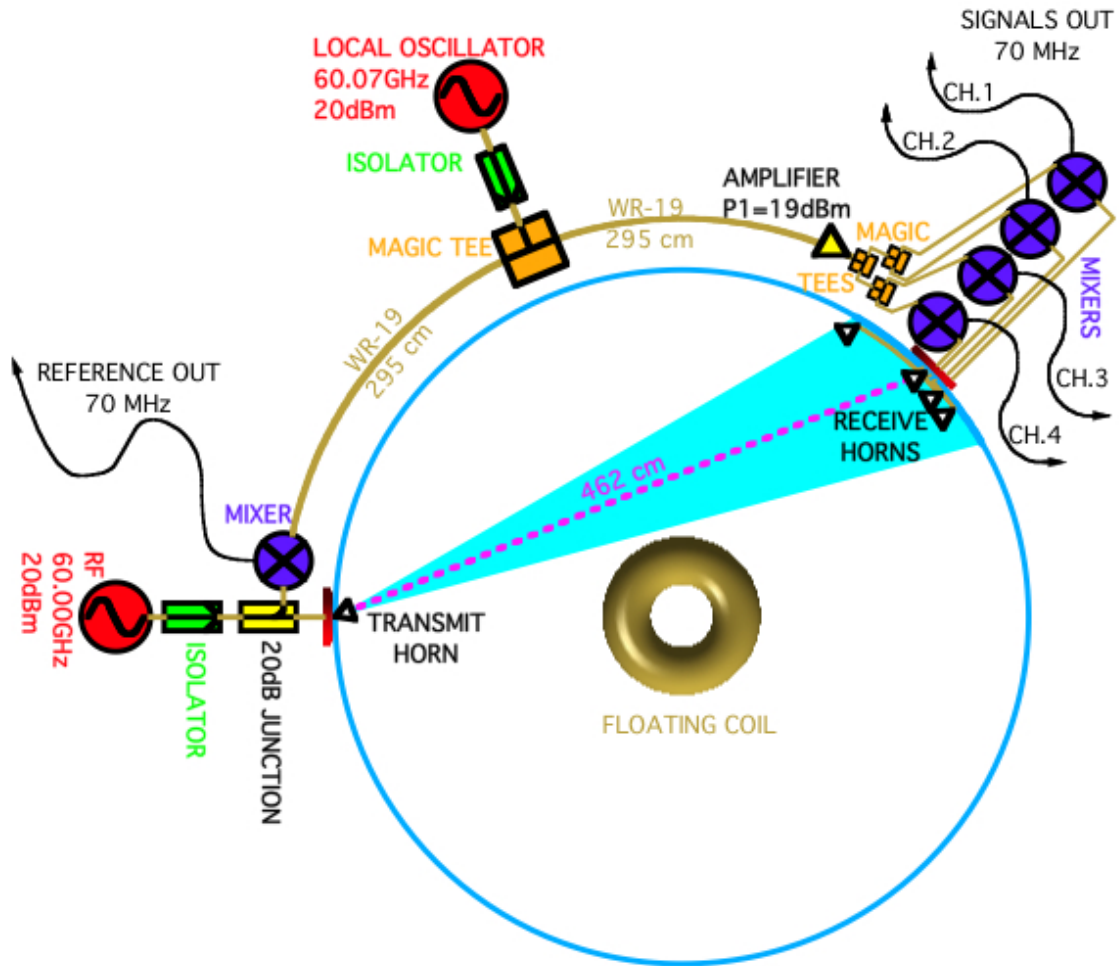
Figure 4-2: Schematic drawing of the LDX microwave interferometer in the equatorial plane of the LDX vacuum chamber as seen from above. A 60 GHz probing beam is transmitted across the LDX vacuum chamber from a west port to a northeast port. The 3 dB portion of the probing beam subtends an angle of about 10°. Due to the geometry of the setup, a beam of width φ subtends an angle of 2φ along the vacuum chamber circumference. Consequently, about 20° of the vacuum chamber wall is illuminated by the probing beam and within this arc are positioned four receivers. A second, free-running oscillator, functioning as an LO, provides much improved phase stability by mixing the probing beam down to an IF of 70 MHz . The LO drives 5 mixers: 4 channels of data and one reference. Phase shifts from the 4 data channels are demodulated in quadrature from their IF carrier waves

equal—indeed, the signal and reference legs differ by a distance equal to the length traveled across the vacuum chamber.

Nevertheless, the entire length across the vacuum chamber, $\Delta\ell$, is only slightly larger than the IF wavelength, λ_{IF}:

$$\Delta\ell = 462 \text{ cm} = 1.08 \ \lambda_{IF}. \tag{4.6}$$

A path length difference of only $1\lambda_{IF}$ translates into phase noise primarily at at the intermediate frequency itself—still much higher than the signals of interest. Consequently, the asymmetry in the interferometer design has a very small effect on the total phase stability, actual measurements of which are provided in §4.4.

Of course, the increase in phase stability in a heterodyne system must come at the expense of some other parameter. Sure enough, the price of heterodyning is that the time resolution of the system is made worse: The minimum discernible time interval increases from approximately the period of the RF, τ_{RF}, to the period of the IF, τ_{IF}. Nevertheless, in the LDX interferometer, as in most heterodyne systems, this has no adverse effects. Because $f_{IF} \gg f_{signal}$, the time resolution, τ_{IF}, is still significantly finer than necessary to follow the signal of interest. Indeed, in the LDX interferometer, $\tau_{IF} \approx 14.3$ ns but the data acquisition system itself only samples every 12.5 μs—and even this is more than fast enough to follow the density evolutions in LDX which typically occur on time scales of 100μs to 0.1s.

Free-Running Oscillators

As just established, heterodyning is necessary to obtain satisfactory phase stability in the LDX interferometer. In order to implement this, a second frequency source is required. The decision to make the second frequency source independent and free-running was inspired by the description of an interferometer built by Domier, Peebles and Luhmann Jr. at UCLA [77]. In particular, the authors make the following point:

> "Low phase noise is dependent on having a stable IF. At low IF this
> usually requires phase locking the oscillators to a highly stable reference

oscillator . . . What is not generally well understood by the plasma physics community is that at high IF two free-running oscillators can produce a low phase noise system without locking."

The reasons for this follow from our general discussion above on the advantages of heterodyning. The phase noise of a realistic (non-ideal) frequency source is generally a rapidly decreasing function of the frequency difference from the nominal output of the source. Consequently, in the case of the LDX interferometer, we expect the 60.07 GHz component of the 60.00 GHz source to be small and, likewise, we expect the 60.00 GHz component of the 60.07 GHz source to be small. At the same time, an IF of 70 MHz is still sufficiently slow that around 850 fringes from the RF and LO are compared during one period of the IF—more than enough for the high frequency noise on *both* the RF and LO sources to be *independently* averaged-out.

An IF on the order of IF $\sim 10^{-3} \times$ RF was considered to be high enough to use free-running oscillators mainly by analogy with the frequencies used in the UCLA interferometer [77]. The reason that precisely 70 MHz was chosen is based on the availability of components. 70 MHz falls right in the middle of "channel 4" in the VHF spectrum—the same "channel 4" on a television set—and consequently there is no shortage of high-quality components available at this frequency.

IF Phase-Locked Loop

Despite the excellent phase stability of the interferometer with free-running oscillators, an IF phase-locked loop (PLL) circuit was designed and built for the LDX interferometer all the same. The PLL operates by comparing the 70 MHz interferometer reference with a high-precision 70 MHz crystal oscillator. The PLL increases its output voltage whenever the phase of the IF reference leads the crystal oscillator and decreases the output voltage whenever the IF lags the crystal. The PLL output is then fed into the varactor-tuning of one of the 60 GHz oscillators to compensate.

It was found, however, that the interferometer's phase stability with the PLL could equal but not surpass the phase stability when the oscillators were free-running. This result was inevitable insofar as the distance from the LO to the PLL and back again is

slightly more than one IF wavelength which places a limit on how fast the information can travel.

Nevertheless, the PLL performs an extremely useful function in that it provides a compensation against the slow drifts of the 60 GHz oscillators (mainly due to temperature fluctuations). This is especially helpful because LDX experiments tend to last the better part of a day and, without the PLL, the frequency difference between the 60 GHz oscillators would need to be periodically retuned. Because the PLL serves mainly as a drift compensation circuit and has no effect on the phase stability, I believe that it is still more correct to refer to the oscillators on the LDX interferometer as "free-running" and not "phase-locked".

4.2.4 Power Considerations

In addition to the issue of phase stability (§4.2.3), ensuring adequate power levels is also a prime concern when dealing with 60 GHz microwaves. This problem is especially important on a physically large device like LDX.

RF Power

The frequency sources used in the LDX interferometer are two Gunn-diode oscillators with rated output powers of 20 dBm (100 mW)[1]. The minimum signal power that can be received by an antenna is set by the noise power, P_{noise}, due to the antenna's temperature, T [78]:

$$P_{\text{noise}} = kT\Delta f. \tag{4.7}$$

Here k is Boltzmann's constant and Δf is the signal bandwidth in Hz. Setting Δf conservatively to 1 MHz, the room temperature noise floor is approximately $P_{\text{noise}} \approx -114$ dBm. Adding to this the insertion losses from the horn antenna and mixer [79], the noise floor is estimated to be

$$P_{\text{noise}} \approx -108 \text{ dBm}. \tag{4.8}$$

---

[1]A table of the microwave components used in the LDX interferometer is given in Appendix A.

For a beam of wavelength λ transmitted between two horns—one with gain G_1 and the other with gain G_2—the total received power at a distance ℓ is given by the Friis Transmission Equation [80]:

$$P_{\mathrm{R}}(\mathrm{dB}) = P_{\mathrm{T}}(\mathrm{dB}) - 10\log_{10}\left[\left(\frac{\lambda}{4\pi\ell}\right)^2\right] + G_1 + G_2, \qquad (4.9)$$

where P_{R} is the received power and P_{T} is the transmitted power.

In LDX, the length across the vacuum chamber from the west port to the northeast port is approximately 462 cm (Fig. 4-2). The antennas used both to transmit and receive the 60 GHz beam are standard gain horns with rated minimum gains of 20 dB. Assuming that most of the 20 dBm oscillator power is transmitted, the power received at the far end of the vacuum chamber will be

$$P_{\mathrm{R}} \approx 20 \text{ dBm} - 80 \text{ dB} + 20 \text{ dB} + 20 \text{ dB}$$
$$P_{\mathrm{R}} \approx -20 \text{ dBm} \qquad (4.10)$$
$$P_{\mathrm{R}} \gg P_{\mathrm{noise}}.$$

The conclusion from Eq.(4.10) is a positive one: The LDX interferometer should have no trouble in measuring a signal transmitted across the length of the vacuum chamber.

LO Power

Ensuring sufficient LO power to drive the mixers is a more difficult task. There are five 60 GHz mixers, each of which must be driven by at least 10 dBm of LO power. The LO is placed along the circumference of the vacuum chamber midway between the transmitting and receiving antennas (Fig. 4-2). The distance between the LO and the mixers is about 3 meters in either direction.

The attenuation factor, α, for a wave propagating along a waveguide is a function of the the wavelength, the waveguide dimensions, the skin-depth, and the resistivity of the waveguide material. For a 60 GHz, TE_{10} wave propagating along WR-15

waveguide the attenuation factor is approximately [81]

$$\alpha \approx -3 \text{ dB/meter}. \tag{4.11}$$

Starting with 20 dBm from the LO oscillator and subtracting 3 dBm due to the power split at the Magic-Tee (Fig. 4-2), it is evidently not possible to transmit the necessary power to drive the mixers at a distance of 3 meters.

The solution (at least in part) is to propagate in a higher mode down a larger waveguide. In the next larger size of waveguide, WR-19, the attenuation factor for a 60 GHz wave is only [81]

$$\alpha \approx -1.6 \text{ dB/meter}. \tag{4.12}$$

This value easily ensures that 10 dBm of power can be propagated in both directions from the LO to the mixers.

This fix was sufficient during the early stage of the LDX interferometer when there was only one channel and two mixers (one at the west port and one at the northeast port). However, once the interferometer was upgraded to four channels, there was no possible way that five mixers (one at the west port and four at the northeast port) could be driven by the unaided LO.

The problem was solved by adding a 60 GHz high-power amplifier in front of the four north-east mixers (Fig. 4-2). The amplifier is capable of outputting 19 dBm and, since this power is split twice in order to divide it four-ways, the power available to drive each of the four mixers is 19 dBm - 6 dBm = 13 dBm, which is a satisfactory value. The ease in upgrading from one to four channels is one of the great advantages of the LDX interferometer design.

Reflected Power

One major worry regarding the design of the LDX interferometer was the power of reflected beams. The interior of the stainless steel vacuum chamber makes an excellent mirror for 60 GHz waves and the concern was that reflected beams would interfere with the main beam thus rendering any output signals indecipherable. A second look

at the Friis Transmission Equation [Eq.(4.9)], however, reassures that this scenario is very unlikely.

According to Eq.(4.10), each pass of the 60 GHz beam across the vacuum chamber results in an extremely large power loss:

$$P_{\text{Loss}} \approx -80 \text{ dBm}. \tag{4.13}$$

Compounded to this are the following points: In order to enter the receiving antenna, a reflected beam would likely need to be reflected multiple times; a reflected beam can, in general, have any polarity but an antenna receives waves of one polarity only; standard gain horns launch fairly directional beams and so only a very small amount of power strays from the direct path. Given all this, the conclusion made was that any reflected beams received by the antennas would be so attenuated in power that interference with the main beam would be minor.

A separate possibility is that reflections from the F-Coil, insofar as they need to be reflected only once to reach the receiving antennas, may still have enough power to cause noticeable interference with the main beam. This scenario is, on the face of it, unlikely because the radiation pattern emitted by a standard gain horn has a fairly high directivity. More importantly, direct measurements (presented in §4.4) show that the effect of reflections off the F-Coil is small.

4.2.5 Multiple Channels from One Transmitted Beam

The phase shift measured by each interferometer channel is a line-integral of the index of refraction along the path of the probing beam. In order to obtain spatial profile information from a line integral, it is necessary to have as many different line integrals (i.e. interferometer channels) as possible. The LDX interferometer takes measurements along four channels, details of which are listed in Table 4.1.

The LDX interferometer exploits the fact that a 60 GHz wave launched in the simplest possible way—from a pyramidal standard gain horn—will spread out into a cone and can therefore be received at multiple locations. The angular portion of an

Table 4.1: Four Channels of the Microwave Interferometer

Channel	Radius of Tangency (cm)	Chord Length (cm)	Launch Angle (deg. above W-E diameter)	Receive Angle (deg. of azimuth)
1	77	476	18	36
2	86	470	20	40
3	96	462	22.5	45
4	125	433	30	60

antenna's radiation pattern where the power is at least 50% (or 3 dB) of the maximum power for a given distance is called the 3 dB beam-width. In the azimuthal plane (H-plane), a standard gain horn has a 3 dB beam-width of about 10° [82]. Receivers placed within the 3 dB portion of a standard gain horn's radiation pattern will receive a wave with the following characteristics:

- Relatively high-power.

- Close approximation to a plane wave at normal incidence. This is especially true in a large device like LDX where, at the far end of the vacuum chamber, a V-band standard gain horn receiver only subtends about 0.4° of arc.

These two features make it possible to operate multiple channels on the LDX interferometer without resorting to complicated microwave optics or an even more complicated system of multiple beams. The simplicity of multi-channel operation is another advantage of the LDX interferometer design.

The scheme further benefits from the geometry of how the beam is launched. Because the beam is transmitted from the circumference of the vacuum chamber, a simple, geometrical sketch shows that the section of the vacuum chamber wall illuminated by the beam subtends an angle φ_{wall} that is twice the angle subtended by the beam itself, φ_{beam}:

$$\varphi_{wall} = 2\varphi_{beam}. \tag{4.14}$$

Thus even with a fairly directional standard gain horn, around 20° of the vacuum

chamber wall is illuminated by the trasmitted beam.

In order to avoid the F-Coil, the beam is transmitted along a chord from a west port on the vacuum chamber to a northeast port (Fig. 4-2), corresponding to a launch angle of 22.5° above the west-east diameter of the chamber. One receiver is located on this direct chord and two others are placed along chords that pass nearer to the F-Coil and nearer to where the pressure and density peaks must be located. Because data from the outer, flatter portion of the plasma was desired, a risk was taken and the fourth receiver was placed on a chord that lies somewhat outside the main portion of the beam (Table 4.1).

To ameliorate somewhat the situation of channel 4, an azimuthal adjust mechanism (Fig. 4-4) was installed on the trasmitting horn which allows its central launch angle to be increased by up to 4°. Additionally, LDX was given a special, custom-built horn as a demonstration piece from Millitech, LLC. This horn, which is larger and thus has a higher gain and narrower beam-waist (Table A.1), was installed on channel 1.

4.2.6 Phase Detection in Quadrature

Adding a 60.07 GHz LO to the LDX interferometer means that the output, instead of being centered around zero is now centered around 70 MHz. Because the signal of interest must now be demodulated from the IF, a heterodyne system requires an additional 70 MHz signal to serve as a reference. This IF reference is output from a second mixer which mixes the RF and the LO *before* the RF beam has entered the plasma (Fig. 4-2). In total, five 70 MHz waves are output from the interferometer: four data channels and one reference (Fig. 4-2).

The desired phase shift information from the plasma is obtained from the data channels by subtracting the reference wave. Essentially the process is exactly what would have happened at a higher frequency had heterodyning not been employed. However, a straightforward demodulation which outputs a voltage proportional to the cosine of the phase difference still leaves ambiguous whether the phase is increasing or decreasing [83]. The solution is to demodulate each data signal twice—once with a
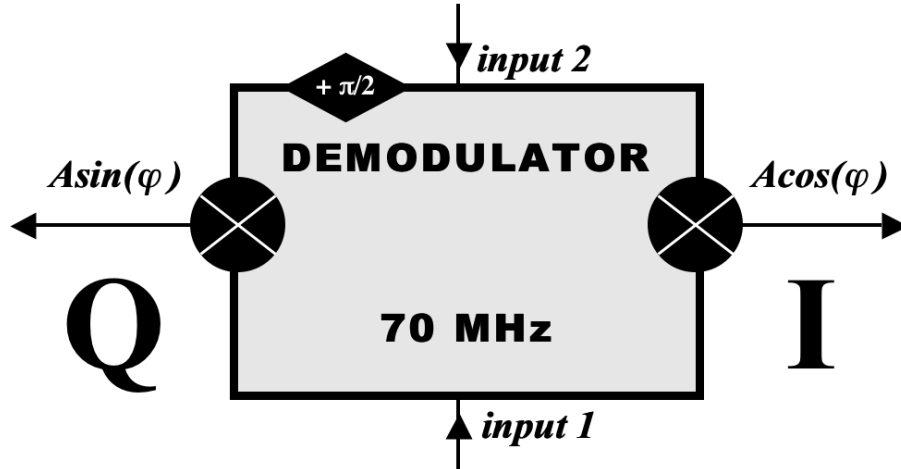
Figure 4-3: Schematic diagram of a demodulator. The two inputs are mixed twice, once with a phase shift of $\pi/2$ applied to one of the inputs. The output "I" is proportional to the cosine of the phase difference between the inputs while the output "Q" is proportional to the sine of the phase difference. Together, I and Q can determine the phase difference unambiguously.

phase shift of 90° added to one of the inputs. This technique, called phase detection in quadrature, is diagrammed in Fig. 4-3. The two outputs—one proportional to the cosine of the phase difference between the inputs and one proportional to the sine of the phase difference—are traditionally called I ("in phase") and Q ("quadrature"), respectively. I and Q together are sufficient to determine the phase unambiguously.

In addition to improving the phase stability, the second advantage of heterodyning (§4.2.3) is that it is much easier to process signals at 70 MHz than at 60 GHz. This is helpful because the five 70 MHz signals need to be amplified and filtered a number of times before they are input into the demodulators.

In general, mixing two signals results in an output, V_{out}, that is proportional both to the cosine of the phase difference, ϕ, as well as the product of the amplitudes of the inputs, A_1 and A_2:

$$V_{out}(t) = A_1(t)A_2(t) \cdot \cos \varphi(t). \qquad (4.15)$$

The consequence of Eq.(4.15) is that amplitude modulations (AM) are impossible to disentangle from frequency modulations (FM) in the output of a basic mixer. It is imperative, therefore, to remove any AM before proceeding with FM demodulation. Equalizing the amplitudes of the 70 MHz signals is accomplished with "limiting" amplifiers (see §4.3.2).

4.3 The Interferometer as Built

4.3.1 Microwave Hardware
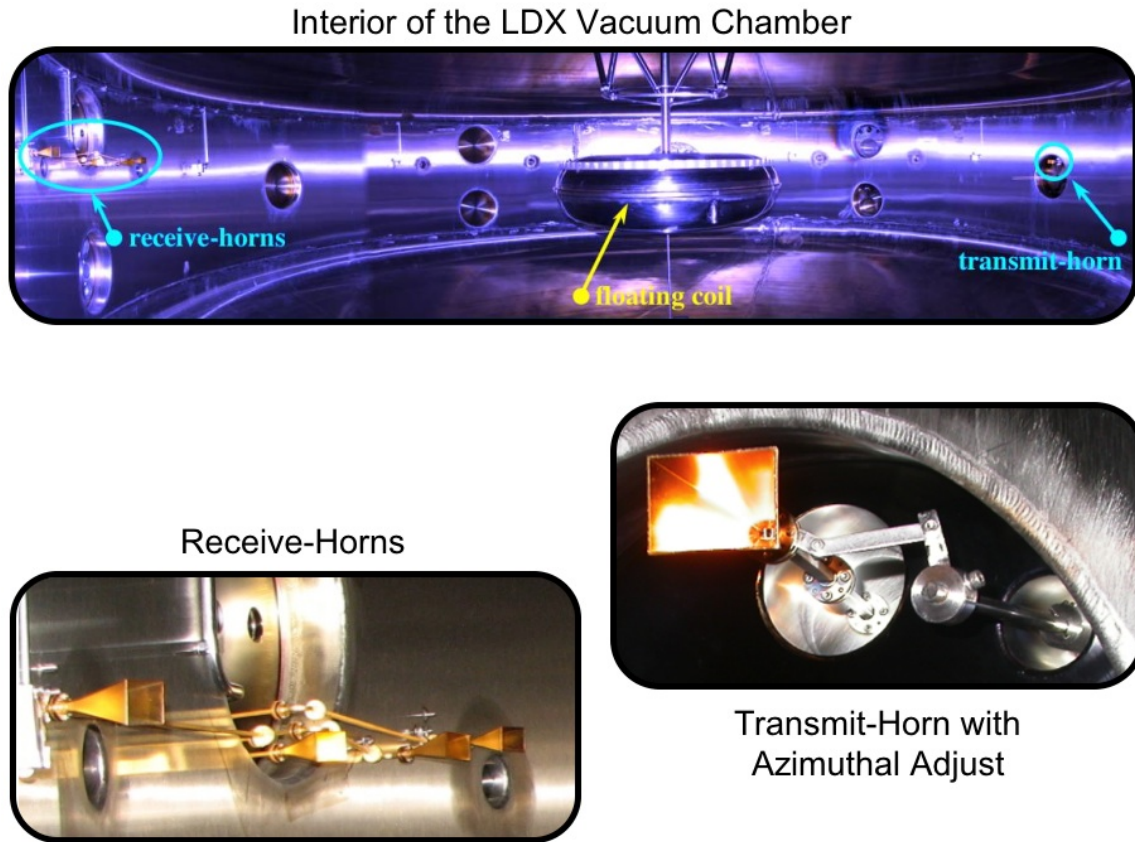
Figure 4-4: Photographs of the microwave components of the interferometer located inside the vacuum chamber. Waveguide flange patterns were machined directly into the stainless steel vacuum flanges in order to make vacuum feedthroughs. The azimuthal adjust on the transmit-horn is a cam that attaches to a vacuum-feedthrough rotation-stage which can be manipulated from outside the vacuum chamber. As the cam is rotated, the horn is pulled a few degrees away from the west-east diameter of the chamber and away from the F-Coil.

NORTHEAST PORT

LO 60.07 GHz
Magic Tee
Varactor Tuning
WR15-WR19 Transition

60 GHz Amplifier
Magic Tee (x3)
60 GHz Mixer (x4)

WEST PORT

60 GHz Mixer
20dB Junction
Voltage Regulator
Isolator 25 dB
Isolator 20 dB
60 GHz Gunn Diode
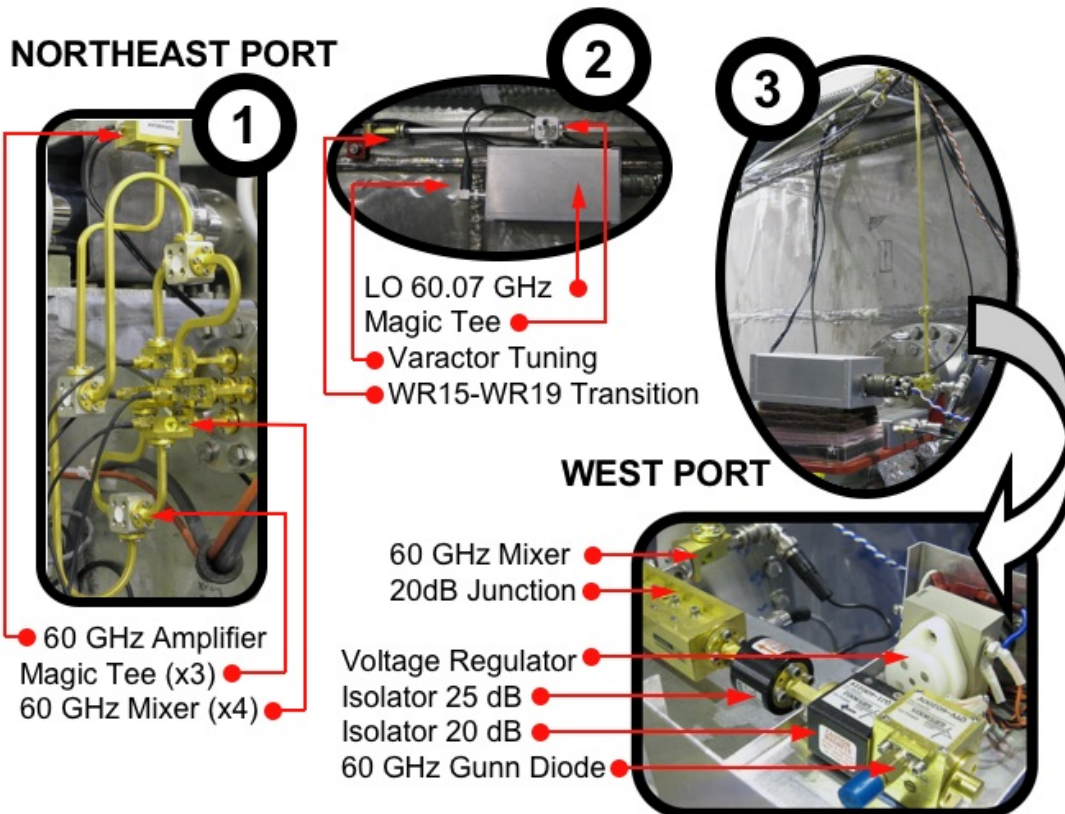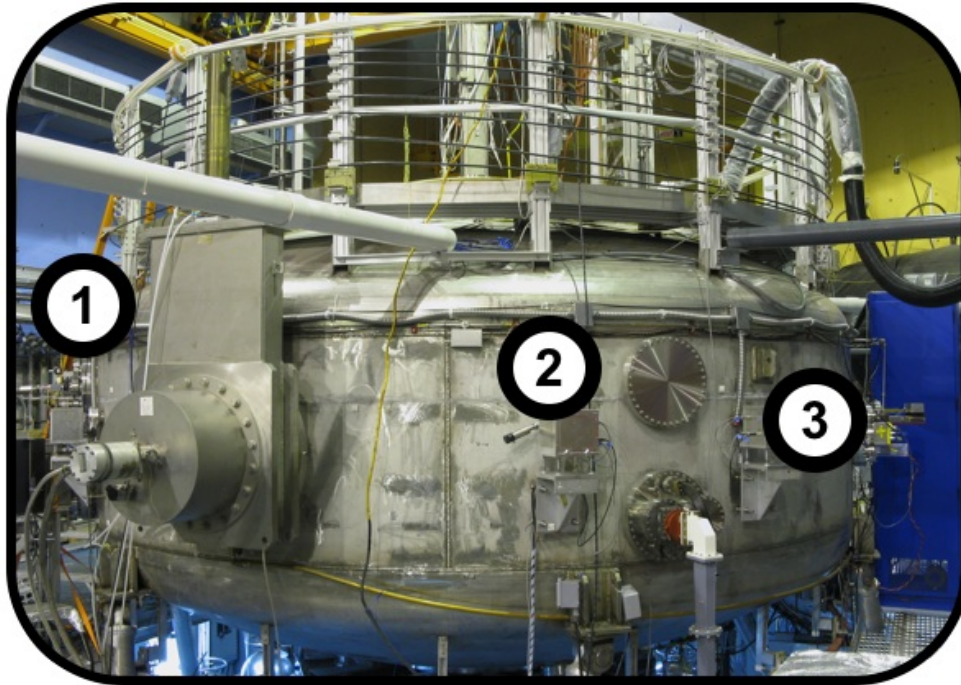
Figure 4-5: Photographs of some of the principal microwave components for the interferometer located outside the vacuum chamber. The upper photograph is a view of LDX looking from the northwest of the laboratory.

4.3.2 IF Hardware
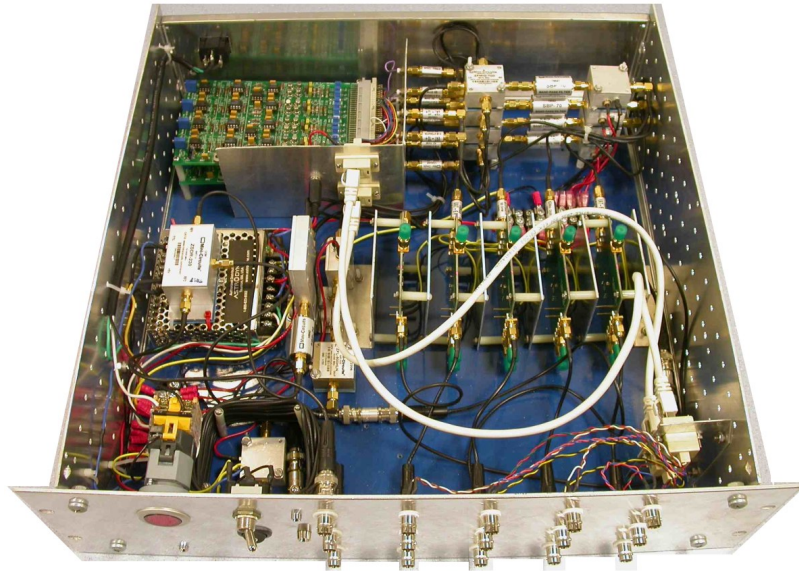
Figure 4-6: Photograph of the IF signal processing box (*alias* "Interferometer Village").
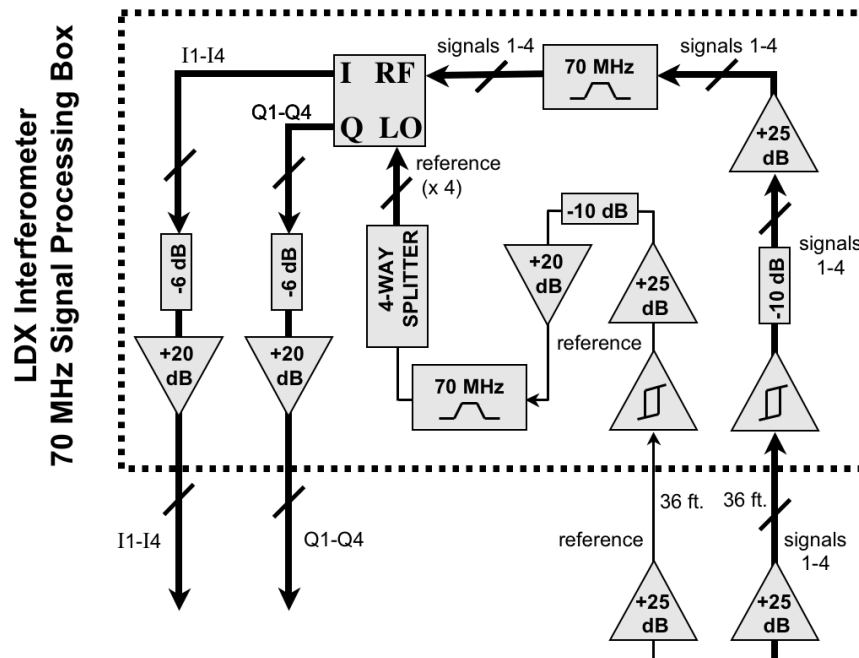
Figure 4-7: Block diagram of the the IF signal processing box. The box has five inputs (four data signals and one reference) and eight outputs (I and Q for each of the four channels). After traveling 36 ft. from their 60 GHz mixers, the waves are sent through a limiter stage which removes any amplitude modulations. The subsequent amplifiers and attenuators ensure that the demodulator inputs have the proper power levels. The 70 MHz bandpass filters are crucial since the limiters output square waves which have frequency components higher than 70 MHz. The attenuators on the outputs of the demodulators facilitate impedance matching with the final amplification stage.
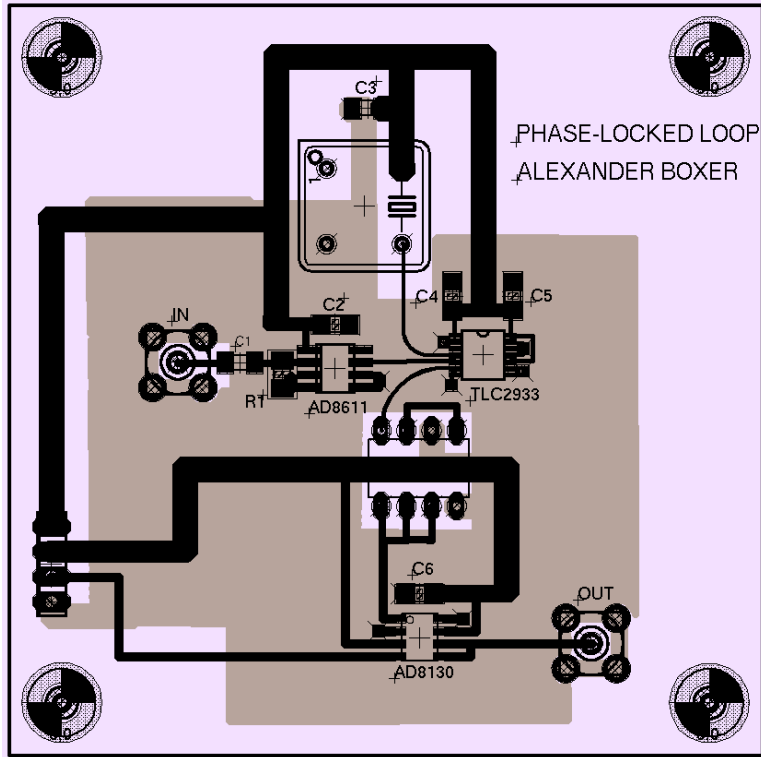
Figure 4-8: Circuit board schematic of the 70 MHz phase-locked loop and frequency bias. The phase-frequency detector compares the phase of the IF reference with a high-precision 70 MHz crystal oscillator. The charge-pump output is passed through a two-pole loop filter and then into one of the inputs of an adder. The second input to the adder serves as a frequency bias in order to set the IF reference to within the PLL's operating range. The frequency bias voltage is adjusted with a dial. The buffered output of the adder is fed into the varactor tuning of the 60 GHz local oscillator. The PLL functions mainly to compensate for slow drifts of the 60 GHz oscillators (§4.2.3). The circuit board was designed using the *EAGLE* Layout Editor.

4.4   Measurements and Calibration

4.4.1   Phase-Unfolding

The purpose of an interferometer is to measure phase shifts. In the LDX interferometer, where the IF signals are demodulated in quadrature, the raw data consists of eight signals: I (proportional to the cosine of the phase shift) and Q (proportional to the sine of the phase shift) for each of the four channels. Once digitized, the eight data signals are processed computationally in order to obtain the phase shifts by themselves.
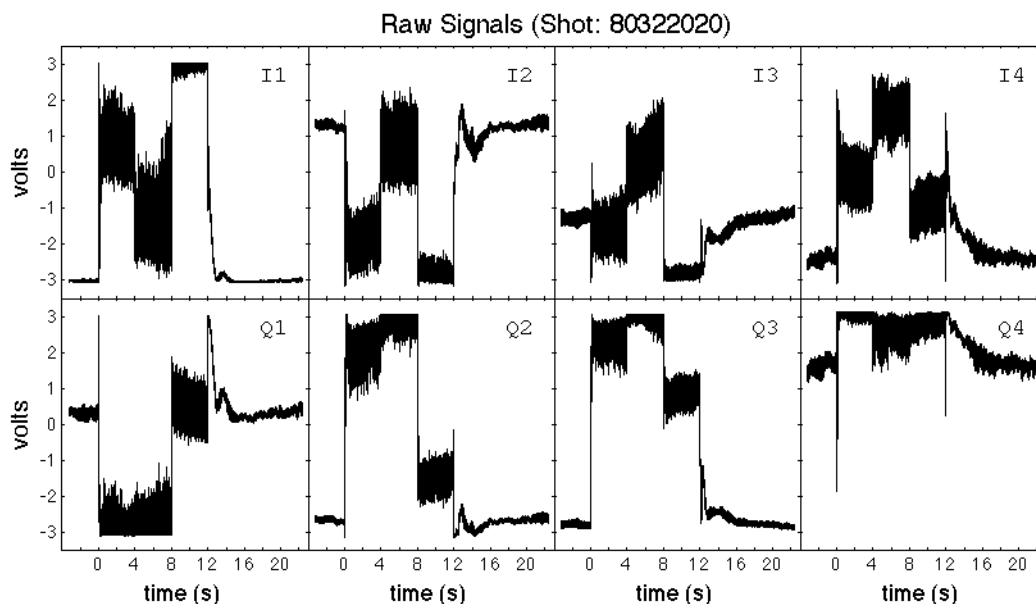
Figure 4-9: Raw data for a typical shot. The shot number indicates to the year ('08), month (March), day (22) and shot number (20) of the plasma discharge.

Individually, both I and Q are ambiguous as to whether the phase is increasing or decreasing (§4.2.6); used in combination however, I and Q can determine the phase unambiguously. This is accomplished by taking the four-quadrant arctangent of I and Q which returns the phase within the interval $[-\pi, \pi]$. The only remaining task is to remove the discontinuities which occur whenever the phase jumps from π to $-\pi$ or vice-versa. This process is called "phase-unfolding".

For a particular plasma discharge or "shot", the raw signals will look like the data shown in Fig. 4-9. The results of the phase-unfolding for this same shot are plotted

Phase-Shift vs. Time

ECRH Heating Sequence
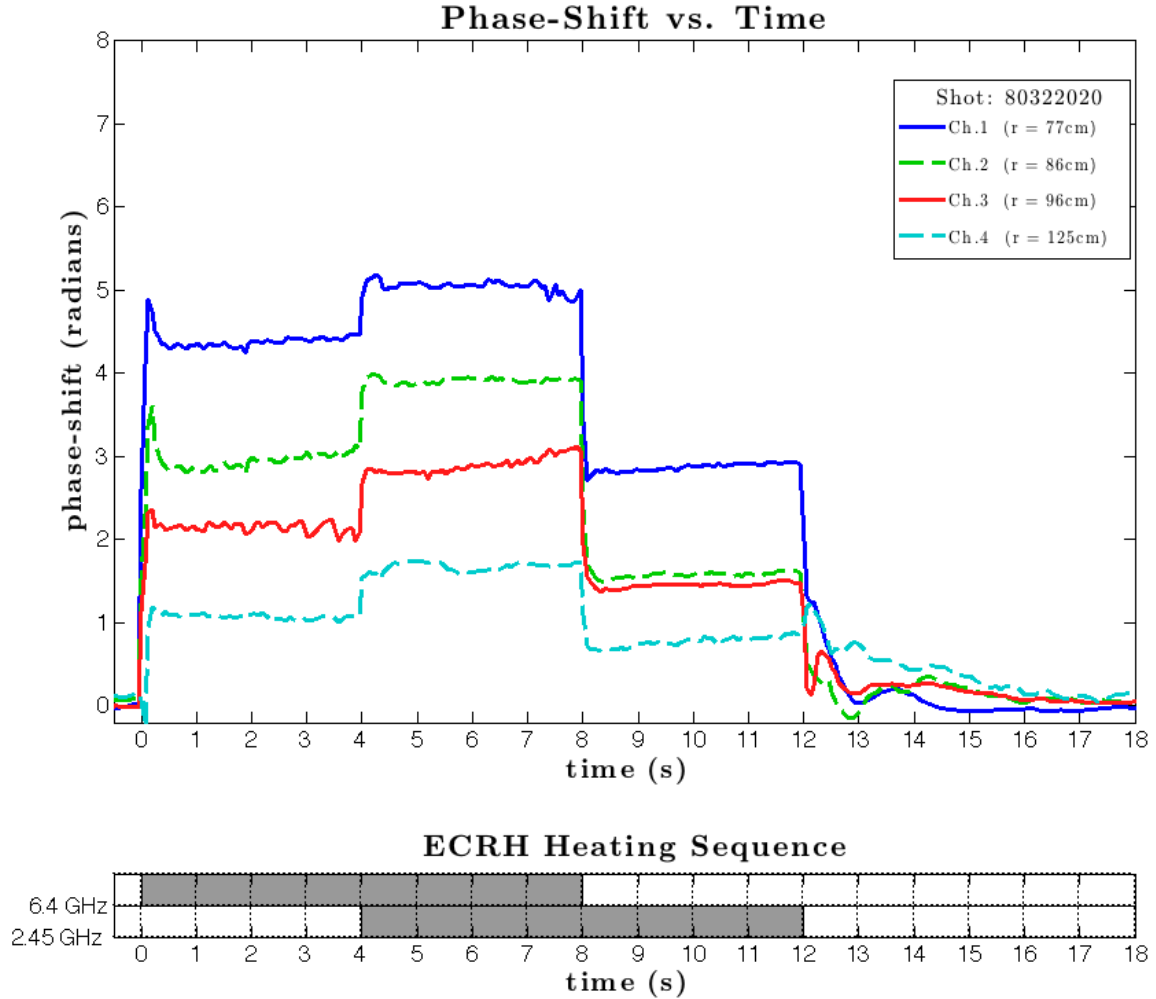
Figure 4-10: Phase shift data for shot 80322020. Four signals are plotted corresponding to the four interferometer channels. Below is a graph showing the ECRH heating sequence for the two microwave sources. Gray shading indicates that the ECRH source is on and no shading indicates that the source is off.

in Fig. 4-10. Because the general shape of the density profiles (and therefore the phase shifts) is determined by the ECRH, the sequence of ECRH heating is plotted in Fig. 4-10 as well. The lower bar represents the 2.45 GHz heating sequence and the upper bar the 6.4 GHz heating sequence. Gray shading in a particular bar indicates that the ECRH source is on; no shading indicates that the ECRH source is off. No actual phase-shifters are present on the LDX interferometer to set the baseline phase for each channel to zero; instead, the measured phase values for each channel at the beginning of every is subtracted as an offset. As can be seen in Fig. 4-10, the maximum phase shift for shot 80322020 was a little less than one fringe (2π).

Raw Signals (Shot: 80516021)
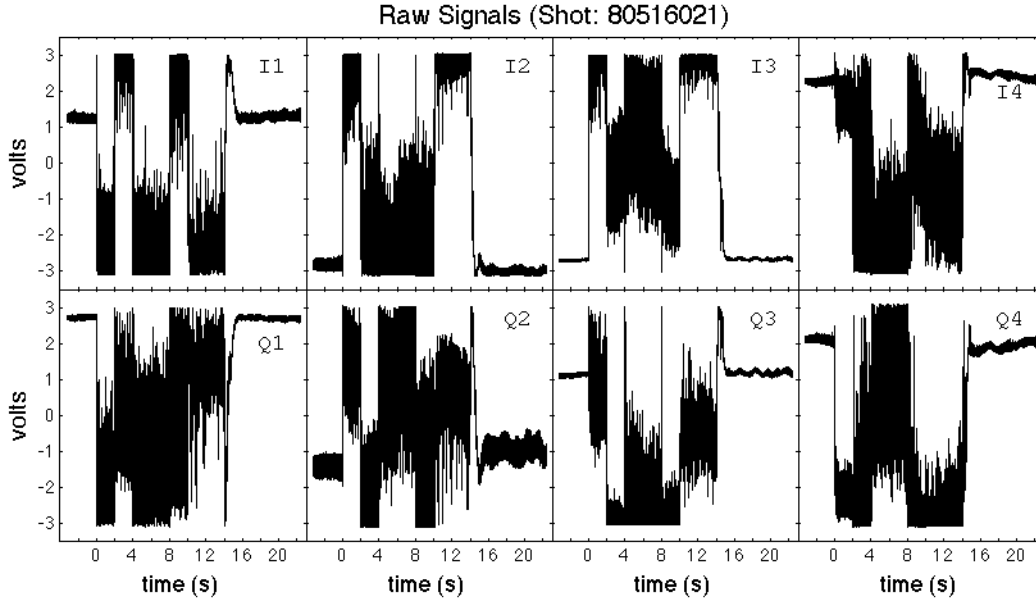
Figure 4-11: Raw data for the shot with the largest phase shift yet measured in LDX. Channel one records a phase shift of nearly 6π.

As a second example, the raw data for shot 8051602—which holds the record for largest phase shift measured to date—is shown in Fig. 4-11. The phase shift data for this shot is plotted in Fig. 4-12. Note the addition of a third microwave source (10.5 GHz) which triples the total heating power (§3.4.6). These figures show that the interferometer can successfully keep track of phase shifts that are as large as nearly three fringes (6π).

4.4.2 Phase Uncertainty

The quality of the LDX interferometer is gauged by two measurements: Signal balance and phase stability. Phase stability characterizes the immunity of the system from random noise originating in the frequency sources and propagating down uneven path lengths. It was to improve the phase stability that heterodyning was incorporated into the interferometer design (§4.2.3). Signal balance is a measure of how closely the outputs of the demodulators, I and Q, approximate ideal sine and cosine waveforms. Both of these quantities are measured in terms of their contribution to the total phase uncertainty of the interferometer
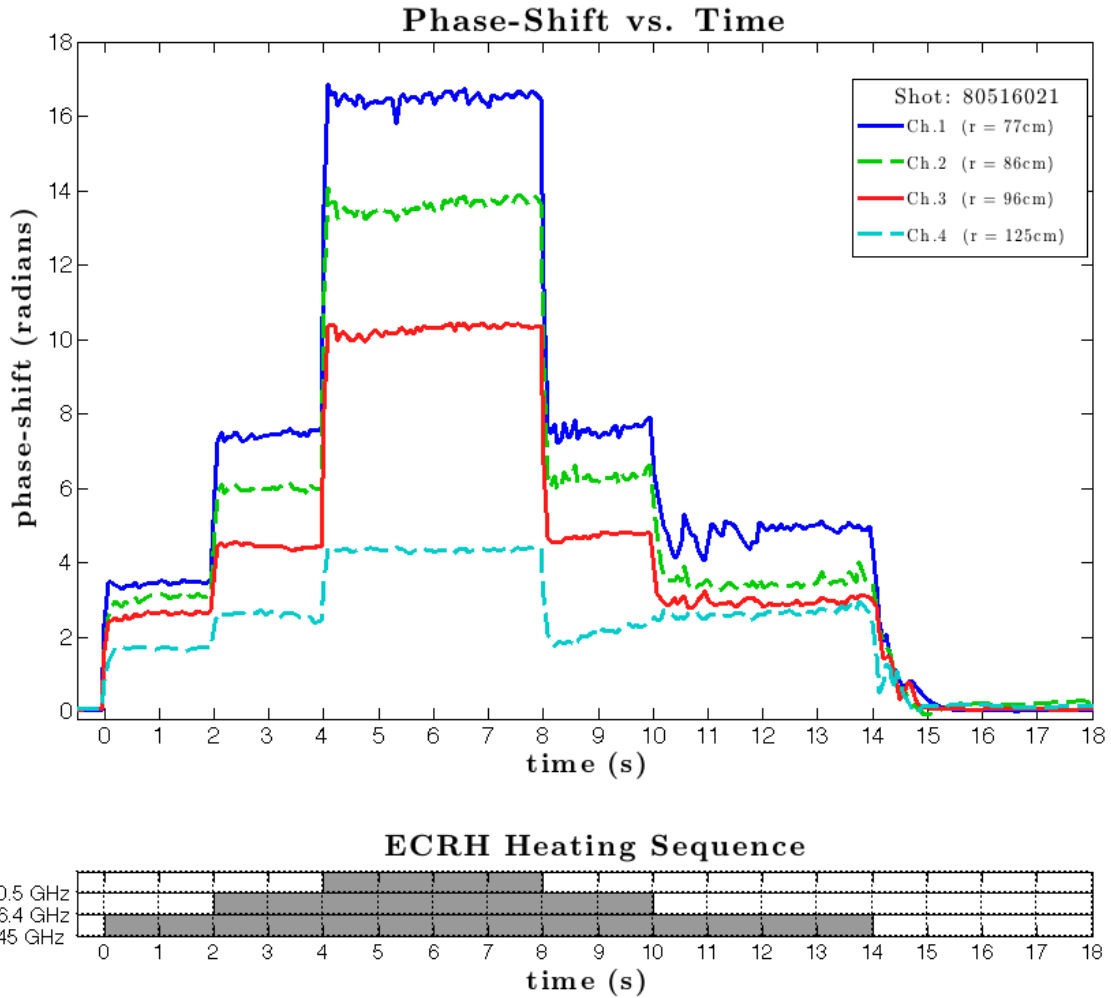
Figure 4-12: Phase shift data for shot 80516021. This shot has the largest phase shift measured in LDX to date, with channel 1 recording a shift of nearly 6π. Note the addition of a third source of ECRH at 10.5 GHz. These data show that the LDX interferometer can successfully keep track of the phase through multiple fringes.
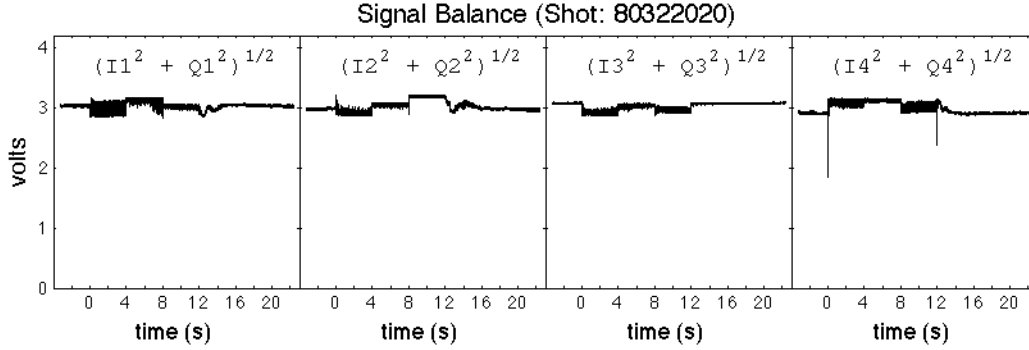
Figure 4-13: Signal balance for shot 80322020. Ideally, $(I^2 + Q^2)^{1/2}$ should remain constant whatever the values of I and Q. The spread of the signal balance can be used to estimate the phase unbalance of each interferometer channel.

Signal Balance

Determining phase shifts requires computing atan(I/Q). Consequently, errors in the computed phase will arise whenever the signals I and Q are not properly balanced whether by (1) amplitude imbalance, (2) amplitude offset, or (3) a phase offset between I and Q that differs from $\pi/2$. Achieving satisfactory signal balance has required no small amount of labor (§4.3.2).

Table 4.2: Phase Errors from Signal Imbalance

Ch. 1	Ch. 2	Ch. 3	Ch. 4
3.5°	3.6°	2.2°	3.5°

There is a straightforward way to quantify the total contribution to the phase error from all three sources signal imbalance. It can be shown analytically and verified by simulation that the errors in the measured quantity $(I^2+Q^2)^{1/2}$—normalized around unity—have nearly identical amplitudes as the errors in the phase computed by atan(I/Q). For this reason we refer to $(I^2+Q^2)^{1/2}$ as the "signal balance".

If the demodulator outputs were ideal, the signal balance would remain constant whatever values I and Q assume. In practice, the channels of the LDX interferometer have signal balances which display some amount of spread (Fig. 4-13) and this spread is taken to equal the phase error resulting from the computation of atan(I/Q). Surveying all the data from the March '08 and May '08 experiments (251 shots), the

Signal Balance (Shot: 80516021)
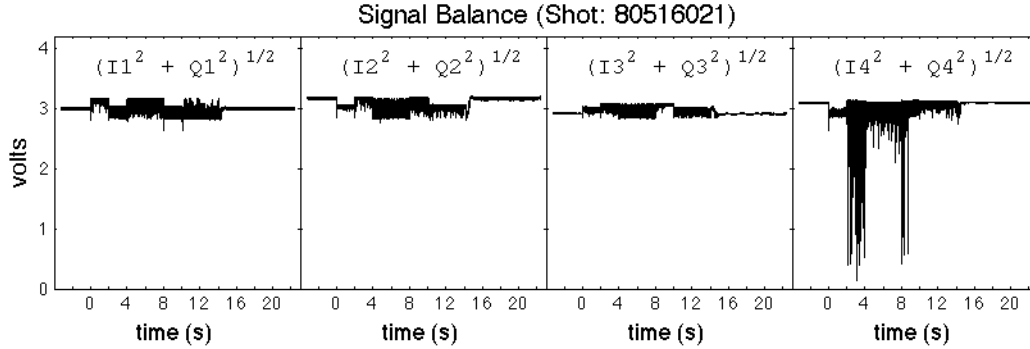
Figure 4-14: Signal balance for shot 80516021. This shot is provides an example of the signal balance failing on channel 4 which lies somewhat outside the main portion of the 60 GHz transmitted beam. Nonetheless, there are enough good points interspersed amongst the bad that the phase can be unfolded as is shown in Fig. 4-12.

phase errors due to signal imbalance have been calculated (as the standard deviation from the mean) and are presented in Table 4.2.

Computing phase errors from the signal balance is unproblematic for interferometer channels 1, 2 and 3. Channel 4 is a special case since it exhibits terrible signal balance for a large percentage of shots ($\sim 14\%$). Instrument-wise, channel 4 is as well-calibrated as the others; rather, the problem arises from the fact that the receiving antenna for channel 4 lies slightly outside the main portion of the 60 GHz transmitted beam (§4.2.5). An example of poor signal stability is shown in Fig. 4-14. What the figure shows is that the amplitudes of I and Q on channel 4 are simultaneously being drawn towards zero. This is not an indication of either a phase or amplitude imbalance but instead that *no signal is being received.*

Thus, in a number of shots either the beam is being entirely refracted away from channel 4's receiving antenna or—another possibility—the normally incident plane wave approximation begins to break down. Because channel 4's chord is outside of the 3 dB portion of the transmitted beam, the gradient of phase over azimuth is much steeper than it is near the beam's center. It is thus conceivable for channel 4's receiving antenna to suffer from "phase-slip", that is, multiple phases being received in the antenna simultaneously and causing destructive interference. Even so, the most likely explanation for the occasionally erratic behavior of channel 4 is that the ray can experience a significant amount of refraction at a steep plasma-vacuum interface.

Because channel 4's chord is the furthest from the center of the vacuum chamber, it will impact the plasma-vacuum interface with the largest angle of incidence and therefore be subject to the largest amount of refraction. A further discussion of this effect along with an estimation of the uncertainties to which it gives rise is presented in §5.4. The shots for which channel 4 exhibits a breakdown in phase balance (as in Fig. 4-14) were not included in the phase error calculations of Table 4.2.

Because of the occasional lack of signal balance, channel 4 would seemingly not be able to return any phase information for the affected shots. In fact, the signal balance only fails in extremely rapid bursts leaving many instances where the signal balance is perfectly fine even within intervals that look hopeless. Thus, with suitable discrimination of points, the phase can be unfolded from channel 4 even when the signal balance appears to fail. This is exemplified by the phase data in Fig. 4-12 which was unfolded from signals whose signal balance is shown in Fig. 4-14.

Phase Stability

The second important quantity of merit for the LDX interferometer is phase stability. Phase stability is a measure of the instrument's immunity to random fluctuations in the frequency sources which can cause phase errors if the signal and reference path lengths are not precisely even. The issue of achieving satisfactory phase stability informed much of the design of the LDX interferometer (§4.2.3) and is the main reason that a heterodyne system was built.

Table 4.3: Phase Instability

Ch. 1	Ch. 2	Ch. 3	Ch. 4
1.1°	1.2°	1.5°	2.3°

Measuring the errors due to phase instability is very simple: The standard deviation is calculated for each channel of phase data during "test-shots" in which no plasma is present. The phase errors found from a survey of 60 such test-shots from February '08 to May '08 are presented in Table 4.3.

Reflections

Reflections, especially from the F-Coil, were discussed as another possible source of phase errors in §4.2.5. This concern can be eliminated by direct measurements which show that the effects are minor. As an extreme test, phase measurements were recorded while the F-Coil was raised and lowered the entire distance from the C-Coil to its maximum vertical position within the vacuum chamber. Quite clearly, if reflections from the F-Coil contribute to the measured phase then this will be evident during these tests. In fact, the measured phase value remains unchanged during these tests (of which there were 17) although the noise in the signal doubles from the baseline phase instabilities reported in Table 4.3.

Therefore during actual plasma discharges, where the F-Coil moves at most a few millimeters (and certainly not a few meters as in these tests), we can safely conclude that the effects of reflections from the F-Coil are negligible. A similar set of tests was also conducted with the moveable probes, but these were seen to not affect the phase or the phase noise in any discernible way.

4.4.3 Calibration

The phase uncertainties quantified in §4.4.2 are small and show that the LDX interferometer can measure phases with precision of approximately $5°$. Since the measured phase shifts are usually in excess of $\pi/2$ for all four channels, the errors in the computed phases are only a few percent.

It remains to be shown, however, that the LDX interferometer actually functions as an interferometer. This is accomplished by going inside the vessel and placing materials with known dielectric constants and known thicknesses in the path of the 60 GHz transmitted beam. The results of one such calibration, conducted on 24 August, 2007, are presented in Fig. 4-15.

The dielectric used was teflon which has a dielectric constant of 2.1 at microwave frequencies [84]. 6"×6" slabs of teflon were held in front of the transmit horn and data was taken for 16 seconds. I and Q , averaged over the duration of each test-shot, were

recorded for each channel. Measurements were taken for 32 different thicknesses of teflon ranging from 0 to 31/32". The data for the last thickness (1") produced outliers for all four channels and was discarded on the assumption that the measurement was somehow faulty.

Encouragingly, all eight signals (I and Q for each of four channels) are well fit to *sin* and *cos* functions with the identical wavenumber, κ_{fit}:

$$
\begin{aligned}
\kappa_{\text{fit}} &= 13.51 \text{ radians per inch of teflon} \\
&= 5.32 \text{ cm}^{-1}.
\end{aligned}
\tag{4.16}
$$

This quantity, κ_{fit}, can be used along with the known dielectric constant of teflon to determine the frequency of the probing wave in the following manner. A wave with wavelength λ traversing a material with dielectric constant ϵ and thickness d will exhibit a phase shift $\Delta\phi$ given by

$$
\Delta\phi = \frac{2\pi}{\lambda}(\sqrt{\epsilon} - 1)d.
\tag{4.17}
$$

Here we have used the fact that for non-magnetic materials, the index of refraction, N, is related to the dielectric constant by $N = \sqrt{\epsilon}$. A sinusoidal signal such as I or Q with phase given by $\Delta\phi$ from Eq.(4.17) will have a wavenumber, κ, given by

$$
\kappa = \frac{2\pi}{\lambda}(\sqrt{\epsilon} - 1).
\tag{4.18}
$$

With this result we can determine the frequency of the probing beam which best fits the calibration data

$$
\begin{aligned}
f(\kappa) &= \frac{c}{\lambda} = \frac{c\kappa}{2\pi(\sqrt{\epsilon} - 1)} \\
f(\kappa_{\text{fit}}) &\approx 57 \text{ GHz}.
\end{aligned}
\tag{4.19}
$$

The frequency calculated in Eq.(4.19) is in accord with the expected value of 60 GHz to within 5%. We assert that this value is sufficiently accurate especially given that the teflon slabs were held in place by hand and the fit was made by eye.

Interferometer Calibration
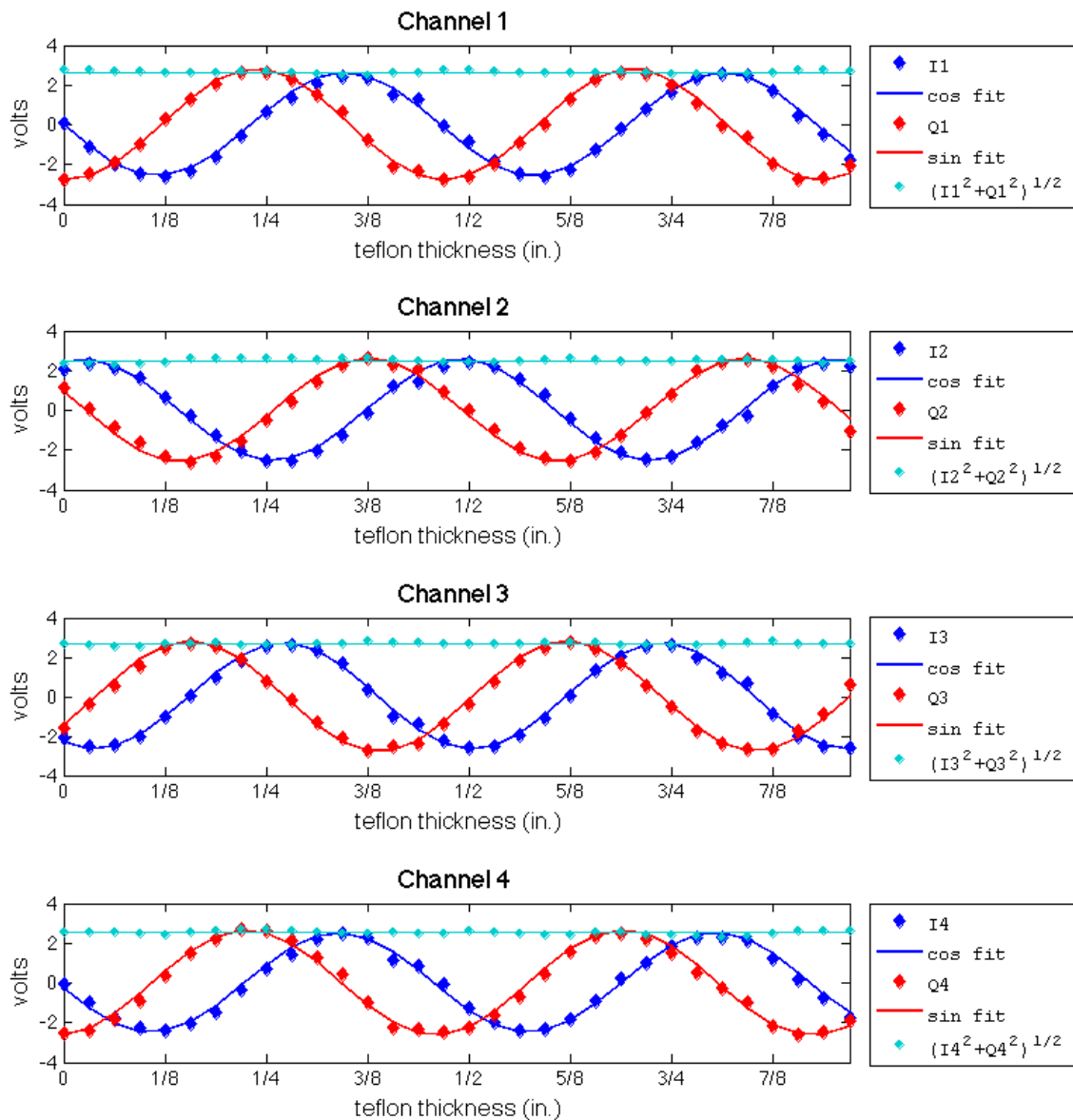
Figure 4-15: Interferometer calibration data, taken 24 August, 2007. Average I and Q values were recorded for test-shots in which slabs of teflon were held in front of the 60 GHz transmitted beam. The measured values closely approximate the expected sine and cosine functions for a 60 GHz wave traversing a dielectric (teflon) of increasing thickness. These results demonstrate that the interferometer correctly measures phase shifts due to the presence of refractive material in the path of the transmitted beam.

Alternatively, the fact that the teflon was held very close to the transmitting horn might have altered the loading of the oscillators thus lowering the output frequency. Nevertheless, the purpose of the calibration test is to demonstrate that the interferometer actually measures phase shifts due to refractive material in the path of the transmitted beam and not due to some complicated and unintelligible interference pattern. In this regard, the conclusion from the data in Fig. 4-15 is unequivocal: The interferometer works.

Chapter 5

From Phase Shifts to Density Profiles

5.1 Line-Integrated Densities

The phase shifts measured by the interferometer are related to the plasma density by the dispersion relation for O-mode propagation through a cold plasma [Eq.(4.2)]:

$$N(\omega) = (1 - n/n_c(\omega))^{1/2} \, .$$

Here N is the index of refraction, n is the plasma density, ω is the frequency of the probing beam and $n_c(\omega)$ is the cutoff density for a wave of frequency ω. The appropriateness of this dispersion relation depends on the appropriateness of the assumptions that the plasma is cold and that the wave propagates in O-mode.

The cold plasma approximation is well-justified because the 60 GHz interferometer beam is propagated electromagnetically across the vacuum chamber with a phase velocity, v_ϕ, that is essentially the speed of light. This is significantly faster than the thermal velocities, v_{th}, of the electrons except, possibly, for a very small number of relativistic electrons resonant with the ECRH. Using a simple fluid approximation

[85], the O-mode dispersion relation in the presence of a warm plasma expands to

$$N(\omega) \approx (1 - n/n_c(\omega))^{1/2} \left[1 - (n/n_c(\omega))^2 \left(\frac{v_{th}}{v_\phi} \right) \right]^{1/2} \quad (5.1)$$

Because $v_{th}/v_\phi \ll 1$, Eq.(5.1) shows that the corrections to the cold plasma dispersion relation can be neglected.

The assumption that the plasma propagates in O-mode is also well-justified. The transmitting and receiving antennas are all positioned in the equatorial plane of the vacuum chamber in order to ensure that $\mathbf{E}_{wave} \parallel \mathbf{B}_{external}$ [Eq.(4.1)]. Given a small misalignment, θ, between $\mathbf{E}_{wave}$ and $\mathbf{B}_{external}$, the errors in index of refraction, N, can be estimated [86] using the Appleton-Hartree formula:

$$N(\omega) \approx (1 - n/n_c(\omega))^{1/2} \left[1 - (n/n_c(\omega))^2 \left(\frac{\omega_c}{\omega} \right) \sin \theta \right]^{1/2}. \quad (5.2)$$

Here ω_c is the electron cyclotron frequency. In LDX, $\omega_c = 6.4$ GHz near the outer ring of the F-Coil and then drops rapidly with the field ($\sim 1/r^3$) towards the edge of the vacuum chamber. In the path of the interferometer beam, therefore, $\omega_c/\omega \ll 1$. Because the corrections due to finite temperature and mode-misalignment are small, we can safely take Eq.(4.2) to be the correct dispersion relation in all subsequent considerations.

As the interferometer beam propagates through the plasma it acquires a phase equal to the line-integral of the beam's wavenumber, k, over the path ℓ

$$\phi = \int k d\ell. \quad (5.3)$$

Using $k = N\omega/c$, the phase becomes

$$\phi = \frac{\omega}{c} \int N \, d\ell = \frac{\omega}{c} \int (1 - n/n_c)^{1/2} \, d\ell. \quad (5.4)$$

The phase shift, $\Delta\phi$, between the wave considered in Eq.(5.4) and a wave propagating

along the same path in the absence of a plasma (i.e., a path for which $N = 1$) will be

$$\Delta\phi = \frac{\omega}{c} \int (N - 1)d\ell. \tag{5.5}$$

Because the LDX interferometer was designed so that $n/n_c \ll 1$ (§4.2.2), the index of refraction, N, can be expanded binomially and Eq.(5.5) rewritten as

$$\Delta\phi = \frac{-\omega}{2cn_c} \int n \, d\ell. \tag{5.6}$$

Note that the phase shift is actually negative; this is due to the fact that a plasma (unlike most materials) has an index of refraction that is less than one. When there is no issue of ambiguity, this negative sign is often dropped as a matter of convenience as it was, for example, in Fig. 4-10 and Fig. 4-12.

Using the value $n_c = 4.46 \times 10^{13}$ cm^{-3} for a 60 GHz wave, we can express the line-integral of the density (which we desire to know) in terms of the phase shift (which is measured)

$$\int n \, d\ell = \frac{-n_c c}{\pi f} \Delta\phi$$
$$\approx -7.11 \times 10^{12} \, \Delta\phi \text{ cm}^{-2}. \tag{5.7}$$

Eq.(5.7) is the fundamental relation that will be used to obtain density information from the interferometer data.

5.2   Abel Inversion

5.2.1   Statement of the Problem

Line-integrated densities by themselves provide an enormous amount of information: They indicate whether the density is rising or falling, whether the profile is becoming more or less peaked, and the presence or absence of any fluctuations. However, in many instances it is desirable to estimate the density profile $n(r)$. In order to extract

$n(r)$ from a collection of line-integrated values, $\int n \, d\ell$, it is necessary to employ some form of mathematical inversion. In the approximation that $n = n(r)$ is a function of radial position only and that the lines over which $\int n \, d\ell$ is evaluated are straight lines, the appropriate inversion to use is Abel inversion.

These two assumptions—axisymmetry and straight-line trajectories—are, we assert, generally valid although neither can be taken for granted and, indeed, neither obtains in all instances. A discussion of the validity of the density profiles computed by Abel inversion and their uncertainties is presented in §5.3 and §5.4.
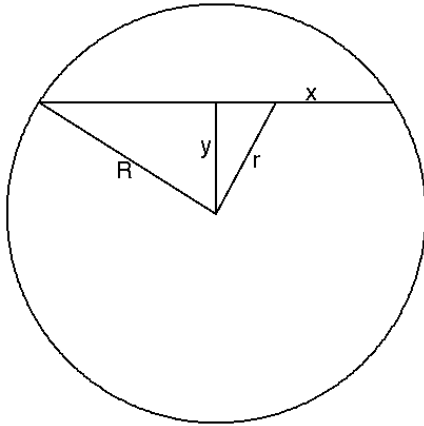
Figure 5-1: Abel inversion geometry. Let $f(r)$ be some axisymmetric function defined over a disc with radius R and let $F(y)$ be the line-integral of $f(r)$ across the disc along the straight-line chord x at height y. Given $F(y)$, the disc function $f(r)$ can be determined by Abel inversion [Eq.(5.9)].

The geometry of Abel inversion is depicted in Fig. 5-1. For a radially symmetric function $f(r)$, the line-integral, F, in the x-direction across a disc of radius R will be a function of the impact parameter, y

$$F(y) = \int_{-\sqrt{R^2-y^2}}^{+\sqrt{R^2-y^2}} f(r) dx. \tag{5.8}$$

Provided that the two assumptions of axisymmetry and straight-line paths are valid, the Abel inversion of $F(y)$ is [87]

$$f(r) = \frac{-1}{\pi} \int_r^R \frac{dF}{dy} \frac{dy}{(y^2 - r^2)^{1/2}}. \tag{5.9}$$

Although the Abel inversion geometry (Fig. 5-1) is most easily imagined in terms of chords that are all parallel—each chord being perpendicular to the same y-axis— a geometry where all the chords fan-out from the same starting-point is entirely

equivalent. This equivalence follows from the axisymmetry of the problem. In either geometry, the relevant parameter is the impact parameter (or, equivalently, the radius of tangency), which is the length of a perpendicular segment from the chord to the center of the disc.

In the LDX interferometer, line-integrated measurements are taken along four chords with radii of tangencies $r = 77$ cm, $r = 86$ cm, $r = 96$ cm and $r = 125$ cm (§4.2.5). We cannot expect to know the radial density profile $n(r)$ with a greater resolution than the spacing between our data points and, consequently, the spatial resolution of the density profiles computed in LDX will not be less than 10 cm or so. Nevertheless, since we are primarily interested in the gross attributes of the density profile—the approximate density magnitude and profile gradient—four data points will be adequate. A fifth data point, however, can be added by using edge density values estimated from one of the probe measurements (§3.5) which we discuss below.

5.2.2   An Additional Data Point from Probe Measurements

The most reliable probe measurements come from the probe named "southwest-top", so-called because of the vacuum port through which it enters. The probe potential is swept from -100 to 50 volts and back at a rate of 150 Hz. For each cycle the electron temperature is estimated by measuring the exponential rise of the probe current with respect to the probe voltage. Then, using this value for the electron temperature, the plasma density at the probe, n_{probe}, is estimated from the ion-saturation current according to [88]

$$n_{\mathrm{probe}} = \frac{e^{1/2}}{A} \left(\frac{m_i}{T_e} \right)^{1/2} \mathrm{I}_{\mathrm{sat}}. \qquad (5.10)$$

Here T_e is the electron temperature, A is the surface area of the probe tip, $\mathrm{I}_{\mathrm{sat}}$ is the measured ion-saturation current and m_i is the mass of the ion species (usually deuterium, but occasionally some percentage of helium is present as well). The electron temperatures measured by the probe are fairly consistently within the range of 20 - 25 eV. However, the uncertainties of these temperatures—which are computed by finding the inverse slope of a logarithmic fit—are likely to be high ($\sim 50\%$).
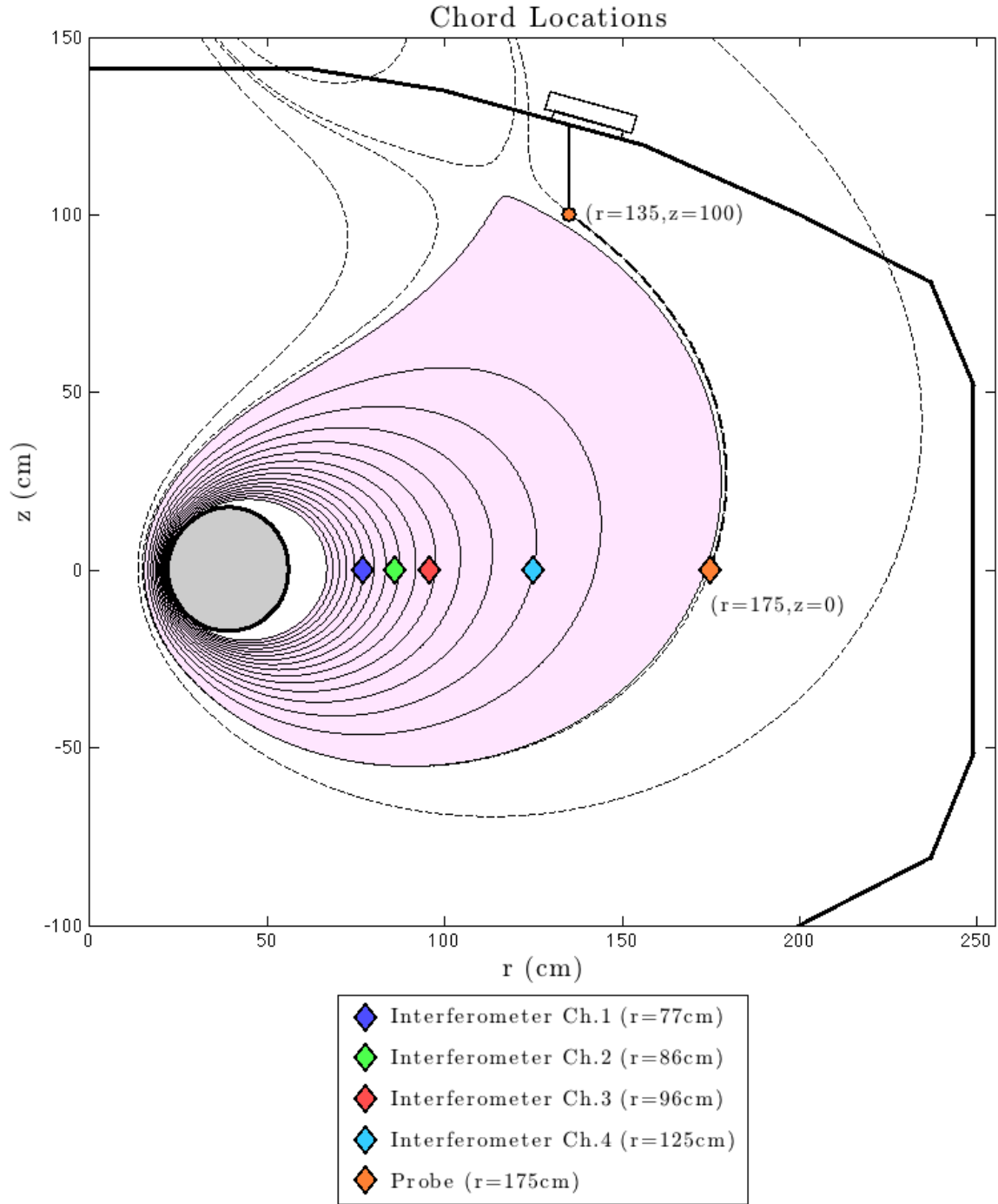
Figure 5-2: Diagram of the radial locations of the interferometer chords along with the equivalent radial position of the southwest-top probe. The LDX vacuum chamber is shown from the front in cross-section. The closed magnetic field lines are drawn with solid black lines and he open field lines are drawn with dashed black lines. The plasma volume is shaded in pink. The interferometer chord locations are indicated by the left-most four diamonds. The southwest-top probe descends vertically into the vacuum chamber from a flange situated on top of the chamber. The probe intersects a field line which is followed (heavy, dashed, black line) to the mid-plane. The equivalent radial position of the probe is indicated by the right-most diamond.

In order to associate the southwest-top probe measurement with a radial position, we must use our model of the magnetic field (§3.4.5) to map the probe position to an L-shell value. The vertical z-position of the southwest-top probe has the capability of being extended or retracted but most often the probe is positioned so that the tip intersects the L = 175 cm field line. Practically, this is the last closed field line (L = 173.5 cm). The locations of the four interferometer chords plus the southwest-top probe position are diagrammed in Fig. 5-2. Recent reconstructions of LDX pressure profiles computed by M. Mauel[1] show that in levitated operation (but not supported operation) LDX plasmas have isotropic pressures. This finding supports the assumption—which we employ here—that the density is constant along field lines.

In addition, the probe measurement, n_{probe}, must be converted into a line-integrated value, F(r = 175 cm), so that it can be used in conjunction with the line-integrated values from the interferometer. This is accomplished by assuming that the plasma density increases linearly from zero at the vacuum chamber wall ($r = 250$ cm) to the measured value n_{probe} (located at $r = 175$ cm) and then integrating over this profile to obtain F(r = 175 cm). Subsequently, after an Abel-inverted radial density profile $n(r)$ has been computed (as described below in §5.2.3) the calculated value of $n(\mathrm{r} = 175$ cm) is compared with the measured value of n_{probe}. Since the value ascribed to F(r = 175 cm) is, in fact, arbitrary, this quantity can be altered so that the Abel-inverted $n(\mathrm{r} = 175$ cm) matches the measured value n_{probe} to any desired precision. It must be emphasized that the assumption of a linear density rise from the chamber wall to $r = 175$ cm is entirely a matter of convenience insofar as it results in values for $n(\mathrm{r} = 175$ cm) which closely approximate n_{probe}. This approximation, however, does not affect the subsequent analysis.

After having undergone these preparatory stages of analysis, the phase shift data from the interferometer can be displayed more informatively as a set of line-integrated density signals. Line integrated densities from a typical shot (one already introduced in Chapter 4) along with the estimated line-integrated density from the southwest-top

---

[1]Reported at the ICC Workshop, Reno, NV, June, 2008
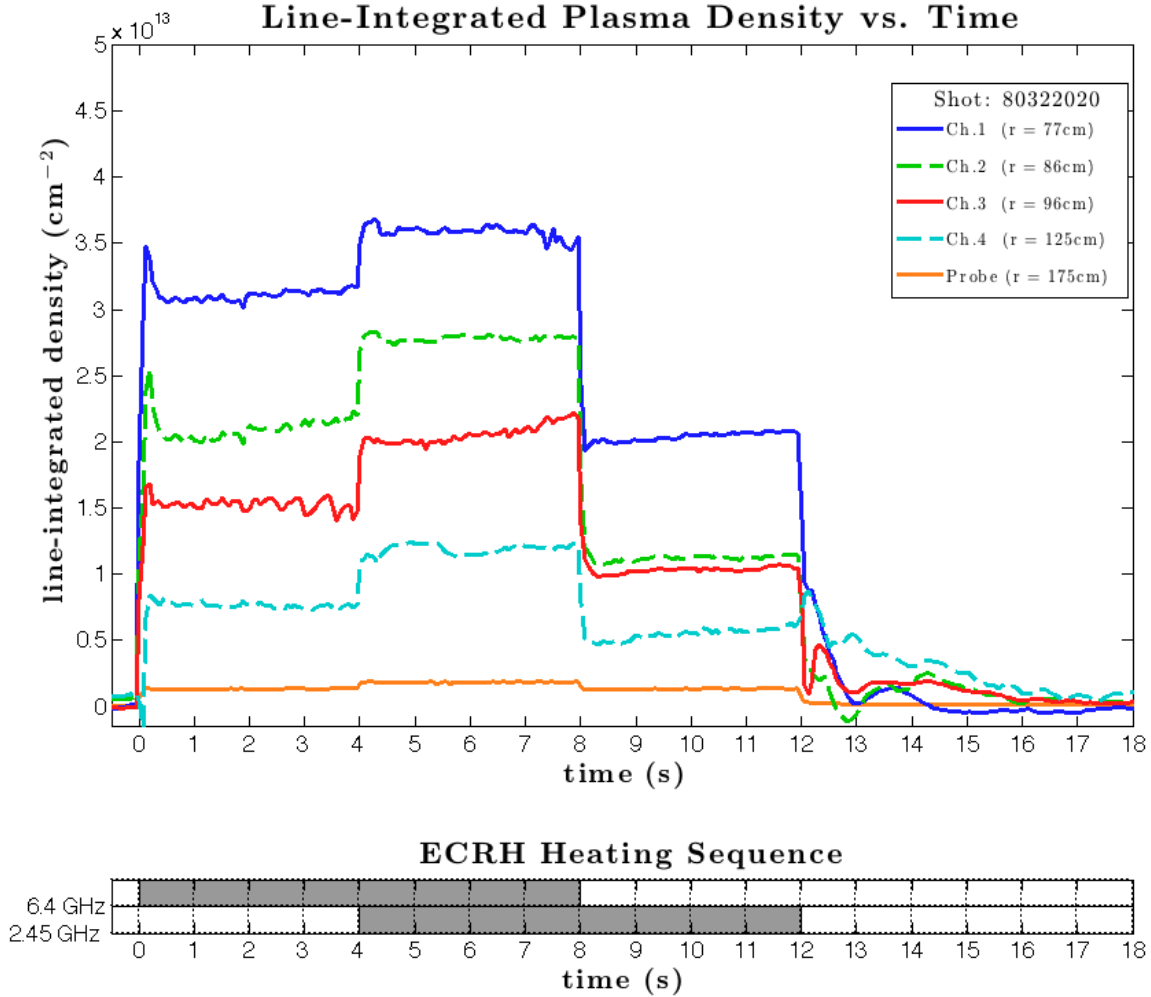
Figure 5-3: The interferometer data is most informatively expressed as line-integrated density signals. These are related to the measured phase shifts simply by a scaling. In addition, a fifth signal is plotted which containins density information from the outer boundary of the plasma as measured by the southwest-top probe. In order that all five signals be comparable, the probe density measurements must first be converted into a line-integrated density signal.

probe are plotted in Fig. 5-3.

5.2.3   Interpolation and Inversion

Abel inversion [Eq.(5.2)] takes as an argument not the line-integral function F(y), but its derivative dF/dy, where y is the impact parameter of the chord (Fig. 5-1). Consequently, Abel inversion is sensitive to the method of interpolation used to construct F(y) from a discrete set of measurements.

A simple linear interpolation of F will not suffice since we cannot have disconti-
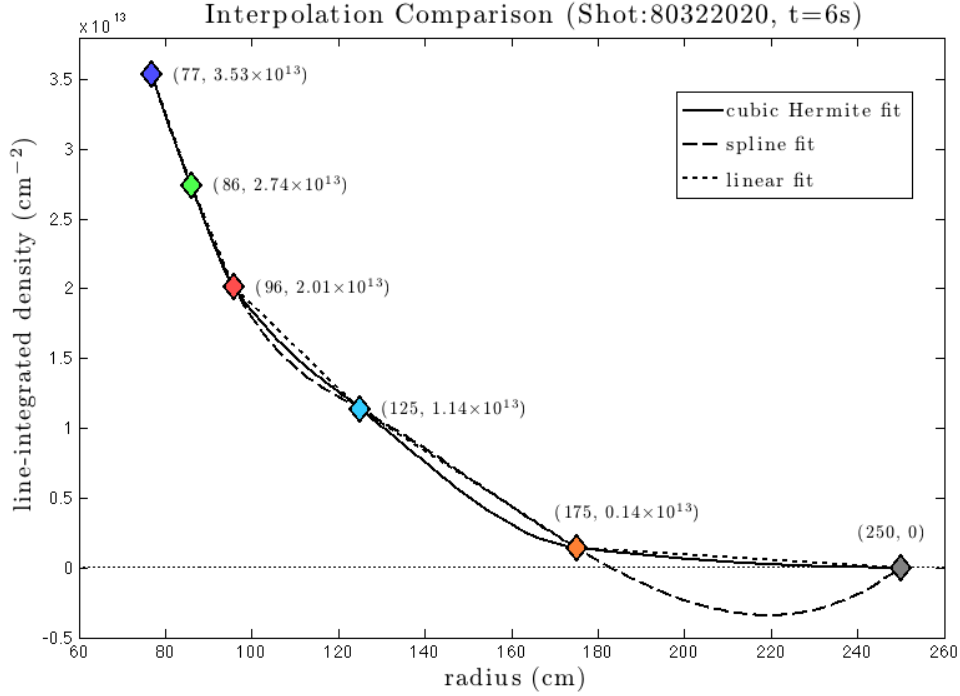
Figure 5-4: A comparison of a cubic Hermite polynomial interpolation, spline interpolation and linear interpolation of the line-integrated density data. Because spline interpolations tend to return functions F(y) with negative values, they are entirely unsuitable for use in Abel inversion. Cubic Hermite polynomial interpolations maintain the sign of the first derivative between data points and, on the whole, produce curves that fit the data very nicely.

nuities in the first derivative dF/dy. A "pseudo-linear" interpolation—in which the sharp corners at the knot-locations are rounded—works well, although it returns inversions that are rather "bumpy". For our analysis, we employ a piecewise, cubic Hermite polynomial interpolation[2]. The advantage of cubic Hermite polynomial interpolation is that the first derivative remains continuous and moreover—unlike a spline interpolation—the first derivative remains monotonic in between data points thus preventing any overshoot. The tendency of a spline fit of F(y) to take on negative values makes it entirely unsuitable for Abel inversion since negative values for the line-integrated density function F(y) are unphysical. Cubic Hermite polynomials, on the other hand, produce curves that seem to follow how the eye naturally connects the data points and—most importantly—do not fall below zero. A comparison of a cubic Hermite polynomial fit, a spline fit and a linear fit to the line-integrated density data for shot 80322020 at 6 seconds is shown in Fig. 5-4. Naturally, the freedom

---

[2]Piecewise cubic Hermite polynomial interpolation (pchip) is a built-in function on MATLAB.
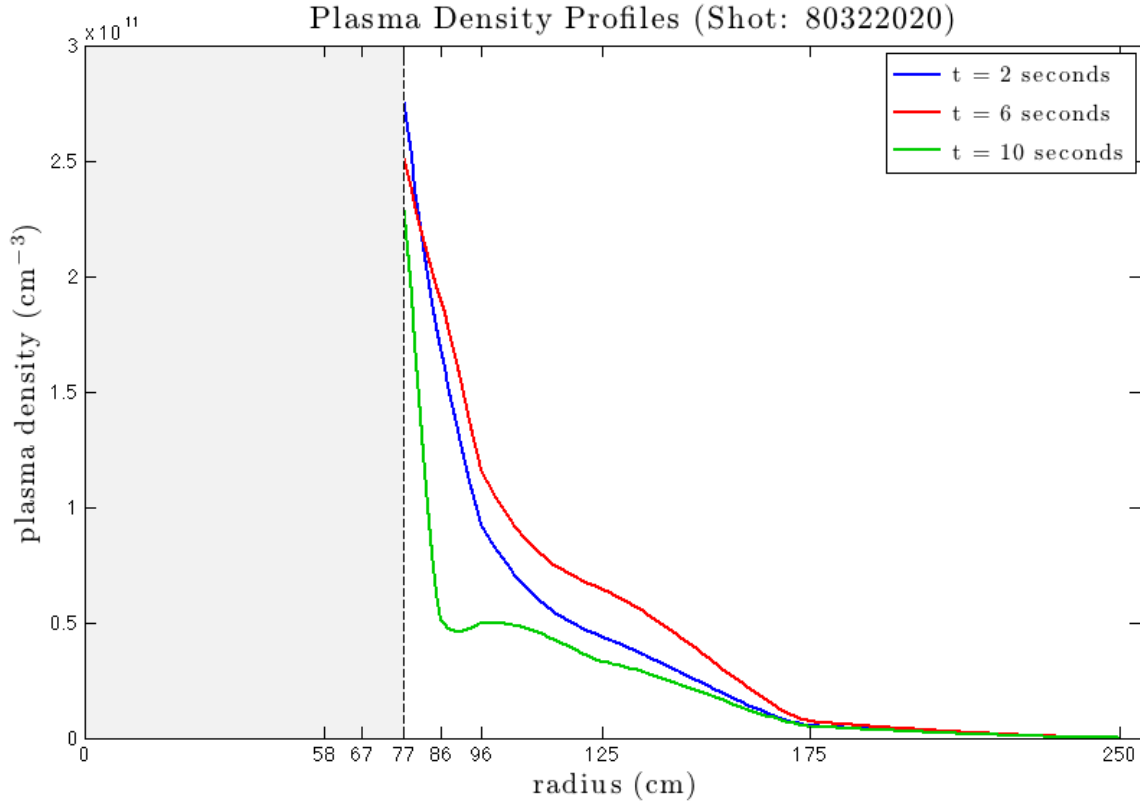
Figure 5-5: Abel-inverted, radial density profiles calculated at three representative times for a typical shot (shot 80322020). On the abscissa are marked the locations of the outer surface of the F-Coil (r = 58 cm), the first closed field line (r = 67 cm), the 4 interferometer chords (r = 77 cm, 86 cm, 96 cm, 125 cm), and the L-shell value of the southwest-top probe (r = 175 cm). No information is available for radial positions inside the innermost measurement (r = 77 cm) and this area is shaded gray. The measured phase-shifts from this shot at 6 seconds are plotted in Fig. 4-10 and the line-integrated densities at 6 seconds are plotted in Fig. 5-3.

to employ different interpolation schemes leads to uncertainties in the Abel-inverted profiles and these are estimated in the following section (§5.3).

Once F(y) has been interpolated from the data at a given instant, an Abel-inverted, radial density profile, $n(r)$, can be computed directly from Eq.(5.2). Radial density profiles at various times for two different shots are plotted in Fig. 5-5 and Fig. 5-6. The two shots, 80322020 and 80516021, were introduced in Chapter 4. We consider these shots to be representative in the sense that shot is 80322020 is a fairly "typical" shot whereas 80516021 is the shot with the highest recorded densities. In shot 80516021, a portion of the gas used to make the plasma was helium (more on this in Chapter 6) and so the ion mass m_i in Eq.(5.10) is calculated assuming a 50-50 mixture of He and D_2. The phase shifts of these shots at one sample time are plot-
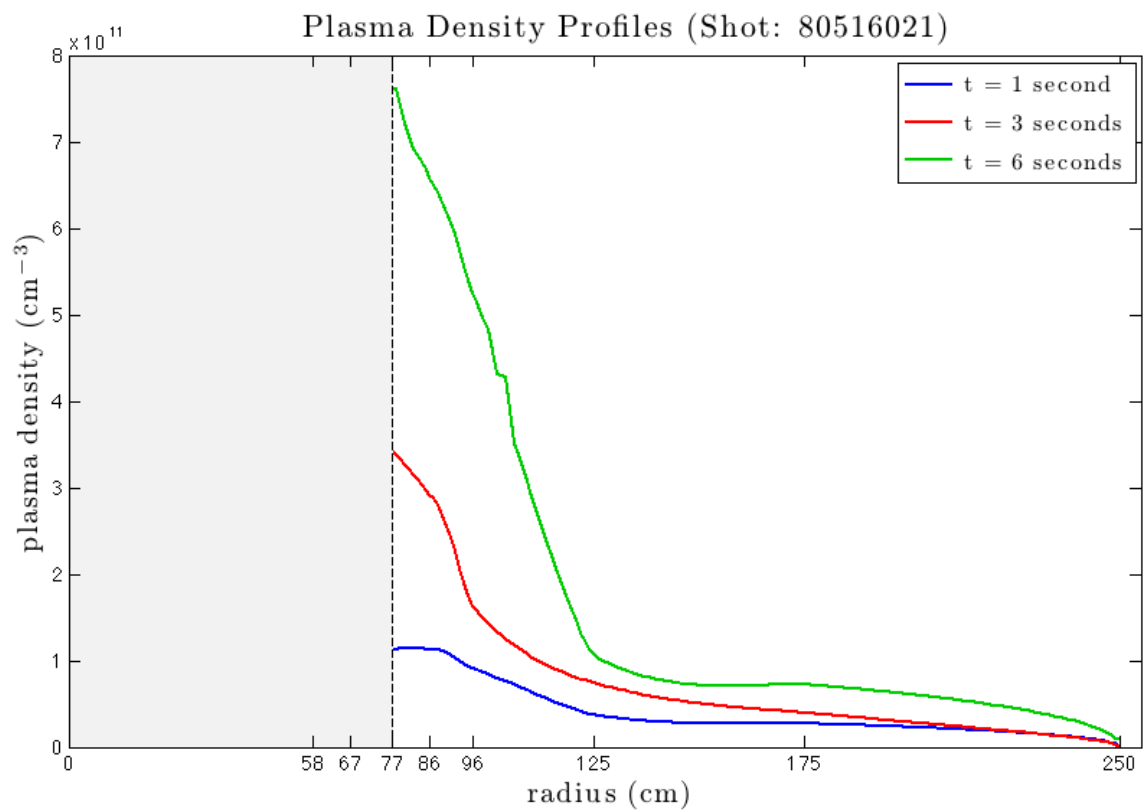
Figure 5-6: Abel-inverted, radial density profiles calculated at three representative times for a the record high density shot (shot 80516021) in which a 50-50 mixture of He and D_2 gas was used. The measured phase-shifts from this shot at 6 seconds are plotted in Fig. 4-12.

ted in Fig. 4-10 and Fig. 4-12; the line-integrated densities for shot 80322020 at one sample time are shown in Fig. 5-3. On the abscissae of these plots are marked the locations of the outer surface of the F-Coil (r = 58 cm), the first closed field line (r = 67 cm), the 4 interferometer chords (r = 77 cm, 86 cm, 96 cm, 125 cm), and the L-shell value of the southwest-top probe (r = 175 cm). No information is available for radial positions inside the innermost measurement (r = 77 cm) and consequently this area is shaded gray.

5.3 Uncertainties in the Radial Density Profiles

5.3.1 Uncertainties from Abel Inversion

Quite clearly, the accuracy with which a full, radial density profile can be computed by inverting only 4+1 data points will be limited. We attempt in this section to quantify the accuracy of these profiles. In our analysis, the uncertainty in the inverted, radial density profiles arises from the uncertainty in the interpolated, line-integrated density function F(y). These uncertainties come from two sources: First there are uncertainties in the line-integrated density measurements; second, there are uncertainties that arise from the non-uniqueness of the interpolated function F(y) used to connect the data points together. Once F(y) is established, however, the Abel-inverted density profile, $n(r)$, computed from Eq.(5.2) is unique.

Any curve F(y) that interpolates the measured data—however arbitrarily—will generate an Abel-inverted profile that, by construction, will reproduce the measured data exactly. The class of all possible profiles is, moreover, not even bounded since there are no upper or lower bounds to the possible curves F(y). In order to establish a family of likely Abel-inverted profiles we must impose some conditions on the interpolating function F(y). In practice, we require that:

- F(y) ≥ 0.

- F(y) is monotonic between two measured data-points.

These two conditions are necessary in order in order to satisfy some reasonable, physical assumptions about the density profile, $n(r)$:

- The density profile $n(r)$ cannot have negative values.

- $n(r)$ does not exhibit large oscillations between measurement locations.

Because the Abel-inverted profile $n(r)$ is a function of the derivative of the interpolation function dF(y)/dy, connecting the data-points in a non-monotonic way gives rise to oscillations in the resulting profile, $n(r)$. That is, if the line-integrated data are interpolated non-monotonically, then the density profile, $n(r)$, must necessarily exhibit at least one peak and one valley in between the measurement locations. Certainly the density profile as a whole need not be monotonic and, for many shots, the data indicate a density maximum outside of $r = 77$ cm. However, in the absence of large and very localized particle sinks, it is unlikely that the density profile has multiple peaks and valleys hiding between the chordal measurement locations.

Restricting F(y) by these considerations eliminates most spline interpolations but not pseudo-linear nor cubic-Hermite polynomial interpolations. A sense of the uncertainty that arises from choosing one interpolation over the other (cubic-Hermite vs. pseudo-linear) is given in Fig. 5-7 where Abel-inverted density profiles are shown for both cases. On the whole the two profiles are very close to each other with the largest errors occurring at the measurement locations themselves (where the slope of the pseudo-linear interpolation is not well-defined). The errors at these locations are listed in Table 5.1.

A larger source of error in the density profile comes from the uncertainty in the measured, line-integrated data. The sensitivity of $n(r)$ to changes in F(y) can be examined directly. Table 5.1 shows the results of modifying by +/- 10% the phase-shift data from the four interferometer channels, labeled as ϕ_1, ϕ_2, ϕ_3, and ϕ_4. Additionally, the density as measured by the southwest-top probe, n_{probe}, is modified by factors of 2 and 1/2. The data come from shot 80322020 at t = 6 seconds and F(y) is computed by cubic-Hermite polynomial interpolation. The results of these modifications appear as changes in the calculated density profile, $\Delta n(r)$, which are tabulated at
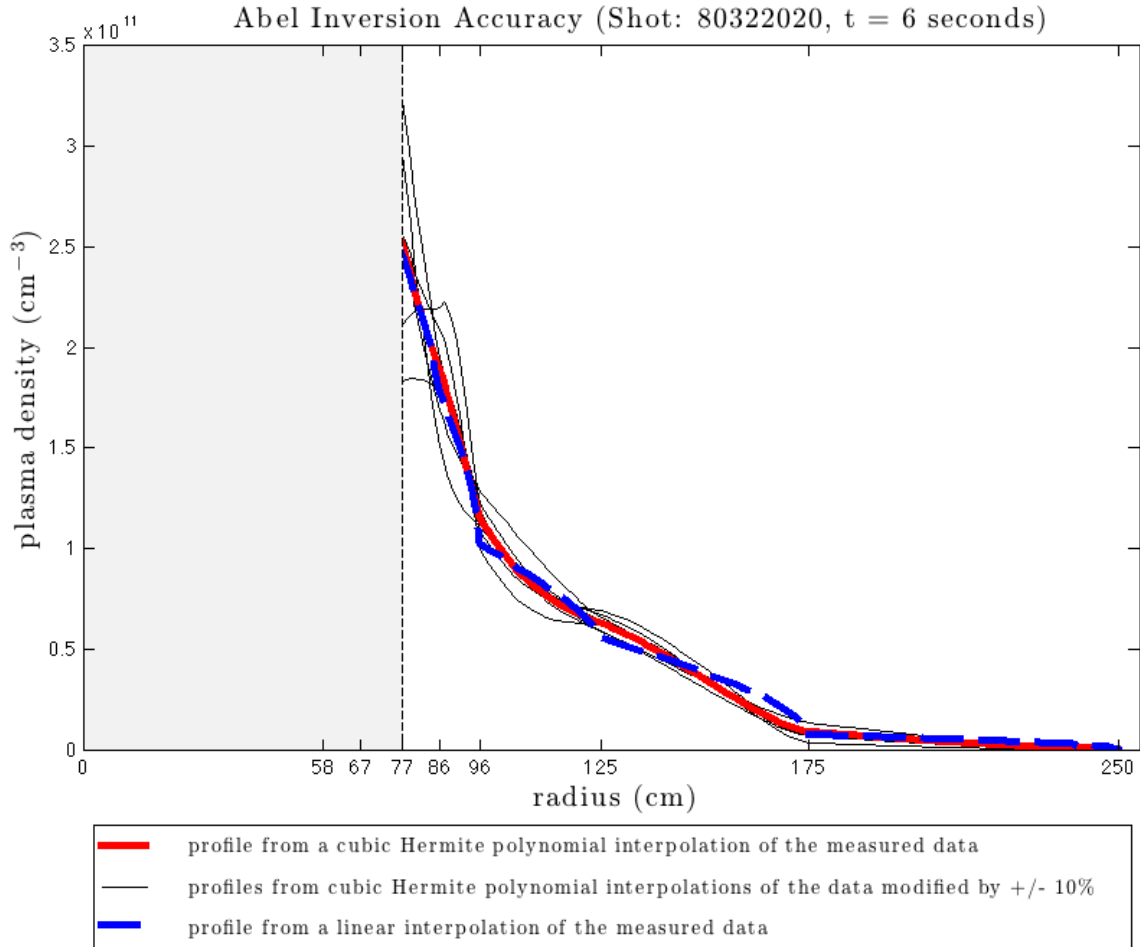
Figure 5-7: Abel inversion accuracy for shot 80322020 at t = 6 seconds. The density profile computed from the measured data interpolated by a cubic-Hermite polynomial is plotted with a heavy, red line. The sensitivity of this profile to the method of interpolation is indicated by plotting the density profile resulting from a pseudo-linear interpolation (heavy, blue, dashed-line). The sensitivity of this profile to errors in the data can also be gauged by plotting the profiles that arise from modified data (thinner, black lines). 10 modified profiles are plotted corresponding to increasing or decreasing by 10% the measured data from each of the four interferometer channels, and by increasing and decreasing the probe data by a factor of 2. The resulting errors in $n(r)$, tabulated in Table 5.1, are larger than the errors in the actual data at the innermost radial locations.

Table 5.1: Abel Inversion Accuracy: Shot 80322020, t = 6 seconds

Modification	$\Delta n_{r=77}$ (%)	$\Delta n_{r=86}$ (%)	$\Delta n_{r=96}$ (%)	$\Delta n_{r=125}$ (%)
$\Delta\phi_1 + 10\%$	28	2.7	0.0	0.0
$\Delta\phi_1 - 10\%$	-27	-4.5	0.0	0.0
$\Delta\phi_2 + 10\%$	-16	16	2.9	0.0
$\Delta\phi_2 - 10\%$	17	-20	-4.7	0.0
$\Delta\phi_3 + 10\%$	0.9	-11	11	2.5
$\Delta\phi_3 - 10\%$	1.4	10	-14	-3.2
$\Delta\phi_4 + 10\%$	0.6	-1.3	-6.0	7.8
$\Delta\phi_4 - 10\%$	0.8	1.3	5.8	-8.6
$2 \times n_{\mathrm{probe}}$	-0.7	-1.0	-1.8	-12
$0.5 \times n_{\mathrm{probe}}$	0.4	0.5	0.8	5.5
linear fit	-2.5	-3.8	-4.3	-9.0

four locations: $\Delta n_{r=77}, \Delta n_{r=86}, \Delta n_{r=96}$ and $\Delta n_{r=125}$.

As can be seen from Table 5.1 and Fig. 5-7, the Abel-inverted, radial density profile is increasingly sensitive to errors at locations closer to the central core. This is because phase-shift data from outer locations is incorporated into all inward values of $n(r)$. A modification in the phase-shift data at an inner location affects a smaller portion of $n(r)$ but the effect is more acute. The consequence of this is that the radial density profile, $n(r)$, can have uncertainties that are greater than the uncertainties in the actual data, especially at interior locations. Thus a 10% error in the measured phase shift of interferometer Channel-1 results in nearly a 30% error of the density at $r = 77$cm.

As this exercise has shown, the uncertainties of the Abel-inverted, radial density profiles, $n(r)$, can be larger than the uncertainties in the actual data (by about a factor of 3 in the core). Since we estimate, conservatively, that the interferometer has a total phase error of around 5% (Tables 4.2 and 4.3), it is likely that the Abel-inverted, radial density profiles, $n(r)$, are only accurate to within around 15% at the innermost locations.

Consequently, while in many instances it is preferable to use the more direct, line-integrated density data, one should not conclude that the radial profiles, $n(r)$, are not sufficiently reliable to be useful. The key point to emphasize is that it is not only the absolute measure of the density profile that is of interest but also the trends of the density profile as a whole. Thus, when considering the radial density profiles of shot 80322020 (plotted in Fig. 5-5), the claim that at t = 6 seconds the plasma density at $r = 100$ cm is 1.0×10^{11} particles per cm^3 is probably only accurate to within 10%. However, the claim that the density has a larger and broader profile at t = 6 seconds than at t = 10 seconds is one that can be made with high confidence. In subsequent analyses, Abel-inverted, radial density profiles will be used to identify trends such as these, i.e., whether the density is increasing or decreasing and whether the profile is becoming broader or more steep in addition to providing estimates of the actual magnitude of the plasma density.

5.3.2 Uncertainties from Refraction

Abel inversion requires that the line-integrals which constitute the function F(y) be computed along straight lines. The trajectories taken by the interferometer beam through the plasma will, however, always be slightly curved due to refraction. In order to quantify the errors from refraction, we have developed a geometric-optics, ray-tracing code that takes as an input any radial density profile, $n(r)$, and returns as output the phase shifts along trajectories corresponding to the four channels of the LDX interferometer.

Ray-Tracing Equations

The basic equation of motion for a ray propagating through a refractive medium in a geometric-optics approximation is [89]

$$\frac{d}{ds}\left(N\frac{d\mathbf{r}}{ds}\right) = \text{grad } N. \qquad (5.11)$$

Here N is the index of refraction as a function of space, $\mathbf{r}$ is the position vector from the origin to a point along the ray's trajectory and s is the path length of the ray.

In the case where the index of refraction function, N, exhibits axisymmetry, i.e. $N(x, y, z) = N(r)$, the equation of motion for a propagating ray [Eq.(5.11)] can be greatly simplified [90]

$$Nr \sin \eta = \text{constant.} \tag{5.12}$$

Here $N = N(r)$ is the index of refraction function, r is the magnitude of the position vector from the origin to a point along the ray and η is the angle made by the position vector $\mathbf{r}$ and the vector $\mathbf{s}$ which is the tangent of the ray at $\mathbf{r}$. Eq.(5.12) is known as the formula of Bouguer and it is analogous to the conservation of angular momentum in mechanics. The geometry of the formula of Bouguer is illustrated in Fig. 5-8.
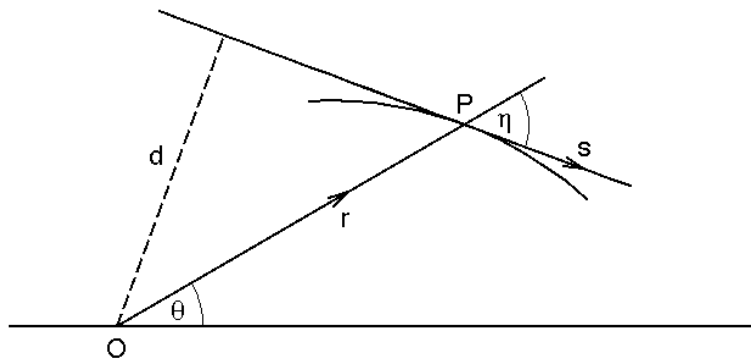
Figure 5-8: Geometry for the formula of Bouguer [Eq.(5.12)]. η is the angle made by the position vector $\mathbf{r}$ and the vector $\mathbf{s}$ which is the tangent of the ray at $\mathbf{r}$.

In the ray-tracing code, the input radial density profile, $n(r)$, is converted into an index of refraction function, $N(r)$, by using Eq.(4.2). The code must then execute two separate routines: First it must determine which rays propagate from the transmitting horn to the four receiving horns; second, the code must determine the phase shifts by integrating along the selected rays according to Eq.(5.6) and Eq.(5.12). In the LDX interferometer, the transmitting and receiving horns are located at fixed positions around the circumference of the vacuum chamber and subtend fixed angles as described in Table 4.1. Selecting the rays which, for a given index of refraction function $N(r)$, propagate between the horns is equivalent to selecting the rays whose trajectories subtend the appropriate angles.

In the formula of Bouguer, each ray is labeled by the constant which appears on the right-hand side of Eq.(5.12). Assume that the ray begins its trajectory propagating horizontally from minus infinity and that the index of refraction, N, at this distance is 1, indicating the absence of any refracting material. Both of these assumptions can be applied to geometry of the LDX interferometer. The constant in Bouguer's formula [Eq.(5.12)] can then be identified with the impact parameter, y, which is the vertical height of the ray above the horizontal axis at minus infinity

$$Nr \sin \eta = y. \tag{5.13}$$

In addition, the radius of tangency of the ray, r_{tan}, will occur where $\sin \eta = 1$ and have the magnitude

$$r_{\text{tan}} = y/N(r_{\text{tan}}). \tag{5.14}$$

Because a plasma has an index of refraction less than 1, it behaves as a diverging lens and refracts the ray outwards (this is opposite to the behavior exhibited in more common materials such as glass). Consequently, the ray's radius of tangency—which is also the minimum radius—must always be greater than or equal to its impact parameter. In turn, r_{tan} in the presence of a plasma must always be less than or equal to r_{tan} in a vacuum.

With these considerations in mind, the rays which for a given index of refraction function $N(r)$ have the correct impact parameter y to subtend an angle Θ can be found with the following formula [90]

$$\Theta(y) = y \int_{r_{\text{tan}}}^{R} \frac{dr}{r\sqrt{N^2(r)r^2 - y^2}}. \tag{5.15}$$

Here R is the outermost radius which, in the geometry of the LDX interferometer, corresponds to the radius of the vacuum chamber, $R = 250$ cm.

Once the correct rays—labeled by y—are found for each interferometer channel by Eq.(5.15), the trajectory of the ray is then integrated according to the formula of Bouguer [Eq.(5.12)]. At the same time, the phase shift along the ray is integrated
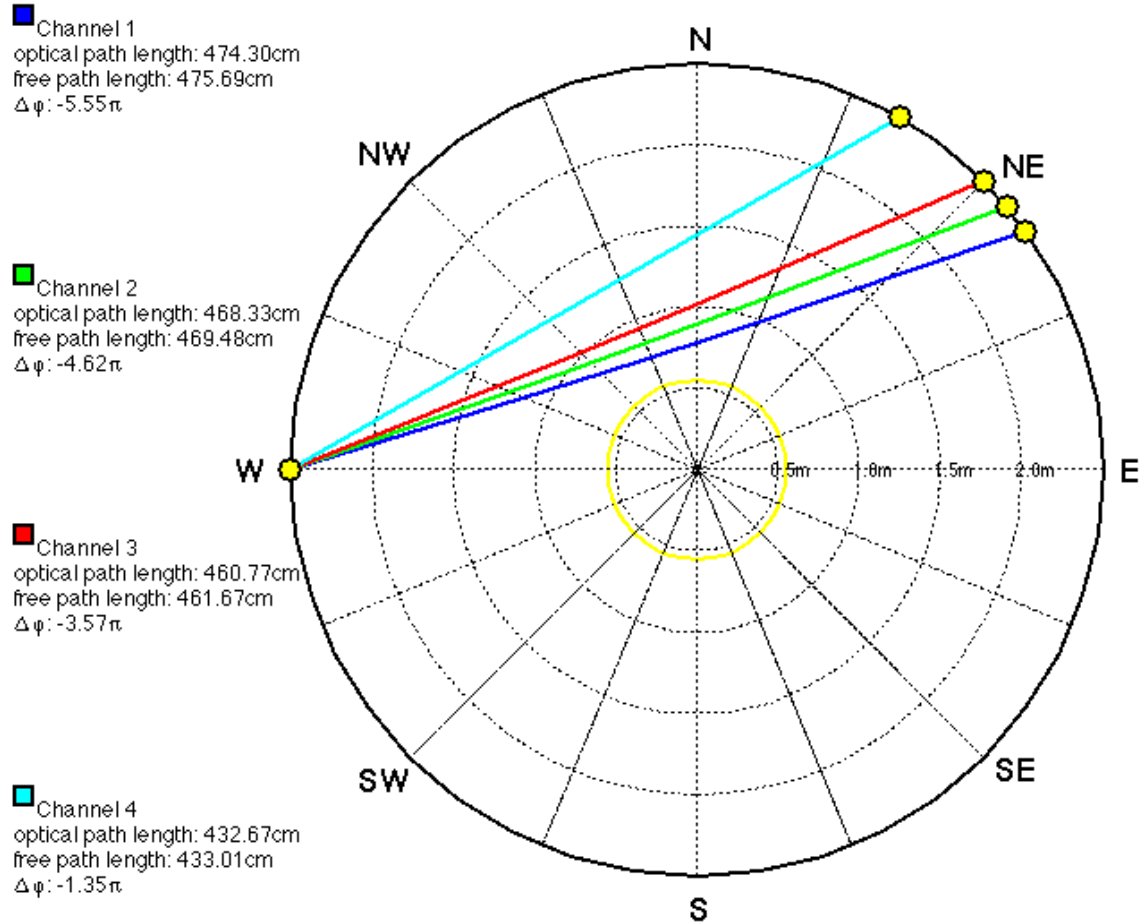
Figure 5-9: Ray-tracing code output. The input radial density profile, $n(r)$, is the Abel-inverted profile calculated from shot 80516021 at t = 6 seconds. This profile (plotted in Fig. 5-6) is the largest density profile measured in LDX. The ray-tracing code plots a figure meant to represent the equatorial plane of the LDX vacuum chamber. The yellow dots around the circumference indicate the locations of the transmitting and receiving horns of the LDX interferometer. Ray trajectories corresponding to the four interferometer channels are plotted. The rays exhibit a small but still perceptible outward bend due to refraction by the plasma. On the left hand side are displayed the optical path length, free path length and phase shift for each interferometer channel. The stepsize used in the integration was 0.005 cm (0.01λ) and the integration errors correspond to phase shift errors of less than 0.1 degree. The fact that even the largest density profiles in LDX give rise to only small deviations from straight-line trajectories demonstrates the soundness of the straight-line approximation used elsewhere.

according to Eq.(5.6). The ray-tracing code outputs the calculated phase shifts for each of the four interferometer channels and displays the ray trajectories graphically. An example is shown in Fig. 5-9 where the input radial density profile, $n(r)$, is the profile calculated by Abel inversion from shot 80516021 at t = 6 seconds. This profile, which is the largest density profile measured in LDX, was displayed earlier in Fig. 5-6.

Comparison of Measured and Simulated Data

Fig. 5-9 shows that even the largest density profiles do not cause the rays to deviate significantly from straight lines. This supports the validity of the straight-line assumption employed in Abel inversion. Nevertheless, refraction will always cause the path traveled by the ray to be longer and—since the longer paths are generally through more plasma—the end result is slightly larger phase shifts. This effect can be seen in Tables 5.2 and 5.3.

In these tables the measured phase shifts at representative times are compared with the phase shifts output by the ray-tracing code. The density profiles used in the ray-tracing code are the profiles computed from the measured data by Abel inversion. As Tables 5.2 and 5.3 show, the simulated phase-shift data is systematically larger than the measured data (note that all the phase shifts are actually negative, but the minus sign has been removed for convenience). Because refraction is ignored, the density profiles computed by Abel inversion will generally *overestimate* the actual profiles.

In general, the errors from refraction are smaller but comparable to the errors arising from Abel inversion. As is to be expected, the refractive errors increase in profiles that are especially large or especially steep or both. For instance the refractive errors for the record high density profile (80516021 at 6 seconds) is estimated to be around 9%. Since the refractive errors are systematic, their effect on the overall shape of the density profile is minimal—i.e., refractive effects should not change the general shape of the profile, only reduce its value by a few percent.

Table 5.2: Refractive Errors: Shot 80322020

Channel	$\Delta\phi$ Measured (rad.)	$\Delta\phi$ Calculated (rad.)	Error (%)
2 seconds			
1	4.454	4.548	2.1
2	3.037	3.071	1.1
3	2.088	2.184	4.6
4	1.072	1.104	3.0
6 seconds			
1	4.974	4.999	0.5
2	3.854	3.862	0.2
3	2.831	2.932	3.6
4	1.603	1.635	2.0
10 seconds			
1	2.950	3.109	5.4
2	1.567	1.627	3.9
3	1.450	1.403	3.3
4	0.857	0.889	3.7

Table 5.3: Refractive Errors: Shot 80516021

Channel	$\Delta\phi$ Measured (rad.)	$\Delta\phi$ Calculated (rad.)	Error (%)
1 second			
1	3.486	3.485	0.03
2	3.167	3.192	0.8
3	2.643	2.693	1.9
4	1.607	1.603	0.2
3 seconds			
1	7.524	7.539	0.2
2	6.089	6.158	1.1
3	4.361	4.349	0.3
4	2.655	2.657	0.1
6 seconds			
1	16.421	17.451	6.3
2	13.476	14.518	7.7
3	10.289	11.225	9.1
4	4.299	4.246	1.2

5.4 Uninvertible Density Profiles

With the caveats of §5.3 kept always in mind, Abel inverted, radial density profiles are nonetheless very useful for estimating the density values as well as identifying trends in the profile dynamics. In general, $n(r)$ profiles can be calculated for every time-sample of line-integrated data (usually 2.048×10^6 samples per shot). Density trends can then be observed directly by animating these profiles over time (see, for example, Fig. 7-9). However there are regularly occurring intervals in which the line-integrated density data cannot be inverted into an $n(r)$ profile. This is the case when the line-integrated density data takes on negative values, is grossly non-monotonic, or both. Quite frequently, in the afterglow period of a shot—during which some plasma density endures even after the ECRH has been turned-off—the line-integrated density data becomes impossible to invert into physically meaningful radial profiles. Similar behavior is also sometimes observed at the very beginning of a shot, right at the onset of the ECRH and the creation of the plasma. Having studied this behavior for many years, we have concluded that the phase-shift data is, in fact, correct but that one or both of the assumptions used in Abel inversion (straight-line paths and axisymmetry) is not valid during these times.

This phenomenon can be seen in one of the shots we have already explored, shot 80322020. The line-integrated density data for this shot was shown previously in Fig. 5-3. In Fig. 5-10, we display only the very end of the shot, from t = 10 seconds to t = 22 seconds. The ECRH is terminated at 12 seconds and the density on all channels rapidly drops to a fraction of its value within 10-20 milliseconds. Subsequently, all of the interferometer channels exhibit fairly intricate oscillations over periods on the order of 1 second. During this time, the line-integrated density profile is anything but monotonic, with the data from the outermost channel, Channel-4, having the largest values. Additionally, both Channels-1 and 2 drop below zero resulting in unphysical line-integrated density values.

Behavior of this sort is observed fairly regularly in the afterglow portion of LDX plasmas and occasionally at the onset of ECRH. The negative overshoot is well in
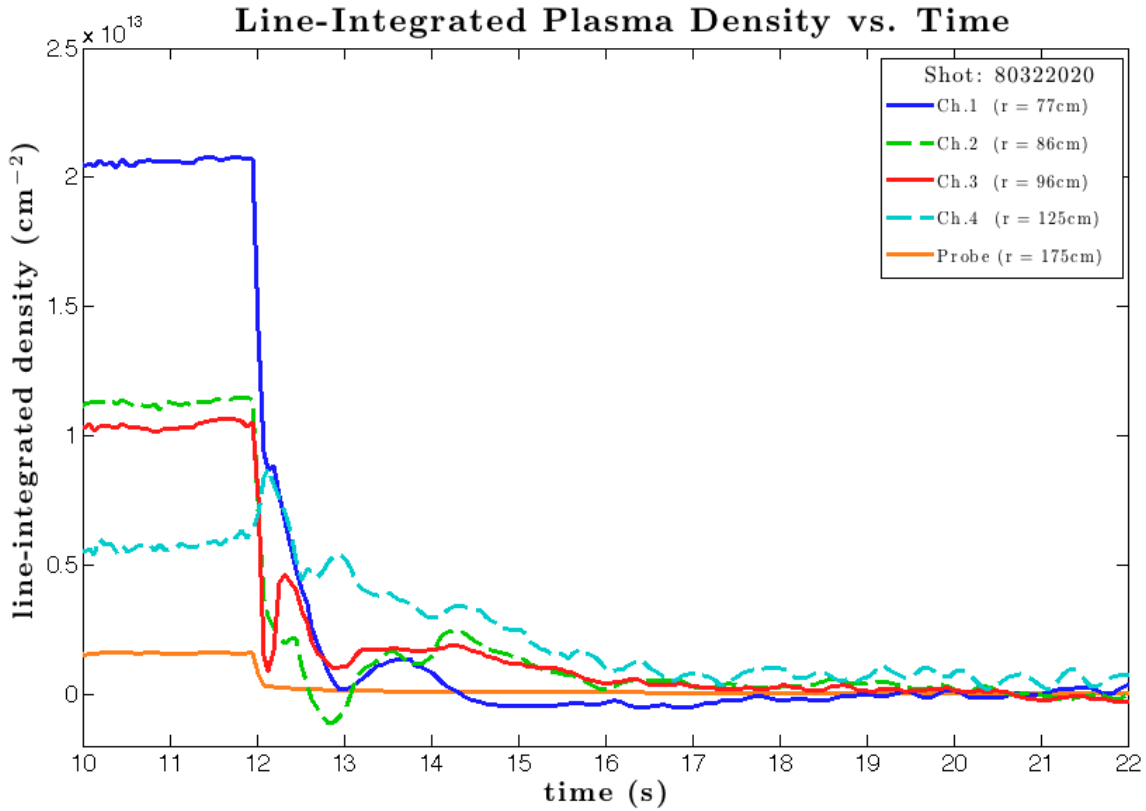
Figure 5-10: Line-integrated density data from the afterglow of shot 80322020. A more complete view of the data from this shot was shown earlier in Fig. 5-3. The ECRH is terminated at t = 12 seconds. The interferometer data subsequently exhibits very complicated behavior which is not tractable by the methods developed earlier in this chapter. The data becomes non-monotonic and Channels-1 and 2 take on negative values. Nevertheless, the evidence indicates that the interferometer is operating properly. Rather, this behavior most likely indicates that the assumption of straight-line ray paths or the assumption of axisymmetric density profiles is not valid during these times.

excess of the interferometer's inherent phase error. Moreover, this behavior occurs at predictable times (e.g., the plasma afterglow) and the 4 channels of data tend to move in synchrony with each other and with the emitted visible light as seen on video recordings of the plasma. All of the interferometer channels always return to their zero level at times when the light from the afterglow has ceased. Likewise, in plasma shots which do not exhibit any afterglow, the interferometer data returns directly to a zero level without any oscillations. All of these facts support the assertion the phase shifts measured by the interferometer are indeed produced by the plasma and not by instrumental errors. Rather, what the data indicates is that the density profiles during these intervals are not amenable to the analytical methods developed earlier in this chapter. More specifically, it must be the case that the plasma at these times is either not axisymmetric or that the assumption of straight-line rays is not valid or both.

Simulations of Ray Scattering off of the Edge of Plasma Cylinder

Our claim is that a properly working interferometer can, under certain circumstances, measure phase shift data that does not yield physical results when treated with Abel inversion. In order to support this claim, we can use the ray-tracing code, described above in §5.3.2, to demonstrate that certain plasma profiles can indeed give rise to data that is similar to that shown in Fig. 5-10. Specifically, we want to address to phenomenon of negative line-integrated density measurements. Because a plasma has an index of refraction that is less than 1, the phase shift acquired by a ray passing through a plasma will be negative [Eq.(5.7)]. Measurements of negative line-integrated density therefore correspond to measurements of *positive* phase shift. In the simulations described below we will examine the circumstances under which positive phase shifts can be acquired by rays traveling through a plasma.

In general, there are a number of ways in which anomalous phase shifts can arise [91] and much of the labor of Chapters 4 and 5 is devoted to addressing these issues one by one. Nevertheless, even with an ideal interferometer, it is straightforward to devise simulations in which positive phase shifts are measured. Here we examine the

Scattering Simulation Geometry
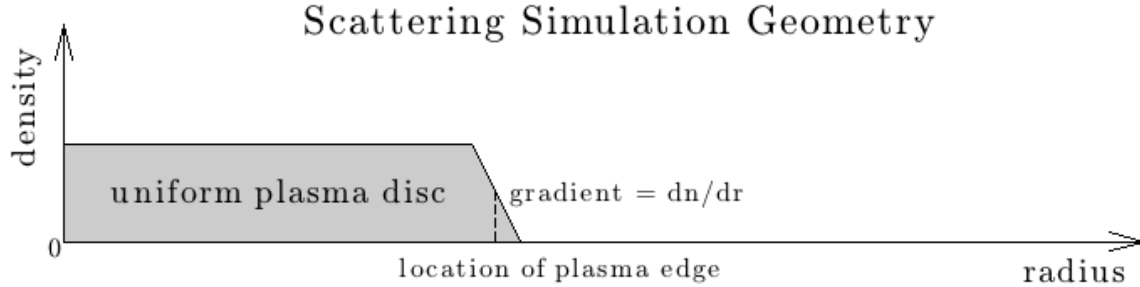
Figure 5-11: Geometry for the simulation of ray-scattering off of a uniform plasma disc. This simple setup is used to demonstrate that rays can acquire both positive and negative phase shifts in the vicinity of a plasma-vacuum interface. The phase anomaly is measured while three parameters are varied: (1) the density of the plasma disc; (2) the gradient of the plasma-vacuum interface; (3) the location of the plasma edge.

simple case of an axisymmetric plasma cylinder of uniform density and simulate the scattering of a ray off the cylinder's edge. A diagram of the simulation geometry is shown in Fig. 5-11. The simulated phase shifts are found to depend upon (1) the density of the cylinder, (2) the gradient of the plasma-vacuum interface, (3) the location of the edge of the cylinder and (4) the impact parameter of the probing ray.

If rays propagate through regions near the center of this profile, the resultant phase shifts will be negative and their magnitudes will be proportional to the line-integral of the density [Eq.(5.7)]. These paths will closely approximate straight lines insofar as the angle of incidence at the plasma-vacuum boundary will be small. For impact parameters outside the edge of the plasma cylinder, the rays will also follow straight-line paths and the phase shifts will be zero since the ray encounters only vacuum. The approximation of straight-line paths breaks down, however, near the inside edge of the plasma cylinder where the angle of incidence approaches 90°.

For example, Fig. 5-12 shows the simulation results for rays propagating near the edge of a plasma cylinder of density $n = 5 \times 10^{10}$ cm^{-3} which extends out to a radius of $r = 85$ cm. The gradient of the plasma-vacuum interface is linear and set to 5×10^{10} cm^{-4}; that is, the transition from vacuum to full density occurs over a 1 cm interval centered around $r = 85$ cm. These are entirely plausible values for an afterglow density although—and this is the whole problem—it is not possible to measure the afterglow density by the methods usually employed.

In Fig. 5-12 we have plotted phase shift vs. *apparent* radius of tangency. The
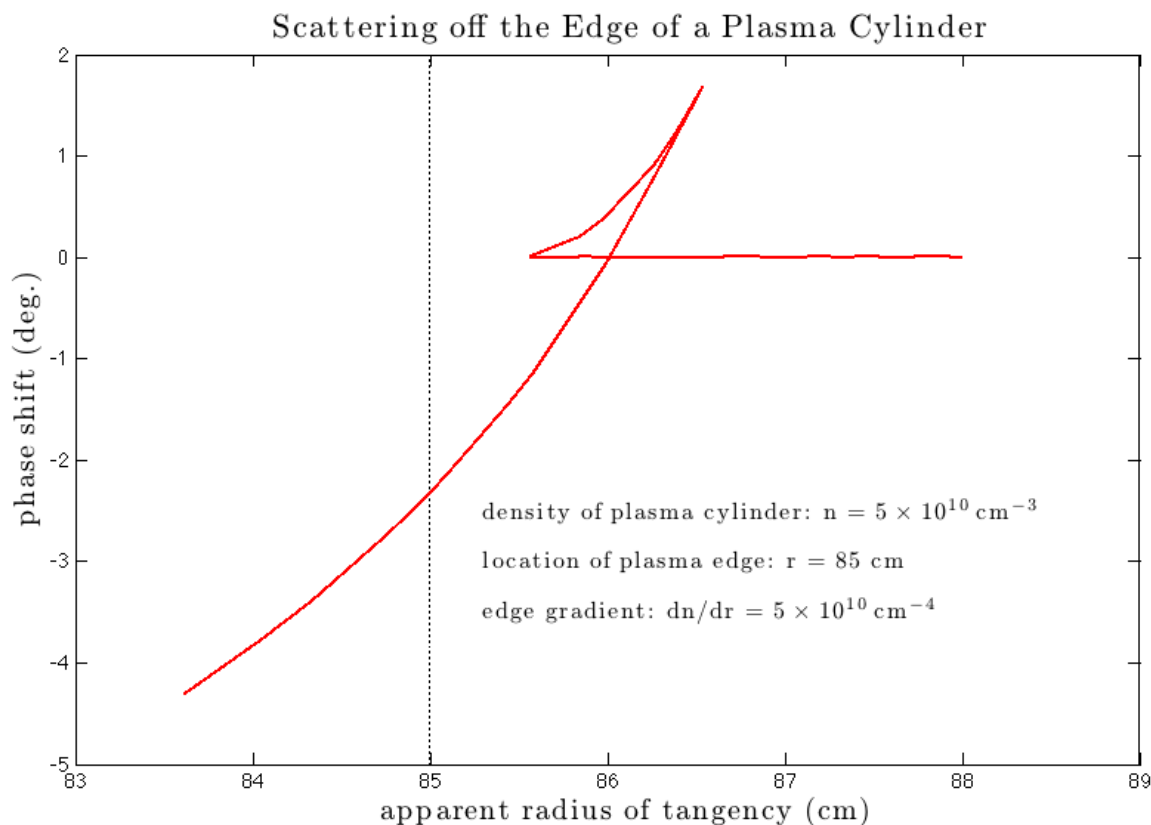
Figure 5-12: Simulated phase shifts for rays scattering off the edge of a plamsa cylinder. These results demonstrate that it is straightforward to simulate anomalous (i.e., positive) phase shifts with a simple, axisymmetric density profile and with rays that follow only the prescriptions of geometrical optics. The apparent radius of tangency is the radius of tangency ascribed to a ray by an observer under the assumption that the ray had reached its receiver-location by a straight-line path. Because of refraction, however, multiple rays can be received at the same location leading—in special circumstances—to the measurement of positive phase shifts. The density profile used in this simulation is a plasma cylinder with uniform density $n = 5 \times 10^{10}$ cm^{-3}, radius $r = 85$ cm and edge gradient $dn/dr = 5 \times 10^{10}$ cm^{-4}. These are not implausible values for LDX plasmas in the afterglow portion of a shot.

141

apparent radius of tangency is the radius of tangency ascribed to a ray by an observer under the assumption that the ray had reached its receiver-location by a straight-line path. Because of refraction, the actual radius of tangency will always be less than the apparent radius of tangency since plasmas behaves like a diverging lens. In the special case of a plasma-vacuum interface, the total phase shift near the boundary can take on both positive and negative values. This is because the extra path-length acquired by the refracted ray occurs mostly in the vacuum region and propagation through this region results in the accumulation of positive phase. Occasionally, this positive phase is enough to offset the negative phase shift acquired during the ray's interaction with the plasma. Note that this effect is *opposite* to what usually occurs with plasma refraction: Usually, refraction leads to larger, *negative* phase shifts (§5.3.2) since the increased path length occurs in regions where plasma is still present.

Fig. 5-12 shows a scenario in which three separate rays have an apparent radius of tangency of 86 cm (corresponding to Channel-2 on the interferometer). Two of the rays have a positive phase shift resulting from significant refraction near the plasma boundary at 85 cm. The third ray is the straight-line ray through the vacuum and it has a phase shift of zero. The resultant phase measured by a receiver at this location will be a superposition of the phases of all three rays and will depend upon their relative intensities. Nevertheless, it is evident that the phase shift in this instance will be positive.

As Fig. 5-12 demonstrates, it is straightforward to simulate anomalous phase shifts with a simple, axisymmetric density profile and with rays that follow only the prescriptions of geometrical optics. In order to estimate the scope of this phenomenon in general, it is necessary to conduct a number of similar simulations while varying the key parameters diagrammed in Fig. 5-11. Because the phase anomaly in our simulations depends upon at least four parameters (cylinder density, edge location, edge gradient, and impact parameter) it is somewhat tricky to display the functional trends. We attempt to show the phenomenon over a broad range of parameters in Fig. 5-13 and Fig. 5-14.

In Fig. 5-13 are plotted the results of varying the plasma cylinder density and
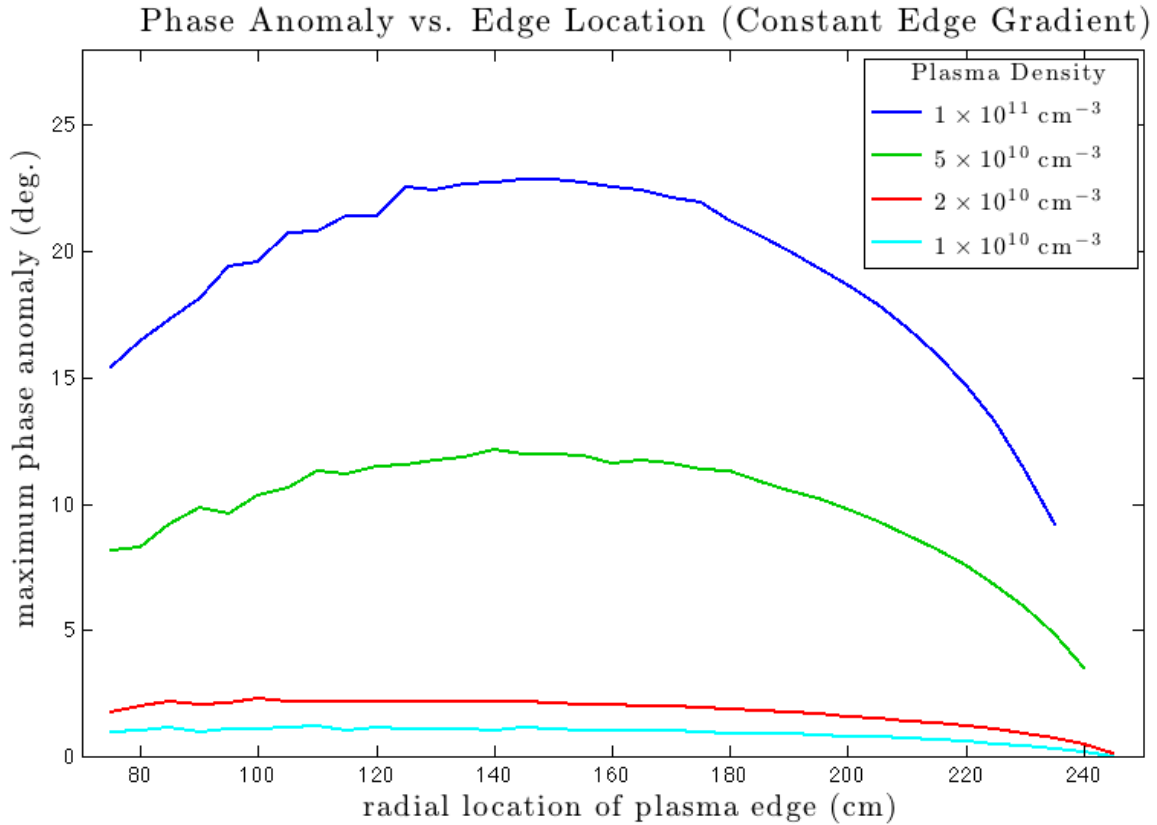
Figure 5-13: Maximum phase anomaly vs. plasma edge location from ray scattering simulations in which the edge gradient is kept fixed. The maximum phase anomaly is the maximum positive phase shift measured at any location for a simulation with given parameters (cylinder density, edge location, and edge gradient). In actuality the maximum phase anomaly will appear to occur at a radius slightly greater than the radius of the plasma cylinder; nevertheless, in this figure the maximum anomaly is, for clarity, aligned with the plasma edge location. The simulation results are shown for 4 different values of the plasma density. In each simulation, the edge gradient is kept fixed and set to a value of $dn/dr = 2 \times 10^{11}$ cm^{-4}.
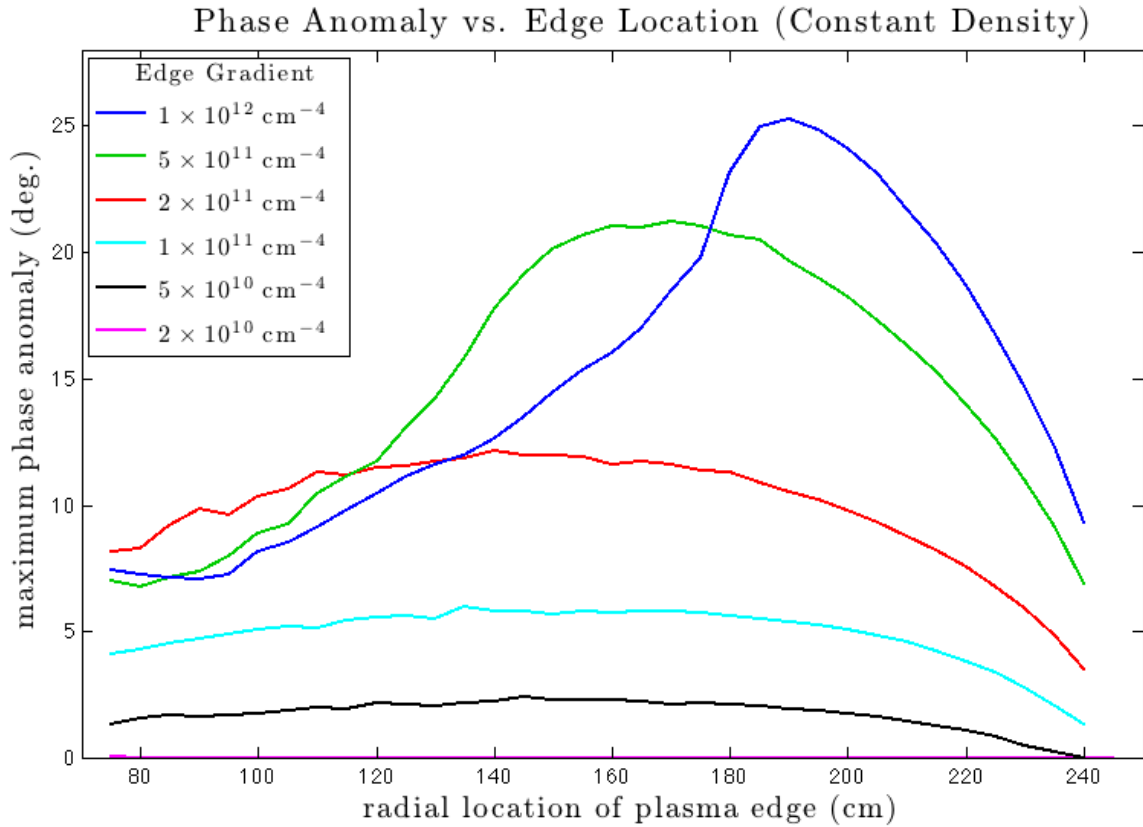
Figure 5-14: Maximum phase anomaly vs. plasma edge location from ray scattering simulations in which the density of the plasma cylinder is kept fixed. Simulations are conducted for plasma cylinders with six different values of edge gradient. In each simulation, the plasma cylinder density is set to $n = 5 \times 10^{10}$ cm^{-3}. The gentlest edge gradient results in maximum phase anomalies near zero and the curve is partially hidden by the x−axis.

edge location while keeping the edge gradient fixed. On the ordinate axis is the *maximum* phase anomaly, which is the largest positive phase shift, while the abscissa represents the radial location of the plasma edge. As was the case in Fig. 5-12, the maximum phase anomaly will not occur at the edge location but rather outwards by a few centimeters. Nevertheless, this subtlety is ignored and the the maximum phase anomaly is aligned with the location of the plasma edge. Four curves are plotted corresponding to four density values of the plasma cylinder. The edge gradient in each case is set to $dn/dr = 2 \times 10^{11}$ cm-4.

Fig. 5-14 is similar to Fig. 5-13. Here the maximum phase anomaly is plotted vs. edge location for six different edge gradients. For these curves it is the density of the plasma cylinder that is kept fixed at $n = 5 \times 10^{10}$ cm-3.

Fig. 5-13 and Fig. 5-14 provide a sense of what density values and gradients are necessary in order to measure significant positive phase shifts. "Significant", in the context of the interferometer measurements, means phase anomalies larger than the maximum phase uncertainty of the interferometer, previously estimated to be less than 5° (Tables 4.2 and 4.3). Fig. 5-14 shows that such anomalies can be produced at fairly modest densities ($n = 5 \times 10^{10}$ cm^{-3}) provided that the gradient of the plasma-vacuum boundary is greater than, approximately, 2×10^{11} cm^{-4}.

It is not known if gradients this steep do in fact occur in LDX plasmas but the notion is not implausible. During the afterglow period, the surviving plasma is composed mainly of trapped, hot electrons whose orbits are likely confined to a narrow shell corresponding to one of the ECRH resonances. The results of Fig. 5-13 and Fig. 5-14 represent, moreover, strong conditions for the observation of anomalous phase shifts. This is because the simulated density profiles were all axisymmetric whereas, presumably, a much wider range of phase shifts could be produced from an arbitrary, non-axisymmetric profile.

It must be stressed, however, that the measurement of positive phase shifts requires the special circumstance of refraction at a plasma-vacuum interface. Refraction within the plasma leads, rather, to larger *negative* phase shifts. Since refraction within the plasma has been established to be small (§5.3.2) we assert that the phase shifts

during the main portion of the shot (in which the ECRH is on) do not suffer from anomalies of the sort discussed here. And this is the key point: That during the main portion of the shot, the analytical methods of Abel inversion can be applied to the density profiles. The fact that anomalous phase shifts arise during select intervals should not call into question those intervals in which the phase shifts are tractable. Nor is it the case that no knowledge of the plasma density can be extracted from data exhibiting anomalous phase shifts. Rather, the anomalous phase shifts tell us, by their very presence, important information about the density values and gradients at those instances even if that information is less comprehensive than what can be obtained by Abel inversion.

Chapter 6

Density Profiles in LDX

6.1   An Observational Atlas

The Levitated Dipole Experiment became fully operational—meaning that plasmas could be confined by the field of by a *levitating* dipole magnet—beginning in December, 2007. Since that time over 250 plasma discharges have been formed, each lasting, on average, about 10 to 12 seconds. As the first and only device of its kind, one of the chief experimental goals of LDX is to acquire enough observational data to begin to characterize the behavior of LDX plasmas over a wide range of input parameters. The LDX interferometer, by providing measurements of the plasma density profiles in both time and space (including the plasma core) has proven especially useful in diagnosing these initial, levitated-mode plasmas.

The measurements presented in this chapter constitute the first survey of LDX plasmas confined by the field of a levitating (as opposed to supported) dipole magnet. As is generally the case with new observations, it is not possible to provide a complete explanation of everything that has been seen. Even so, evidencing the salient density-trends and mapping-out their general features is essential for evaluating the initial, levitated-mode performance of LDX and informing future areas of investigation.

Input Parameters

Quantifying the differences between plasmas confined by a levitating dipole coil vs. a dipole coil that is held in position with mechanical supports is one of the principal objectives of LDX. On account of substantial changes made to both the interferometer and LDX as a whole, only measurements made from December, 2007 onwards are considered. Although only a small minority of these shots (about 25 out of 250) have been made in supported-mode, this data-set nonetheless provides an important benchmark against which the shots in levitated-mode can be compared.

Once the F-Coil is in position, LDX plasmas are created and heated by the application of ECRH microwaves at different frequencies (§3.4). Selecting which ECRH sources are on and when is thus one of the principal means by which LDX plasmas are controlled and shaped. However different shots with the same sequence of ECRH will not necessarily yield similar data. As in other plasma-confinement devices, the conditions inside the vacuum chamber play a dominant role in determining what plasma parameters are attainable. In LDX, fortunately, much of the disparate plasma data can be rationalized by means of just one simple measurement of the vacuum conditions: an ion-gauge reading of the background pressure of neutral particles.

Essentially all LDX data, whether from the interferometer or other diagnostics, exhibits clear trends once the vessel ion-gauge pressure reading is set as the abscissa. While the total number of neutral particles input into the vacuum chamber can be controlled externally, the ion-gauge pressure measurement depends upon a variety of more complicated transport processes and, consequently, cannot be governed with any great precision. In practice, therefore, time-instances of interest are chosen for a collection of plasma shots and the data measured at those instants are then ordered according to increasing background pressure. All of the shot/time databases used in this chapter are provided in Appendix B. The selected time-values always correspond to times when the line-integrated densities measured by the interferometer have attained a steady-state, flat-top appearance.

Additionally, recent experiments with different gases have revealed that plasma

species is another key input parameter. So far, plasmas have been made from deuterium and helium and these exhibit starkly different behaviors.

In the remainder of this chapter, we will present plots that summarize the behavior of LDX plasmas in terms of the most important input conditions, which we have identified to be:

- Levitated vs. mechanical support of the F-Coil.

- Input ECRH frequencies and power.

- Neutral background pressure as measured by the vessel ion-gauge.

- Plasma species (D_2 vs. He).

The following plots are meant to serve as an observational compendium, or atlas of sorts, indicating what plasma is likely to be produced for a specified set of input conditions. There are many ways of presenting the data and the figures presented below were selected as being simultaneously the most informative and the most clear.

6.2   Line-Integrated Density Trends

The basic interferometer data for an individual shot is most informatively displayed as four line-integrated plasma density measurements vs. time (see, for example, Fig. 5-3). In order to exhibit how the density changes across multiple shots in response to changes in the external, input parameters it is necessary to employ a different graphical scheme. The first step is to compile databases of individual shots and instances which correspond to given sets of input parameters. For example, Table B.1 is a list of instances during which a D_2 plasma was heated with the full 15 kW of ECRH. For each of the shots and each of the times listed, the line-integrated density data is collated along with the vessel ion-gauge pressure. Occasionally, some shots are represented by more than one time-instant, and this implies simply that the given ECRH combination occurred multiple times during the same shot, or that the
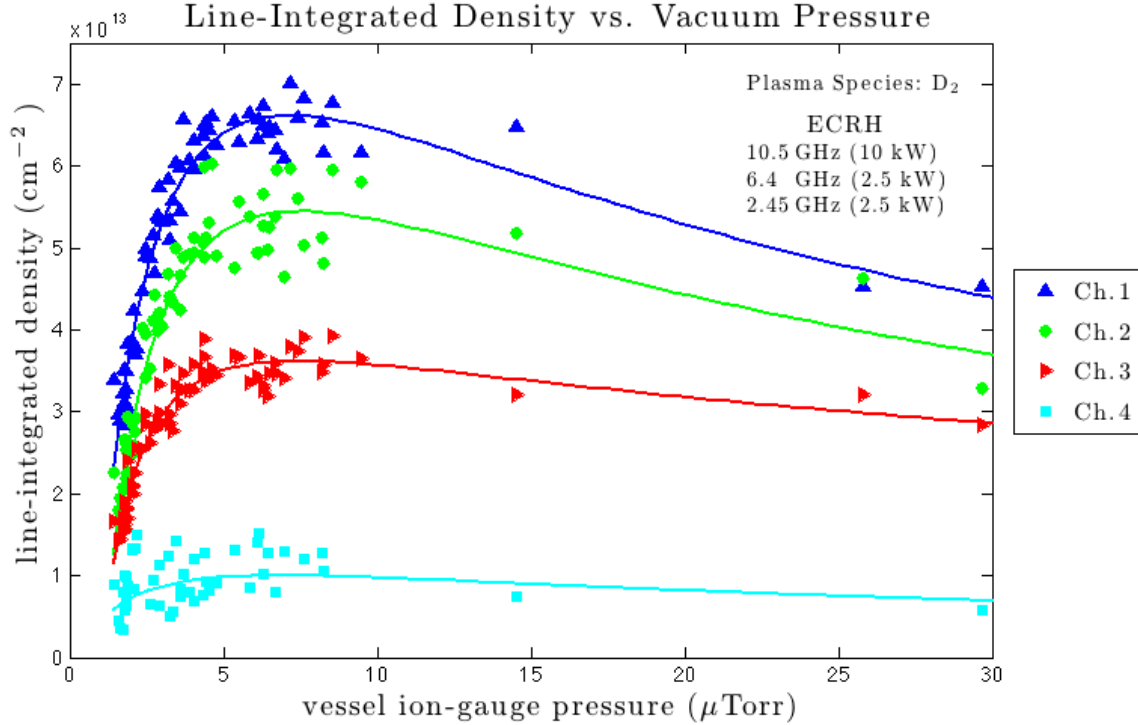
Figure 6-1: Line-integrated density vs. vacuum pressure for D_2 plasmas heated by three frequencies of ECRH with a combined input power of 15 kW. The data points correspond to measurements made for the shots and times listed in Table B.1. The trend-lines for each channel have the approximate functional form $\log(x)/x^a$. The general behavior of the density is, initially, to increase rapidly with neutral pressure attaining a maximum at around 5-7 μTorr. Subsequent increases of pressure correspond to gently declining density measurements.

sequence was sustained for an especially long time. The result of graphing the line-integrated density data associated with Table B.1 arranged by increasing ion-gauge pressure is shown in Fig. 6-1.

In order to more easily visualize the density-trends, the data were fit to functions of the form

$$y(x) = a_0 \log(x - a_1)/(x - a_2)^{a_3}. \tag{6.1}$$

Here x is the independent variable (corresponding to the ion-gauge pressure) and a_0, a_1, a_2 and a_3 are parameters of the fit. The functional form of Eq.(6.1) was inspired in part by the superficial resemblance of the density trend-lines to the shape of ionization cross-section curves. For example, the most standard approximation for the total ionization cross-section of atoms or molecules by electron impact is given

by the Binary-Encounter Bethe formula [92], [93],

$$\sigma_{\text{BEB}}(t) = \frac{c_0}{t+c_1}\left[\frac{c_2\log t}{2}\left(1-\frac{1}{t^2}\right) + (2-c_2)\left(1-\frac{1}{t}-\frac{\log t}{t+1}\right)\right]. \qquad (6.2)$$

Here the independent variable, t, is a function of the energy of the incident electron and c_0, c_1 and c_2 are constants. As is clear by inspection, the leading order terms of Eq.(6.2) are contained in Eq.(6.1). Fundamentally, however, there is no particular justification for using Eq.(6.1); insofar as the fit is meant as an aid to the eye, the appropriateness of Eq.(6.1) derives from the fact that it fits the data remarkably well. We will offer some further speculation about the physical significance of the trend-line shapes in §6.5.

Figure 6-1 demonstrates the importance of the background, neutral pressure as a determinant of plasma density. The four channels of line-integrated density are seen to rise rapidly with increasing background pressure, reaching a maximum at around 5-7 μTorr and then slowly tapering-off with increasing ion-gauge readings. Quite clearly, controlling the ECRH alone is not sufficient to shape the plasma profiles in LDX. Nevertheless, Fig. 6-1 suggests that LDX profiles *can* be made largely reproducible once the background, neutral pressure is taken into consideration.

In order to compare the line-integrated density trends over a range of input parameters, we can make plots similar to Fig. 6-1 that correspond to different sequences of ECRH, levitated vs. supported-mode operation and D_2 vs. He plasmas. However, since each set of line-integrated density data consists of four curves (one for each channel of the interferometer), it is more convenient to retain only the data from Ch.1 when comparing across input parameters.

Figure 6-2 shows the effects of different ECRH powers and frequencies on D_2 plasmas over a range of neutral pressures. Only the data and trend-lines corresponding to interferometer Ch.1 are plotted for each set of input parameters. As in Fig. 6-1, the line-integrated density data is seen initially to rise rapidly with increasing pressure. Here, however, we note that different ECRH combinations result in line-integrated density maxima at different ion-gauge pressures. For instance, with only 2.5 kW of
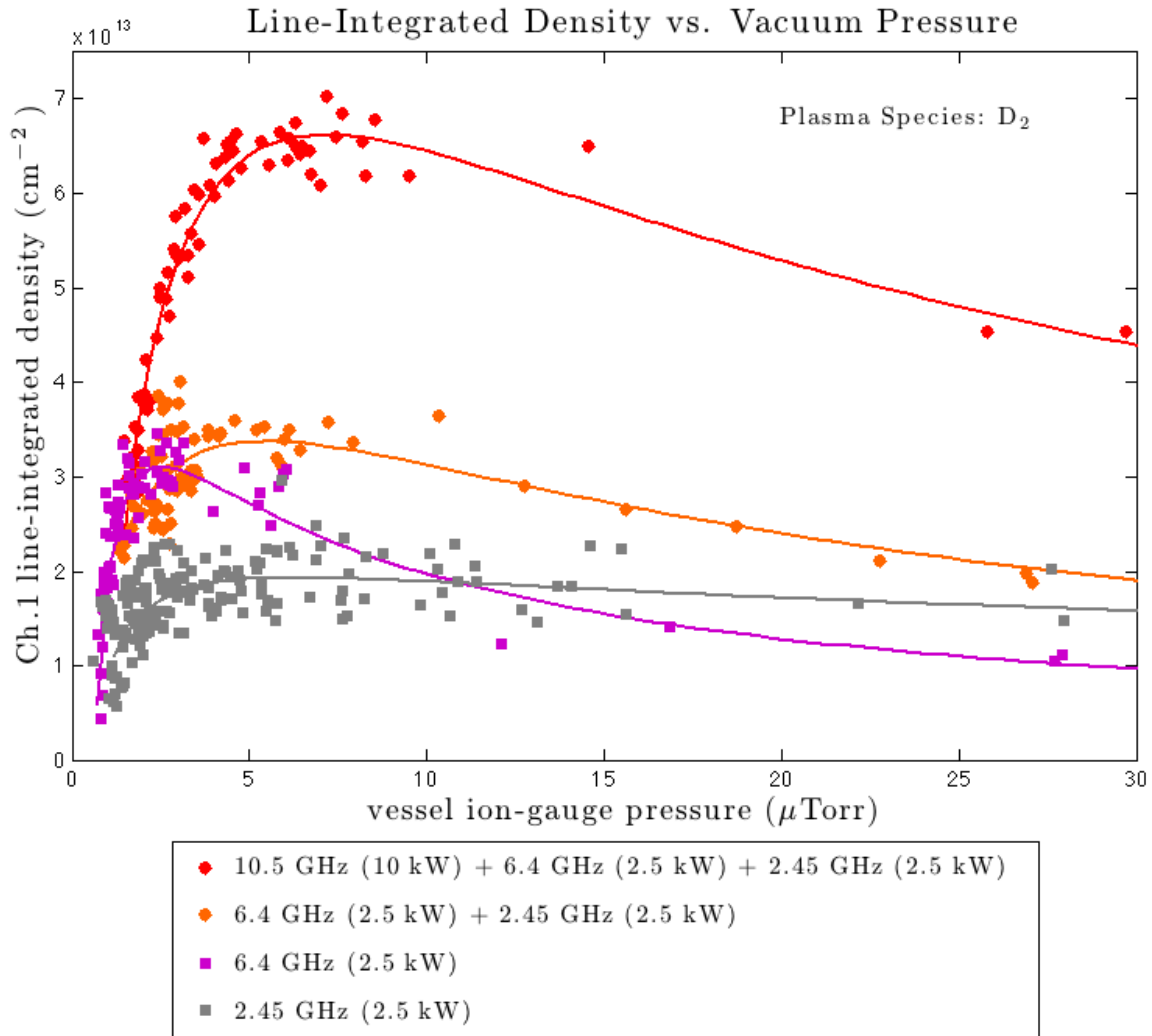
Figure 6-2: Line-integrated densities from interferometer channel-1 ($r = 77$ cm) vs. ion-gauge pressure for various input ECRH powers and frequencies. The shots and times corresponding to these data are listed in Tables B.1, B.2, B.3 and B.4.

6.4 GHz ECRH, the line-integrated density attains a maximum at around 2 μTorr whereas the same power of ECRH at 2.45 GHz appears to reach a maximum closer to 5 μTorr and the application of all three ECRH sources results in a maximum at around 7 μTorr. Also of interest is the fact that, beyond its maximum, the density produced by the 6.4 GHz microwaves falls quite rapidly with increasing neutral pressure whereas the density from the 2.45 GHz ECRH remains fairly flat.

A similar plot, Fig. 6-3, shows the differences between levitated-mode and supported-mode plasmas as well as between D_2 and He plasmas. By levitating the central, dipole coil the majority of particle losses along the field-lines is eliminated which ought to lead to better confinement and higher densities. Fig. 6-3 demonstrates that improvement in density that results from levitation is to increase the line-integrated value at the core ($r = 77$ cm) by about a factor of 3 when heated by the same ECRH combination. Interestingly, this improvement is also dependent upon the background, neutral pressure; the maximum occurs at around 5 μTorr, but subsequent increases in background pressure correspond to a slow convergence of the levitated-mode and supported-mode densities heated by 5 kW ECRH.

An entirely unexpected result is the dramatic difference in densities between He and D_2 plasmas. As seen in Fig. 6-3, the densities of He plasmas attain levels that are double or triple the levels of similar D_2 plasmas. The actual level of He in the vacuum chambers during helium experiments—which always directly followed D_2 experiments—was not known precisely. The ion-gauge pressure must be calibrated according to what species of gas is present in the vacuum chamber and, for these data, the neutral gas was estimated to be a 50-50 mixture of both He and D_2. Unlike with D_2, He plasmas increase monotonically with increasing neutral pressure. The record-high density in LDX was achieved with a He plasma (shot 80516021, shown previously in Fig. 4-12) and the implication of Fig. 6-3 is that even higher densities can be produced in LDX with the current ECRH sources provided that the plasma is made from He and the background pressure is increased beyond 30 μTorr.
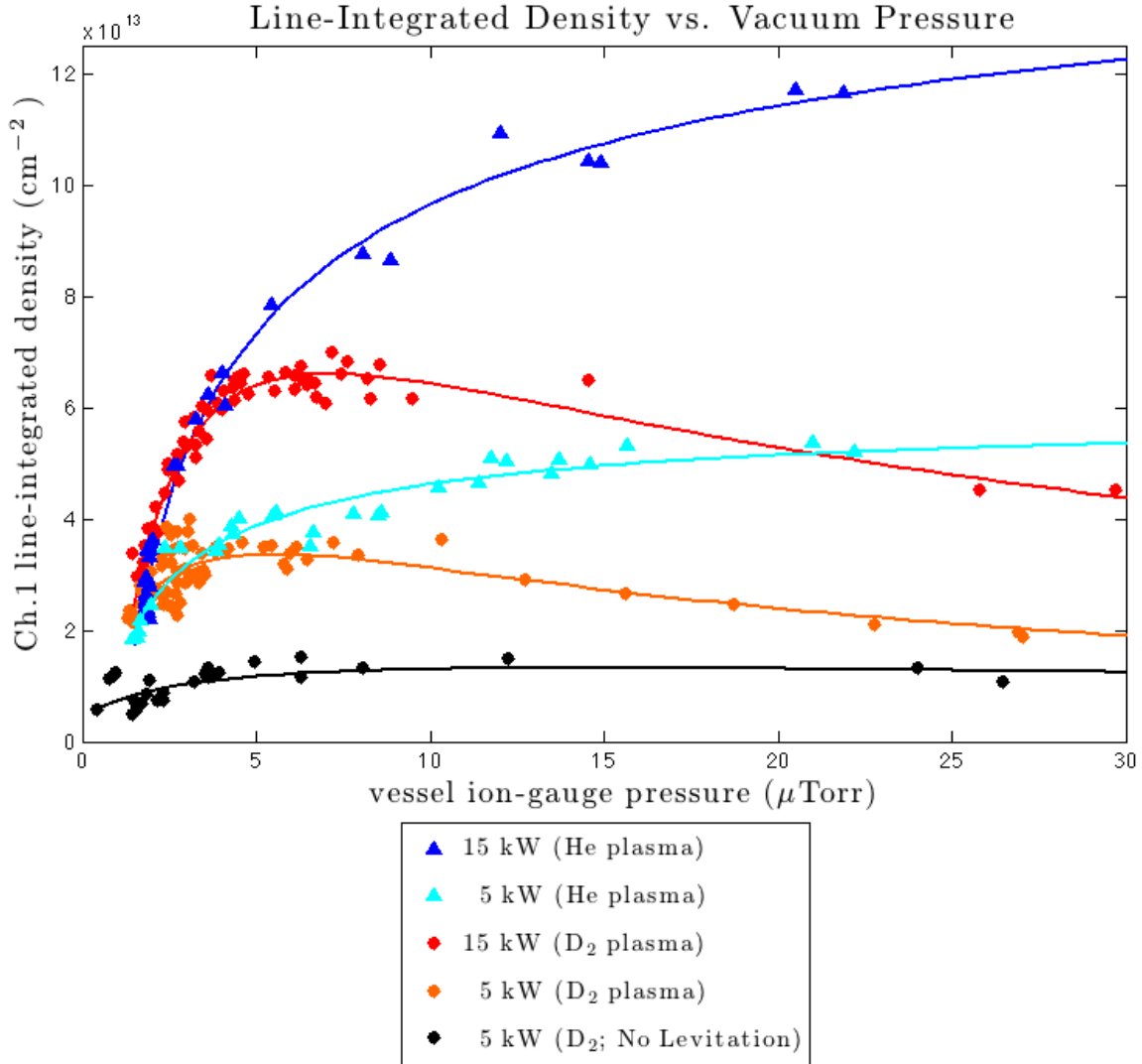
Figure 6-3: Ch.1 line-integrated densities vs. ion-gauge pressure for various input ECRH powers showing the difference between levitated-mode and supported-mode plasmas and between He and D_2 plasmas. The shots and times corresponding to these data are listed in Tables B.1, B.2, B.5, B.6 and B.7. In general, levitated-mode plasmas achieve higher densities than supported-mode plasmas under similar conditions. More surprisingly, He plasmas achieve higher densities than D_2 plasmas with similar input ECRH. The figure indicates that at higher neutral pressures, even higher densities are attainable with He plasmas using the current set of ECRH sources.

6.3 Plasma Current Trends

Another set of measurements which exhibit a clear trend once they are ordered according to ion-gauge pressure is the plasma diamagnetism. As discussed in §2.4.1, charged particles in the presence of a dipole magnetic field will drift azimuthally around the dipole's center. This motion of the charged-particles results in a current that can be considered as either a combination of single-particle drifts or, equivalently, as a solution of the MHD fluid equations in the presence of an anisotropic pressure. In both cases the resulting current, $\mathbf{J}$, comes out to be [94]

$$\mathbf{J} = \frac{\mathbf{B}}{B^2} \times \left(\nabla P_\perp + \frac{P_\parallel - P_\perp}{B^2} (\mathbf{B} \cdot \nabla)\mathbf{B} \right). \qquad (6.3)$$

Here $\mathbf{B}$ is the magnetic field and $P_\perp$ and $P_\parallel$ are the perpendicular and parallel components of the plasma pressure tensor.

In LDX, the azimuthal plasma current increases as the plasma is energized by ECRH. By virtue of carrying a current, the plasma will produce a magnetic field whose strength can be measured by magnetic diagnostics. If it is recalled that the empirical foundation of electrodynamics is that parallel currents attract and anti-parallel currents repel then it becomes clear that the plasma current in LDX must be parallel to the current in the F-Coil; indeed, this is the basis of MHD equilibrium for a dipole-confined plasma. Thus a flux-loop, located around the circumference of the LDX vacuum chamber at the equatorial mid-plane will measure an increase in magnetic flux due to the presence of a plasma current. In LDX, the circumferential flux-loop is named "flux-loop 5".

A similar phenomenon occurs in the Earth's magnetosphere where the azimuthal plasma current is called the "ring-current". Occasionally, certain solar disturbances cause an explosive growth in the intensity of the ring-current which is registered on Earth as a geomagnetic storm [95]. Since the ring-current must be parallel to the currents which give rise to Earth's magnetic field, an observer on the surface of the Earth—which is in between the two current sources—will see a *decrease* in the local magnetic field during a geomagnetic storm. The DST-index (Disturbance Storm Time

index), which is one of the standard ways of recording space weather, simply records changes in the local magnetic field at the surface of the Earth. A sudden decreases in the DST-index, which is the marker of a geomagnetic storm, indicates an increase in the Earth's ring-current. Flux-loop 5 on LDX is therefore analogous to the DST-index with the exception that the DST-index is a measure of the field and not the flux.

The advantage of knowing the total magnetic flux due to the plasma current is that this measurement contains information about the plasma energy. Plasma-β, which is the ratio of the plasma thermal pressure to the background magnetic pressure, is related to the plasma current, $\mathbf{J}$ on account of $\mathbf{J}$'s relation to the pressure P through Eq.(6.3). It must be reiterated, however, that flux-loop 5 does not measure the plasma current but rather the magnetic flux of the plasma current; more specifically, what is measured is the plasma's magnetic dipole-moment. Thus an increase in flux as measured by flux-loop 5 could correspond to one of two things: an increase in plasma current, or, an outward motion of the plasma leading to an increase in the area enclosed by the plasma current.

Because the measurements of flux-loop 5 have an ambiguity in their relation to the plasma current, they cannot be used by themselves to compute the plasma-β. Nevertheless, without requiring a full reconstruction of the pressure profile, flux-loop 5 does provide a handy way to estimate the energy stored in the ring-current in LDX in much the same way that the DST-index can be used to estimate the energy of the ring-curent in the Earth's magnetosphere. It turns out that the ring-current energy, E, is related to changes in the measured magnetic field, ΔB by a simple ratio [95], [96],

$$\frac{\Delta B}{B_0} = \frac{2E}{3E_0}. \tag{6.4}$$

Here B_0 is the field as measured in the absence of the ring-current and E_0 is a constant which, in the case of the Earth, is equal to the energy of the Earth's dipole field at the Earth's surface. Thus in the approximation that the area enclosed by the ring-current in LDX does not change too much, Eq.(6.4) indicates that the plasma current energy
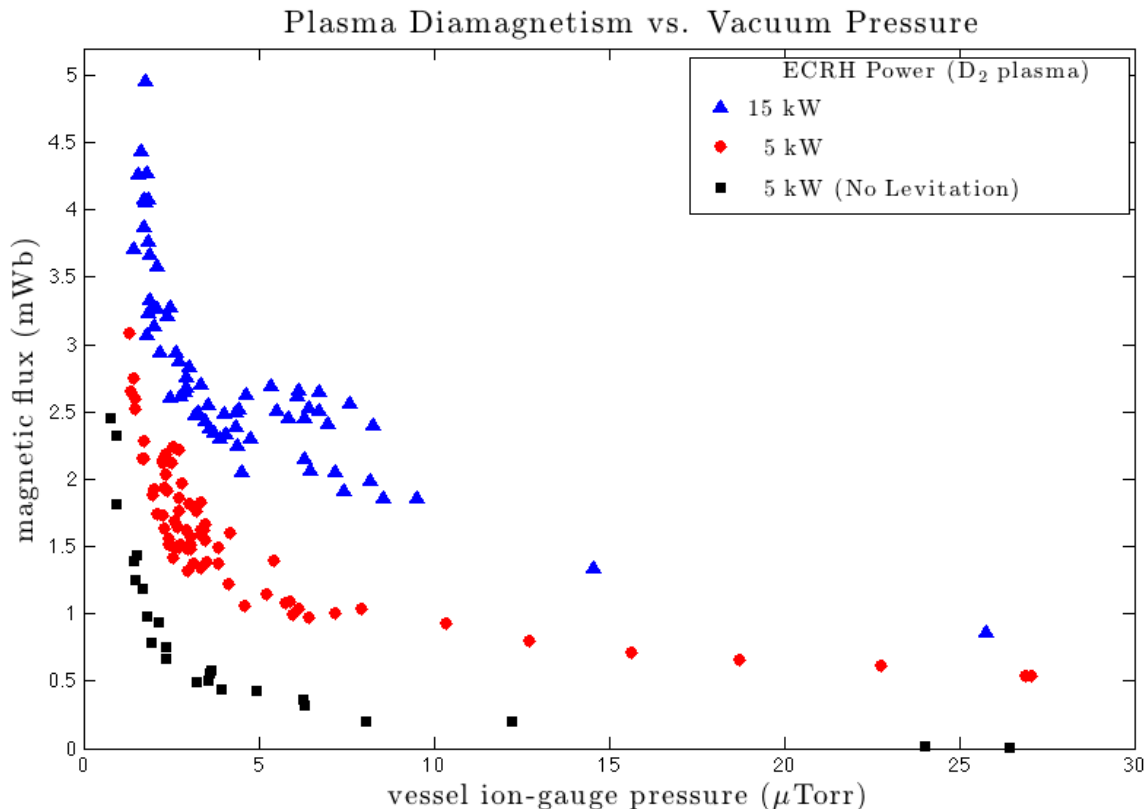
Figure 6-4: Plasma diamagnetism as measured by flux-loop5 vs. neutral particle pressure. Flux-loop 5 encircles the circumference of the LDX vacuum chamber at the mid-plane and measures the magnetic dipole moment due to the plasma ring-current. In the approximation that the area enclosed by the ring-current does not change significantly, the changing flux measured by flux-loop 5 will be linearly related to the energy stored in the ring current according to Eq.(6.4). The figure shows that levitated-mode plasmas have larger dipole moments than supported-mode plasmas; likewise, the plasma dipole moment increases with increasing ECRH power. On the whole, the flux decreases with increasing background pressure. However, for plasmas heated by 15 kW, a bump is seen at around 7 μTorr which corresponds to the plasma density peak (see Fig. 6-1). The shots and times corresponding to these data are listed in Tables B.1, B.2 and B.5.

is linearly related to the magnetic flux as measured by flux-loop 5.

Figure 6-4 shows the plasma diamagnetism, as measured by flux-loop 5, vs. ion-gauge pressure for three different data sets. Unlike the line-integrated density trends (plotted in §6.2), the diamagnetism decreases rapidly with increasing neutral pressure and the decrease is, for the most part, monotonic. The implication of this is that most of the stored energy in the plasma is made from the small population of hot electrons ($E > 10$ keV) that are resonant with the ECRH microwaves. Increasing the neutral pressure increases the density of background electrons (Fig. 6-2, Fig. 6-3) but evidently decreases the hot electron population, whether by collisions with neutrals,

collisions with the bulk electrons or some other process (cf. §6.5).

As hoped for, the diamagnetism of levitated-mode plasmas is higher (by a factor of 2-3) than in supported-mode plasmas with the same input ECRH. Increasing the ECRH power from 5 kW to 15 kW for levitated-mode plasmas likewise increases the plasma diamagnetism. Even so, the most exciting feature of Fig. 6-4 is that a small but noticeable bump appears in the 15 kW data at around 5-7 μTorr. This background pressure corresponds exactly to the density peak for D_2 plasmas heated by 15 kW of ECRH as shown in Fig. 6-1. One explanation for this is that, at this pressure, the stored energy in the background plasma is large enough to be comparable to the stored energy of the hot electron population. If correct, this would be an encouraging result for LDX which has the goal of confining high-pressure plasmas that are thermalized. Alternatively, the bump could mean only that the area enclosed by the hot-electron plasma current has increased at these pressures.

Not plotted in Fig. 6-4 are the data for helium plasmas. On the whole, the data is similar, thus evidencing that species is not as crucial in the production of hot electrons as it is in the production of the background density. Just as with D_2 plasmas, a bump appears for the 15 kW, He data, but it is located more towards 7-10 μTorr. More interestingly, a bump can be seen on the 5 kW, He data, thus supporting the notion that a sufficiently high background density can account for a noticeable portion of the plasma ring-current and total stored energy.

6.4   Radial Density Profile Trends

In the plots of §6.2, the plasma density trends were exhibited in terms of line-integrated density measurements from interferometer Channel-1. Using the Ch.1 measurements as a proxy for the density as a whole has the advantages that it is convenient and free from the uncertainties which are inevitably introduced by further analysis. Nevertheless, we still desire to know how the density *profiles*—that is, their shape as well as their magnitude—behave under various experimental conditions. One especially direct way to obtain profile information is to plot the ratio of
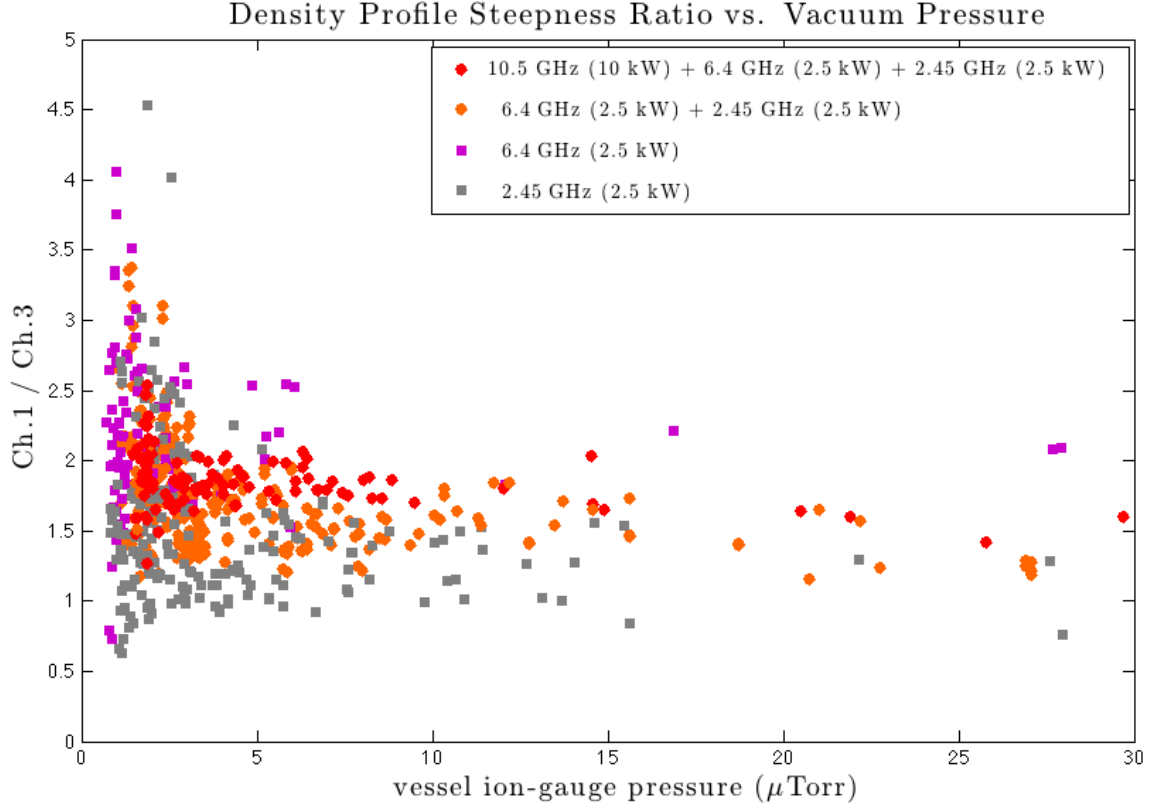
Figure 6-5: A rough measure of density profile information is obtained by computing the "steepness ratio" which is the ratio of line-integrated densities from interferometer channels 1 and 3. The shots and times corresponding to these data are are taken from Tables B.1, B.2, B.3, B.4, B.6 and B.7. At low background pressures—corresponding to under-fueled plasmas—the profiles are generally quite steep. At higher pressures, the steepness ratios remain fairly constant and are roughly the same for plasmas heated by different input ECRH powers and frequencies. Slight differences are nevertheless noticeable; for example, plasmas heated only with 6.4 GHz microwaves are steeper than plasmas heated only with 2.45 GHz microwaves. Remarkably, there is no difference on account of plasma species (D_2 or He). Comparing this figure with Fig. 6-2 supports the idea that the shapes of the plasma density profiles are generally independent from the density magnitudes.

line-integrated density measurements of interferometer Channels-1 and 3. We name this quantity the "steepness ratio" and trends of steepness ratio vs. neutral pressure for different types of plasmas are plotted in Fig. 6-5.

At low background pressures ($< 3 \ \mu$Torr), when the plasmas are under-fueled, the steepness ratios of Fig. 6-5 exhibit the largest amount of scatter, most often on the high-side, indicating that the corresponding density profiles are steep. At higher neutral pressures ($\geq 5 \ \mu$Torr), the steepness ratios remain fairly constant. On the whole, the steepness ratios in the flat portion of Fig. 6-5 are roughly the same for plasmas heated with different ECRH combinations. Even so, plasmas heated only

159

with 6.4 GHz microwaves (purple squares) have slight but noticeably higher steepness ratios than plasmas heated with all three ECRH sources (red circles); these in turn are slightly steeper than plasmas heated with 6.4 GHz and 2.45 GHz together (orange circles); lastly, plasmas heated with 2.45 GHz only (grey squares) have the least steep density profiles.

Figure 6-5 shows that the steepness ratios remain roughly constant with neutral pressure (once the plasmas have sufficient fueling) whereas Fig. 6-2 shows that the density-magnitudes first increase and then decrease at higher background pressures. Also remarkable is the fact that the steepness ratios for a given combination of input ECRH is independent of the species of plasma (D_2 or He). This is in stark contrast to the density-magnitudes as seen in Fig. 6-3. All of these facts support the notion that the shapes of the plasma density profiles are independent from the density magnitudes.
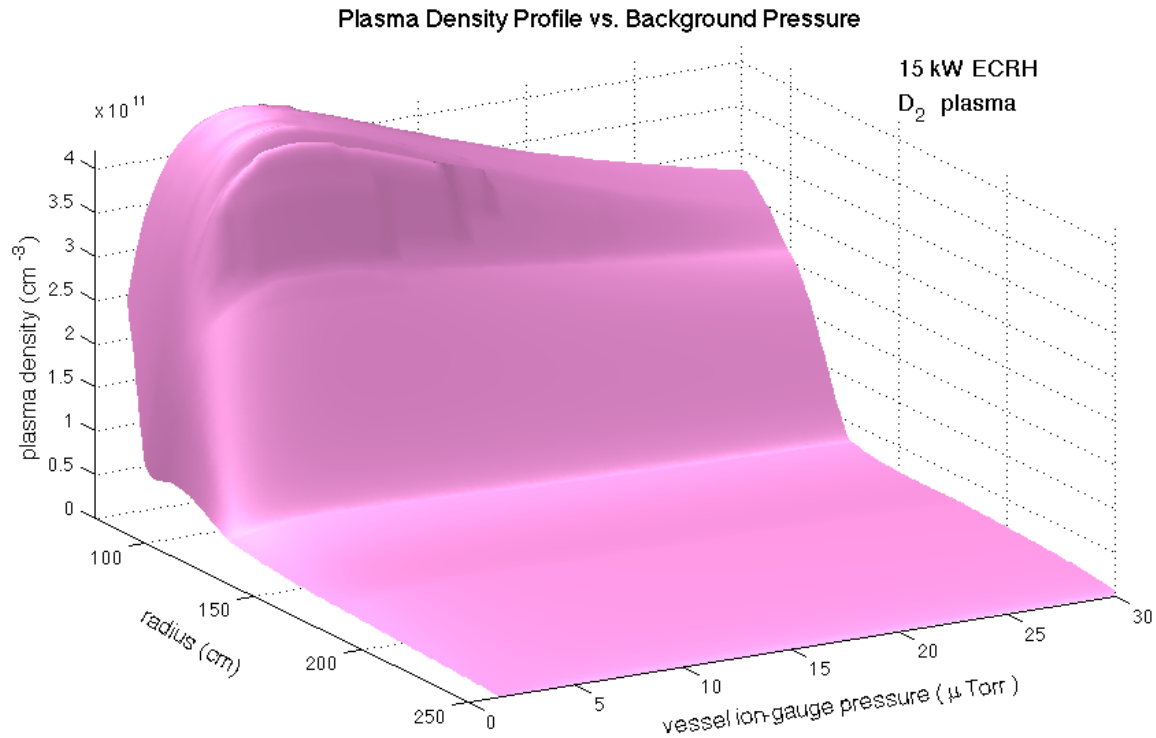
Figure 6-6: Abel-inverted density profiles for D_2 plasmas heated by 15 kW of ECRH (shots and times in Table B.1) plotted vs. background, neutral pressure. In order to produce a smoother image, the Abel inversions for this figure were calculated not from the data itself, but from the data trend-lines discussed and plotted in Fig. 6-1 along with a similar trend line for the probe data

A more detailed but also more elaborate method of looking at the density profile

160

trends entails computing Abel-inverted radial density profiles (§5.2) for the data-sets of Appendix B. For example, Fig. 6-6 shows a 3D plot of the smoothed density profiles for D_2 plasmas heated by all three ECRH sources vs. neutral pressure.

More pressingly, we want to know what relation the plasma density profiles have (or do not have) to the theoretically predicted density profiles described in Chapter 2. In §2.5 it was established that a dipole-confined plasma which is stationary to interchange modes is characterized by the presence of an equal number of particles per flux-tube. In an ideal dipole, where the field drops-off with radius as $1/r^3$, the corresponding flux-tube volume, V, will have the form $V \sim r^4$. This relation will be slightly different in LDX which has a more complicated field-geometry, as previously calculated in §3.4.5. The correct relationship is determined here below.

In a general magnetic geometry, plasma parameters are most appropriately expressed not as functions of position but as functions of the magnetic flux ψ. When assessing the density profiles in LDX it is therefore preferable to fit the profiles to functions of ψ as opposed to functions of r. In order to compare the density profiles in LDX with the predicted $1/V$ profile, it will be necessary to express $1/V$ as a function of ψ as well.

In order to compute ψ for the magnetic geometry of LDX, we employ the identity

$$\psi = \rho A_\phi, \tag{6.5}$$

where ρ is radial position in cylindrical coordinates and A_ϕ is the azimuthal component of the magnetic vector potential [57]. By the procedure outlined in §3.4.5 we can compute numerical functions for both $\mathbf{B}$ and A_ϕ in LDX. Knowing A_ϕ allows us to compute ψ and knowing the field, $\mathbf{B}$, we can integrate around each field line to produce a numerical function for the flux-tube volume, V, defined similarly to Eq.(2.15)

$$V \equiv \oint d\ell/B. \tag{6.6}$$

Possessing numerical functions for both V and ψ in the mid-plane ($z = 0$), it becomes possible to express $1/V$ as a function of ψ. The result of a least-squares fit

Fitting the Inverse Flux-Tube Volume (1/V) to a Function of Ψ

$$1/V \propto \Psi^{4.45}$$

$$V \equiv \oint d\ell/B$$

inverse flux-tube volume

flux-function fit

radius (cm)
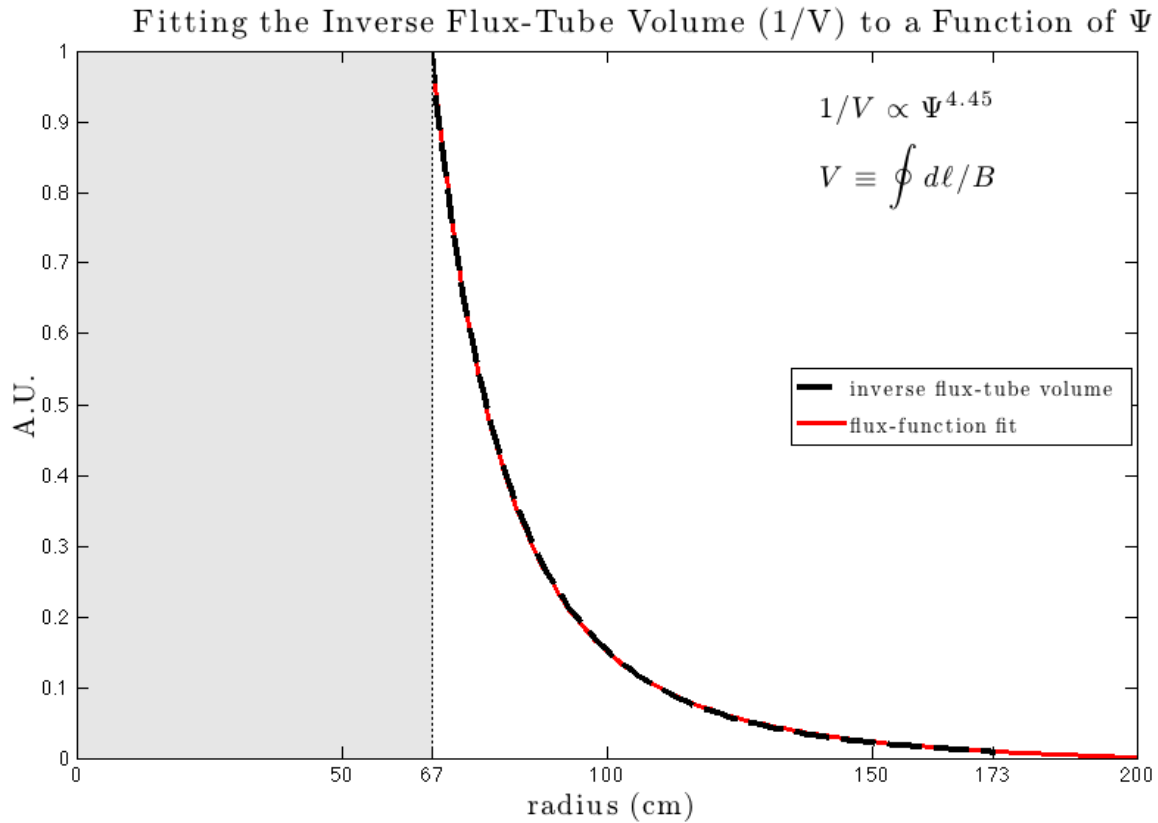
Figure 6-7: Instead of expressing plasma parameters such as the density as functions of radial position, it is preferable to express them in terms of the flux-function ψ. In order to compare the density to the predicted $1/V$ profile, where V is the volume of a flux-tube, it is necessary to express $1/V$ as a function of ψ as well. Whereas in an ideal dipole, $1/V \propto \psi^4$, in the more complicated magnetic geometry of LDX, we see that the best fit is $1/V \sim \psi^{4.45}$. The flux-tube volume is only defined for closed field-lines and therefore $1/V$ (dashed, black line) is only plotted from $r = 67$ cm to $r = 173$ cm. The flux-function ψ (solid, red line) by contrast extends outwards to arbitrary distances.

is shown in Fig. 6-7. Whereas in an ideal dipole $1/V \propto \psi^4$, in the magnetic geometry of LDX,

$$1/V \sim \psi^{4.45}. \tag{6.7}$$

Accordingly, a density profile n that is stationary to interchange modes and characterized by an equal number of particles per flux-tube will, if expressed in terms of the flux-function ψ, have the form

$$n_{\text{stationary}}(\psi) \sim \psi^{4.45}. \tag{6.8}$$

To each density profile, $n(r)$, we can associate a number called the "steepness exponent" which is the exponent, α, of the flux-function ψ producing the best-fit according to

$$n(r) = A_0 \psi(r)^\alpha + n_\infty \tag{6.9}$$

Here n_∞ is simply a constant density that corresponds to a density pedestal at the edge of the vacuum chamber. Density profiles that have steepness exponents greater than 4.45 are steeper than the stationary profile and profiles that have steepness exponents less than 4.45 are broader than the stationary profile.

There are two methods of finding the best-fit steepness exponent for a set of measured, line-integrated density data. The first method is to perform a search is parameter space for the profile $n(r)$ given by Eq.(6.9) whose *line-integrals* most closely match the measured data. Figure 6-8 shows an example of this method of fit for shot 80516021 (the record density shot) at $t = 3$ seconds, when the plasma was heated by two of the three ECRH sources. The points graphed are the data and flux-function reconstruction of the *line-integrated* density. For this particular example, the best-fit steepness exponent was 3.4, indicating a fairly broad density profile.

The second method of associating a steepness exponent to the data is to compute the Abel-inverted radial density profile $n(r)$ and then fit the flux-function ψ directly according to Eq.(6.9). Although this method has the disadvantage that it relies upon the Abel-inverted density profile (which has more uncertainty than the data on which
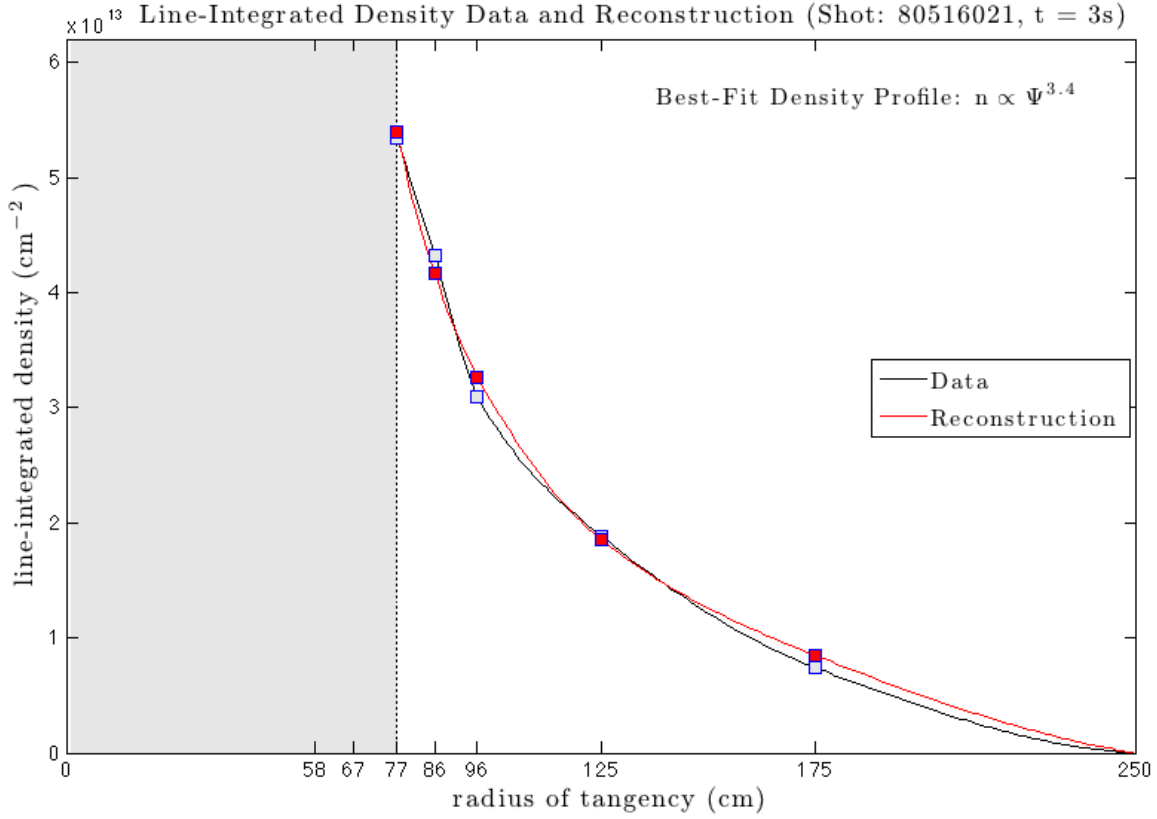
Figure 6-8: The most direct way to fit a flux-function of the form given by Eq.(6.9) to the data is by comparing the *line-integrals* of the function to the measured data. Shown here is result of this process for the record-high density shot (80516021) at an instant in which the plasma is heated by only 5 kW of ECRH. The data is plotted as gray squares connected by a black curve. The best-fit reconstruction is plotted as red squares connected by a red curve. The fit is determined by a least-squares comparison to the four interferometer measurements but not the probe measurement. No information is available for positions inside of $r = 77$ cm and this area is shaded gray. The locations on the abscissa correspond to the outermost location of the F-Coil (58 cm), the first closed field-line (67 cm), the locations of the four interferometer channels (77-125 cm), the location of the probe (175 cm), and the edge of the vacuum vessel (250 cm). The best-fit steepness exponent for this profile is 3.4 indicating a somewhat broader profile than the stationary density profile which is characterized by a steepness exponent of 4.45. A Comparison with an alternate method of computing the steepness exponent suggests that the this quantity has an uncertainty of ± 0.2.

it is based), the chief advantage is that it is computationally much faster. Because the two methods generally produce the same steepness exponents to the first decimal place we employ this second method for the sake of expediency. The discrepancy of the two methods provides an indication of the uncertainty in the steepness exponent which we set at +/- 0.2.

Associating a steepness exponent to the data affords the best means of viewing trends in the radial density profiles. A scan of steepness exponents vs. neutral, background pressure is presented in Fig. 6-9. As was the case with the more simplistic steepness ratio (Fig. 6-5) there is no significant difference between D_2 and He plasmas and here both sets of data have been combined together. Another similarity is that at very low background pressures (< 3 μTorr), the density profiles tend to be quite steep, leveling-off at around 5 μTorr and staying reasonably constant at higher pressures. The steepness exponents of Fig. 6-9 do however show a slight but noticeable decrease with increasing pressure. The profile differences between plasmas heated with different input ECRH combinations—somewhat evident in Fig. 6-5—is more clear in Fig. 6-9. Whereas plasmas heated with all three sources of ECRH have steepness exponents above 4 (close to the stationary value of 4.5), plasmas heated with just the two, lower-frequency ECRH sources have steepness exponents closer to 3.5. The smooth trend-lines in Fig. 6-9 were made by computing the steepness exponents for the trend-lines previously calculated for the scans of line-integrated density vs. vacuum pressure (see, for instance, Fig. 6-1 and Fig. 6-6).

The implication of Fig. 6-9 is that the density profiles gradients are affected by the input ECRH but not by species and, for the most part, not by background pressure (at least once the plasmas have sufficient fueling). On the other hand, Fig. 6-2 and Fig. 6-3 show that the magnitudes of the profiles are determined by all of these parameters (ERCH, species and neutral pressure). Evidently, the density profile shapes are generally independent of the profile magnitudes.

For a given set of input parameters, therefore, we can identify a "maximum" density profile. The "maximum" density profile is that profile which, for a specified ERCH combination and plasma species, has the maximum density. Four such profiles
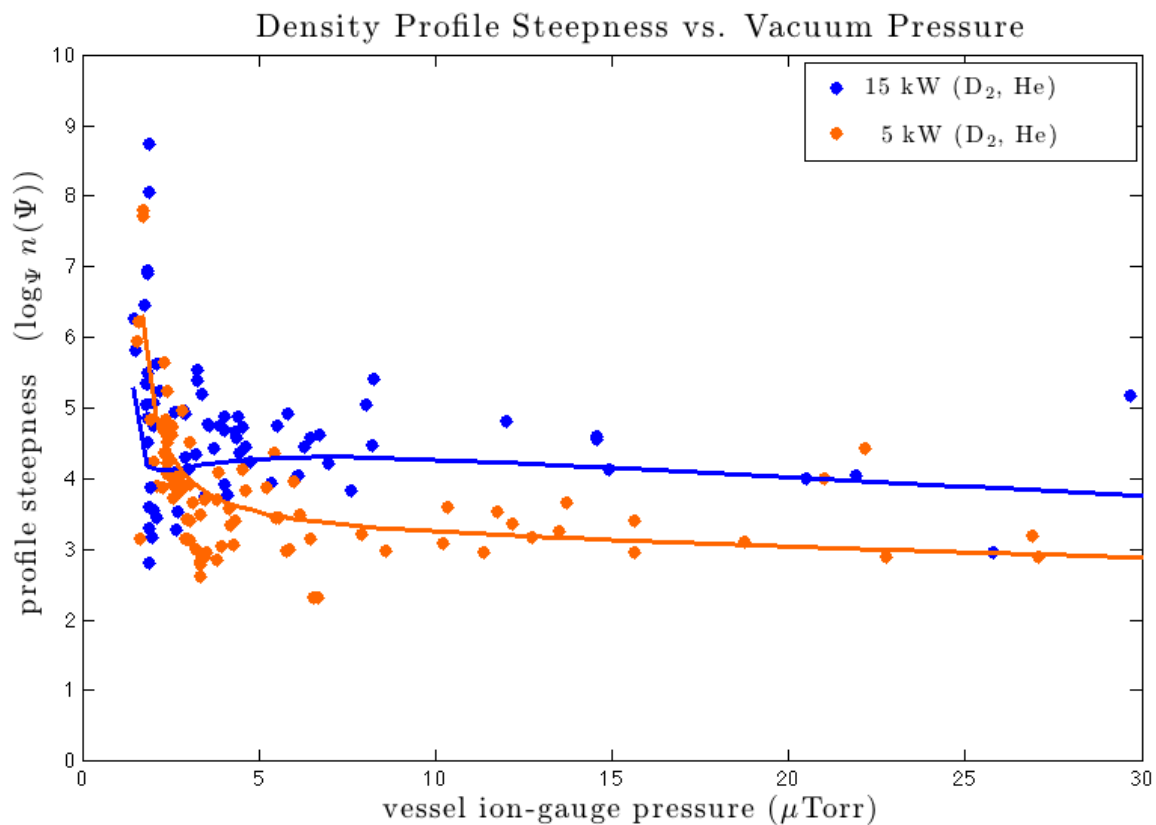
Figure 6-9: Best-fit steepness exponents are found for plasmas with different input ECRH combinations and graphed according to increasing neutral pressure. The data correspond to the shots and times of Tables B.1, B.2, B.6 and B.7. Unlike with the magnitudes of the densities, the density profiles show no dependence on the species of plasma (D_2 or He) and so here these data sets are combined. As in Fig. 6-5, under-fueled plasmas are seen to have especially steep profiles. The steepness exponents level-off after around 5 μTorr and decrease only subtly with increasing background pressure. Plasmas heated with all three sources of ECRH (blue dots) have steepness exponents slightly higher than 4 (close to the stationary value of 4.45) whereas plasmas heated by only the two lower-frequency sources have steepness exponents closer to 3.5. The trend-lines are made by fitting a flux-function not to the Abel-inversions of the data, but to the Abel-inversions of the data's trend-lines as, for example, shown previously in Fig. 6-1.
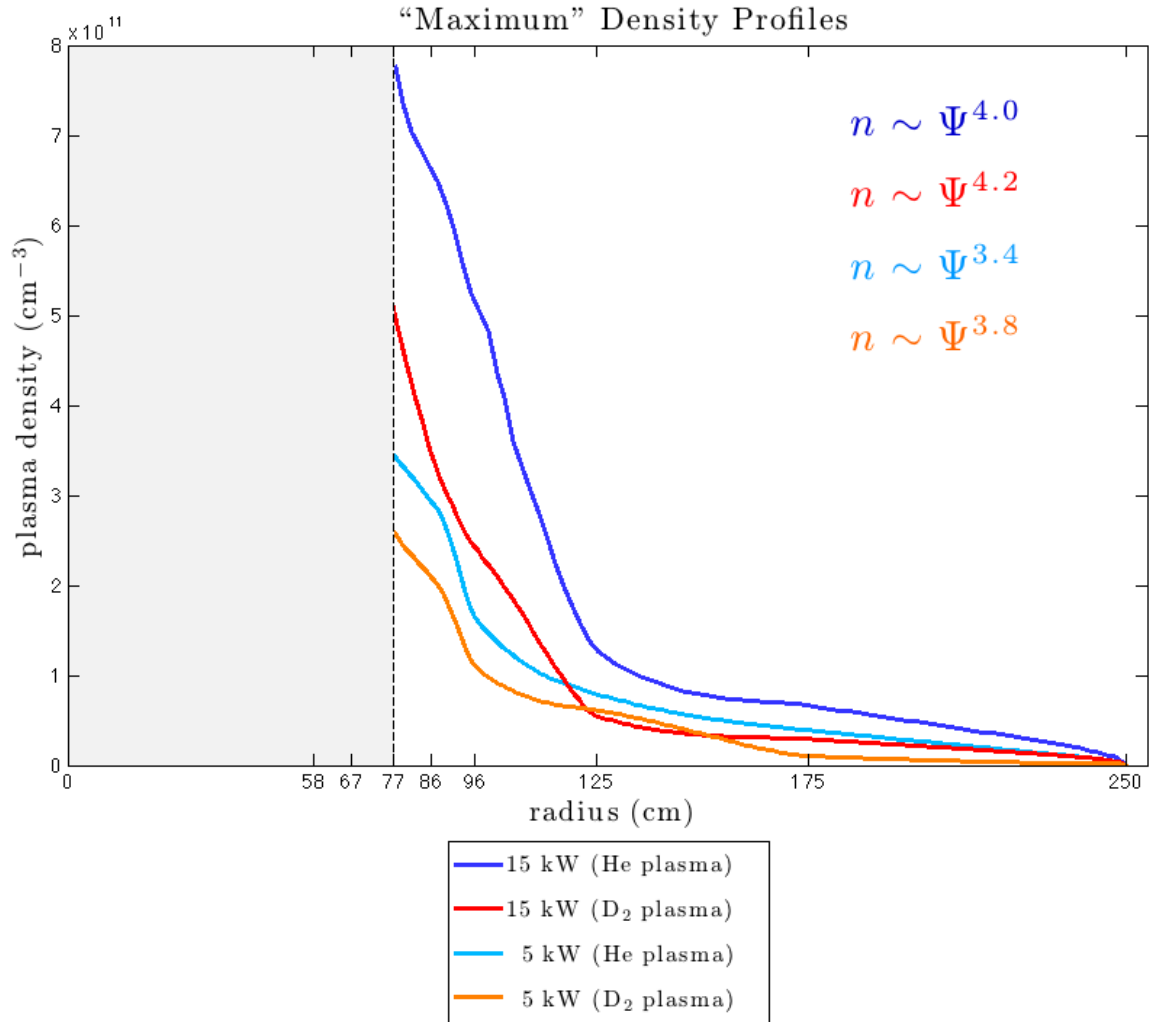
Figure 6-10: The implication of Fig. 6-5 and Fig. 6-9 is that the density profile gradients are, to a large extent, independent of both species and background pressure. Since the profile magnitudes are dependent on these parameters, it is useful to plot the "maximum" density profiles that can be obtained for a given set of input conditions. In the upper-right portion of the figure, the steepness exponents for each of the four "maximum" profiles are listed. The 5 kW, D_2 profile has a steepness exponent fairly close to the predicted value of 4.45. The parameters corresponding to these four profiles are presented in Table 6.1.

are displayed in Fig. 6-10 and their corresponding input parameters listed in Table 6.1. Under present experimental conditions, the profiles in Fig. 6-10 corresponding to D_2 plasmas represent the optimal confinement that can be achieved for a given ECRH combination. The 15 kW case approaches, quite closely, the theoretically predicted density profile characterized by a steepness exponent of 4.45. For the He plasmas, the profiles shown here are maximum only in a provisional sense since the implication of Fig. 6-3 is that even larger profiles can be obtained with more neutral fueling.

Table 6.1: "Maximum" Density Profile Parameters

Shot	Time (sec.)	Species	Pressure (μTorr)	ECRH: 10.5 GHz (10 kW)	6.4 GHz (2.5 kW)	2.45 GHz (2.5 kW)	Steepness Exponent ($\pm$ 0.2)
80516021	6	He	21.9	X	X	X	4.0
80515029	6	D_2	7.0	X	X	X	4.2
80516021	3	He	15.6	—	X	X	3.4
80321017	6	D_2	4.6	—	X	X	3.8

6.5 Energy and Particle Balance: First Clues

In order to evaluate the performance LDX and to assess whether a similar dipole-confinement scheme might one day offer a route to fusion energy, it is necessary to understand the energy and particle balance within the device. At present, LDX simply does not have the diagnostic capabilities (no measurements of the temperature in the core and no measurements of the pressure of the bulk density) to answer these questions in any detail. However, the data from the interferometer presented here can offer some initial clues and suggest directions for future research.

We can take as a starting point a qualitative formula [72] for the particle balance of the bulk electron density, n_b, in terms of the density of neutral particles, n_0, and the density of the smaller population of hot electrons, n_h:

$$\frac{dn_b}{dt} = n_0(n_b\langle\sigma v\rangle_b + n_h\langle\sigma v\rangle_h) - \frac{n_b}{\tau_{\text{ECRH}}} - \frac{n_b}{\tau_{\chi b}}. \qquad (6.10)$$

The meaning of Eq.(6.10) is simply that the change in density of the bulk electrons is equal to the ionization rate of the neutral particles minus the rate at which the background electrons are accelerated into the "hot" population by ECRH (with characteristic confinement time τ_{ECRH}), minus the rate of cross-field transport (characteristic confinement time $\tau_{\chi b}$).

Likewise, an equivalent formula for the particle balance of the hot electron density, n_h, can be written as

$$\frac{dn_h}{dt} = \frac{n_b}{\tau_{\text{ECRH}}} - \frac{n_h}{\tau_h}. \qquad (6.11)$$

The interpretation of Eq.(6.11) is that the change in density of the hot electrons is established by the balance between a source term (the number of bulk electrons promoted to hot electrons by ECRH) and a loss term, characterized by a confinement time τ_h. The hot electron confinement time, τ_h, is determined by scattering from both neutrals and the background electrons, both of which can lead to either cross-field transport or slowing-down. The relative contributions to the hot-electron confinement time, τ_h, can be estimated by computing collision frequencies for neutral-hot and bulk-hot scattering. In both cases, the collision frequency ν will have the general form

$$\nu = n\langle \sigma v_h \rangle \tag{6.12}$$

where n is the density of the relevant target population, σ is the relevant cross-section and v_h is the hot electron velocity.

For neutral-hot collisions, the required cross-section is the *total* electron-impact cross-section, σ_T. Measurements of this quantity for electron collisions with neutral H_2 gas can be found in the literature for energies up to 750 eV [97]; at higher energies, we use simply the ionization cross-section [92], [93], bearing in mind that this will be *smaller* than the total cross-section by a factor of order unity. For bulk-hot collisions, the cross-section will be Coulomb-like ($\sigma \propto v^{-3}$), and we employ a high-velocity approximation found in reference [98].

Tables 6.2 and 6.3 show the collision frequencies for neutral-hot and bulk-hot collisions for a variety of possible parameters. The target densities (neutral particles in Tables 6.2 and bulk electrons in Tables 6.3) have been made roughly comparable insofar as

$$1 \ \mu\text{Torr} \approx 3.3 \times 10^{10} \ \text{particles per cm}^3 \tag{6.13}$$

As is evident from the tables, the neutral-hot collision frequency is always larger than bulk-hot collision frequency. The difference is about a factor of 100 for "warm" electrons (1 keV) and as great as 10^4 for electrons at 100 keV.

The simple, two-population model of Eq.(6.10) and Eq.(6.11) captures some of the important features exhibited by the data presented in this chapter. In particular at

Table 6.2: Hot-Electron/Neutral Collision Frequencies (Hz)

Pressure	Hot Electron Temperature		
(μTorr)	1 keV	10 keV	100 keV
0.01	21	16	2.2
0.1	2.1×10^2	1.6×10^2	22
1	2.1×10^3	1.6×10^3	2.2×10^2
10	2.1×10^4	1.6×10^4	2.1×10^3

Table 6.3: Hot-Electron/Bulk-Electron Collision Frequencies (Hz)

Bulk Density	Hot Electron Temperature		
($\times 10^{10}$ cm^{-3})	1 keV	10 keV	100 keV
0.01	3.7×10^{-1}	1.2×10^{-2}	3.7×10^{-4}
0.1	3.7	1.2×10^{-1}	3.7×10^{-3}
1	37	1.2	3.7×10^{-2}
10	3.7×10^2	12	3.7×10^{-1}

low neutral pressures, Eq.(6.10) indicates that the production of bulk electrons from ionization can be in competition with the promotion of those electrons to the hot population resulting in a relatively large hot-electron fraction, n_h/n_b. This behavior was noted previously in earlier LDX experiments concerned with the production and stabilization of the hot electron interchange instability [72].

At high neutral pressures, the neutral-hot collision frequency can be so large that for most LDX shots (which indicate the presence of hot electrons) the density of neutrals in the core must be very small. However, increased neutrals at the edge often means increased bulk electrons throughout the plasmas and these extra bulk electrons can reduce the number of hot electrons. This notion is consistent with the measured trend of plasma diamagnetism—which is due mainly to the hot electrons— decreasing rapidly with increasing vacuum pressure as shown in Fig. 6-4.

Regarding the bulk electrons, Eq.(6.10) may provide some justification for the functional form of the density trend-lines proposed in Eq.(6.1). If the neutral pressure is responsible in some way for regulating the velocity of the ionizing electrons then

the bulk density would indeed be expected to have the form of a cross-section graph (where electron energy is plotted on the abscissa). The dramatic difference in densities between He and D_2 plasmas (Fig. 6-3) is surprising, though, because the ionization cross-section for helium is *smaller* than that for deuterium by about a factor of 2 all energies [92], [93]. Evidently, it is the cross-field loss term of Eq.(6.10) which must be responsible for establishing the species-dependent aspects of particle balance. One obvious way in which this might be achieved is if the confinement is determined simply by the outflow of ions out along field lines at the ion sound-speed, c_s:

$$c_s \sim \sqrt{T_e/M_i}. \tag{6.14}$$

Here T_e is the electron temperature and M_i is the ion mass. Helium, being twice as massive as deuterium would, accordingly, have a smaller sound speed and, by this reckoning, a longer confinement time as well.

In LDX, the edge of the plasma generally extends outwards past the last closed field line (as evidenced by probe measurements). In this region, known as the scrape-off layer, the confinement will be determined by the speed at which particles, following their field lines, strike the walls of the vacuum chamber. The edge plasma, therefore, behaves as a low-pressure "plasma-source": more input power increases the scrape-off layer density but not the temperature [99].

Evidence that the edge plasma in LDX does indeed behave as a low-pressure plasma-source comes from the measurements of the southwest-top probe. This probe is located at the magnetic separatrix dividing the regions of closed and open field lines (§5.2.2). Figure 6-11 shows quite convincingly that over all experimental conditions, the edge temperature remains remarkably flat. The edge density, on the other hand, displays a dependence on both the input ERCH power and the plasma species (and, to a lesser extent, the neutral pressure). Note further that the levitated and non-levitated edge densities for plasmas heated with 5 kW are roughly comparable whereas the core densities for these same cases are seen in Fig. 6-3 to be radically different.

171
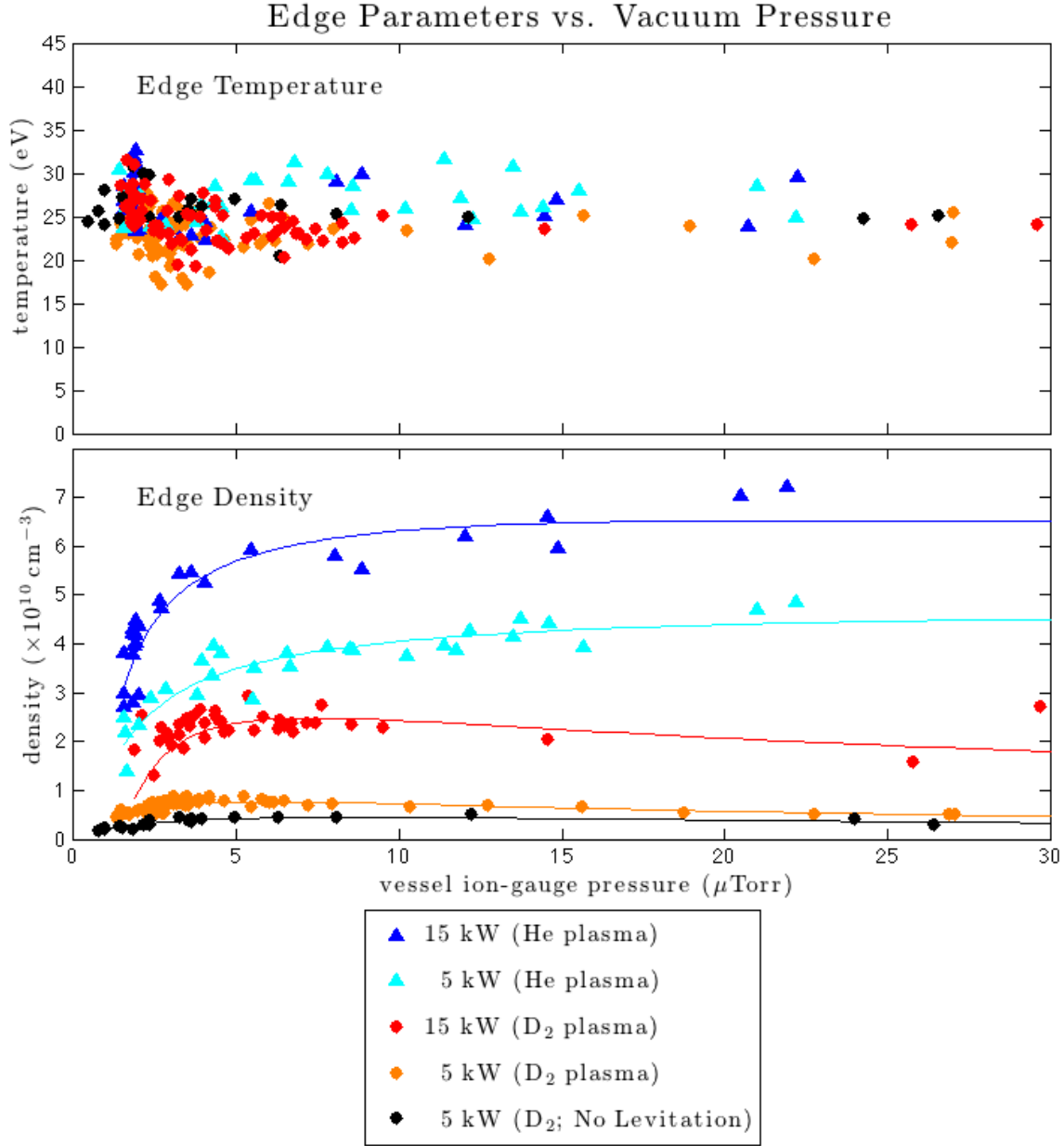
Figure 6-11: Edge measurements made by the southwest-top probe support the hypothesis that the edge portion of the plasma (where the field lines are open) behaves like a low-pressure "plasma-source". The upper graph shows that the edge temperature remains remarkably flat over all experimental conditions and over all background pressures. The lower graph shows that, like the core densities (Fig. 6-3), the edge density is dependent on input ECRH and plasma species (and, to a lesser extent, neutral pressure). Considered as a plasma source, the edge density is determined by a balance between the number of particles created, which is proportional to the input ECRH power, and the losses which are determined by the (species-dependent) acoustic outflow of ions along field lines into the vacuum chamber wall. The shots and times corresponding to the data shown here are listed in Tables B.1, B.2, B.5, B.6 and B.7.

The notion that LDX core densities with He are higher than core densities with D_2 (Fig. 6-3) because the He losses are lower in the scrape-off layer suggests that LDX plasmas can be modeled as a low-pressure plasma-source at the edge attached to an amplifier in the core. Recall that the fundamental notion of dipole confinement [Eq.(3.2)] is that the condition $\delta(pV^\gamma) = 0$ implies that

$$p_{peak} = p_{edge} \left(V_{edge}/V_{peak} \right)^\gamma .$$

That is, the peak pressure (and density) in the core of LDX, where the field lines are closed, will be determined by the pressures and densities achievable at the edge, where the field lines are open. In this way, the dipole portion of LDX behaves as a large "amplifier" for the low-pressure plasma-source at the edge.

By extension, the source/amplifier hypothesis implies that the peak pressures in the plasma core can be optimized simply by optimizing the pressure in the scrape-off layer. While this would be desirable, there is unfortunately no clear evidence that the core densities can be determined from a simple "amplification" of the edge-densities. One complicating factor may arise from the core plasma not always beginning at the magnetic separatrix. For instance, in Fig. 6-10 the location of the "knee" in the density profile is clearly seen to move outwards with increasing ECRH power. Perhaps with increased heating power, such geometrical effects may be eliminated and the source/amplifier hypothesis might be in better accord with the measured data.

Chapter 7

Observations of Plasma Self-Organization

7.1 Introduction

In Chapter 6 we presented measurements showing (amongst other things) that the density profiles of plasmas in LDX exhibited much less of a dependence on the experimental conditions than did the density magnitudes. That is, LDX plasmas evidence a certain degree of "profile consistency". Importantly, LDX density profiles are often observed to approximate the form which is predicted to be "stationary" to MHD interchange modes, especially for plasmas heated with all three ECRH sources and provided with a sufficient level of fueling (see Fig. 6-9). Stationary density profiles, which were introduced in Chapter 2, are characterized by the presence of an equal number of particles per flux-tube. The fact that LDX plasmas exhibit stationary profiles at all is remarkable since it is unlikely that such an arrangement would result from a simple balance of sources (localized at the ECRH resonance zones) and sinks—some additional processes must therefore be at work.

In this chapter we present some of our most exciting observations—observations which underscore that some process is indeed working to drive LDX plasmas closer to the the stationary, equal particle per flux-tube density profile. For a small number of shots (listed in Table 7.1), the plasma is observed to "spontaneously" transition

to a density profile that more closely approximates the stationary profile. These transitions are referred to as spontaneous insofar as they occur without any changes in the externally-controlled experimental parameters that are known to affect the plasma density (e.g fueling or ECRH).

Table 7.1: Shots Exhibiting a Spontaneous Density Transition

shot	*times* (sec.)
80322013	4.63, 8.66, 12.38
80322014	9.71, 12.59
80322015	10.39
80322027	9.82
80322030	9.75
80514024	4.63, 9.08, 12.43
80515035	11.81

The remainder of this chapter proceeds as follows: A description of the special circumstances and characteristic features of a spontaneous density transition is provided in §7.2. Because the interferometer is, at present, the main diagnostic for observing the core plasma, only partial information about this phenomenon is available. Consequently, it is not possible to determine definitively what triggers these density transitions or what sustains them. Nevertheless, we do possess enough clues to engage in some fruitful speculation. In §7.3 we examine what role ECRH power deposition may play in the triggering of a density transition. In §7.4 we link the observations of spontaneous density transitions to the prediction that self-organized convection will, through large-scale flux-tube mixing, maintain the plasma in pressure and density profiles that are stationary to MHD interchange modes (cf. §2.5.3). In particular, we explore the hypothesis that the profiles attained after a density transition are sustained by a convective-cell drifting azimuthally around the vacuum chamber.
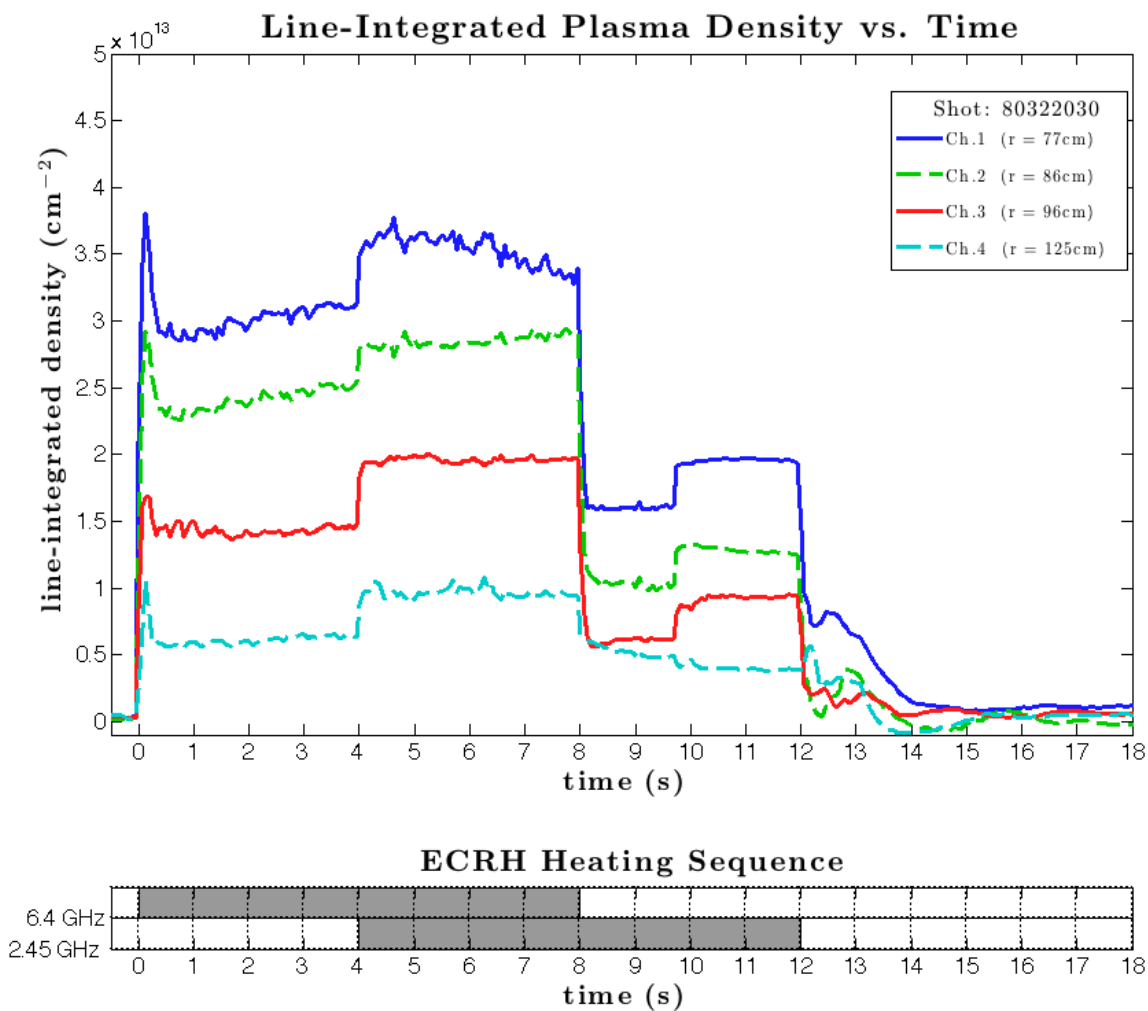
Figure 7-1: Line-integrated density measurements for shot 80322030. For the most part, the magnitude of the density measurements is determined by the input ECRH. However, at 9.75 seconds, the density profile is rearranged without any external impetus.

7.2 Description of the Phenomenon

7.2.1 Characteristic Features of a Density Transition

Rearrangement of the Bulk Density Profile

An example of data from a shot with a density transition is shown in Fig. 7-1. The measured line-integrated densities along the four interferometer chords show that for this shot (80322030) density changes in time are largely determined by the sequence of ECRH. This behavior is similar to the other plasma shots we have plotted (Figs. 4-10 and 4-12). However, at around 9.75 seconds, something remarkable happens in shot 80322030: the density is rearranged (over a period of about 20 milliseconds) into an entirely new profile without any impetus from a change in the ECRH or any other externally controlled parameter (e.g., the pressure of neutral particles).

Characteristic ECRH and Neutral Pressure

The appearance of a density transition occurs rarely and only in conjunction with a specific sequence of ECRH: A period of heating at 2.45 GHz only (total power: 2.5 kW) that directly follows a period of heating at both 6.4 GHz and 2.45 GHz (total power: 5 kW)—see, for example, Fig. 7-1. From our discussions of Chapter 6, it is clear that the neutral pressure cannot be overlooked when discussing the density of LDX plasmas, however the relation here is not as strong as with the ECRH. The density transitions listed in Table 7.1 are found to occur over a range of neutral pressures—generally within 3-8 μTorr—and it seems unlikely that neutral pressure alone is the trigger.

Characteristic Mode Structure

A closer look at the measurements from Channel-1 (Fig. 7-2) show that the density in the moments directly preceding the transition at 9.75 seconds is marked by large-amplitude, inverse-sawtooth oscillations with frequencies around 25-30 Hz. These inverse sawteeth precede all of the observed density transitions and appear to affect

Ch.1 Line-Integrated Density vs. Time (Shot: 80322030)
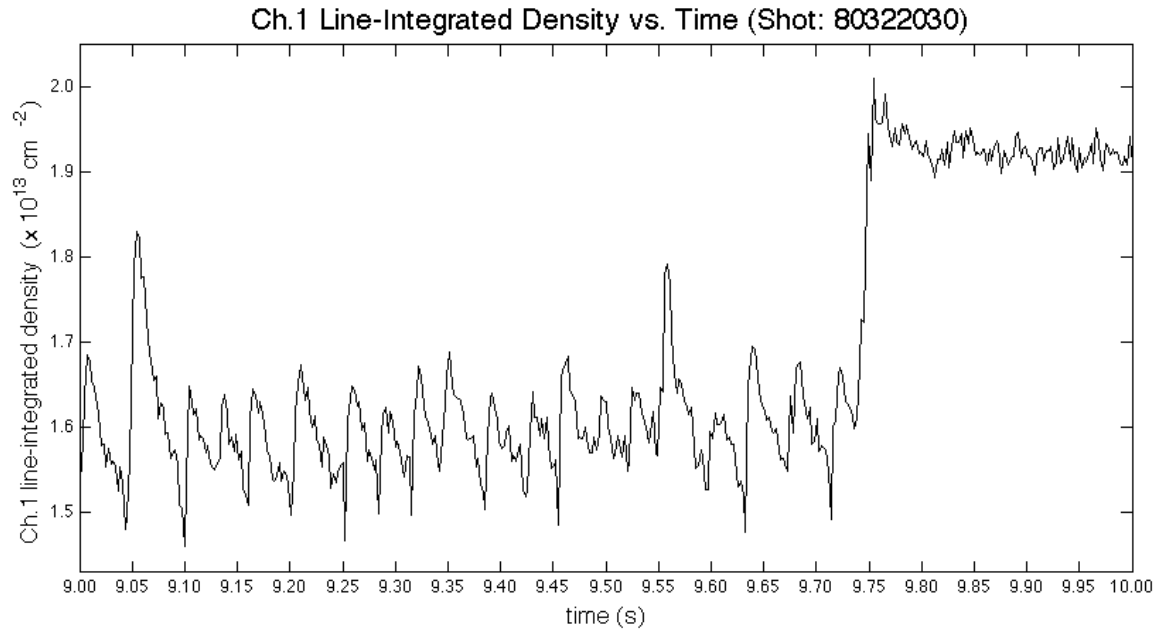
Figure 7-2: A closer look at the line-integrated density for just Channel-1 of the interferometer in the period around the density transition at 9.75 seconds for shot 80322030. In the period directly preceding the transition, the density measurements are marked by large-amplitude inverse-sawtooth oscillations at frequencies of approximately 25 Hz. These oscillations disappear, and the density becomes more quiescent, in the period following the density transition.

the inner chords (Ch.1, Ch.2) most strongly. After the density transition the inverse-sawtooth oscillations quiet down.

A second, characteristic mode associated with density transitions is seen on a spectrogram of the Ch.1 data from shot 80322030 (Fig. 7-3). In conjunction with the density transition at 9.75 seconds, the spectrogram reveals the appearance of a strong, quasi-coherent mode at approximately 500 Hz. This 500 Hz mode is associated with the higher-density interval of the transition and is always seen most strongly on interferometer Channel-1 indicating that the mode is localized in the plasma core.

Relation to Other Diagnostics

In order to speculate about the nature and cause of these plasma density transitions, it is helpful to have as many clues as possible. Unfortunately, the evidence indicates that these events occur in the core of the plasma and therefore are not recorded by most of the diagnostics on LDX. Many of the diagnostics which might be expected to register these events, such as the visible cameras or the V-band radiometer, show

179
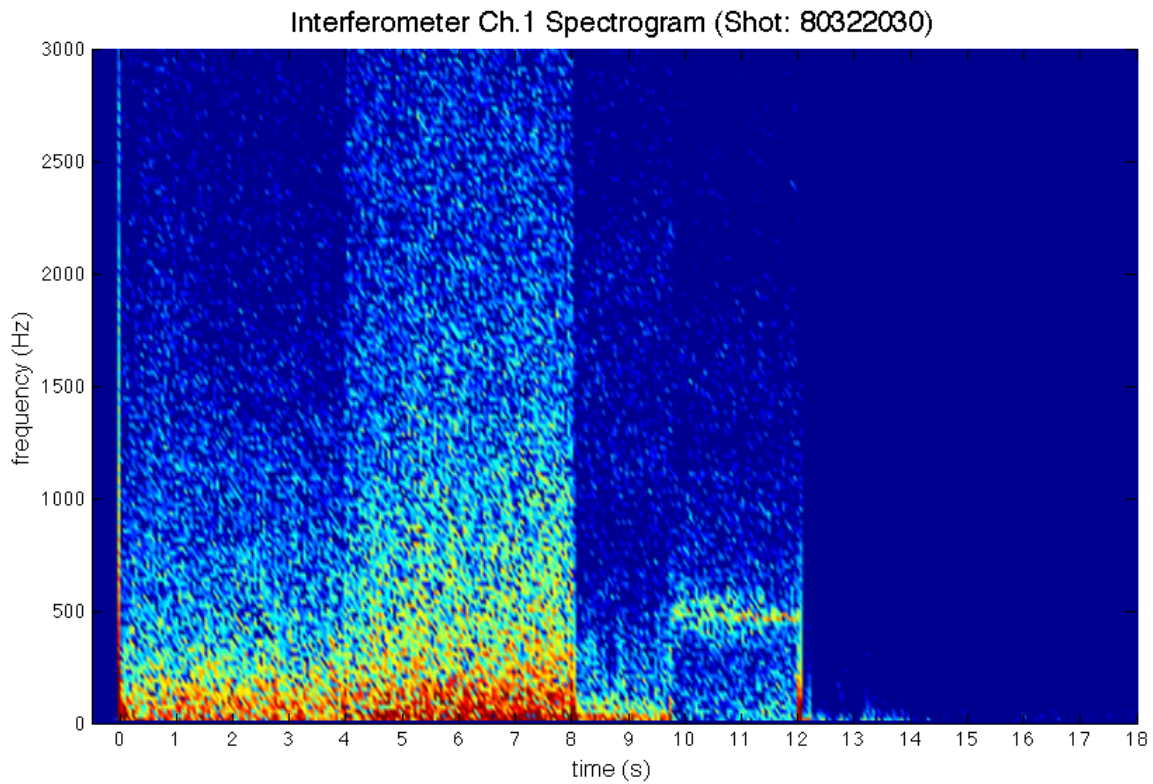
Figure 7-3: Spectrogram of line-integrated density from interferometer Channel-1, shot 80322030. The plasma exhibits a broad-band frequency structure for most of the shot, with the intensity increasing during the period of 5 kW of input ECRH. At 9.75 seconds, in conjunction with the density profile transition, a strong, quasi-coherent mode appears at approximately 500 Hz.

NaI X-Ray Detector Intensity vs. Time
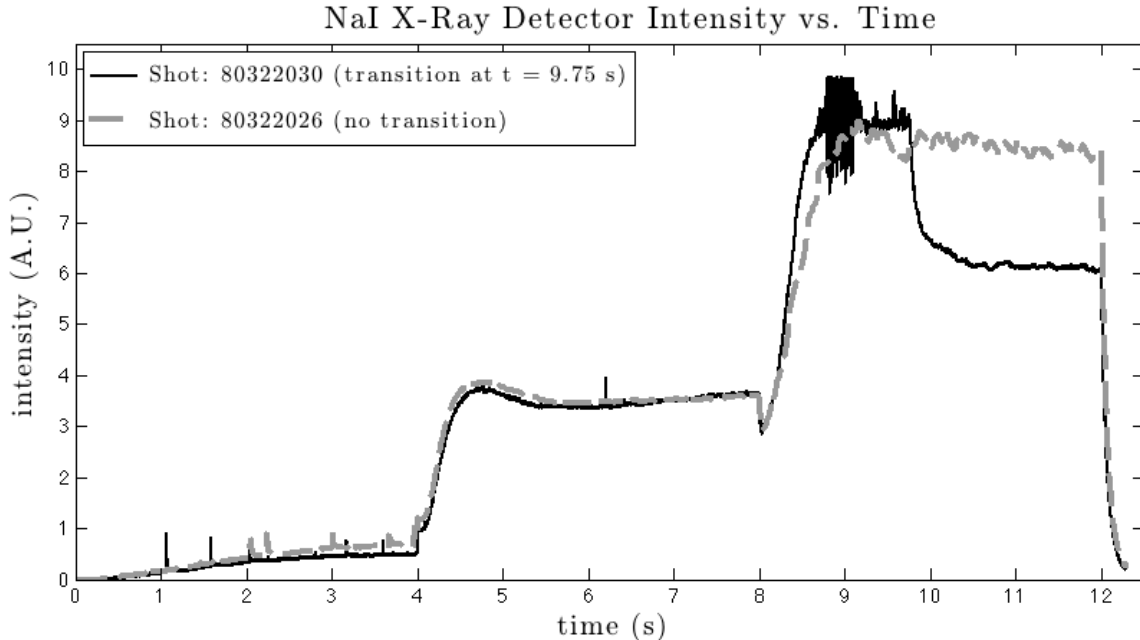
Figure 7-4: The X-rays measured by the NaI detector are primarily target X-rays from hot electrons striking the F-Coil. One of the two ECRH sources (6.4 GHz) is terminated at 8 seconds leading to a period of enhanced X-ray emission. However, in shot 80322030, a density transition at 9.75 seconds marks the beginning of a period of lower X-ray emissions when compared to a similar shot (80322036) which lacks a density transition.

no response at all. Flux-loop 5—used as a proxy for the plasma stored energy in §6.3—occasionally shows a very slight tick subsequent to a density transition, but not consistently nor in consistent up/down direction. A full reconstruction of the hot-electron pressure from all of the magnetics signals does suggest that the stored energy after a density transition is slightly higher (by about 10%) than before the transition. It is hoped that a new photodiode array and fast-camera (both expected for a campaign of experiments in Fall of '08) will be able to observe the 500 Hz mode seen by the interferometer.

Intriguingly, the only diagnostic (in addition to the interferometer) which shows a definitive correlation with the density transitions is the NaI X-ray detector. The X-ray detector, due to its orientation on the LDX vacuum chamber, measures primarily the X-rays emitted by hot electrons striking the F-Coil. Figure 7-4 shows the X-rays measured for two similar shots, one with a density transition and one without. The termination of the 6.4 GHz ECRH at 8 seconds begins a period of enhanced

transport into the F-Coil leading to increased emission of target X-rays as seen in Fig. 7-4. However, in shot 80322030, the density transition at 9.75 seconds marks the beginning of a period of much lower X-ray emission. In contrast, the X-ray emissions remain high in shot 80322026 in which no density transition occurs and where the density remains in a profile similar to the pre-transition profile of shot 80322030 (but without any major sawteeth oscillations).

7.2.2   The Creation of an Unstable Profile

Although it is visually more complicated, perhaps the most compelling display of density profile rearrangement occurred in shot 80322013. Fig. 7-5 shows the line-integrated density data for this shot along with a chart of the ECRH heating sequence. In this shot, the input ECRH was altered every 2 seconds, modulating between periods when both the 2.45 GHz and 6.4 GHz sources were on (total power: 5 kW) and period when only the 2.45 GHz source was on (total power: 2.5 kW). A spectrogram of this shot is shown in Fig. 7-6. Shot 80322013 is especially dramatic because density profile transitions are induced on three separate occasions in the same shot.

As is evidenced by Figs. 7-5 and 7-6, the density profile after each transition is nearly identical to the profile which initially obtains in the period of 0-2 seconds. LDX density transitions are, therefore, best thought of not as the transition *to* a new, high-density profile, but rather the transition *from* an unstable, lower-density profile. Although the higher-density profile (marked, especially, by the presence of the 500 Hz mode) is not always created with 2.45 GHz heating at the beginning of a shot, its presence at the beginning of shot 80322013 establishes that this profile is not solely produced in conjunction with a density transition. Evidently, the abrupt change in microwave heating caused by the termination of the 6.4 GHz source is capable of driving the plasma into an alternate, lower-density profile. Sometimes, as in shot 80322026 (see Fig. 7-4), the profile remains in this lower-density profile; at other times, as in the shots of Table 7.1, the plasma is rearranged into a higher-density profile.
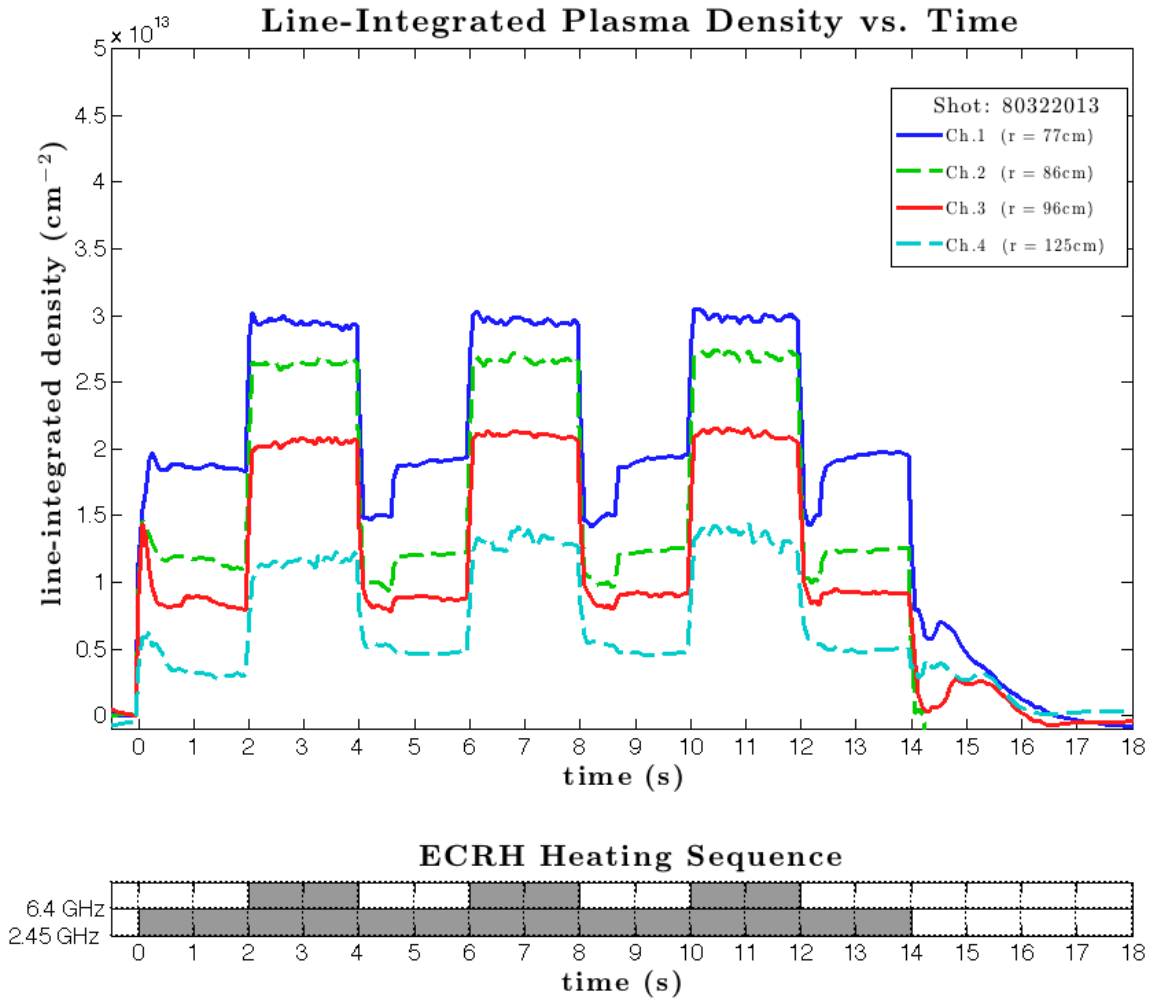
Figure 7-5: Line-integrated density measurements for shot 80322013. Spontaneous density transitions are observed at 3 separate instances. Moreover, this shot makes clear that the density transitions are restoring the plasma to the profile that obtained initially, in the period 0-2 seconds.
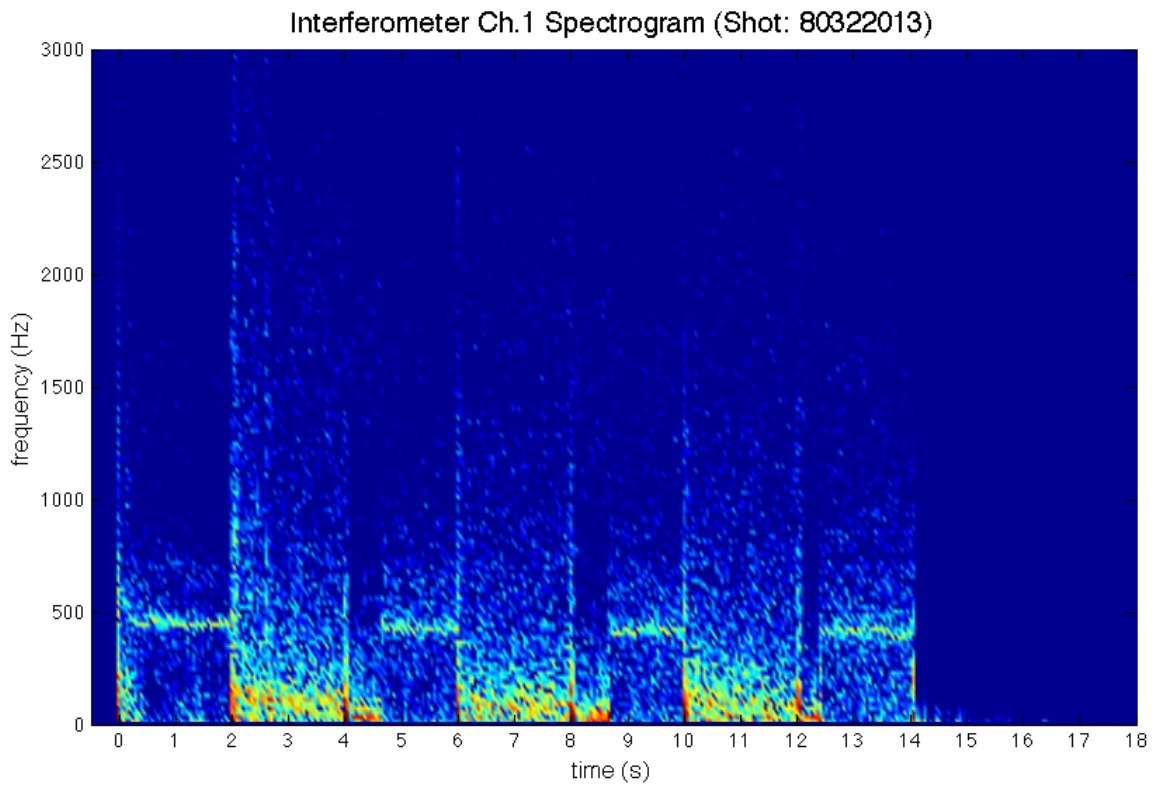
Figure 7-6: Spectrogram of line-integrated density from interferometer Channel-1, shot 80322030. The 500 Hz mode is seen not only in conjunction with each of the 3 density profile transitions but also in the initial 2-second period when the plasma was heated with only the 2.45 GHz source.

7.3 Microwave Heating Considerations

In §7.2, above, we presented the main empirical features which characterize spontaneous density transitions. In this section and the next we speculate on what may trigger these profile transitions and what may maintain them. Because ECRH has such a strong effect on the density profile (especially evident when the sources are turned on and off), its role in triggering a density transition cannot be overlooked. Here we examine the interaction between the heating microwaves and the density profile around the time of a density transition.

As we have noted (§7.2), spontaneous density transitions occur only during periods when the plasma is heated with the 2.45 GHz ECRH source alone. In Chapter 6 we saw that plasmas heated with combinations of 2 or 3 sources of ECRH exhibited clear trends once the relevant parameters (e.g., the neutral pressure) were taken in account. Plasmas heated with only 2.45 GHz exhibit similar trends, but with significantly more variability. In fact, plasmas heated with only 2.45 GHz differ from other types of LDX plasmas in a number of important ways. One fact to keep in mind is that the 2.45 GHz ECRH source is the only source with a fundamental resonance in the equatorial plane (§3.4.6 and see also Fig. 7-8 below) whereas the fundamental resonances of the other ECRH sources intersect the F-Coil. The presence of an equatorial resonance likely leads to a further localization of the power deposition since much of the heating occurs upon a small number of field-lines.

The most unique feature of plasmas heated with only 2.45 GHz microwaves is that they are routinely over-dense. That is, 2.45 GHz -heated plasmas attain densities that are higher than their cutoff density, n_c, above which the plasma becomes reflective to that frequency of microwaves thus preventing any subsequent heating. This behavior is not observed in LDX for any other ECRH source or combination of sources. Figure 7-7 shows that in shot 80322030, the density is over-dense both before and after the density transition at 9.75 seconds. Thus, independent of the density-transition phenomenon, 2.45 GHz density profiles exhibit a complicated interrelation between the input heating microwaves and the plasma density.
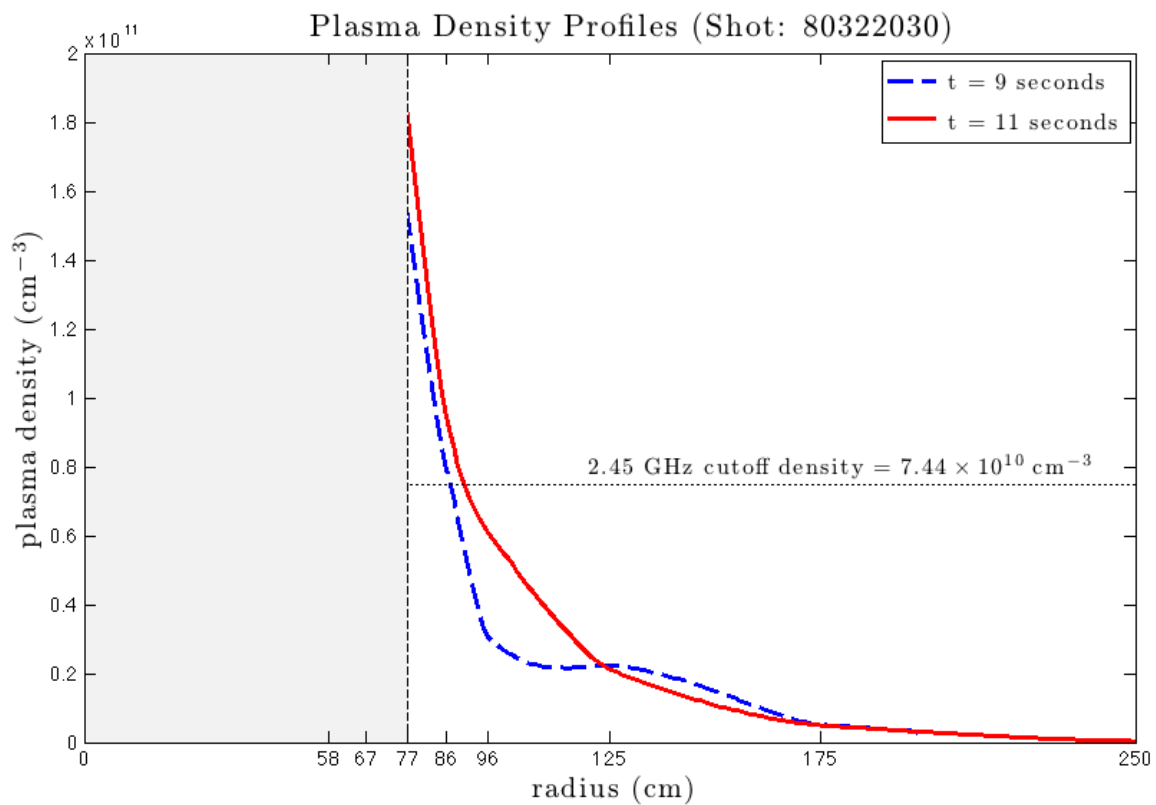
Figure 7-7: Abel-inverted radial density profiles for shot 80322030 before and after the spontaneous density transition (t = 9.75 s). Both profiles are over-dense near the core—a feature unique to plasmas heated with only 2.45 GHz microwaves. For this shot, the density transition affects the plasma primarily at around 100 cm.

186

Measurements of over-dense plasmas are surprising but they place LDX in the good company of other experiments which have recorded similar behavior. Most significantly, over-dense plasmas have been observed in Mini-RT, a levitating dipole experiment at the University of Tokyo. Mini-RT is a smaller, prototype version of the RT-1 experiment (see §2.6 and Table 2.3). Plasmas in Mini-RT are heated with 2.5 kW of microwave power at 2.45 GHz. Probe measurements of the density taken all the way inside the plasma core indicate that when the central, dipole coil is levitated, the plasma density profile exhibits a very steep profile with peak densities near 1.6×10^{11} cm^{-3}—well over twice the 2.45 GHz cutoff density [100].

The Mini-RT team has hypothesized that their over-dense plasmas may be the result of mode-conversion processes which convert the original 2.45 GHz ECRH microwaves into electron Bernstein waves (EBW's). Direct probe measurements supporting this theory were recently reported in reference [101]. Whether such mode conversion occurs in LDX is beyond the scope of this thesis; however, we are excited to report that LDX can corroborate Mini-RT's measurements of over-dense plasmas. These measurements from different dipole facilities underscore the unique and unexpected physics of dipole-confined plasmas.

A second, important case of over-dense plasmas produced by heating at 2.45 GHz was reported in the TORPEX experiment, a small, toroidal device at the École Polytechnique in Lausanne. The authors measure densities well in excess of the 2.45 GHz cutoff density and provide evidence that most of the ionization is due not to the microwaves coupling to the electrons at the cyclotron resonance but rather to coupling at the upper-hybrid resonance [102].

Upper-hybrid waves are electrostatic waves similar to basic Langmuir waves (which resonate at the plasma frequency, ω_p) but with the magnetic field enhancing the restoring force such that the resonant frequency ω_{UH} becomes

$$\omega_{UH} = \sqrt{\omega_p^2 + \omega_{ce}^2}. \qquad (7.1)$$

Here ω_p is the plasma frequency and ω_{ce} is the electron-cyclotron frequency. The
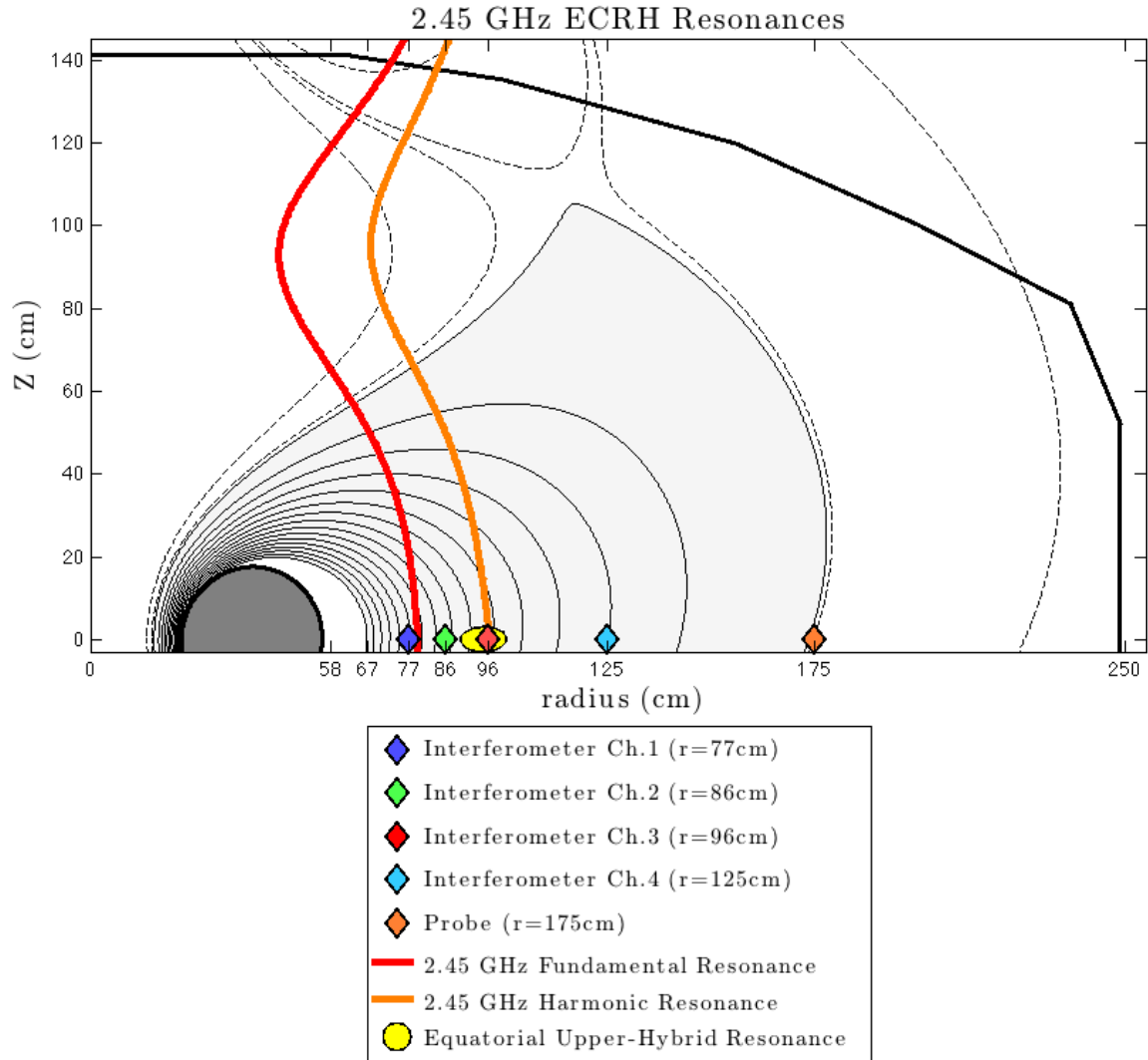
Figure 7-8: Diagram of various resonance locations for 2.45 GHz microwaves in LDX. The outline of the LDX vacuum chamber is indicated by thick, black lines and the F-Coil is represented as a dark, gray circle. The plasma volume—defined by the first and last closed field lines—is shaded light gray. The cyclotron resonances are functions of the magnetic field strength only. The location of the fundamental cyclotron resonance is marked by a thick, red line; the location of the first harmonic cyclotron resonance is marked by a thick, orange line. The location of the upper-hybrid resonance on the equatorial mid-plane is marked by a yellow oval. This resonance-location has a dependence on the plasma density: the higher the density the further outwards the resonance. The chordal locations of the interferometer channels, along with the edge probe, are shown by colored diamonds.

fact that upper-hybrid frequency is a function of the plasma frequency, ω_p means that—unlike the cyclotron resonance—the location of the upper-hybrid resonance is a function of the plasma density. In LDX, as in most devices where the gradient of both the density and the magnetic field point inwards, the location of the upper-hybrid resonance will be further away from the central core than the cyclotron resonance.

In Fig. 7-8 we plot some of the resonance locations for 2.45 GHz microwaves. The heavy, solid lines indicate the locations of the fundamental cyclotron resonance (red) and its first harmonic (orange). The location of the upper-hybrid resonance at the equatorial mid-plane is indicated by a yellow oval. The size of the oval is meant to indicate the dependence of the resonance location on the plasma density. In shot 80322030, for example, the equatorial upper-hybrid resonance is located near 92 cm at $t = 9$ seconds. At 11 seconds, which is after the density transition at 9.75 seconds, the density has increased and so the location of the upper-hybrid resonance increases as well, to approximately 98 cm.

Understanding the mechanisms of power deposition into the plasma from RF heating near the cyclotron and upper-hybrid resonances often requires more rigorous, fully non-linear treatments. Although it is not our intent to examine how, precisely, the plasma is heated, we reference two experimental papers that may be relevant for future studies in LDX. In Ref. [103], Grek and Porkolab present observations that plasma heating can occur above the cyclotron frequency on account of mode-conversion brought about through a parametric decay instability. Similar observations of "anomalous heating" due to parametric instabilities were also reported by Okabayashi et $al.$ in the FM-1 Spherator [104]. In both instances, the parametric instability is initiated by a sufficiently high amplitude of the input RF. In LDX, such high amplitudes may occur near cutoff where the group velocity of the RF waves approaches zero.

A comparison of the density profiles in Fig. 7-7 with the 2.45 GHz resonance locations in Fig. 7-8 reveals that heating at the upper-hybrid resonance is, in the absence of some process of convection, insufficient to explain the observations of over-dense plasmas in LDX. This is because the plasma attains densities higher than

189

the cutoff density at locations inwards of 95 cm—that is, inwards of the location of the upper-hybrid resonance. However, in the absence of any convection, heating at the upper-hybrid resonance should result in a source of particles located *at* the upper-hybrid resonance.

On the other hand, comparing Figs. 7-7 and 7-8 does suggest that coupling at the upper-hybrid resonance may be connected with the onset of a density transition. Because the density transitions are usually observed to occur at the location of either the second or third interferometer chords ($r = 86$ cm and $r = 96$ cm), it may very well be the case that ionization at the upper-hybrid or first harmonic cyclotron resonance plays a key role in the triggering of a density transition.

It may also be the case that upper-hybrid heating is not involved. The fact that the inverse sawteeth fluctuations (Fig. 7-2) occur near $r = 77$ cm implies that the trigger for the density transitions may happen further inwards. The location of the inverse-sawteeth as well as the speed with which the density rises at each oscillation suggests that the bulk density may be interacting with the hot-electron population located in the core. Perhaps the rapid loss of bulk density after the 6.4 GHz is switched-off (see Fig. 7-1) changes the hot-electron fraction in such a way as to make the plasma vulnerable to hot electron interchange modes (HEI's, cf. Ref. [72]). If, at some point, the HEI's are stabilized, the bulk density may be allowed to increase and this may account for the observation of a spontaneous density transition. However, other HEI signatures are not seen during this time (e.g., on the probes or radiometer) which complicates the HEI hypothesis.

Alternatively, we note that before the density transition, the density profile is especially steep near the core (Fig. 7-7) and, depending on the temperature profile (which is unknown), this *may* indicate that the pressure profile is also very steep in this region. If the pressure profile at some instant becomes steeper than allowed by the stability condition [Eq.(2.30)], MHD interchange instabilities may develop leading to flux-tube mixing. Once started, flux-tube mixing may be essential for maintaining the pressure and the density in their stationary profiles as we discuss in the next section.

7.4 Density Transitions as Plasma Self-Organization

7.4.1 Predictions of Non-Linear MHD Theory

Perhaps the most remarkable feature of the spontaneous density transitions observed in LDX is that the plasma is rearranged into not just any profile, but into a profile that approximates more closely the profile that is stationary to MHD interchange modes. In many instances, as we will discuss below, the measured density profile after a transition exactly matches the predicted, stationary density profile to within experimental uncertainty.

The notion that the pressure and density profiles that are stationary to MHD interchange modes are somehow "preferred" or "natural" is an idea that was introduced in Chapter 2 and especially in §2.5.3. To recapitulate, it was Thomas Gold who first intuited that a dipole-confined plasma may be maintained in stationary profiles by convective process that is analogous to the thermal convection of a compressible fluid under the influence of gravity [2]. By this account, an interchange mode does not cause the violent loss of confinement of the plasma, but rather induces a convective process that works to restore the plasma back to a pressure profile that is marginally stable against interchange modes. This convection consists of large-scale flux-tube mixing that homogenizes the plasma such that each flux-tube contains the same number of particles and the same entropy. The resulting pressure and density profiles are therefore stationary, meaning that the profiles remain the same even while subject to interchange modes. This physics is encoded in Eq.(2.32):

$$pV^{\gamma} = constant$$

$$nV = constant.$$

The hypothesis that flux-tube mixing is an important process in LDX is vital since otherwise there is no reason to suppose that the stationary density profiles should be observed at all, especially since LDX is heated with ECRH, a process that generates particle-sources in localized regions. Further understanding of the mechanisms that

can bring about flux-tube mixing was provided more recently (and more rigorously) by the non-linear MHD analyses of Pastukhov and Chudin [4] and Kouznetsov *et al.* [5]. Both papers treat the 2-dimensional analogue of LDX—a hardcore Z-pinch. Kouznetsov approached the problem using a quasi-linear analysis of MHD transport. Pastukhov employed a fully non-linear, numerical analysis of the "reduced" MHD equations. Although these two efforts differ in some important details, they both reach the same conclusion: A plasma that is displaced from the marginally stable pressure profile will be subject to a process of convection which acts to return the plasma back to the marginally stable profile. The convective process which enforces the stationary pressure and density profiles is called "self-consistent convection" by Pastukhov while Kouznetsov uses the term "self-organization". The LDX group, in accord with Kouznetsov's terminology, has chosen to label the spontaneous density transitions observed in LDX as examples of self-organization.

In plasma physics, self-organization is commonly found in the context of field-reversed configurations and refers to behavior resulting from the conservation of magnetic helicity ($H_B \equiv \frac{1}{2} \int \mathbf{A} \cdot \mathbf{B} \, dV$). However, the term "self-organization" refers more universally to any system that exhibits an *apparent* decrease of entropy. A review article by Hasegawa [105] clarifies how a large class of non-linear systems in which some dissipation is present can exhibit self-organization if there are grossly unequal time evolutions of quantities that would be conserved in the absence of dissipation. Under the right circumstances, the unequal dissipation is manifested in the apparent ordering of one of the two quantities—that is, a tendency of the one quantity towards lower mode numbers (a process called an "inverse cascade").

In this light, the formation of a convective cell is regarded as self-organization in that the energy stored in particle motion (which is initially unordered and dispersed over a broad band of modes) is channeled into large-scale, ordered motion in a much narrower band of modes. The appearance of a strong, quasi-coherent 500 Hz mode (see Figs. 7-3 and 7-6) in conjunction with density transition events is suggestive of just this sort of large-scale motion. In turn, this large-scale motion may be evidence of a large, convective cell drifting toroidally around the vacuum chamber, transporting

the particles and energy necessary for maintaining the pressure and density in their "self-organized" profiles.

If the convective cell were to perfectly enforce the stationary density profile (corresponding to an equal number of particles per flux-tube) then it could not be detected as a fluctuation by the interferometer. The fact that the 500 Hz mode is only seen on the innermost channel must therefore explained by supposing that it is near 77 cm that the density begins to roll-over and deviate from the stationary form. An additional argument supporting the self-organization hypothesis is that the resulting density profile does indeed approach the profile predicted for marginality. These observations are presented below.

7.4.2   Towards a "Natural" Density Profile

Non-linear theory predicts that convective cells will form, bringing about the large-scale flux-tube mixing necessary to maintain the plasma density and pressure near their marginally stable profiles. For the density, this means that the plasma will be driven to a profile characterized by an equal number of particles per flux-tube [Eq.(2.28)]

$$nV = constant.$$

In the magnetic geometry of LDX, this condition can be expressed in terms of the flux-function, ψ [Eq.(6.8)]

$$n(r) \sim \psi(r)^{4.45}.$$

In all of the shots exhibiting a spontaneous density transition (listed in Table 7.1), the density profile after the transition is found to be closer to the predicted, "natural" density profile. This is especially true for the density transition shots from March, 2008 (shot numbers beginning with "803"). For the two density transition shots of May, 2008 (shot numbers beginning with "805"), the behavior is less clear, but a case can be made that the trend is seen in portions (as opposed to the entire) density profile. The data presented in this section is from the most clear of the March density transitions, shot 80322030.
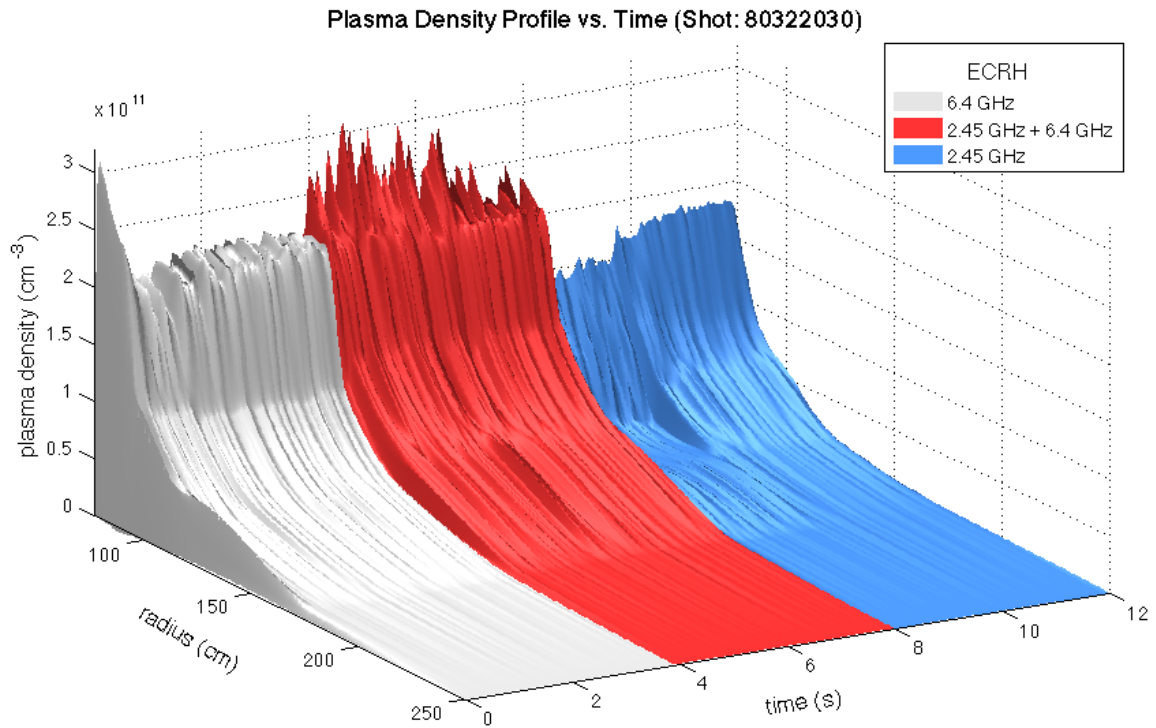
Figure 7-9: 3-dimensional plot showing the time evolution of the Abel-inverted radial density profiles for shot 80322030. The three different colors indicate the three different combinations of ECRH heating. At 8 seconds, the 6.4 GHz microwaves are terminated and a period commences where the plasma is heated with 2.45 GHz microwaves only (blue coloring). From 8 seconds until 9.75 seconds, the density profile exhibits two distinct gradients: a relatively flat profile from the edge until about 100 cm and a relatively steep profile from 100 cm inwards. At 9.75 seconds, a spontaneous density transition occurs and the plasma density fills-in near 100 cm resulting in a more uniform density profile.
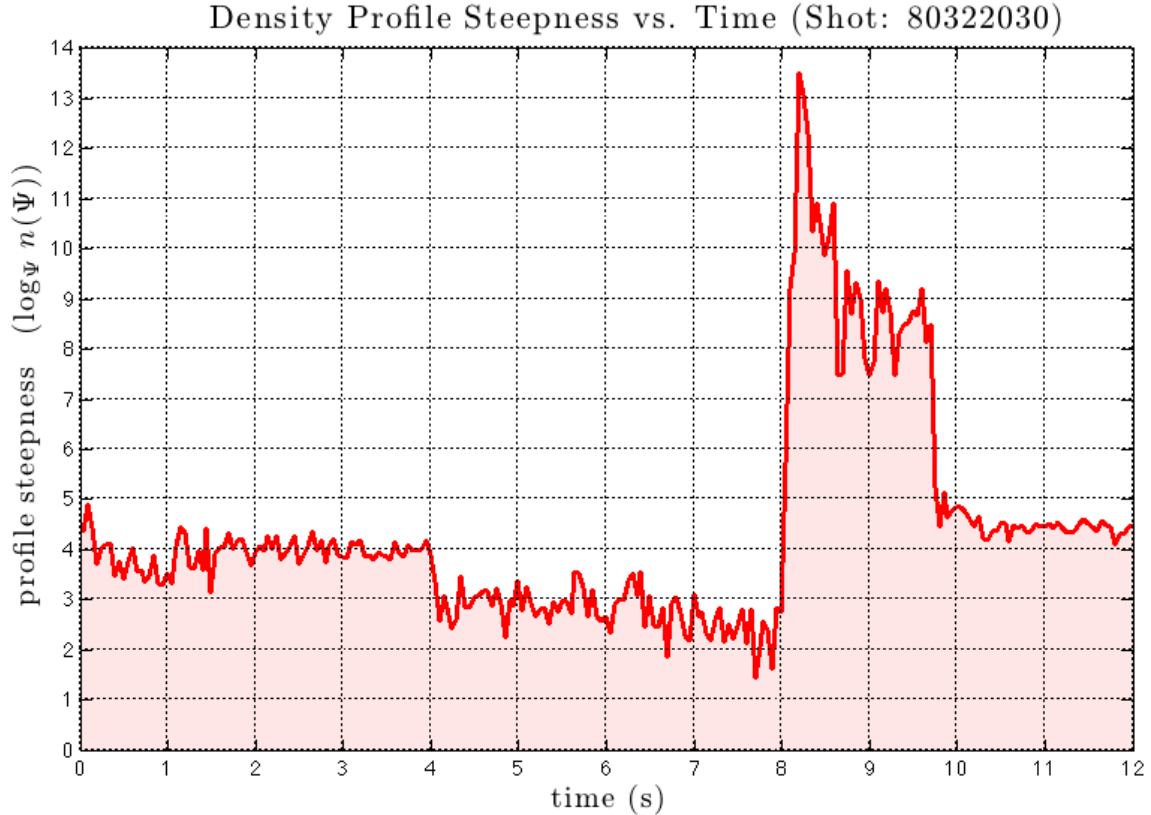
Figure 7-10: Density profile steepness vs. time for shot 80322030. A density transition occurs in this shot at $t = 9.75$ seconds (see Fig. 7-1). The profile steepness is measured in terms of the steepness exponent, introduced in §6.4. Just before the density transition, in the interval 8-9.75 seconds, the steepness exponents are in excess of 10 indicating very steep profiles. The uncertainties at these times are judged to be higher than usual since the density profile has almost two distinct gradients (flat outside of 100 cm and steep inside of 100 cm). After the density transition (9.75-12 seconds), the steepness exponents are approximately 4.5 $\pm$ 0.2 which corresponds to the ideal, $n \sim 1/V$ density profile.

The Abel-inverted, radial density profiles at two instants—one before and one after the density transition—were shown previously in Fig. 7-7. A 3-dimensional plot showing the full time evolution of the density profile is provided in Fig. 7-9. Both of these figures show that the density profile just prior to the transition (at 9.75 seconds) is quite flat up until approximately 100 cm, inside of which the density increases with a very steep gradient. By contrast, after the transition (at 9.75 seconds) the density at 100 cm "fills-in" resulting in a profile with a more uniform gradient.

One way to quantify the the extent to which the density profile tends towards the natural profile after a density transition event is to plot the steepness exponents of the density profile vs. time. The steepness exponent was introduced in §6.4 and is

simply the exponent of the flux-function, $\psi(r)$, that corresponds to a best-fit of the density profile, $n(r)$. These exponents are estimated to have an uncertainty of ± 0.2. A steepness exponent of 4.45 corresponds to the "natural" ($n \sim 1/V$) density profile.

Fig. 7-10 shows the steepness exponents plotted vs. time for shot 80322030. In the period directly preceding the density transition (8 to 9.75 seconds), the profile is seen to have very steep gradients with steepness exponents in excess of 10. Although the density profile by itself says nothing about the pressure (and the temperature profile is not measured in LDX), the unusual steepness of the density profile at this time may suggest that the pressure profile is also very steep. If at some instant the pressure profile becomes supercritical [Eq.(2.30)], an MHD interchange mode will occur and this may trigger the density transition at 9.75 seconds.

Because the profiles in the period 8-9.75 seconds have almost two distinct gradients (the profiles are relatively flat up until approximately 100 cm) the fit is poor and the uncertainties in the steepness exponent are undoubtedly larger than ± 0.2. After the transition (9.75 to 12 seconds), the profile gradients becomes much gentler, the fits become quite good and the steepness exponents match the ideal value of 4.45 within experimental uncertainty. After the density transition, therefore, the plasma has approximately a $1/V$ profile and so, approximately, an equal number of particles per flux-tube.

Perhaps the most compelling way to show how the density in shot 80322030 approaches the ideal profile after the density transition is to plot the number of particles per flux-tube both before and after the transition. Fig. 7-11 shows a plot of particles per flux-tube vs. radial distance at two moments of shot 80322030, one before the density transition (9 seconds) and one after (11 seconds). The number of particles is computed by multiplying the radial density profile by the flux-tube volume (also a function or radius) for a tube which has a flux of 1 weber. The flux-tube volume function is found by computing $V = \oint d\ell/B$ for various field-lines and associating to these values the radii where the field-line crosses the equatorial plane.

Because the flux-tube volume increases very rapidly with radius near the last closed field-line ($r = 173.5$ cm), the quantity $n \, dV$ becomes less reliable at larger
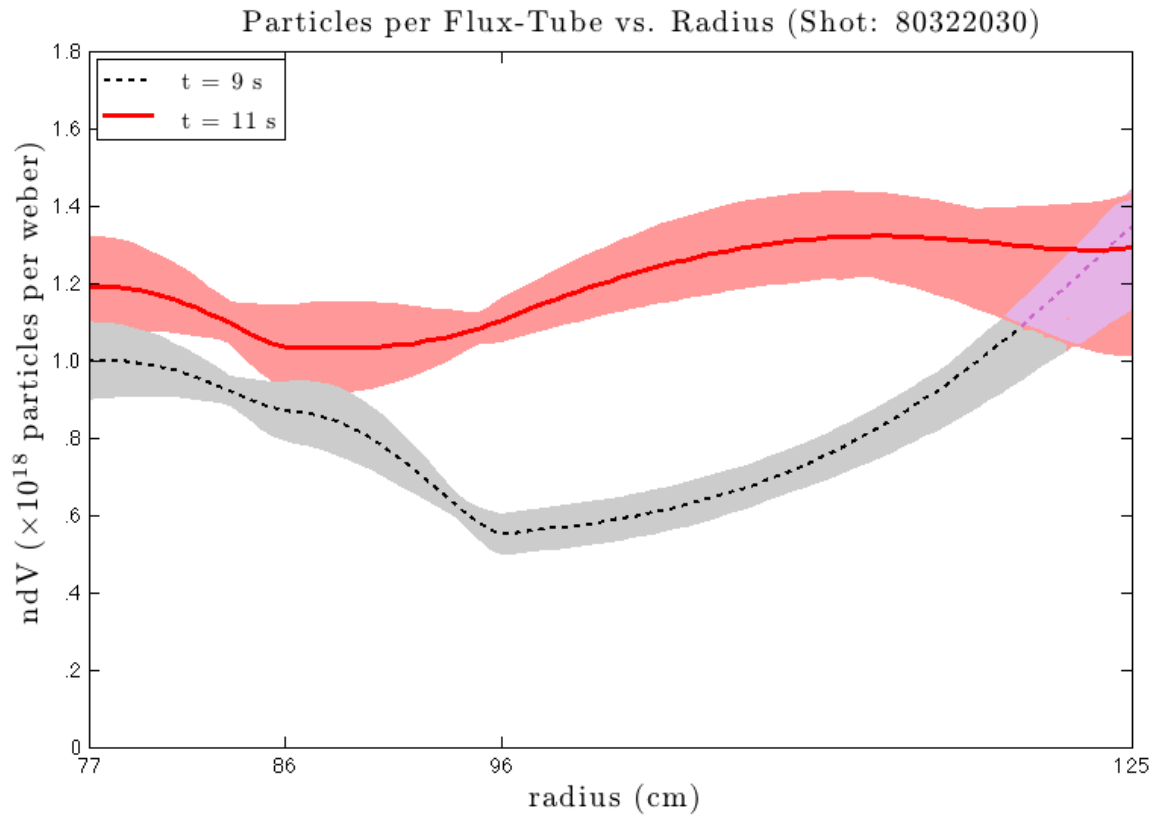
Figure 7-11: The number of particles within a 1 weber flux-tube as a function of radius for shot 80322030 at times before and after the density transition ($t = 9.75$ s). nV after the transition (red curve) is significantly flatter than nV before the transition (black curve). This provides direct confirmation that after the transition, the density profile closely approximates the ideal $nV = constant$ profile. The principal curves at either instant are surrounded by shaded envelopes which indicate the uncertainty in the density profile measurements. These envelopes were formed by computing multiple Abel-inverted density profiles at each instant from data modified by the experimental uncertainty of approximately 5% (see §5.3).

radii. Consequently, the figure shows only those radii that are within the innermost and outermost chords of the interferometer, although the densities computed for these inner locations necessarily depend on the probe density measurement at $r = 175$ cm. In order to indicate the uncertainties, both curves are surrounded by an envelope made by altering the measured, line-integrated densities by $\pm$ 5% and the probe measurement by factors of 2. This is the same method used in §5.3 except that here we use the measured value of the uncertainty ($\pm 5° \rightarrow \pm 5\%$) whereas in §5.3 a more extreme case of $\pm 10\%$ was examined.

Fig. 7-11 shows explicitly what was only hinted at in earlier plots of the radial density profiles (Figs. 7-7 and 7-9), namely that right before the density transition (at 9.75 seconds) there is a "hole" in the density profile at around 100 cm. After the density transition, this hole is filled-in. The insight from Fig. 7-11 is that after the density transition, the density profile is clearly seen to have a more uniform number of particles per flux-tube. The nV curve is much flatter in the period after the transition than before thus providing the most direct confirmation that the density profile has moved closer to the ideal $1/V$ (equal particle per flux-tube) form.

Although density transitions in LDX are rare and their exact cause remains mysterious, these events are of great interest to the experiment because they underscore in a dramatic way the tendency of LDX plasmas to form and maintain the peaked density profiles predicted by theory. Testing these theories is the main experimental goal of LDX, but ultimately, a fuller understanding must await new experiments with new measurement capabilities. Some thoughts on the future of LDX and the LDX interferometer are presented in our next and final chapter.

Chapter 8

Conclusion

8.1 Summary

In this thesis we have presented our research on the density profiles of plasmas made in the Levitated Dipole Experiment. Many elements of this work are unique. First there is the experiment itself: LDX is the only levitated dipole experiment in the world that exploits plasma compressibility to achieve stability. Second, our research entailed the building of a unique scientific instrument: a 4-channel interferometer designed expressly to operate in the unique geometry of LDX. Moreover, the interferometer is currently the primary diagnostic on LDX for measuring beyond the scrape-off layer and into the plasma core. Lastly, our measurements are the first in LDX for plasmas confined by a *levitating* (as opposed to supported) dipole coil.

Because the theoretical foundations of plasma confinement in a dipole magnetic field are not widely known, we began, in Chapter 2, with a general overview of the nature of dipole confinement. In particular we stressed the theoretical predictions that flux-tube mixing should drive the plasma towards naturally peaked pressure and density profiles. An overview of the Levitated Dipole Experiment, which was built to test these predictions, was provided in Chapter 3.

The design, construction and calibration of the microwave interferometer was described in detail in Chapter 4. The LDX interferometer is found to reliably measure phase shifts that are accurate to within 5° corresponding to uncertainties of just a

few percent.

In Chapter 5 we developed some analytical tools to transform the raw phase-shift data of the interferometer into information about the plasma density. In particular, we discussed the method of converting line-integrated density data into radial density profiles by means of Abel inversion. The uncertainties of the densities computed by this process are inherently larger than the uncertainties of the data itself, a feature which is compounded at locations closer to the core where the calculated densities have uncertainties estimated at 15%.

Using these methods of analysis, we presented in Chapter 6 a compilation of our density profile measurements for LDX plasmas. We observed that the density magnitudes in LDX are functions of ECRH, vacuum pressure, plasma species and levitated vs. supported mode of operation. On the other hand, the density profile gradients are found to be more constant over a wide range of experimental conditions, with no observed species dependence and a much reduced dependence on vacuum pressure and ECRH. Thus LDX plasmas have a tendency to exhibit "profile consistency" in the density. For plasmas heated by 15 kW of ECRH—and at sufficiently high neutral pressures—the density profiles closely approximate the $1/V$ form (corresponding to an equal number of particles per flux-tube) predicted by theory. Lastly in Chapter 6, we presented some basic energy and particle balance equations for LDX plasmas.

Non-linear analyses suggest that dipole-confined plasmas can be maintained in the ideal, $1/V$ density profile by a process of self-organized convection. In Chapter 7 we presented evidence indicating that such a process may have been observed in LDX. Although the mechanisms and triggers are poorly understood, LDX plasmas have been observed to exhibit spontaneous rearrangements of the density profile. These density transitions are accompanied by a quasi-coherent 500 Hz fluctuation on the innermost interferometer chord which may indicate the presence of a large-scale convective cell drifting azimuthally around the vacuum chamber. Additional support for the self-organization hypothesis comes from the fact that the density profiles after the transition are always closer to the ideal, $1/V$ form and oftentimes the agreement is exact within experimental uncertainty.

8.2 Future Directions

The main goal of this thesis was to characterize the behavior of LDX plasma densities under a variety of experimental conditions. Because of the newness and novelty of LDX it seemed best to give our research a scope that was perhaps more broad than deep. Many of the features discovered here would make excellent topics for more focused study, especially the phenomenon of spontaneous density transitions.

One of the top priorities for LDX in the near term is to develop greater diagnostic capabilities, especially with regard to the plasma pressure and temperature of the bulk, background plasma. Two such instruments are in the concept stage: a suite of X-ray detectors to measure bremsstrahlung radiation (Matt Davis) and a radiometer to measure parallel-field synchrotron radiation through the bore of the F-Coil (Paul Waskov). At a more advanced stage of development are two diagnostics designed for detailed fluctuation studies: a photodiode array to observe visible-light fluctuations throughout the entire plasma including the core (Jen Ellsworth) and a probe array to measure the spatial structure of fluctuations in the scrape-off layer (Ryan Bergmann).

In addition to improved diagnostics, the other chief priority for LDX is more microwave heating power. Currently LDX is heated with three ECRH sources with a combined power of 15 kW. Because LDX plasmas occupy such a large volume, the experiment is characterized an extremely low power to volume ratio. As a result, LDX plasmas are likely to have low bulk-temperatures with most of the input power going towards ionization as opposed to heating. In order to rectify this, new microwave sources will be added in the near future. The first of these will be a pair of 28 GHz gyrotrons which each emit approximately 20-30 kW of continuous heating power. It is hoped that these sources will be operational sometime in the upcoming year.

With additional ECRH capabilities, the maximum densities in LDX may increase by as much as 1-2 orders of magnitude. If so, the interferometer will no longer be able to function in its current arrangement since the effects of refraction will become too large. The most likely adaptation is simply to move the interferometer horns further from the core so that the beam traverses a lower-density portion of the plasma. A

reflectometer is planned (Darren Garnier) to complement the interferometer as a density diagnostic and take over the task of measuring the core densities once the interferometer horns are moved.

Although LDX is now almost ten years old, the ability to conduct true, levitated-dipole experiments was achieved only within the last ten months. In many respects, LDX is just now getting started. For this reason it is hoped a new grant will be awarded, extending the experiment's life from 2009 to 2012. In that time, the increased diagnostics and heating capabilities may help LDX answer some of its main science questions. Undoubtedly, more discoveries and more enigmas will arise as well. Beyond that date, who would dare to predict? It is possible that LDX may give rise to newer and larger dipole devices which may one day confine fusion-grade plasmas. It is also possible (perhaps even likely) that LDX may be the last of its kind. And so, to my colleagues who will carry-on after I go, I hope my work here was of value to you. I leave it to you now along with my warmest admiration an my heartiest encouragement. Good luck, LDX!

Appendix A

Interferometer Hardware

Table A.1: Principal Microwave Components

Component	Vendor	Part No.	Quantity
60 GHz Gunn-diode oscillator varactor-tuned, 20 dBm output	Quinstar	QTV-6020OV	2
Gunn-diode voltage regulator	Quinstar	QCR-4C000	2
Pyramidal standard gain horn 23 dB gain	Millitech	SGH-15-RP000	4
Pyramidal custom gain horn 26 dB gain	Millitech	RFH-15F-0000	1
60 GHz balanced mixer	Millitech	MXP-15-RSXSL	5
60 GHz power amplifier 19 dBm max output	Terabeam-HXI	HHPAV-3B-023	1
Magic Tee	Quinstar	QJH-VN6000	5
20 dB directional coupler	Millitech	CL3-15-R2000	1
20 dB isolator	Quinstar	QJI-60021V	2
27 dB isolator	Quinstar	QIF-60000V	1
Pres-U-Windisc mica vacuum window	Aerowave	15-1502	6
Custom waveguide segments	Aerowave / Quinstar	—	> 10

Table A.2: Principal IF Components

Component	Vendor	Part No.	Quantity
70 MHz demodulator	Mini-Circuits	ZFMIQ-70D	4
Amplifier 9 dBm max output	Mini-Circuits	ZFL-500LN	10
Amplifier 16 dBm max output	Mini-Circuits	ZFL-500HLN	1
70 MHz bandpass filter	Mini-Circuits	SBP-70	5
Attenuators 6 and 10 dB	Mini-Circuits	VAT-*	12
Limiting amplifier	Analog Devices	AD8309	5
PLL chip	Texas Instruments	TLC2933	1
PLL input comparator	Analog Devices	AD8611	1
PLL output adder	Analog Devices	AD8130	1

Appendix B

Shot/Time Database

Table B.1: ECRH: 10.5 GHz (10 kW), 6.4 GHz (2.5 kW), 2.45 GHz (2.5 kW); D_2 plasma

$shot$	t (sec.)	$shot$	t (sec.)	$shot$	t (sec.)	$shot$	t (sec.)
80514011	6	80514038	4	80515001	6	80515041	6
80514012	6	80514038	11	80515008	6	80515042	6
80514013	6	80514039	4	80515018	6	80515043	6
80514014	6	80514039	10	80515026	6	80515044	5
80514015	6	80514040	4	80515027	6	80515044	7
80514016	6	80514040	10	80515028	6	80515045	5
80514029	11	80514041	4	80515029	6	80515045	7.5
80514030	11	80514041	10	80515030	6	80515046	6
80514031	11	80514042	4	80515031	6	80516001	2
80514032	11	80514042	10	80515032	6	80516001	7
80514033	11	80514043	4	80515033	6	80516001	12
80514034	11	80514043	10	80515035	6	80516005	5
80514035	4	80514044	4	80515036	6	80516005	10
80514035	11	80514044	11	80515037	6	80516008	5
80514036	4	80514045	11	80515038	6	80516008	10
80514036	11	80514046	11	80515039	6	80516012	5
80514037	4	80514047	11	80515040	6	80516012	10
80514037	11	—	—	—	—	—	—

Table B.2: ECRH: 6.4 GHz (2.5 kW), 2.45 GHz (2.5 kW); D_2 plasma

$shot$	t (sec.)	$shot$	t (sec.)	$shot$	t (sec.)	$shot$	t (sec.)
80321015	6	80321040	5	80322016	6	80322023	3
80321016	6	80321040	8	80322017	6	80322026	6
80321017	6	80322007	6	80322018	6	80322027	6
80321018	6	80322008	6	80322019	6	80322030	6
80321019	6	80322009	6	80322020	6	80322036	6
80321025	6	80322011	3	80322021	3	80322037	6
80321026	6	80322011	7	80322021	8	80322038	6
80321030	2	80322011	11	80322022	1	80322039	6
80321030	8	80322012	3	80322022	2	80322040	6
80321034	6	80322012	7	80322022	3	80322041	6
80321035	6	80322012	11	80322022	4	80322043	6
80321036	6	80322013	3	80322022	5	80322044	6
80321037	6	80322013	7	80322022	6	80322045	6
80321038	6	80322013	11	80322022	7	80322047	6
80321039	1	80322014	3	80322022	8	80322048	6
80321039	5	80322014	7	80322022	10	80322049	6
80321039	8	80322014	11	80322023	11	80322050	6
80321040	1	80322015	6	80322023	7	80322051	6

Table B.3: ECRH: 6.4 GHz (2.5 kW); D_2 plasma

shot	t (sec.)	shot	t (sec.)	shot	t (sec.)	shot	t (sec.)
71213005	1.5	80321016	2	80322018	2	80322049	2
71213006	1.5	80321017	2	80322019	2	80322050	2
71213011	9	80321018	2	80322020	2	80322051	2
71213012	1.5	80321019	2	80322023	1	80514010	9
71213013	1.5	80321025	2	80322023	5	80514020	5.5
71214006	1.5	80321027	6	80322023	9	80515009	3
71214007	1.5	80321036	2	80322023	13	80515009	9
71214008	1.5	80322007	2	80322026	2	80515011	9
71214009	1.5	80322008	2	80322027	2	80515034	3
71214010	1.5	80322009	2	80322030	2	80515034	9
71214011	1.5	80322011	1	80322036	2	80516010	3
71214012	1.5	80322011	5	80322037	2	80516010	8
71214013	1.5	80322011	9	80322038	2	80516010	13
71214015	2.5	80322011	13	80322039	2	80516011	3
71214017	6	80322012	1	80322040	2	80516011	8
71214020	2	80322012	5	80322041	2	80516011	13
71214020	8	80322012	9	80322043	2	80516012	3
71214032	1.5	80322012	13	80322044	2	80516012	8
71214032	5	80322015	2	80322045	2	80516012	13
71214032	9	80322016	10	80322047	2	80516015	8
80321015	2	80322017	10	80322048	2	80516015	13

Table B.4: ECRH: 2.45 GHz (2.5 kW); D_2 plasma

shot	t (sec.)	shot	t (sec.)	shot	t (sec.)	shot	t (sec.)
80321015	9	80514015	12	80514032	1	80515030	1
80321016	9	80514016	1.5	80514032	5	80515030	12
80321017	9	80514017	2	80514032	13	80515031	1
80321018	9	80514017	9	80514033	1	80515031	12
80321019	9	80514018	2	80514033	5	80515032	1
80321025	9	80514018	9	80514033	13	80515032	12
80321031	6	80514019	2	80514034	1	80515033	1
80321036	9	80514019	9	80514034	5	80515033	12
80322007	10	80514021	2	80514034	13	80515035	1
80322008	10	80514021	11	80514035	1	80515035	12
80322009	10	80514022	1	80514035	13	80515036	1
80322013	1	80514022	13	80514036	1	80515036	12
80322013	5	80514022	9	80514036	13	80515037	1
80322013	9	80514022	5	80514037	1	80515037	12
80322013	13	80514023	1	80514037	13	80515038	1
80322014	1	80514023	5	80514038	1	80515038	12
80322014	5	80514023	13	80514038	13	80515039	1
80322014	9	80514023	9	80514039	1	80515039	12
80322014	13	80514024	1	80514039	13	80515040	1
80322015	9	80514024	5.5	80514040	1	80515040	12
80322016	2	80514024	9.5	80514040	13	80515041	1
80322017	2	80514024	13.5	80514041	1	80515041	12
80322018	10	80514025	1	80514041	13	80515042	1
80322019	10	80514025	5	80514045	1	80515042	12
80322020	10	80514025	9	80514045	5	80515043	1
80322026	10	80514025	13	80514045	13	80515043	12
80322027	9	80514026	1	80514046	1	80515044	1
80322030	9	80514026	5	80514046	5	80515044	12
80322036	10	80514026	9	80514046	13	80515045	1
80322037	10	80514026	13	80514047	1	80515045	12
80322038	10	80514027	1	80514047	5	80515046	1
80322039	10	80514027	5	80514047	13	80515046	12
80322040	10	80514027	9	80515001	1	80516002	12
80322041	10	80514027	13	80515001	12	80516002	7
80322043	10	80514028	1	80515008	1	80516002	2
80322044	10	80514028	5	80515008	12	80516003	3
80322045	10	80514028	9	80515018	1	80516003	8
80322047	10	80514028	13	80515018	12	80516004	3
80322048	10	80514029	1	80515023	2	80516004	8
80322049	10	80514029	5	80515026	1	80516005	3
80322050	10	80514029	13	80515026	12	80516009	3
80322051	10	80514030	1	80515027	1	80516009	8
80514010	1.5	80514030	5	80515027	12	80516013	2
80514010	9.5	80514030	13	80515028	1	80516013	5
80514011	1	80514031	1	80515028	12	80516013	7
80514012	1	80514031	5	80515029	1	80516014	3
80514013	12	80514031	13	80515029	12	80516014	8
80514014	12	—	—	—	—	—	—

Table B.5: ECRH: 6.4 GHz (2.5 kW), 2.45 GHz (2.5 kW); D_2 plasma; no levitation

shot	t (sec.)	shot	t (sec.)	shot	t (sec.)	shot	t (sec.)
71213002	8	80321013	6	80322005	6	80322025	10
71213003	4	80321014	6	80322006	6	80322052	7
71213003	8	80321020	6	80322024	2	80322053	6
71214018	4	80321021	6	80322024	6	80322054	6
80321010	6	80321024	6	80322024	10	80322055	6
80321011	6	80322003	6	80322025	2	80322056	6
80321012	6	80322004	6	80322025	5	—	—

Table B.6: ECRH: 10.5 GHz (10 kW), 6.4 GHz (2.5 kW), 2.45 GHz (2.5 kW); He plasma

shot	t (sec.)	shot	t (sec.)	shot	t (sec.)	shot	t (sec.)
80516017	6	80516026	6	80516030	13	80516032	9
80516018	6	80516027	6	80516031	5	80516032	11
80516019	6	80516028	6	80516031	7	80516032	13
80516020	6	80516029	6	80516031	9	80516033	5
80516021	6	80516030	5	80516031	11	80516033	7
80516022	6	80516030	7	80516031	13	80516033	9
80516023	6	80516030	9	80516032	5	80516033	11
80516024	6	80516030	11	80516032	7	80516033	13
80516025	6	—	—	—	—	—	—

Table B.7: ECRH: 6.4 GHz (2.5 kW), 2.45 GHz (2.5 kW); He plasma

shot	t (sec.)	shot	t (sec.)	shot	t (sec.)	shot	t (sec.)
80516017	3	80516021	3	80516025	3	80516028	9
80516017	9	80516021	9	80516025	9	80516029	3
80516018	3	80516022	3	80516026	3	80516029	9
80516018	9	80516022	9	80516026	9	80516030	3
80516019	3	80516023	3	80516027	3	80516031	3
80516019	9	80516023	9	80516027	9	80516032	3
80516020	3	80516024	3	80516028	3	80516033	3
80516020	9	80516024	9	—	—	—	—

Bibliography

[1] ROSENBLUTH, M.N., and LONGMIRE, C.L. "Stability of Plasmas Confined by Magnetic Fields". *Annals of Physics*, Vol. 1, Issue 2, pp. 120-40, May, 1957.

[2] GOLD, T. "Motions in the Magnetosphere of the Earth". *Journal of Geophysical Research*, Vol. 14, No. 9, pp. 1219-24, September, 1959.

[3] HASEGAWA, A. "A Dipole Field Fusion Reactor". *Comments on Plasma Physics and Controlled Fusion*, Vol. 11, No. 3, pp. 147-51, 1987.

[4] PASTUKHOV, V.P. and CHUDIN, N.V. "Plasma Convection near the Threshold for MHD Instability in Nonparaxial Magnetic Confinement Systems". *Plasma Physics Reports*, Vol. 27, No. 11, pp. 907-21, October, 2007. Translated from *Fizika Plazmy*, Vol. 27, No. 11, pp. 963-77.

[5] KOUZNETSOV, A., FREIDBERG, J.P. and KESNER, J. "Quasilinear theory of interchange modes in a closed field line configuration". *Physics of Plasmas*, Vol. 14, No. 10, 102501, October, 2007.

[6] EGELAND, A., and BURKE, W.J. *Kristian Birkeland: The First Space Scientist*. Springer, Dordrecht, The Netherlands, 2005.

[7] STØRMER, C. *The Polar Aurora*. Clarendon Press, Oxford, 1955.

[8] ALFVÉN, H. "On the Motion of a Charged Particle in a Magnetic Field". *Ark. f. mat., astr. o. fysik,* **27 A**, (No. 22), 1940.

[9] FERMI, E. "On the Origin of Cosmic Radiation". *Physical Review*, Vol. 75, No. 8, pp.1169-74, April 15, 1949.

[10] ALFVÉN, H. *Cosmical Electrodynamics*, § 2.3. Clarendon Press, Oxford, 1950.

[11] VAN ALLEN, J.A. "Energetic Particles in the Earth's External Magnetic Field". In C.S. Gillmor and J.R. Spreiter, editors, *Discovery of the Magnetosphere*, History of Geophysics, volume 7, page 242. American Geophysical Union, Washington, D.C., 1997.

[12] VAN ALLEN, J.A. op.cit., p. 243.

[13] ibid., p. 245.

[14] HESS, W.N. *The Radiation Belt and Magnetosphere*, Cap. 5. Blaisdell Publishing, Waltham, MA, 1968.

[15] JOHNSTON, W.R. "High-altitude nuclear explosions". www.johnstonsarchive.net/nuclear/hane.html.

[16] KURAN, P., director. *Nukes in Space: The Rainbow Bombs*. Visual Concept Entertainment (VCE), 1999.

[17] BISHOP, A.S. *Project Sherwood: The U.S. Program in Controlled Fusion.* Addison-Wesley, Reading, MA, 1958.

[18] BRAAMS, C.M., and STOTT, P.E. *Nuclear Fusion: Half a Century of Magnetic Confinement Fusion Research.* Institute of Physics Publishing, Bristol, U.K., 2002.

[19] SHAFRANOV, V.D., BONDARENKO, B.D., and GONCHAROV, G.A. "On the History of the Research into Controlled Thermonuclear Fusion". *Physics–Uspekhi*, **44** (8), pp. 835-65, 2001.

[20] BROMBERG, J.L. *Fusion: Science, Politics, and the Invention of a New Energy Source.* The MIT Press, Cambridge, MA., 1982.

[21] KRUSKAL, M. "Asymptotic Theory of Hamiltonian and other Systems with all Solutions Nearly Periodic". *Journal of Mathematical Physics*, Vol. 3, No.4, pp. 806-28, July-August, 1962.

[22] BORN, M. *The Mechanics of the Atom.* J.W. Fisher and D.R. Hartree, trans. G. Bell and Sons Publishing, London, 1927.

[23] LANDAU, L.D. and LIFSHITZ, E.M. *Mechanics*, volume 1 of *Course of Theoretical Physics*, Chapter VII. Butterworth-Heinemann, Oxford, U.K., third edition, 1998.

[24] KULSRUD, R.M. "Adiabatic Invariant of the Harmonic Oscillator". *Physical Review*, Vol. 106, No.2, pp. 205-7, April 15, 1957.

[25] GOLDSTON, R.J. and RUTHERFORD, P.H. *Introduction to Plasma Physics.* Institute of Physics Publishing, Bristol, U.K., 2000.

[26] NORTHROP, T.G. and TELLER, E. "Stability of the Adiabatic Motion of Charged Particles in the Earth's Field". *Physical Review*, Vol. 117, No.1, pp. 215-25, Jan. 1, 1960.

[27] STRUTT, J.W., Lord Rayleigh. "Investigation of the Character of the Equilibrium of an Incompressible Heavy Fluid of Variable Density". *Proceedings of the London Mathematical Society*, Vol. 14, pp. 170-7, eq. 13, April 12, 1883.

[28] TAYLOR, G.I. "The Instability of Liquid Surfaces when Accelerated in a Direction Perpendicular to their Planes. I.". *Proceedings of the Royal Society of London, Series A.*, Vol. 201, No. 1065, pp. 192-6, eq. 5, March 22, 1950.

[29] BATCHELOR, G. *The Life and Legacy of G.I. Taylor*, page 242. Cambridge University Press, Cambridge, U.K., 1996.

[30] ibid., pp. 202-3.

[31] LEWIS, D.J. "The Instability of Liquid Surfaces when Accelerated in a Direction Perpendicular to their Planes. II.". *Proceedings of the Royal Society of London, Series A.*, Vol. 202, No. 1068, pp. 81-96, June 22, 1950.

[32] BISHOP, A.S. *Project Sherwood*. op. cit., cap. 9.

[33] BROMBERG, J.L. *Fusion*. op. cit., cap. 4.

[34] ROSENBLUTH, M.N., and LONGMIRE, C.L. "Stability of Plasmas Confined by Magnetic Fields". op. cit., eq. 31.

[35] ibid., eq. 36.

[36] FREIDBERG, J.P. *Ideal Magnetohydrodynamics*, § 2.1. Plenum, New York, 1987.

[37] MCILWAIN, C.E. "Coordinates for Mapping the Distribution of Magnetically Trapped Particles". *Journal of Geophysical Research*, Vol. 66, No. 11, pp. 3681-91, November, 1961.

[38] ibid., p. 3685.

[39] WALT, M. *Introduction to Geomagnetically Trapped Radiation*, chapter 7. Cambridge atmospheric and space science series. Cambridge University Press, Cambridge, U.K., 1994.

[40] ibid., chapter 6.

[41] PARKER, E.N. "Geomagnetic Fluctuations and the Form of the Outer Zone of the Van Allen Radiation Belt". *Journal of Geophysical Research*, Vol. 65, No. 10, pp. 3117-30, October, 1960.

[42] LANDAU, L.D. and LIFSHITZ, E.M. *Fluid Mechanics*, volume 6 of *Course of Theoretical Physics*, § 4. Butterworth-Heinemann, Oxford, U.K., second edition, 2007.

[43] RUSSEL, C.T. "The dynamics of planetary magnetospheres". *Planetary and Space Science*, Vol. 49, pp. 1005-30, 2001.

[44] SOUTHWOOD, D.J. and KIVELSON, M.G. "Magnetospheric Interchange Instability". *Journal of Geophysical Research*, Vol. 92, No. A1, pp. 109-16, January 1, 1987.

[45] LIEMOHN, M.W. and CHAN, A.A. "Unraveling the Causes of Radiation Belt Enhancements". *Eos*, Vol. 88, No. 42, pp. 425-6, October, 2007.

[46] SCHINDLER, K. "Laboratory Experiments Related to the Solar Wind and the Magnetosphere". *Reviews of Geophysics*, Vol. 7, Nos. 1, 2, pp. 51-75, February-May, 1969.

[47] LEHNERT, B. "Confinement of Charged Particles by a Magnetic Field". *Nature*, Vol. 181, No. 4605, pp. 331-2, February 1, 1958.

[48] LEHNERT, B. "Confinement of Charged Particles by a Magnetic Field". *Journal of Nuclear Energy, Part C*, Vol. 1, No. 1, pp. 40-8, 20 March, 1959.

[49] LEHNERT, B., BERGSTRÖM, J., et al. "Plasma Confinement and Heating in the Internal Ring Device F IV". *Plasma Physics and Controlled Nuclear Fusion Research*, Vol. 1, pp. 59-74, 1971.

[50] FERRON, J.R., WONG, A.Y., DIMONTE, G. and LEIKIND, B.J. "Interchange stability of an axisymmetric, average minimum-B magnetic mirror". *Physics of Fluids*, Vol. 26, No. 8, pp. 2227-33, August, 1983.

[51] BRAAMS, C.M. and STOTT, P.E. *Nuclear Fusion*. op. cit., p.119.

[52] MAUEL, M.E., WARREN, H.H. and HASEGAWA, A. "An Experiment to Measure Collisionless Radial Transport of Energetic Electrons Confined by a Dipole Magnetic Field". *IEEE Transactions on Plasma Science*, Vol. 20, No. 6, pp. 626-30, December, 1992.

[53] YOSHIDA, Z., OGAWA, Y. et al. "First Plasma in the RT-1 Device". *Plasma Fusion Research: Rapid Communications*, Vol. 1, No. 8, pp. 1-2, 2006.

[54] MAHAJAN, S.M. and YOSHIDA, Z. "Double Curl Beltrami Flow: Diamagnetic Structures". *Physical Review Letters*, Vol. 81, No. 22, pp. 4863-6, 30 November, 1998.

[55] KESNER, J. "Stability of electrostatic modes in a levitated dipole". *Physics of Plasmas*, Vol. 4, No. 2, pp. 419-22, February, 1997.

[56] GARNIER, D.T., KESNER, J. and MAUEL, M.E. "Magnetohydrodynamic stability in a levitated dipole". *Physics of Plasmas*, Vol. 6, No. 9, pp. 3431-4, September, 1999.

[57] FREIDBERG, J.P. *Ideal Magnetohydrodynamics*. op. cit., chapters 6, 8.

[58] KESNER, J. and MAUEL, M.E. "Plasma Confinement in a Levitated Magnetic Dipole". *Plasma Physics Reports*, Vol. 23, No. 9, pp. 742-50, 1997. tans. from *Fizika Plazmy*, Vol. 23, No. 9, pp. 801-10, 1997.

[59] ZHUKOVSKY, A. and GARNIER, D.T. "Operation of the Levitated Dipole Experiment Floating Coil". *IEEE Transactions on Applied Superconductivity*, Vol. 16, No. 2, pp. 898-901, June, 2006.

[60] HASEGAWA, A., CHEN, L. and MAUEL, M.E. "A D-^{3}He Fusion Reactor Based on a Dipole Magnetic Field". *Nuclear Fusion*, Vol. 30, No. 11, pp. 2405-13, 1990.

[61] TELLER, E., GLASS, A.J., FOWLER, T.K., HASEGAWA, A. and SANTARIUS, J.F. "Space Propulsion by Fusion in a Magnetic Dipole". *Fusion Technology*, Vol. 22, pp. 82-97, 1990.

[62] KESNER, J., GARNIER, D.T., HANSEN, A., MAUEL, M. and BROMBERG, L. "Helium catalysed D-D fusion in a levitated dipole". *Nuclear Fusion*, Vol. 44, No. 1, pp. 193-203, January, 2004.

[63] CAROPPO, F. "Ultissime dal Futuro: Speciale MIT". *Newton*, June 1, 2001.

[64] ZHUKOVSKY, A., MORGAN, M., GARNIER, D., RADOVINSKY, A., SMITH, B., SCHULTZ, J., MYATT, L., POURRAHIMI, S. and MINERVINI, J. "Design and fabrication of the cryostat for the floating coil of the Levitated Dipole Experiment (LDX)". *IEEE Transactions on Applied Superconductivity*, Vol. 10, No. 1, pp. 1522-5, March 2000.

[65] GARNIER, D.T., HANSEN, A.K., KESNER, J., MAUEL, M.E., MICHAEL, P.C., MINERVINI, J.V., RADOVINSKY, A., ZHUKOVSKY, A., BOXER, A., ELLSWORTH, J.L., KARIM, I., ORTIZ, E.E. "Design and initial operation of the LDX facility". *Fusion Engineering and Design*, Vol. 81, Nos. 20-22, pp. 2731-2380, November, 2006.

[66] ZHUKOVSKY, A., SCHULTZ, J., SMITH, B., RADOVINSKY, A., GARNIER, D., FILATOV, O., BELJAKOV, S., EGOROV, V., KUCHINSKY, V., MALKOV, A., BONDARCHOUK, E., KORSUNSKY, V. and SYTNIKOV, V. "Charging Magnet for the Floating Coil of LDX". *IEEE Transactions on Applied Superconductivity*, Vol. 11, No. 1, part 2, pp. 1873-6, March 2001.

[67] SCHWINGER, J., DeRAAD, L.L, MILTON, K.A, and TSAI, W. *Classical Electrodynamics*, pages 334–5. Westview Press, Boulder, CO, 1998.

[68] JACKSON, J.D. *Classical Electrodynamics*, § 5.5. John Wiley and Sons, Inc., New York, NY, second edition, 1998.

[69] HANSEN, A.K., MAHAR, S., BOXER, A.C., ELLSWORTH, J.L, GARNIER, D.T., KARIM, I., KESNER, J., MAUEL, M., ORTIZ, E.E. "Initial Results of Multi-Frequency Electron Cyclotron Heating in the Levitated Dipole Experiment". In *16th Topical Conference on Radiofrequency Power in Plasmas*, Park City, UT, April 11, 2005. AIP.

[70] ORTIZ, E.E. *Observation of the Hot Electron Interchange Instability in a High Beta Dipolar Confined Plasma.* PhD dissertation, Columbia University, Department of Applied Physics, 2007.

[71] KARIM, I. *Equilibrium and Stability Studies of Plasmas Confined in a Dipole Magnetic Field Using Magnetic Measurements.* PhD dissertation, MIT, Department of Nuclear Engineering, 2007.

[72] GARNIER, D., HANSEN, A. MAUEL, M., ORTIZ, E., BOXER, A., ELLSWORTH, J., KARIM, I., KESNER J., MAHAR, S. and ROACH, A. . "Production and study of high-beta plasmas confined by a superconducting dipole magnet ". *Physics of Plasmas*, Vol. 13, No. 5, 056111, May, 2005.

[73] GARNIER, D.T., BOXER, A.C., ELLSWORTH, J.L, HANSEN, A.K., KARIM, I., KESNER, J., MAUEL, M.E., ORTIZ, E.E. and ROACH, A. "Stabilization of a low-frequency instability in a dipole plasma". *Journal of Plasma Physics*, doi:10.1017/S0022377808007071, Accepted for publication, April, 2008.

[74] STIX, T.H. *Waves in Plasmas*, chapter 1. AIP Press, New York, 1992.

[75] HARTFUSS, H.J., GEIST, T. and HIRSCH, M. "Heterodyne methods in millimetre wave plasma diagnostics with applications to ECE, interferometry and reflectometry". *Plasma Physics and Controlled Fusion*, Vol. 39, No. 11, pp. 1693-1769, November, 1997.

[76] DONNÉ, A.J.H. "High spatial resolution interferometry and polarimetry in hot plasmas". *Review of Scientific Instruments*, Vol. 66, No. 6, pp. 3407-23, June, 1995.

[77] DOMIER, C.W., PEEBLES, W.A. and LUHMANN Jr., N.C. "Millimeter-wave interferometer for measuring plasma electron density". *Review of Scientific Instruments*, Vol. 59, No. 8, pp. 1588-90, August, 1988.

[78] BALANIS C.A. *Antenna Theory: Analysis and Design*, § 2.18. John Wiley & Sons, Inc., New York, NY, second edition, 1997.

[79] MILLITECH Technical Note. "Overview of Calculating System Minimum Detectable Signal". Rev. 01C091701. © Millitech, LLC.

[80] BALANIS, C.A.. *Antenna Theory*. op. cit., §2.17.

[81] HEALD, M.A. and WHARTON, C.B. *Plasma Diagnositcs with Microwaves*, § 9.1.1. Robert E. Krieger Publishing Co., Huntington, NY, 1978.

[82] ibid., §9.3.

[83] HUTCHINSON, I.H. *Principles of Plasma Diagnostics*, § 4.2. Cambridge University Press, Cambridge, UK, second edition, 2002.

[84] LIDE, D.R., ed. *CRC Handbook of Chemistry and Physics*, § 13-5. CRC Press., Boca Raton, FL, 84th edition, 2003.

[85] HEALD, M.A. and WHARTON, C.B. *Plasma Diagnositcs with Microwaves*. op. cit., §3.3.

[86] HUTCHINSON, I.H. *Principles of Plasma Diagnostics*. op. cit., §4.3.

[87] ibid., §4.4.

[88] ibid., eq. 3.2.20.

[89] BORN, M. and WOLF, E. *Principles of Optics*, § 3.2. Cambridge University Press, Cambridge, UK, 7th edition, 2002.

[90] ibid.

[91] HEALD, M.A. and WHARTON, C.B. *Plasma Diagnositcs with Microwaves*. op. cit., Chapter 4.

[92] NIST Electron-Impact Cross Section Database. http://physics.nist.gov/PhysRefData/Ionization/intro.html.

[93] KIM, Y., Rudd, M.E. "Binary-encounter-dipole model for electron-impact ionization". *Physical Review A*, Vol. 50, No. 5, pp. 3954-67, November, 1994.

[94] GARCIA, O.E. "Collective motions in non-uniformly magnetized plasmas". *European Journal of Physics*, Vol. 24, No. 4, pp. 331-9, July, 2003.

[95] DAGLIS, I.A., THORNE, R.M., BAUMJOHANN, W. and ORSINI, S. "The Terrestrial Ring Current: Origin, Formation, and Decay". *Reviews of Geophysics*, Vol. 37, No. 4, pp. 407-38, November, 1999.

[96] DESSLER, A.J. and PARKER, E.N. "Hydromagnetic Theory of Geomagnetic Storms". *Journal of Geophysical Research*, Vol. 64, No. 12, pp. 2239-52, December, 1959.

[97] WINGERDEN, B.V., WAGENAAR, R.W. and DE HEER, F.J. . "Total cross sections for electron scattering by molecular hydrogen". *Journal of Physics B*, Vol. 13, No. 17, pp. 3481-91, September, 1980.

[98] NRL Plasma Formulary. Huba, J.D., ed. 2002 Revised Edition. Office of Naval Research. Arlington, VA, p. 32.

[99] LIEBERMAN, M.A. and LICHTENBERG, A.J. *Principles of Plasma Discharges and Materials Processing*, § 10.2. John Wiley and Sons, New York, NY, 1994.

[100] OGAWA, Y., MORIKAWA, J., OHKUNI, K., YAMAKOSHI, S., GOTO, T., MITO, T., YANAGI, N. and IWAKUMA, M. "ECH Plasma Experiments on an Internal Coil Device with a High Temperature Superconductor Coil". *Fusion Science and Technology*, Vol. 47, No. 1T, pp. 63-70, January, 2005.

[101] YATSUKA, E., SAKATA, D., KINJO, K., MORIKAWA, J. and OGAWA, Y. "Direct Measurement of a Mode-Converted Electron Bernstein Wave in the Internal Coil Device Mini-RT". *Plasma and Fusion Research: Rapid Communications*, Vol. 3, 013, 2008.

[102] PODESTÁ, M., FASOLI, A., LABIT, B., McGRATH, M., MÜLER, S.H. and POLI, F.M. "Plasma production by low-field side injection of electron cyclotron waves in a simple magnetized torus". *Plasma Physics and Controlled Fusion*, Vol. 47, No. 11, pp. 1989-2002, November, 2005.

[103] GREK, B. and PORKOLAB, M. "Observation of Plasma Heating Due to Parametric Instabilities at the Upper Hybrid and at the Cyclotron Harmonic Frequencies". *Physical Review Letters*, Vol. 30, No. 18, pp. 836-9, April, 1973.

[104] OKABAYASHI, M., CHEN, K. and PORKOLAB, M. "Experimental Investigation of Plasma Heating by a High-Frequency Electric Field near the Electron Cyclotron Resonance in the FM-1 Spherator". *Physical Review Letters*, Vol. 31, No. 18, pp. 1113-6, October, 1973.

[105] HASEGAWA, A. "Self-organization processes in continuous media". *Advances in Physics*, Vol. 34, No. 1, pp. 1-42, January, 1985.